Single-Molecule Studies of Ion Channels Expressing Unnatural Amino Acids

Thesis by:

Jai Anand Pattur Shanata

In Partial Fulfillment of the Requirements

for the Degree of

Doctor of Philosophy

California Institute of Technology

Pasadena, CA 91125

2011

(Defended June 1, 2011)

Dedicated to Brandi Shanata
The best partner I could hope for
Whose kindness, intelligence, and support
Surpass my wildest dreams every*day*

Acknowledgments

This section is important; I started it ~ 5 years ago—it is the first section of my thesis that I began writing. In many ways it is still a work in progress, but I hope that it now at least conveys a sense of my appreciation for the incredible support I have received both specifically here at Caltech and broadly in getting to this stage in my life. I will acknowledge people from several categories: research mentors, members of the Dougherty and Lester Labs, other academic resources, the GSC, Student Affairs, and Caltech Administration, my pre-Caltech education, my family and friends, and a variety of other support.

Research Mentors

Professor Dennis Dougherty is a truly special person. A gifted scientist, he is also incredibly funny and empathetic. Dennis is an awesome adviser who was a great fit for me. I cannot possibly think of a way to express my gratitude or convey the incredible support he provided me in just a few words. So, while Dennis is generally a man of few words, I will take the liberty to use a few extra words, as is my nature, to try to recognize some of the many ways in which he supported me.

Throughout my time in the Dougherty group, I had a weekly meeting with Dennis. On numerous occasions, I left Dennis' office with a significantly different outlook than when I entered it. A specific subset of ~ 10 roughly 30 minute conversations are probably the most insightful, revolutionary, and critical to the

development of my scientific thinking: certainly they constitute the most productive 5 hours in my graduate career. Dennis made those happen and knew when to make them happen (I don't know how!).

Whether Dennis fully realized it or not, > 95% of the time he gave exactly what I needed: interesting discussions of science, encouragement, and even the occasional gentle but firm push to counteract my perfectionist nature and propel me to the finish line. In an extremely important way, Dennis taught me not to care so much about details, when they aren't important—his comments on my inveterate editing were very didactic! Dennis' capacity to motivate, reassure, and ultimately inspire the best in his graduate students is, as far as I can tell, unparalleled. In many ways, this seems to arise from the fact that Dennis highly tailors his mentoring to each of his graduate students as individuals. At the core, his expectations of us are what we need to reach the goals that we each articulate for ourselves. Yet, they are consistently high expectations. As Dennis put it once—a good sign that we're engaged in our research project is that we're thinking about our science in our morning showers. And yet, Dennis also strongly demonstrates the value and importance of time with family and friends, as well as taking vacation.

Perhaps one of Dennis' qualities that has consistently impressed me most is his understanding of the mundane (i.e., banal notation) *and also scientific concepts* at a general level. This makes communication with him facile (one doesn't have to sweat the details), but also highlights his approach to science. So-called experts in a field may thrive based on their 'deep' understanding of

their subject, but Dennis adds to this an important desire to understand broader impacts of our research, and the role of science and teaching in the world. Dennis regularly impressed me with his ability to see from different perspectives —he doesn't need standardized forms of presentation, he just gets it.

Early in my time at Caltech, Dennis opened my eyes to an unfortunate reality—we have far too little time both in graduate school and life. This forced me to think more carefully about the commitments that I took on both in lab and more broadly in life. I still find this limiting reality to be deeply saddening, but Dennis' clear early guidance on this issue helped me to overcome a frantic effort to take on every worthwhile experiment and task and focus on a few of the most important. I particularly want to recognize Dennis' resolute support of my interests outside of lab—TAing, GSC academics committee, GSC Chair, and taking a sabbatical for an external teaching experience. These greatly enhanced my career. Dennis has been a stalwart advocate of his students, even when it was not necessarily in the immediate best interest of that student's experiments in lab. Perhaps this is because he recognizes the importance of the whole person to the development of good scientists.

Professor Henry Lester is great on a log. By this, I mean that my one-on-one conversations with Henry have always been fantastic, personalized learning experiences. I particularly enjoyed the few occasions that Henry jumped into lab with me. Henry also made it a point to specifically inquire about how I felt about my projects, progress, and life. His questions sparked organic conversations,

which gave me an opportunity to reflect on my time in the lab and how I felt both intellectually and emotionally—something that I always wanted and planned to do more of but which otherwise rarely happens.

While Henry is well known for his infectious passion for science, I had the opportunity of seeing Henry in other capacities beyond the lab. From his time as Chair of the Faculty Board, Henry made a strong impression on me when he commented ‘if a few students come to me with a concern, then I have to do something about it’. Later, as Chair of the Caltech Mental Health Task Force (MHTF), Henry and some of his committee members attended dinners that the Graduate Student Council hosted to discuss graduate student mental health and invited us to present our findings to the full task force.

From sharing his excitement about science, to caring about me as a person, to working together on quality of life issues for graduate students, Henry has been an instrumental part of my time here at Caltech.

Bruce Cohen taught me both about performing single-channel recording and data analysis in QuB. He also shared his deep understanding and knowledge of background literature with me. For the first year-and-a-half at Caltech, Bruce was, in many ways, the direct mentor to whom I was closest and, as a result, shaped the scientist I am today.

Bruce helped me to think beyond my immediate experiments to what the implications are, and how my results fit (or don’t) into the bigger picture of science. At the same time, he helped me to realize the importance of every

single piece of data, especially for single-channel recording. I also greatly appreciate that, throughout my time at Caltech, Bruce has clearly been interested in my success and willing to give strong advice about how to achieve my career goals.

My science and professional life have greatly benefitted from conversations with the three other members of my Thesis Committee: Professor Peter Dervan, Professor Doug Rees, and Professor Bil Clemons. As my Committee Chair, Peter has given me useful advice and taken a clear interest in my career. In addition to being on my Thesis Committee, I had the opportunity to TA Chem 1B with Doug for two years. I appreciate Doug's thoughtful approach both to the specific course material and to the way we taught it.

Dougherty and Lester Labs

In addition to these fabulous mentors, I would like to acknowledge the support, both scientifically and personally, that I received from other graduate students, SURFs (Summer Undergraduate Research Fellows), and high school student interns, in the Dougherty group as well as postdocs and graduate students in the Lester lab. Although for advice and discussion of single-channel experiments and results, my three mentors were my first stop, for everything else, I turned primarily to those in my bay. My time at Caltech was greatly enhanced by ***hundreds*** of conversations with Mike Torrice, Amy Eastwood, Kiowa Bower, Katie McMenimen, Ariele Hanek, Sean Kedrowski, Angela Blum,

Nyssa Puskar, Darren Nakamura, Maggie Thompson, and Jinti Wang. My science benefited significantly from collaborations with several lab-mates, including separate projects with: Kristin Gleitsman and Shawna Frazier, Joanne Xiu and Nyssa Puskar, Ximena Da Silva, Angela Blum, and Nyssa Puskar, and Maggie Thompson.

I would like to thank Lori Lee for taking the time to be my first mentor in the Dougherty group, before I had even officially joined, and introducing me to some of the lab's molecular biology as well as the people. Mike Torrice was a cohesive, nucleating force in lab. I had the fortune of sitting next to him for my first 3 years and it wasn't unusual for our conversation topics to range from free will, to race, to improving the editorial standards of Chemical and Engineering News photographs, to race, to creating graphs of the distribution of the political affiliations of the lab. And we would start again the next day. Overall, Mike taught me that people are more resilient than they might seem and my life is richer for talking and laughing with him. Mike is also a talented scientist, and I appreciate his feedback on my candidacy proposals and numerous discussions about our science.

Ariele Hanek taught me to use the OpusXpress early in my time in lab. Then, for the next few years, she continued to be a considerate lab mate with great advice on science and life. Ariele also provided useful feedback on my candidacy research report. Kiowa Bower was a good friend and supportive lab mate throughout my time in the Dougherty group. He brought a very positive attitude to lab every day and is an incredibly caring person. He, too, provided

thoughtful feedback on my candidacy research report. Kristin Gleitsman is as inspired a scientist as she is a mother. I genuinely enjoyed working with her on what turned into the 'ELFCAR' project (Chapter 3) and the hard work she puts into her science makes her a great collaborator. She also has a breadth of interest and talents in science—from lab to computational work. Kristin's dedication to her students as a TA encouraged me to work harder as a TA for Chem 1B and helped to keep up my interest and enthusiasm in teaching during graduate school. In addition to the graduate students who I worked directly with on single-channel recording (Shawna Frazier, Maggie Thompson, and Ximena Da Silva), I strongly appreciate the effort that Kristin, Ariele, and Kiowa made to learn the strengths and weaknesses of single-channel recording and help to integrate this new type of data into our lab.

While our research projects never significantly overlapped, Sean Kedrowski and I did bond over our enthusiasm for talking about stocks, science, and politics. I enjoyed working with Kay Limapichat (as well as Katy Muzikar and Brinton Seashore-Ludlow) to TA Chem 3A in 2005–2006. Angela Blum shaped the lab with her rigorous work ethic and strong critical thinking skills. She is tenacious and often argues persuasively for her views. Angela and I made time on several occasions, though regrettably with diminishing frequency over the years, to discuss our shared interest of teaching at small liberal arts colleges. I treasure those conversations that we did have, and I look forward to continuing these mutually beneficial conversations about teaching and research in the liberal arts environment in the coming years.

I had the great pleasure of collaborating on two projects with Nyssa Puskar. She also has the gift of being able to read situations and inject the right amount of humor or seriousness. Nyssa is committed to a positive, productive lab environment and she is a genuinely good person. Noah Duffy is very thoughtful, both in his science, in his overall approach to life, and, perhaps most importantly, thoughtful of others. I truly appreciate that, sadly rare, trait of his—he's really made the Dougherty lab a better place. Maggie Thompson is a hard worker and dedicated scientist. She will succeed at whatever she puts her mind to. I particularly enjoyed the few months we spent working together on single-channel recording. Ximena da Silva impresses me. She is as thoughtful about others feelings and life as she is about the planning and execution of her projects in lab and writing. She is also much smarter than she gives herself credit for being. I've really enjoyed collaborating with Ximena on the varenicline single-channel recordings. Kristina McCleary has opted to tackle a particularly challenging set of projects. I wish her luck as she moves to push the Dougherty group's science forward. Ethan Van Arnam is someone who is excited about science, excited about life and shares his excitement freely. Because of this amazing characteristic, Ethan has been one of a few students that really helped to bring back healthy, strong energy to our lab.

Erin Lamb, too, has restored a sense of personality and vibrancy to the lab that we'd been missing for a couple of years. I was genuinely excited when Fan Liu joined the lab, albeit as a joint student with the Goddard group. The direct involvement of theory and computation again in our research will be beneficial for

everyone. Fan is also a good person and thoughtful scientist. I've only recently had a chance to start getting to know Chris Marotta, and I've been impressed. If you've followed what I've written above, then perhaps you will understand what I mean when I say that Chris seems like a great fit for our lab. He couples immense scientific curiosity with good people skills and a genuine desire to contribute to the lab as a collaborative process.

I would also like to recognize the advice of senior members of the lab: Amanda Cashin, Steve Spronk, Joanne Xiu, and Erik Rodriguez. I look forward to the contributions of the newer students in our lab: Oliver Shafaat, Tim Miles, and Clint Regan. I also enjoyed spending time with Sam Ettinger, Wesley Yu, and Laurel German, who were summer students in the Dougherty lab.

In addition to their immense help in coordinating all things Henry and Lester lab related, perhaps what I will remember most about Eloisa Imel and Purnima Deshpande is the day that we moved Opus 2 to our lab… that was an interesting experience. Purnima, and others in the Lester lab, were also incredibly helpful in finding specific DNA constructs when needed and in using Lester lab equipment. Pam Fong offered invaluable advice on minimizing and eliminating electrical noise in electrophysiological recordings.

Other Academic Resources

The Chemistry Option is the largest at Caltech and my research has benefited significantly from the support of several Caltech staff and faculty. The first line of contact and support has been the three Chemistry Option

Administrators: Dian Buchness, Laura Howe, and Agnes Tong. I have especially enjoyed working with Agnes over the past three years—she really cares about our graduate careers and us as people. There have also been three Chemistry Faculty Option Representatives during my time at Caltech: Professor Dennis Dougherty, Professor Brian Stoltz, and Professor Peter Dervan. Each has made themselves available to graduate students and left their own mark on the chemistry degree program. The broader Division—Chemistry and Chemical Engineering (CCE)—has also benefitted from the strong leadership of Division Chairs Professor David Tirrell and Professor Jackie Barton. I would also like to thank Division Administrator Paul Carroad, who is incredibly dependable and works long hours, as well as the rest of the CCE support staff whose efforts greatly improved my ability to focus on getting my research done.

Instructor Jane Raymond, had a strong desire to ensure that all Caltech undergraduates were exposed to some well-established chemical techniques, including through Chem 3A. I was a TA for her in 2005-2006. In the summer of 2009, I was invited to work on further revisions to Chem 3A, focusing on updates to the TA manual, syllabus, grading approach, and material provided to students in handouts and pre-lab lectures. The overall course revisions were coordinated by Yoshie Narui in conjunction with Professor Mitchio Okumura and Professor Doug Rees. I enjoyed working with them, appreciated this opportunity to put into action some of what I'd learned while being a lab TA and head grader for Chem

3A in 2005-2006, and look forward to the changes that a new instructor will bring to this portion of Caltech's core curriculum in chemistry.

The GSC, Student Affairs, and Caltech Administration

Beyond my research and teaching interests, I had one 'hobby' of sorts during my time at Caltech. That hobby was trying to understand and improve the graduate student experience. I primarily engaged in these pursuits via the Graduate Student Council (GSC) Board of Directors (BoD). Many members of the GSC Steering Committee and BoD were a pleasure to work with and I wish to recognize their collective efforts on behalf of graduate student quality of life: David Doll, Artemis Ailianou, Anna Beck, Becky Tucker, Phil Boettcher, Alex Lockwood, Dan Bower, Megan Dobro, Ronnie Bryan, Cory Tobin, Lauren Edgar, Jacob Sendowski, Terry Gdoutos, Deva Thevamaran, Patrick Sanan, Luke Boosey, Paul Nelson, Dmitriy Tseliakhovich, Danielle Brown, Joe Meyerowitz, Toni Lee, Rosemary Rhode, Jelena Culic-Viskota, Maggie Osburn, Rob Craig, Eve Stenson, Paul Pirogovsky, Jose Mendoza-Cortes, Trevor Currie, Milo Lin, Gloria Sheng, Brett Cornell, and Annie Liu. I never expected to participate in graduate student government; but working with these individuals makes me grateful to have had a chance to do so. I also directly benefitted in ways too numerous to name from time with this group of dedicated graduate students.

I would like to acknowledge two of those that I worked with in particular: David Doll and Artemis Ailianou. I don't know what I would have done without David. We had a tough year as Chair/Advocacy Chair. David cares about

people; he is one of the most genuinely good people I've met and incredibly dependable. I was grateful in my last several months as GSC Chair to have an active, thoughtful, and dedicated Vice Chair, who is currently the GSC Chair: Artemis Ailianou. Her approach to the GSC has continued to nurture the relationships that we've been building across Caltech and she's played an uncompromising role in reaching out to graduate students across the institute: her compassion is inspiring.

Between May and July of 2009, Caltech lost three students. A fourth death occurred in December and a faculty suicide occurred in January of 2010, Professor Andrew Lange. I acknowledge Brian, Jackson, Long, Daphne, and Andrew because I learned from them how the Caltech community could come together in the face of great personal adversity. I genuinely believe that Caltech is a better place after the mid- and long-term response to these tragedies.

I have a tremendous amount of respect for Professor Joe Shepherd, who has one of the hardest sets of jobs on campus—in addition to his 'day job' of being a faculty member, research mentor, instructor, etc., he also takes on a phenomenal amount of administrative work to try to help graduate students as Dean of Graduate Studies. As if he didn't have enough on his plate, Joe also generously took time to serve as a mentor to me. One instance that stands out are his words to me before I made a few remarks at a community gathering in

response to Jackson Wang's death. In both serious, such as that, and light moments, Joe has shared his experience and knowledge with me.

During my time as GSC Chair, I had a weekly meeting with Dr. Felicia Hunt and we grew into our roles together. Over those months I came to know and understand that graduate students were not only in good hands but also in the hands of a good person. She single-handedly managed to assure me that many of the concerns facing graduate students were shared concerns of Caltech's faculty, administrators, and staff. I did my best, though not always successfully, to convey this truth to graduate students.

After coming to understand Felicia's uncompromising commitment to graduate student quality of life, I slept much better at night. I am greatly comforted on behalf of graduate students knowing that, even as I am no longer able to dedicate time to proactively advocate for graduate student quality of life, Felicia will continue to be there hoisting the baton. As with Dennis, I'm not sure if Felicia realizes the full impact she's had on my thinking. She helped me to more directly confront stereotypes, learn to be tactful and productive, plan effectively, and in general my brain was stretched and reshaped by my interactions with Felicia. I will carry these memories and experiences with me as I move through life.

There are many other Caltech staff and administrators whose contribution to making Caltech even better I would like to acknowledge. These individuals spend long hours working for graduate students. A key group is the members of

the Graduate Studies Office. In addition to Professor Joe Shepherd and Dr. Felicia Hunt, Assistant Dean Natalie Gilmore, Icy Ma, and Gillian Bellinger have provided me with countless hours of advice and encouragement. Professor Anneila Sargent, as Vice President for Student Affairs, has provided both a compassionate ear and megaphone for improving graduate student quality of life. I also had the pleasure of working with Suzette Cummings, who kept everything moving smoothly. Perhaps more than anyone else, Tom Mannion (Senior Director of Student Activities and Programs) works tirelessly to improve student happiness and mental health—he puts in long hours to achieve these goals. Tom took the undergraduate student President and I to dinner every week. These meetings got us off campus and helped build bridges between the graduate and undergraduate communities. Dimitris Sakellariou helped the GSC to understand the financial limitations and opportunities available to us, patiently walking us through a complicated situation. I also wish to recognize Peter Daily and Caltech Dining Services who have come through for graduate students at numerous difficult times. I learned a lot from Professor Melany Hunt (Vice Provost) about teaching quality at Caltech. I also appreciate that Melany has lent her support to the Caltech Project for Effective Teaching (CPET) teaching certificate program. Julia McCallin and a wide variety of staff in Human Resources worked with graduate students to ensure good benefits. Specifically, I appreciate Julia's work on the MHTF and Angelica Santana's tireless efforts on health care negotiations.

I hope that Dr. Kevin Austin knows the extent to which his views are respected by Caltech faculty and across the institute. As one example, I emailed a couple of faculty in chemistry after Long Phan's death asking them about any advice they had on how to proceed in terms of response. They both got back to me immediately with a shared single piece of advice—talk to Kevin because he will know what to do. They were absolutely correct. The entire Caltech Health and Counseling Center, nurses, doctors, and staff, work hard at keeping all students as physically and mentally health as is possible in a highly stressful and intense environment. The student community at Caltech also greatly benefits from the work of Dr. Lee Coleman, Training Director of the Counseling Center. I have also had an opportunity to see firsthand how Kevin and Lee provide frontline and long-term support of graduate students—they are incredible resources for us all.

There are many other offices that have made my graduate experience better including: the registrar's office and the bursar's office, to name just a few.

In 2007 President Jean-Lou Chameau gave a talk on teaching as part of the CPET seminar series. It was refreshing to hear a university president discuss the role of teaching at a research institute. In particular, Jean-Lou emphasized the role of teaching through mentoring of research students. During my time as GSC Chair in 2009-2010, I had ample opportunity to interact with Jean-Lou and I've found him to be strong supporter of graduate students. I am also deeply moved by Jean-Lou's combination of kindness, intelligence, thoughtfulness, and empathy. Under his guidance, Caltech has become and will

continue to be a better place. Graduate students have also benefitted from the hospitality of Dr. Carol Carmichael.

My Pre-Caltech Education

I would also like to acknowledge the dozens of teachers that I had in elementary school (Kainalu Elementary), middle school (Castle Rock Middle School), and high school (Douglas County High School). I was fortunate enough to have had a great and supportive learning environment throughout these steps, and especially from the International Baccalaureate (IB) program at Douglas County High School. Public education in the US worked for me. Another influential figure during middle and high school was my Scout Master Michael Kruger. Without his leadership and scouting, I would have done very little other than school work during this time in my life.

My primary scientific mentoring began in college. I had the incredible opportunity to learn—both in class/lab and out—from every member of the Cornell College Chemistry Department. Professor Charley Liberko was my first research mentor. He was hands on in lab with us when we wanted him to be, and gave us plenty of room to learn on our own. I *loved* taking his organic chemistry classes. I'm also thankful for Professor Jeff Cardon who, both as a research mentor and professor in multiple classes, taught me to think carefully about experiments during the planning stage. Another Cornell chemist who taught me the value of being careful and thorough—in this case in calculations

and executing experiments—was Professor Truman Jordan. Truman was also my advisor for my first year at Cornell College. The confidence he expressed in me from day 1 helped me to tackle tough material and enjoy it. Professor Cindy Strong is *incredibly* smart and *immensely* caring. Advanced Analytical Chemistry with Cindy was one of the most enjoyable courses I've ever taken—and helped me to see some of the many ways in which chemistry is applied. Professor Addison Ault has more passion and enthusiasm for organic chemistry than anyone else I know. He is a great role model and inspiration to generations of aspiring organic chemists. Professor Craig Teague set high expectations for us in physical chemistry and provided a rigorous learning environment. Andrea Pionek was a great resource as a lab instructor. Linda Halsey was a great support, especially in my roles as a research student and chemistry department tutor. As a whole, I am immensely humbled by the time and effort that the Cornell College Chemistry Department made for me as a student. As a student, I particularly enjoyed conversations on a range of topics with Charley and Craig.

The Cornell biologists and physicists also challenged me and ensured that I received a top-notch education: Professors Craig Tepper, Andy McCollum, Marty Cardon, Barbara Christie-Pope, Bob Black, Kara Beauchamp, Derin Sherman, and Lyle Lichty. I wish to thank Carol Brokel for creating a sense of community among scientists at Cornell College

I also had the tremendous benefit of taking courses and working with each member of Cornell's philosophy department: Professor Paul Gray, Professor Jim White, and Professor Karen Brown. Professor Jim White was my mentor through

my philosophy honors project. I truly appreciate his advice and guidance as I tackled the field of philosophy of mind. Jim also taught me the incredible value of studying philosophy, a field which is underappreciated by some, yet foundational to every aspect of the human experience.

During college, Brandi and I had the pleasure of being members of Rho Zeta Omicron (The Rhozes). The Rhozes are a special, caring, and responsible group of young women whose community service, academic record, and campus presence greatly enhance the Cornell community. They continue to be a strong support network for us.

I had the great fortune of returning to Cornell College for 5 months in the fall and winter of 2010-2011 to teach general chemistry and organic chemistry. During this time, I *once again* received unparalleled support and guidance from **each** of the Cornell faculty listed above as well as many staff. In addition I had productive conversations with the newest member of the Chemistry and Biology Departments, Professor Brian Nowak-Thompson, and Biology Department (Professor Leonard Gannes), and enjoyed working with Diane Gingerich-Feil, Laboratory Instructor, and the new stockroom manager, Jana Klein. I would especially like to recognize Professor Craig Teague, who went above and beyond his duties as Department Chair in supporting me as I taught my first courses. Craig not only coordinated office space, IT, and course support, he also made opportunities for me to see the non-teaching aspects of what faculty do.

He even covered classes for me when I went on job interviews. Craig continues to be a great mentor and friend.

Family and Friends

My dad (Jagy Pattur) is a true humanist—he taught me, both through his thoughts and actions, what it means to think and live a life that puts an emphasis on people. He taught be to able cry about sad things (and there are lot of those); then, to stand up and do something about them. He likes the phrase 'breaking out of the mold' and taught me to value this type of out-of-the-box thinking that I've found invaluable as a scientist. One of hundreds of instances of my dad putting his beliefs into action occurred when we were buying a Christmas tree many years ago. It was snowing, and the high school student who was working that night was particularly polite and helped secure the tree to the top of the car even in the bitter cold. My dad pulled out a few dollars to tip him, but the kid replied that his manager didn't allow him to accept tips. My dad's reply was: "I can give money to whoever I want to."

I will treasure many fond memories of my dad, including a night when I was 8 years old and we stayed up together (until 11 pm!) working on math problems for me to get caught up after I was sick. I also appreciate his years of involvement in Boy Scouts. For two Indians who had just come from Hawaii, sleeping overnight in an igloo built of snow was a pretty remarkable experience less than a year after arriving in Colorado.

When we got married, Brandi and I selected, as a guiding principle, a core value that we hold; that of peace. In the last several months, my dad has upped the ante in raising the value that society places on making thoughtful, peaceful discourse and actions more prevalent. These pictures speak for themselves:

Figure 1. My dad's motorhome

Figure 2. In addition to the numerous peace symbols on my dad's new car, he has chosen the license plate "Shanata", the last name that Brandi and I selected: it means "peaceful".

During my time in graduate school, as I continued to strike out on my own as a newlywed passionate about science, I also came to learn that my mom (Marquita Pattur) knew more about me than I thought she did. When I expressed my interest in a new possible career path, my mom wasn't at all surprised, rather she immediately supported me in what had taken me years to figure out. This willingness to help me forge my own path wasn't new. My Mom gave me lots of freedom as I grew up, from choosing whether I was ready for kindergarten to my own hair style (even when she didn't like it).

My mom also helped me to value learning broadly. During my 6th grade year, my mom, dad, and I lived in and traveled across the US (all contiguous 48 states) in a motorhome and I was homeschooled. My mom made a tremendous effort to help place my schoolwork in the context of the historical sites and natural wonders that we were visiting. As a result, starting with middle school I had a whole new perspective, and learning has been a core value of mine since then.

I guess it could go without saying that I will never be able to repay my parents for everything that they've done for me over the past few decades – but I will say it anyway. They provided me with a happy childhood, a loving environment, and the financial and emotional support to get me to college. More importantly, my parents taught me, and still maintain, that *I can do anything*. That's exactly what parents should teach their children, and I believe it is true.

The support and encouragement of my wife's family, including Dennis Logan, Mary Logan, and Ashli Logan, has meant a lot to me, too. Spending time

with them is always a welcome escape from work, and a truly relaxing experience. They have provided a caring and supportive home away from home.

The second to last person I would like to acknowledge is Mark Kendall. As my best friend for over a decade, in many ways no one understands me better than Mark does. He has been an incredible source of emotional support and has dedicated countless hours to listening to me; he always makes time to do so.

Laughter may not be the best medicine, but it is close. I've spent more time laughing—many times literally rolling on the floor while doing so—with Mark than anyone else. I suspect that that will still be true in a decade; he has a truly spectacular sense of humor. Equally important, though, is that I can always count on him. Mark is intense about what matters most, and deeply passionate about the things he values. With these qualities Mark was an incredible friend through high school, college, and the first two years of graduate school.

Then, in 2007, Mark enrolled at Caltech! Since then he has provided me with distractions when that's what I've needed, and with ample encouragement. He also has provided a valuable different perspective on my science. He (and Brandi) are the ones who read my research proposals for my proposal exam in my final year of graduate school. And, it is with Mark that I can most readily discuss what is and is not working in lab; my science even benefitted from his expertise in physics. Last but not least, Mark has also been my computer tech support, including free backup storage on his server for *all* of the single-channel

data that I've collected during the past 5 years (> 100 GB; though this represents only ~ 10% of his server's capacity).

While the driving scientific (and financial) support for my thesis work comes from Dennis, I'm a human being, and for the past decade I have received emotional support from the most incredible person I've met—my wife, Brandi Shanata. Brandi has a rare combination of intelligence, kindness, and wisdom—especially for someone so young and beautiful. I arrived at Cornell College in late August of 2001 with high expectations for the quality of education that would be available to me but with no expectations with respect to dating, let alone romance.

By mid October of 2001, I was spending every meal and evening with Brandi. I was falling in love. The phrase that Brandi and I started using early to describe our relationship was that it just felt 'natural'; we are a 'perfect match', as best as we can tell. I don't know how I got so lucky. And, there are several other characteristics that make her an exceptional partner. She has exceptionally clear thoughts and her well-formed and well-supported beliefs helped to challenge some of my stereotypes, especially early on in our relationship. Brandi also knows how to help direct my energy to more efficient pursuits. When I'm feeling that our country—or humanity as a whole—may be a bit off-track, all I have to do is think of my wife. Knowing that there are people like Brandi in this world gives me all the evidence I need to restore my confidence in humanity.

Brandi's support of me over a number of years has been a key element of my success. I will list just a few instances of times when Brandi's support has made all the difference in the world during graduate school. In my first year Brandi sustained me through the grueling combination of TAing, selecting and starting in a research lab, and taking classes. And again, in my second year, as I focused on acquiring and analyzing data for candidacy. And again, through a few years of projects with varying levels of success and the corresponding ups and downs. And again during the exceptionally busy and emotionally draining time as GSC Chair (May 2009-September 2010), Brandi played a particularly important role. During this time, her support allowed me to continue to make research progress while maintaining the duties of my elected position and explore this passion of mine. Perhaps it was during this time that Brandi's willingness to support my nontraditional sleep schedule was the most trying for her, yet she persevered to allow me to achieve my goals. And again in October 2010–February 2011, when I was a Visiting Lecturer at Cornell College, Brandi packed up a big chunk of our lives in Pasadena, moved us to Mount Vernon, Iowa, then brought us back home to Pasadena while I focused on teaching, applying for faculty positions, and going on interviews. And now, again, as I'm writing my thesis.

I've told several GSC BoD members as they retire that I wish that we had been better able to recognize their efforts. That statement is true—but infinitely more so—for Brandi. I just don't know how to express my appreciation. In many ways, I think that our success as a couple derives from our team approach. But,

for the last few years, Brandi has borne the lion's share of our 'team' work. I look forward to trying to repay her all throughout our lives together. Perhaps most of all, I look forward to raising a family together.

Other Support: Loyola University, Music, Funding, and My Computer

In my final few months as a graduate student at Caltech, I had the opportunity to begin transitioning to my new role as a faculty member at Loyola University, New Orleans. This process was facilitated by the Caltech Chemistry Ph.D. requirements of writing 3 research proposals before defending the thesis. As I finalized my research proposals for implementation at Loyola University, I had the strong support of the Loyola Chemistry Department as I completed budgets, selected a lab space, thought more about teaching, and selected a textbook to use for teaching Organic Chemistry (in conjunction with CJ Stephenson).

These details, and numerous others are just the beginning of what the next phase of my career holds for me—and I'm very grateful to have the support of the Loyola family as I move forwards. In my dozens of hours of conversations with the chemistry faculty, I have found them to be genuine and supportive. And, already, Lyle Henderson, Office Manager has been a great source of information.

During my time in graduate school, I have spent thousands of hours listening to music. Key themes that I've appreciated have included: passion,

peace, and social justice. My life-long favorite musical genre is classical music and, before graduate school when I had time to play the piano, I most enjoyed playing pieces by Mozart, but I have come to appreciate other music in the past several years, too. I am thankful to the hundreds of musicians who have shared their enjoyable, interesting, and challenging work with us.

The work described in the following pages was supported by the NIH (NS 34407; NS 11756) and the California Tobacco-Related Disease Research Program of the University of California, grant number 16RT-0160. I was also partially supported by an NRSA training grant.

Last but not least, the vast majority of non-lab bench work was, technically, performed by the computer pictured below. I just told it what to do. It listened very faithfully (usually). I truly could not have completed my thesis without it as well as the single-channel rig and a variety of other equipment described in Chapter 2.

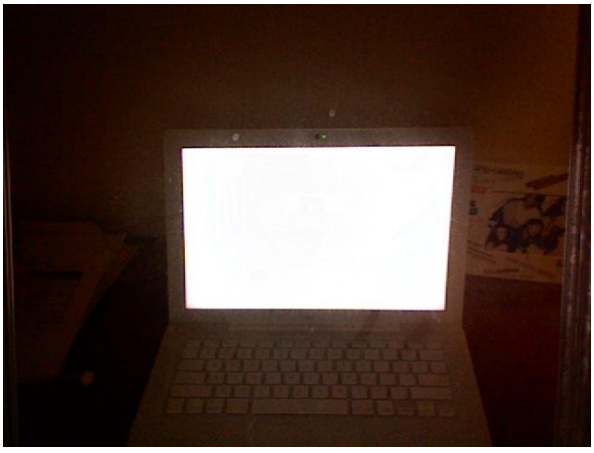

Figure 3. My computer (MacBook) for most of graduate school. Photo credit: MacBook's built in camera (with the help of a mirror)

Table of Contents

Chapter 1

Introduction:

Brains, Chemistry, and Electrophysiology

1.1 Overview and Motivation

Brains are important; really important. Don't even try to imagine your life without your brain, it will make your head hurt. Yet, a comprehensive description of human brains is not yet at hand. Why not? For one, the human brain is immensely complex. It contains hundreds of billions of nerve cells (neurons) each of which make thousands of connections (synapses) with each other. The resulting network with > 10^{14} synapses makes it the single most complex entity we know of on Earth(*1, 2*). Understanding the human brain may well present the greatest challenge science faces today.

Neuroscience aims to elucidate brain structure and function. One ultimate goal is to explain how our experiences arise from what happens in our brains. Given the unique complexity of the human brain, neuroscience also has the potential of helping us to understand what it means to be human. On the other hand, there is the possibility that humans will never be able to understand and completely describe what's physically going on in our brains. Moreover, these physical brain processes give rise to our everyday experiences may be even more complicated(*3*). There are a wide range of perspectives on the relationship between our physical body, including brain, and our experiences. Learning about the physical aspects of brains will undoubtedly help us to understand the human experience.

In reality, the grants that supported the work described in this thesis don't aim to understand the human brain with the goal of offering better explanations of the human experience. They are, in fact, *much* more targeted than that.

Fortunately, in addition to better explanations of the human experience, understanding how brains function may enable advances in a wide variety of fields including medicine, learning and memory, and control of our bodies to name just a few. Key aspects of brain function include how information is encoded and transmitted in brains. This thesis will focus on the latter.

One core type of information transfer in the brain is a signaling process that occurs at synapses. Here, an electrical signal is converted to a chemical signal when small molecules called neurotransmitters are released. These small molecules diffuse across the synaptic cleft and bind to integral membrane proteins called ion channels which are thereby activated. These neurotransmitters act as ligands for the ion channels, and the activation process of ion channels is termed gating, so these types of channels are termed ligand-gated ion channels (LGICs). LGICs mediate rapid synaptic transmission in the central nervous system (CNS) and peripheral nervous system (PNS)(*4*). In the case of the nicotinic acetylcholine receptors (nAChRs) that are the focus of this thesis, activation results in a conformational change that opens a central pore. Ions flowing through this open pore produce currents that are an electrical signal. Thus, at the synapse, an electrical signal is converted to a chemical signal, then back to an electrical signal at ion channels (**Figure 1.1**).

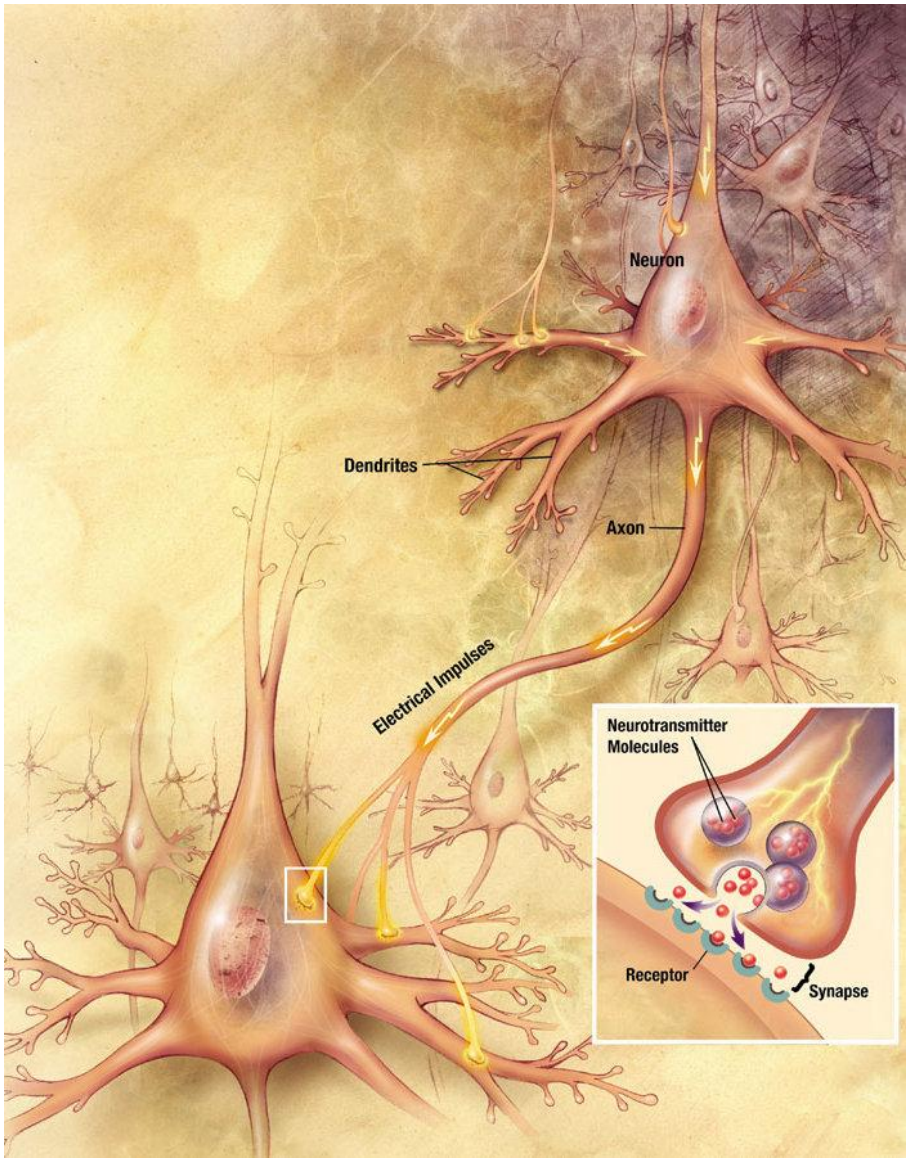

Figure 1.1. An artist's rendition of neurons, axons, synapses, and electrical and chemical signaling in brain cells. The image is taken from "Chemical Synapse", *Wikipedia: The Free Encyclopedia*, http://en.wikipedia.org/w/index.php?title=Chemical_synapse&oldid=423746201.

The control of neuroreceptors such as ion channels that regulate our thoughts and actions is, at its core, a set of chemical questions. As chemists, we seek to simplify the complexity of brains, and even individual synapses, to the interactions between a few molecules that we can probe systematically. I will

now introduce some specific ion channels and their functional environment (Section 1.2) and the general method—electrophysiology—that we use to study their function (Sections 1.3, 1.4, and 1.5). Then I will describe the use of nonsense suppression, which allows us to perform structure-function studies on neuroreceptors (Section 1.6), and summarize my dissertation work (Section 1.7).

1.2 Cell Membranes and Ion Channels

1.2.1 Electrophysiology of Cell Membranes

The cell membrane is permeable to a variety of ions through membrane spanning proteins with pores (ion channels). In the case of LGICs, when the appropriate number of agonist molecules are bound, each ion channel has a characteristic conductance (g). If the current that flows through the ion channel varies with voltage, it is called a slope conductance. Thus the current (I) flowing through the channel should vary with voltage and resistance (R) as given by **Equation 1.1.**

$$g = \frac{I}{V} = R^{-1} \qquad \textbf{(Equation 1.1)}$$

The slope conductance can be determined by making a plot of I versus V. In some cases, this plot is non-linear, a phenomena called rectification. The potential at which the current through the ion channel goes to 0 is known as the reversal potential (V_{rev}), and can vary with ion concentration, as given by the Nernst potential. Additionally, empirical studies using the single-channel recording method described below have shown that the conductance of the muscle-type nAChR varies with the monovalent ion in the order: $K^+ > Cs^+ > Na^+$

> Li^+ *(5, 6)* . Often, though, measurements can only be taken at a single voltage. In this case, conductance is reported simply with respect to the applied pipette potential; this value is known as the chord conductance.

Early studies of LGICs focused on one of many types of synapses—those found at the neuromuscular junction. These studies exploited the fact that the synapses here are more readily amenable to electrophysiological studies, as they can be impaled with multiple electrodes and be easily denervated (they are usually innvervated by only one presynaptic neuron). Thus, initial studies of synaptic transmission were done in this region, the so-called motor end plate. Separately, an ionic theory of membrane excitation was developed to describe the propagation of action potentials, with early studies of the giant squid axon revealing previously unknown kinetic properties of membrane permeability(*7, 8*). Further work by Katz and Miledi(*9, 10*) capitalized on the noise produced by acetylcholine-induced potentials to estimate channel open time.

1.2.2 Structure and Function of the Nicotinic Acetylcholine Receptors

Results of experiments in muscle-type and neuronal nAChRs are reported in this thesis. The nAChRs are members of the 'Cys loop' superfamily, which gets its name from a loop formed by a disulphide bond between two cysteine residues (**Figure 1.2**). As with other membrane proteins, LGICs are difficult to crystallize, largely due to the fact that they function simultaneously in the hydrophobic cell membrane and hydrophilic cytoplasm and extracellular matrix. Consequently, structural information about nAChRs comes from a variety of

indirect studies. For example, the acetylcholine binding protein (AChBP) is a water soluble protein with high sequence identity (15 – 28%) with the extracellular domain (ECD) of the LGICs, and it has been crystallized(*11*). Additionally, a cryo-EM structure of *Torpedo* nAChR (4 Å)(*12*) gives us structural information about the transmembrane domain (TMD), and further structural studies of variously modified Cys loop receptors continue(*13-15*).

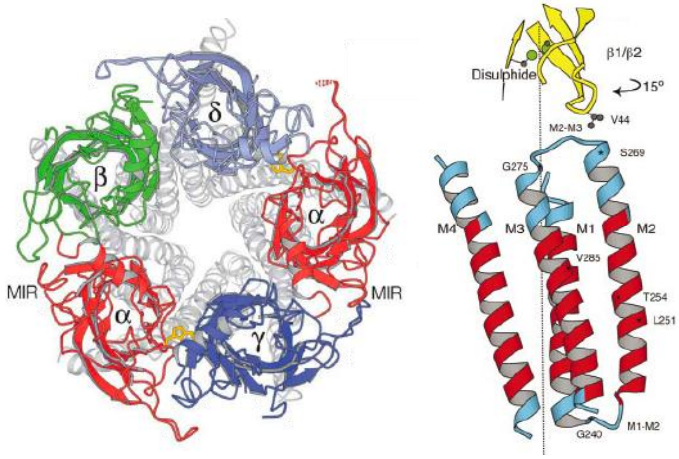

Figure 1.2. Left: nAChR pore and surrounding 5 subunits as viewed from the extracellular side. Right: The topology of the transmembrane domain α-helices, including the disulphide link at the top. M2 at the far right is the channel-lining helix and position L251 is the 9' position (see text). From(*11*)

The four membrane spanning sections (M1 – M4) of each of the five subunits are α-helices (**Figure 1.2**). M2 is found to physically line the ion channel pore, and a common numbering system(*16*) for LGICs denotes 0' as the residue found at the intracellular end of M2 and 20' as the residue at the extracellular edge of the membrane. The 9' position is a universally conserved leucine, which impacts gating of the ion channel(*17, 18*). In order for the nAChR to open, it must first bind two molecules of agonist at binding sites far removed

from the pore (~ 50 Å away, in the ECD). These two binding sites are found at the α1-δ and α1-γ interfaces for fetal nAChRs with subunit composition $(\alpha1)_2\beta1\gamma\delta$, or at the α1-δ and α1-ε interfaces for adult nAChRs with subunit composition $(\alpha1)_2\beta1\varepsilon\delta$(*5*). For the neuronal α4β2 receptor, there appear to be two functional stoichiometries: $(\alpha4)_2(\beta2)_3$ and $(\alpha4)_3(\beta2)_2$(*19, 20*). We term these A2B3 and A3B2, respectively. There are presumably two binding sites in each stoichiometry, located at the α4-β2 interfaces. This coupling of the sequential, bimolecular binding of small molecules (agonist) to the conformation (open or closed) of the channel is referred to as allostery. In order to understand what happens during this allosteric transition, information beyond the static snapshots that structural studies provide is needed.

1.3 Expression of Functional Ion Channels in *Xenopus Laevis* Oocytes

In order to study the function of ion channels, they need to be present in the cell membrane. For the experiments described in this thesis, all channels were characterized by whole-cell (Section 1.4) and/or single-molecule (Section 1.5) electrophysiology. Electrophysiology is a functional assay of ion channels. In one mode of electrophysiological recording, two electrodes are inserted into a cell. One electrode monitors the potential (voltage) relative to ground, while the other passes current in order to maintain the cell's membrane potential at a user-determined potential (voltage clamp). This technique is referred to as two-electrode voltage clamp (TEVC). Our lab has emphasized

TEVC, as well as Western blots and more recently microscopy(*21*), to make determinations about ion channel function and expression. On the other hand, single-channel recording, as the name implies, is a single-molecule technique. It provides the direct observation of the basic operational properties—opening and closing (gating)—of ion channels, one at a time.

In the experiments described here, both whole-cell and single-channel experiments were achieved by heterologous expression of LGICs in stage V or VI *Xenopus laevis* (*X. laevis*) oocytes. For expression of wild type receptors and conventional mutants, the RNA injected into oocytes is the mRNA for each subunit of the desired receptor. For expression of LGICs with site-specific incorporation of unnatural amino acids, mRNA with a stop codon (UAG) is co-injected with tRNA that has been ligated to the desired unnatural amino acid (see Section 1.6 for details). The development and implementation of these oocyte expression methods, as they pertain to optimizing recording by both single-channel and whole-cell methods, is covered in detail in Chapter 2.

The *X. laevis* oocyte is a particularly convenient heterologous expression system because the cells are large. They are ~ 1 mm in diameter for the stage V/VI oocytes that we use. RNA can be injected directly into them under a microscope(*22*). The cell is then incubated for hours to days, depending on the LGIC and the specific experiment (see **Figure 1.3** for description). One important set of controls is monitoring channels that occur natively in oocytes(*23, 24*). Details of the procedures I developed for appropriate single-channel control experiments for these endogenous channels are described in Chapter 2.

However, for both single-channel and whole-cell experiments, it is important that the outermost layer of the oocyte—follicular cells—be removed before electrophysiology is performed, and preferably before the oocyte is injected with RNA. The follicular cells themselves have channels that can interfere with accurate electrophysiological characterization.

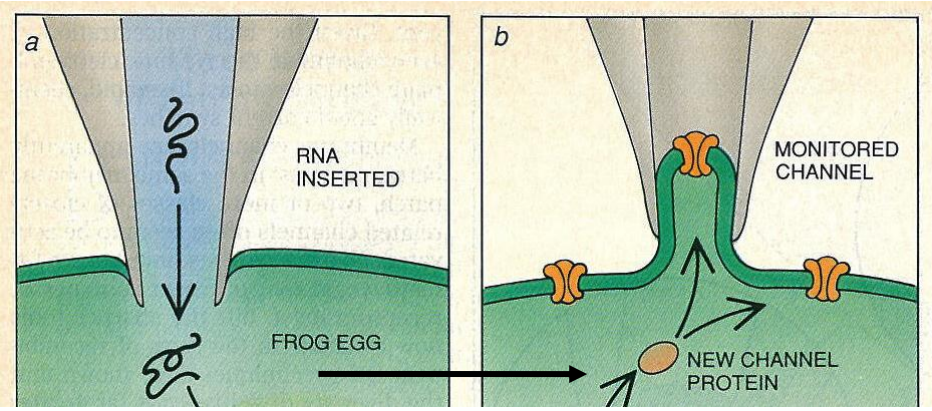

Figure 1.3. Schematic showing details of incorporation of RNA (black squiggly line) into the *X. laevis* oocyte and subsequent protein synthesis, followed by appropriate assembly of the ion channel and insertion into the oocyte's membrane. At right, the ion channel is then monitored in an electrically isolated cell-attached patch in a single-molecule experiment. In our experiments, the glass needle used to inject the RNA into the oocyte is significantly larger than the pipette used to record single-channel activity. Adapted from(*25*)

1.4 Whole-Cell Recording of LGICs

Once expressed in *X. laevis* oocytes, LGICs can be recorded *en masse* by TEVC (**Figure 1.4**). For nAChRs, typically 100,000–10,000,000 channels are expressed on an oocyte. It is the sum of the current flowing through all of these channels that is measured in TEVC. The relationship between the channels of receptors expressed and the measured whole-cell current is based on the single-channel conductance (g) and is explored in more detail in Chapter 2. Chapter 3

describes how variations in expression—measured by changes in maximal current, I_{max}—can be used to learn about channel gating and allosteric transitions.

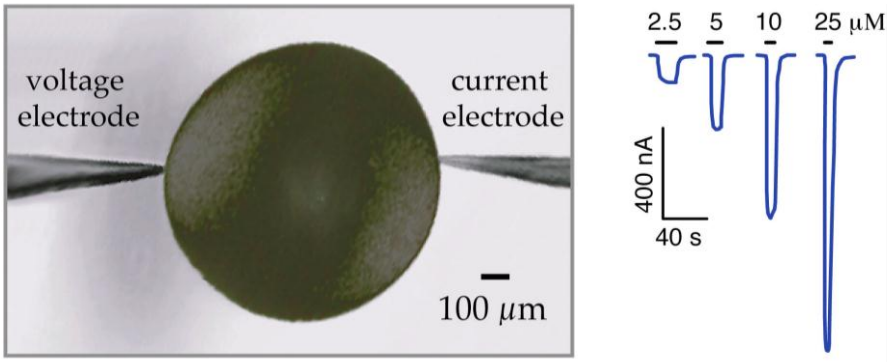

Figure 1.4. Left: TEVC on a *X. laevis* oocyte. The oocyte is impaled with two separate electrodes, defined in the figure. The scale bar represents ~ 1/10th of a typical stage V or VI oocyte's diameter (100 μm). Right: Sample traces from a TEVC experiment showing the current that must be injected into an oocyte in order to keep the oocyte at the preset potential (voltage clamp). In this case 10s to 100s of nA are required when doses of 2.5 to 25 μM are applied; the agonist is ACh. The large downward deflections represent the openings of hundreds of thousands of ion channels. Agonist is typically applied for 10 – 20 seconds, though longer drug applications may be required for low concentrations (nM), when binding can be the rate-limiting activation step.

The basic design of these experiments is to apply increasing concentrations of agonist (**Figure 1.4, Right**) until further increases to agonist concentration do not elicit further increases in the whole-cell current. The dose-response relation then is plotted and fitted to the Hill equation, **Equation 1.2** (**Figure 1.5**).

$$\frac{I}{I_{\max}} = \frac{1}{\left(1+\left(\frac{(EC_{50})}{[A]}\right)^{n_H}\right)} \qquad \textbf{(Equation 1.2)}$$

I is the current elicited at any given dose of agonist (A) and n_H is the Hill coefficient.

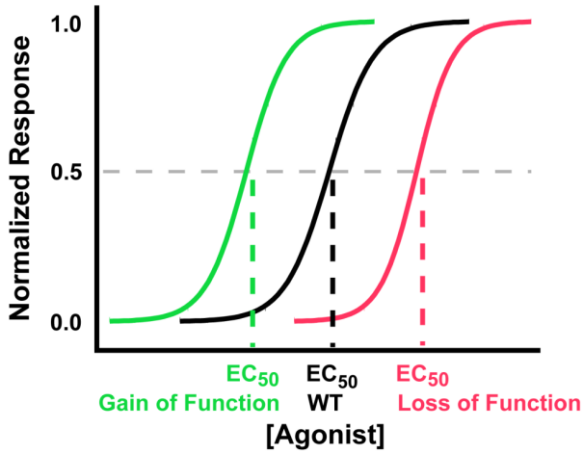

Figure 1.5. Examples of dose-response curves in which the normalized current response (I/I_{max}) is plotted against the concentration of agonist applied. In each case, the concentration needed to reach the half-maximal response, EC_{50}, is denoted with a dotted line. The black dose-response curve represents a wild type (WT) ion channel. The green dose-response curve represents a perturbation (typically a mutation or change in agonist) that caused less agonist to be needed to activate the channel. More commonly, a perturbation produces a loss of function, represented by the dark pink dose-response curve, and corresponding increase in EC_{50}. Fitting the dose-response curve to the Hill equation also produces n_H, which increases with increasing steepness of the dose-response curve. Since, in each case, responses are normalized, the dose-response curve doesn't give information about the number of receptors expressed on the oocyte. That information is in the parameter I_{max}.

1.5 Single-Channel Recording of LGICs

1.5.1 A Brief History of Single-Channel Recording

In 1976, Erwin Neher and Bert Sakmann published the first ever direct observation of current fluctuations on the order of a few picoamperes (pA) through denervated frog muscle fibers (**Figure 1.6**)(*26*).

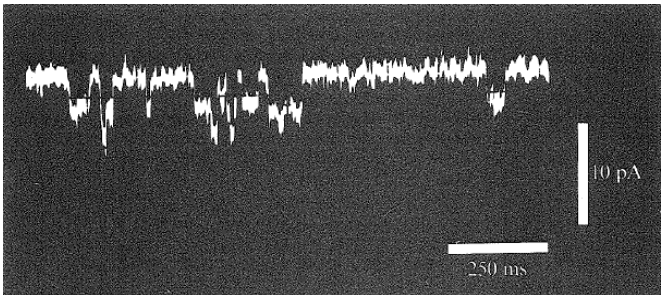

Figure 1.6. This is the first published single-channel trace, from(*27*). The recording, in frog muscle fiber, was obtained at a temperature of 8° C. The membrane potential was -120 mV and the trace is displayed at a cut-off frequency of 200 Hz. The white scale bars indicate that the trace is ~ 1 second long and that the current fluctuations are a few pA.

In these experiments, highly polished glass electrodes with inner tip diameters of 3 – 5 µm and containing Ringer's solution with 0.2 µM suberyldicholine added were gently pressed against denervated frog muscle fiber within 200 µm of two other electrodes, which were operated in TEVC mode in order to clamp the membrane potential. In doing so, Neher and Sakmann showed for the first time that the currents, which had been routinely observed during electrophysiology (i.e., on the motor endplate) were in fact comprised of unitary currents attributable to single ion channels. Unfortunately, the specific electrical characteristics (both current amplitude and event duration) that could be determined from such a recording configuration were limited by the background noise present. The technique became much more useful after a set of revisions to the method was published in 1980. This updated technique facilitated higher resistance connections between the recording electrode and cell, commonly called gigaseals(*28*). In 1981, Hamill *et al.*(*29*) outlined a set of procedures for obtaining high resistance seals on the order of 10^9 to 10^{11} ohms (1 – 100 gigaΩ) that made the technique feasible.

In 1980, Hamill and Sakmann(*30*) also demonstrated the effect of membrane potential on single-channel current. Note that the potentials for V_{memb} and $V_{pipette}$ have opposite signs (i.e., $V_{pipette} = -V_{memb} = V_{out} - V_{in}$). By convention in electrophysiology, currents flowing into the cell are shown as downward deflections. **Figure 1.7** demonstrates that the current observed increases with increasing polarization (more negative V_{memb}). Each ion channel is thought to have a characteristic conductance. These observations were just the first of many as this technique, termed single-channel recording, rapidly advanced the characterization of ion channels in various cell preparations, as well as those reconstituted in liposomes and planar lipid bilayers(*31, 32*). At present, the technique of single-channel recording is in use in hundreds of labs worldwide.

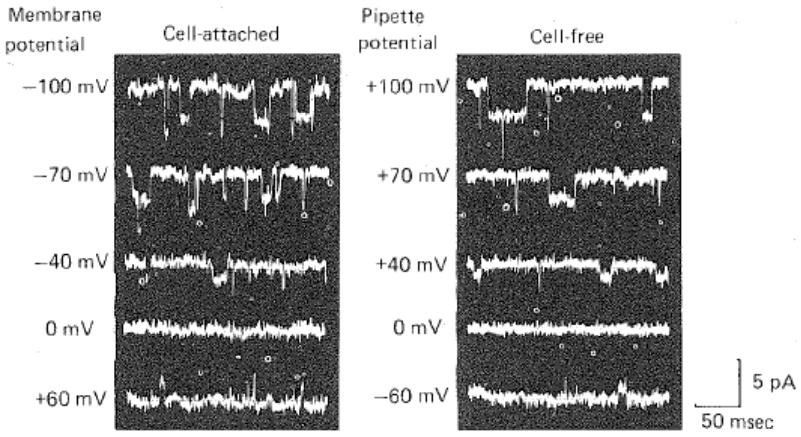

Figure 1.7. The current through nAChR channels depends on the membrane (left) and pipette (right) potentials. The current can flow either into or out of the cell or membrane patch, depending on the potential. As with whole-cell data, the convention is to show inward currents as downward deflections. Traces are from(*33*).

1.5.2 Single-Channel Recording and Ion Channel Kinetics

A significant advantage over other electrophysiology measurements, such as TEVC to measure EC_{50}, is the more specific models that can be developed from single-channel data. EC_{50} is a composite of the rate at which the agonist associates with the receptor (binding) and as well as that agonists' ability to induce the conformational change that results in current flow through the ion channel (gating). For the nAChR and assuming two equivalent binding sites, we can write a mechanism for the interrelation of various kinetically, and presumably physically, distinct configurations of the receptor. This is summarized in **Model 1.1**.

$$2A + R^c \underset{k_{-1}}{\overset{2k_1}{\rightleftharpoons}} A + AR^c \underset{2k_{-1}}{\overset{k_1}{\rightleftharpoons}} A_2R^c \underset{\alpha}{\overset{\beta}{\rightleftharpoons}} A_2R^o \qquad \textbf{(Model 1.1)}$$

Here R^c is a closed receptor and R^o is open. As with the Hill equation for whole-cell data, the EC_{50} is also related to these single-channel parameters by **Equation 1.3**(*34*).

$$EC_{50} = \frac{K_D}{\sqrt{\Theta + 2} - 1} \qquad \textbf{(Equation 1.3)}$$

This expression directly relates the macroscopic property of EC_{50} to microscopic rate constants since:

$$K_D = \frac{k_{-1}}{k_1} \text{ and, } \Theta = \frac{\beta}{\alpha} .$$

A derivation for **Equation 1.3** is provided in **Appendix A**. For large values of Θ (>> 1), EC_{50} can be approximated by(*35*):

$$EC_{50} \approx \frac{K_D}{\sqrt{\Theta}}.$$

If the binding equilibrium is saturated, then the maximal probability that a channel is open ($P_{open,max}$) depends only on the gating parameters, as is shown in **Equation 1.4**.

$$P_{open,max} = \frac{\beta}{\beta+\alpha} \qquad \textbf{(Equation 1.4)}$$

Single-channel data enable the detailed kinetics of binding and gating shown in **Model 1.1** to be determined, and as such have been an influential technique in the formulation of models of nAChR activation and gating (*36-52*). As **Equation 1.3** shows, single-channel kinetics can also be related to whole-cell measurements. Significant further discussion of performing single-channel and whole-cell recording separately and jointly can be found in Chapter 2. Significant further discussion of the theory and practice of single-channel data analysis can be found in **Appendix B**. Specific types of analysis used are summarized in the relevant chapters.

1.6 Unnatural Amino Acids and the Cation-π Interaction

In order to obtain a more detailed understanding of LGICs, a common technique is to mutate one or more amino acids by site-directed mutagenesis. This technique allows for any amino acid to be converted to one of the other 19 naturally occurring amino acids. In most cases, these mutations produce significant steric and/or electronic perturbations. As chemists, we are interested

in atomic-level control of LGICs. We achieve this with a technique called nonsense suppression, which allows for the incorporation of a nearly limitless variety of unnatural amino acids. The combination of structural changes followed by functional studies allows for physical organic chemistry to be performed on the signaling molecules that govern our thoughts and actions(*53, 54*).

1.6.1 Incorporation of Unnatural Amino Acids

We heterologously express ion channels of interest in *X. laevis* oocytes as described in Section 1.3(*22*). Unnatural amino acids are incorporated by engineering the amber stop codon (nonsense suppression) in the mRNA and a correspondingly modified anticodon of a tRNA. This suppressor tRNA is then chemically aminoacylated with the unnatural amino acid to be incorporated(*55-58*). The mRNA and tRNA are then injected into oocytes. The technique is shown in **Figure 1.8** and further details are described in the caption. This methodology has been used to incorporate a wide range of unnatural amino acids and α–hydroxyacids into various ion channels (**Figure 1.9**)(*55, 59*). Once successfully incorporated, protein function is studied using single-channel and whole-cell electrophysiology.

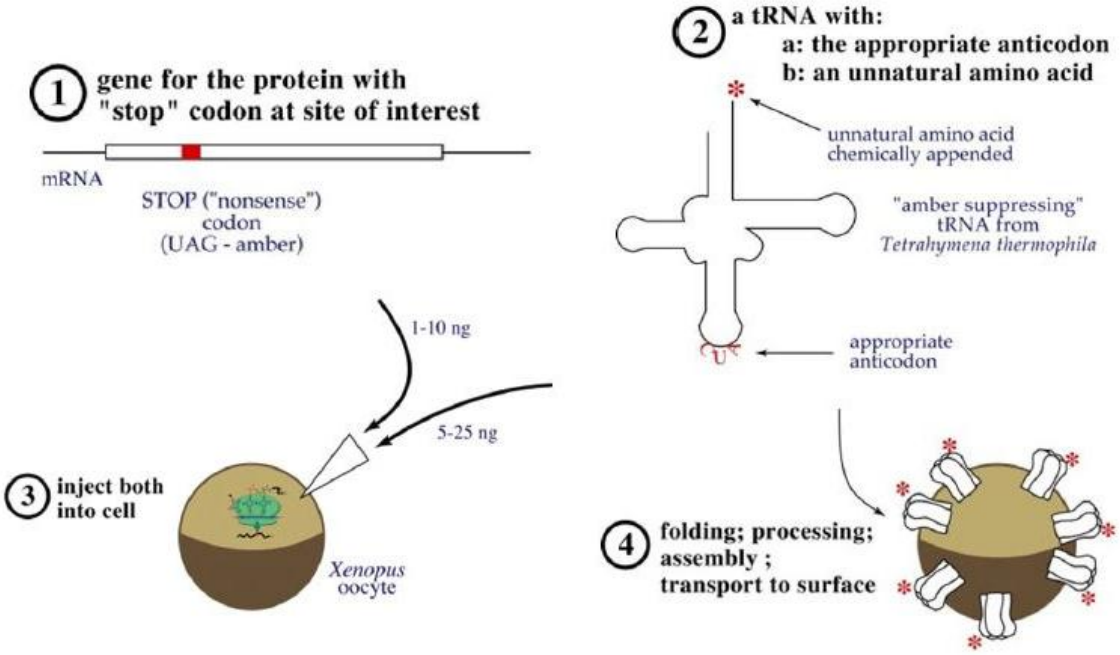

Figure 1.8. An overview of the 4-step technique for expressing ion channels with unnatural amino acids in *X. laevis* oocytes. 1) *In vitro* transcription is used to produce mRNA with the UAG stop codon at the site where the unnatural amino acid will be introduced. 2) Separately, suppressor tRNA is made, coupled to dCA, and chemically appended (ligated) to the unnatural amino acid (represented by a red asterisk, *). This unnatural amino acid will be introduced site-specificlly at the UAG codon location. 3) Several ng each of the mRNA and tRNA are co-injected into *X. laevis* oocytes. 4) The oocyte is then incubated for several hours to several days, depending on the experiment. During this time, the oocyte translates the injected mRNA into ion channels and uses the injected suppressor tRNA with an anticodon which recognizes the UAG stop codon. The result is site-specific incorporation of the unnatural amino acid in each ion channel. The oocyte then folds and assembles these mutated ion channel subunits and transports them to the cell surface, where they form functional ion channels. See Chapter 2 for detailed discussion of methods and subsequent electrophysiology that I've used to characterize these ion channels.

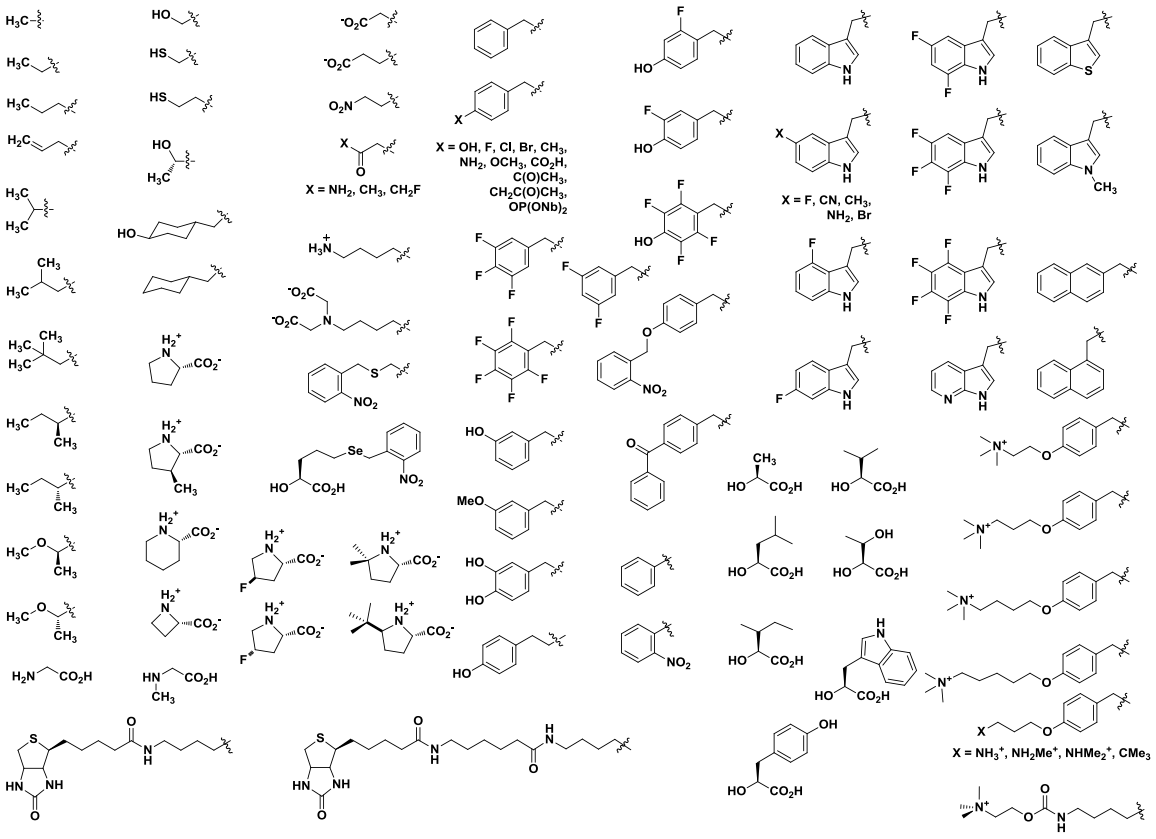

Figure 1.9. This figure shows many of the unnatural amino acid side chains that have been incorporated by nonsense suppression in the Dougherty group. The fluorinated indoles (tryptophan side chains) are the ones that are predominantly used in this thesis. They are in the upper right-hand corner.

1.6.2 The Cation-π Interaction

The electron density in the π system of aromatic rings interacts favorably with a positive charge. The resulting stabilizing interaction is termed a cation-π interaction (**Figure 1.10**)(*60*). The strength of the cation-π interaction can be modulated by altering the electron density in the aromatic ring. Fluorinated tryptophans are unnatural amino acids that provide a particularly subtle systematic perturbation series. Hydrogen and fluorine are relatively similar in size: the C—F bond is not that much longer than the C—H bond.

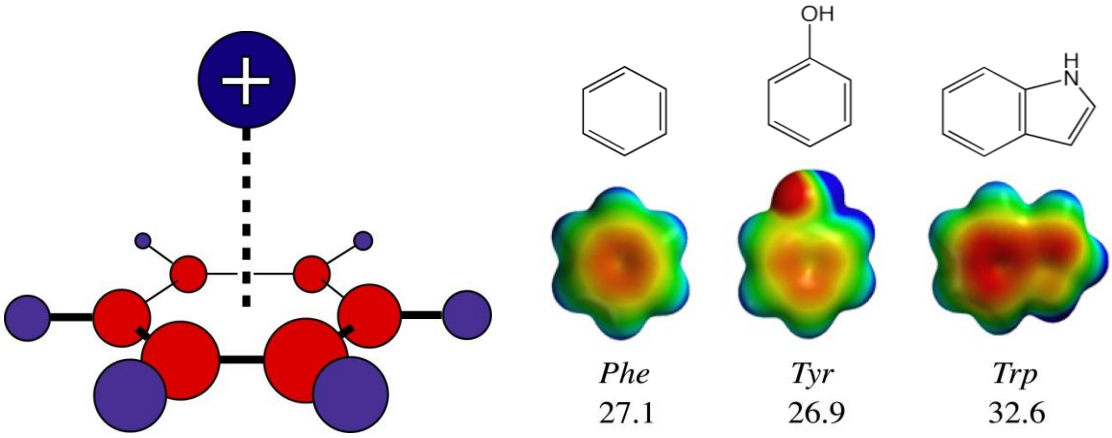

Figure 1.10. Left: A representation of the cation-π interaction—an interaction of a positive charge with the electron density of a π system in an aromatic ring. Right: The side chains of the three aromatic amino acids: Phe, Tyr, and Trp. Below each is the corresponding electrostatic potential surface. In these plots, 'warmer colors' (red and orange) represent regions of higher electron density, as measured by interaction with a probe positive charge (sodium ion). 'Colder colors' (blue) represent relatively positively charged regions. The cation-π binding abilities are given below (units: kcal mol^{-1}). Phe and Tyr have similar values, but the indole side chain of tryptophan has a significantly higher cation-π binding energy.

On the other hand, the C—F bond is significantly more polar than the C—H bond, and so swapping out a single H with F on tryptophan changes the cation-π binding ability significantly. The effect is cumulative, with each successive fluorine that is added to an aromatic ring further decreasing the electron density in the π system available to participate in the cation-π interaction (**Figure 1.11**).

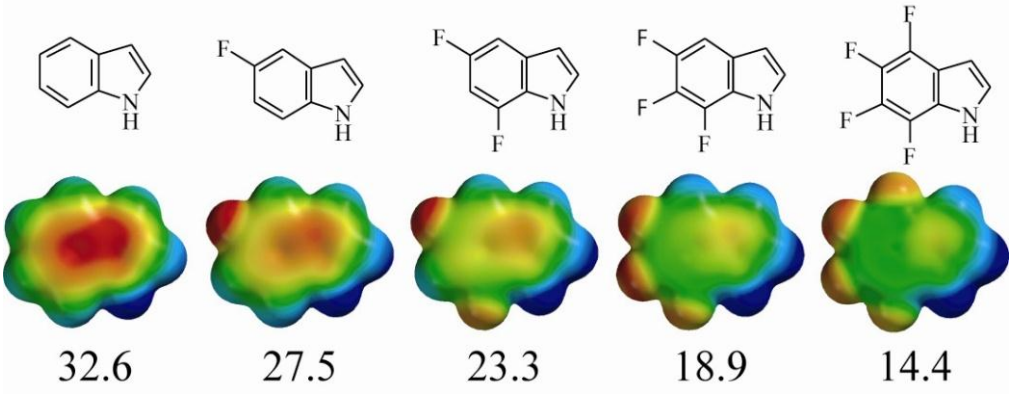

Figure 1.11. Top: from left to right, the chemical structures of indole, monofluoro-, difluoro-, trifluoro-, and tetrafluoro-indole. Middle: the calculated electrostatic potential surfaces for the same molecules in the same orientations. The color scheme has the same meaning as in the previous figure. Bottom: corresponding cation-π binding energies, in kcal mol^{-1}, for each molecule

At the binding site of Cys-loop receptors, an aromatic binding box is conserved, and for convenience the 5 residues that comprise it are often referred to based on their loops: TryA, TrpB, TyrC1, TryC2, and TrpD (**Figure 1.12**).

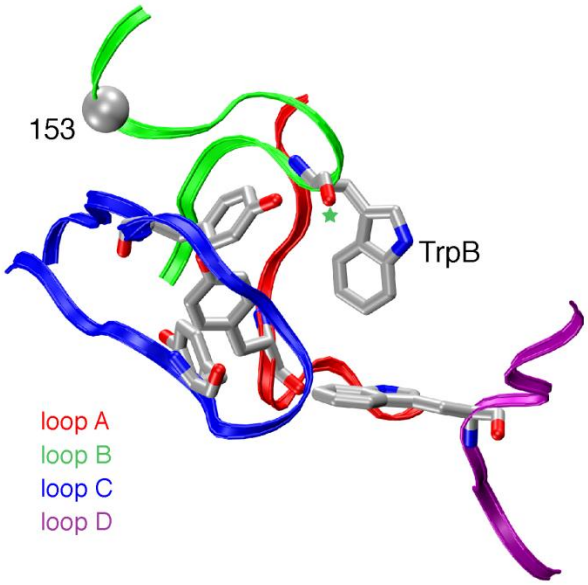

Figure 1.12. The binding site of AChBP, which is thought to resemble that of nAChRs. Loops A–D are the four principal elements that directly define the binding site. TrpB, which is the focus of studies in Chapters 3 and 5 is highlighted. Loop C contributes two aromatic residues (TyrC1 and Tyr C2). The other loops each contribute one (TyrA, TrpB, and TrpD). This image is of pdb file 1I9B(*11*).

1.6.3 A Cation-π Interaction at TrpB

The cation-π interaction is of interest in LGIC function and has wide-ranging biological significance(*60-63*), including stabilization of protein secondary structure. One study showed that 25% of all tryptophans in the Protein Data Bank (pdb) participated in a cation-π interaction(*64*). In the context of the binding site of the muscle-type nicotinic acetylcholine receptor (nAChR), a significant cation-π interaction at TrpB (α1W149) was identified by our group over a dozen years ago (**Figure 1.13**)(*65*) using the combined techniques of unnatural amino acid mutagenesis and whole-cell electrophysiology.

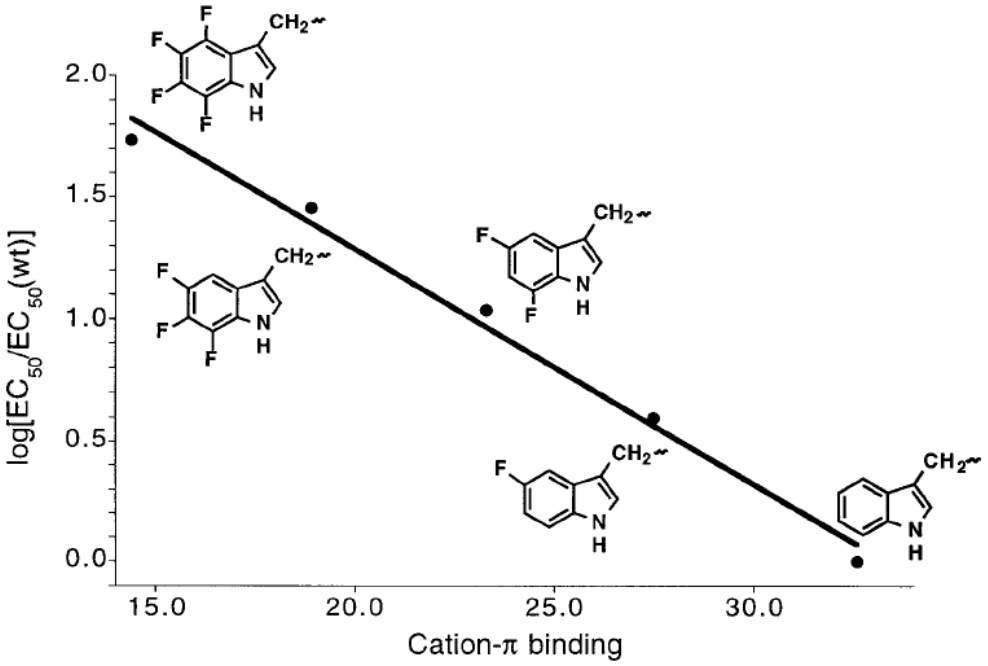

Figure 1.13. A 'fluorination plot' at α1TrpB in the fetal, muscle-type nAChR with the agonist ACh. This graph shows the relationship between the ratio of EC_{50}s for a receptor with monofluoro-, difluoro-, trifluoro-, and tetrafluoro-TrpB. Incorporated by nonsense suppression. From(*65*)

The evidence for the interaction between ACh and TrpB is the strong correlation between nAChR channel function and the decreasing cation-π binding ability of a series of increasingly fluorinated tryptophans (**Figure 1.13**). Such a systematic relationship was not found at any of the other four amino acids of the aromatic binding box. The functional measure used in these experiments was based on whole-cell electrophysiology (Section 1.5). The value measured, EC_{50}, is the concentration of agonist (A) required to elicit half-maximal current response. Because of the position of the residue (TrpB), which is not only far away from the channel gate, but specifically is in the aromatic binding box (**Figure 1.12**), the 'fluorination plot' (**Figure 1.13**) strongly suggests that ACh makes a cation-π interaction to TrpB. However, EC_{50} is an equilibrium measurement that depends on both binding and gating (**Equation 1.3**). Therefore, the increase in EC_{50} that occurs with increasing fluorination could not be definitively ascribed to either a decrease in agonist binding or a decrease in channel gating.

1.7 Dissertation Work

My dissertation aimed to provide even more convincing evidence for cation-π interactions by using single-channel recording on ion channels expressing unnatural amino acids. The first step was to build an electrophysiology rig to perform single-channel recording, and to develop techniques to combine single-channel and whole-cell recording with nonsense suppression. These methods are detailed in Chapter 2.

Having established the feasibility of the combined use of single-channel and whole-cell recording, in Chapter 3 we developed a method to identify the functional interactions of amino acids that are physically far apart in a protein. This is fundamentally a whole-cell recording method to find allosteric interactions in ion channels. The significance of this method is strongly supported by single-channel measurements. Additionally, the relationship between the single-channel gating equilibrium constant, Θ, and the whole-cell measurement of EC_{50} is considered.

In Chapter 4, I describe my progress towards measuring the channel opening rate of the fetal and adult muscle-type receptors. Multiple different agonists are used, including acetylcholine, choline, and tetramethylammonium (TMA). Single-channel data are reported for the wild-type receptors as well as for receptors with the unnatural amino acid 5-F-Trp (monofluoro-Trp). Data are reported for multiple concentrations for a mutated fetal nAChR, and QuB is used to fit various possible models and estimate a gating equilibrium constant, Θ, for this mutant.

Chapter 5 describes the combined application of single-channel, whole-cell, and unnatural amino acid mutagenesis to the specific question of how two molecules—nicotine and Chantix® (varenicline)—bind to the α4β2 brain receptor.

In Chapter 6, I describe single-channel experiments that establish a method for distinguishing between the two known stoichiometries of the wild type α4β2 receptor.

A note on nomenclature. In some of the chapters of this thesis, the muscle-type α1 receptor is referred to simply as α. This is based on the how the relevant manuscript was published and need for clarification. When not specified, the muscle-type nAChR refers to the fetal receptor: $(\alpha1)_2\beta1\gamma\delta$. In all cases, α4 is specified as such. In many instances, such as throughout Chapter 5, the receptors being studied are the α4β2 containing an L9'A mutation in the α4 subunit. In these cases, 'wild type' refers to the receptor with this pore domain mutation. On the other hand, in Chapter 6, the α4β2 is the actual wild type (rat) receptor, with no mutation in the pore domain.

1.8 References

1. Drachman, D. A. (2005) Do we have brain to spare?, *Neurology 64*, 2004-2005.
2. Kandel, E. R., Schwartz, J. H., and Jessell, T. M. (2000) *Principles of neural science*, 4th ed., McGraw-Hill, Health Professions Division, New York.
3. Damasio, A. R. (1999) How the brain creates the mind, *Sci Am 281*, 112-117.
4. Karlin, A. (2002) Emerging structure of the nicotinic acetylcholine receptors, *Nat Rev Neurosci 3*, 102-114.
5. Mishina, M., Takai, T., Imoto, K., Noda, M., Takahashi, T., Numa, S., Methfessel, C., and Sakmann, B. (1986) Molecular distinction between fetal and adult forms of muscle acetylcholine receptor, *Nature 321*, 406-411.
6. Sakmann, B., Methfessel, C., Mishina, M., Takahashi, T., Takai, T., Kurasaki, M., Fukuda, K., and Numa, S. (1985) Role of acetylcholine receptor subunits in gating of the channel, *Nature 318*, 538-543.
7. Hodgkin, A. L., and Huxley, A. F. (1945) Resting and action potentials in single nerve fibres, *The Journal of physiology 104*, 176-195.
8. Hodgkin, A. L., and Huxley, A. F. (1952) Propagation of electrical signals along giant nerve fibers, *Proceedings of the Royal Society of London. Series B, Containing papers of a Biological character 140*, 177-183.

9. Katz, B., and Miledi, R. (1970) Membrane noise produced by acetylcholine, *Nature 226*, 962-963.
10. Katz, B., and Miledi, R. (1971) Further observations on acetylcholine noise, *Nature: New biology 232*, 124-126.
11. Brejc, K., van Dijk, W. J., Klaassen, R. V., Schuurmans, M., van Der Oost, J., Smit, A. B., and Sixma, T. K. (2001) Crystal structure of an ACh-binding protein reveals the ligand-binding domain of nicotinic receptors, *Nature 411*, 269-276.
12. Unwin, N. (2005) Refined Structure of the Nicotinic Acetylcholine Receptor at 4A Resolution, *J Mol Biol 346*, 967-989.
13. Chen, L. (2010) In pursuit of the high-resolution structure of nicotinic acetylcholine receptors, *J Physiol 588*, 557-564.
14. Hilf, R. J., and Dutzler, R. (2008) X-ray structure of a prokaryotic pentameric ligand-gated ion channel, *Nature 452*, 375-379.
15. Hilf, R. J., and Dutzler, R. (2009) A prokaryotic perspective on pentameric ligand-gated ion channel structure, *Curr Opin Struct Biol 19*, 418-424.
16. Charnet, P., Labarca, C., Leonard, R. J., Vogelaar, N. J., Czyzyk, L., Gouin, A., Davidson, N., and Lester, H. A. (1990) An open-channel blocker interacts with adjacent turns of alpha-helices in the nicotinic acetylcholine receptor, *Neuron 4*, 87-95.
17. Filatov, G. N., and White, M. M. (1995) The role of conserved leucines in the M2 domain of the acetylcholine receptor in channel gating, *Molecular pharmacology 48*, 379-384.
18. Kearney, P. C., Zhang, H., Zhong, W., Dougherty, D. A., and Lester, H. A. (1996) Determinants of nicotinic receptor gating in natural and unnatural side chain structures at the M2 9' position, *Neuron 17*, 1221-1229.
19. Moroni, M., Zwart, R., Sher, E., Cassels, B. K., and Bermudez, I. (2006) alpha4beta2 nicotinic receptors with high and low acetylcholine sensitivity: pharmacology, stoichiometry, and sensitivity to long-term exposure to nicotine, *Molecular pharmacology 70*, 755-768.
20. Xiu, X., Puskar, N. L., Shanata, J. A., Lester, H. A., and Dougherty, D. A. (2009) Nicotine binding to brain receptors requires a strong cation-pi interaction, *Nature 458*, 534-537.
21. Pantoja, R., Rodriguez, E. A., Dibas, M. I., Dougherty, D. A., and Lester, H. A. (2009) Single-molecule imaging of a fluorescent unnatural amino acid incorporated into nicotinic receptors, *Biophysical journal 96*, 226-237.
22. Quick, M. W., Naeve, J. C., Davidson, N., and Lester, H. A. (1992) Electrophysiology of a Gaba Transporter Expressed in Xenopus Oocytes, *Faseb J 6*, A93-A93.
23. Reifarth, F. W., Clauss, W., and Weber, W. M. (1999) Stretch-independent activation of the mechanosensitive cation channel in oocytes of Xenopus laevis, *Biochim Biophys Acta 1417*, 63-76.
24. Silberberg, S. D., and Magleby, K. L. (1997) Voltage-induced slow activation and deactivation of mechanosensitive channels in Xenopus oocytes, *J Physiol 505 (Pt 3)*, 551-569.

25. Neher, E., and Sakmann, B. (1992) The patch clamp technique, *Sci Am 266*, 44-51.
26. Neher, E., and Sakmann, B. (1976) Single-channel currents recorded from membrane of denervated frog muscle fibres, *Nature 260*, 799-802.
27. Neher, E., and Sakmann, B. (1976) Single-Channel Currents Recorded from Membrane of Denervated Frog Muscle-Fibers, *Nature 260*, 799-802.
28. Sigworth, F. J., and Neher, E. (1980) Single Na+ channel currents observed in cultured rat muscle cells, *Nature 287*, 447-449.
29. Hamill, O. P., Marty, A., Neher, E., Sakmann, B., and Sigworth, F. J. (1981) Improved patch-clamp techniques for high-resolution current recording from cells and cell-free membrane patches, *Pflugers Arch 391*, 85-100.
30. Hamill, O. P., and Sakmann, B. (1980) A Cell-Free Method for Recording Single-Channel Currents from BIological Membranes, *Proceedings of the Physiological Society*, 41P-42P.
31. Tank, D. W., Miller, C., and Webb, W. W. (1982) Isolated-patch recording from liposomes containing functionally reconstituted chloride channels from Torpedo electroplax, *Proceedings of the National Academy of Sciences of the United States of America 79*, 7749-7753.
32. Miller, C. (1986) Ion Channel Reconstitution, 231-273.
33. Hamill, O. P., and Sakmann, B. (1981) A Cell-Free Method for Recording Single-Channel Currents from Biological-Membranes, *J Physiol-London 312*, P41-P42.
34. Kalbaugh, T. L., VanDongen, H. M., and VanDongen, A. M. (2004) Ligand-binding residues integrate affinity and efficacy in the NMDA receptor, *Molecular pharmacology 66*, 209-219.
35. Akk, G., Zhou, M., and Auerbach, A. (1999) A mutational analysis of the acetylcholine receptor channel transmitter binding site, *Biophys J 76*, 207-218.
36. Fenton, A. W. (2008) Allostery: an illustrated definition for the 'second secret of life', *Trends Biochem Sci 33*, 420-425.
37. Auerbach, A. (2005) Gating of acetylcholine receptor channels: brownian motion across a broad transition state, *Proceedings of the National Academy of Sciences of the United States of America 102*, 1408-1412.
38. Chakrapani, S., Bailey, T. D., and Auerbach, A. (2004) Gating dynamics of the acetylcholine receptor extracellular domain, *The Journal of general physiology 123*, 341-356.
39. Grosman, C., Zhou, M., and Auerbach, A. (2000) Mapping the conformational wave of acetylcholine receptor channel gating, *Nature 403*, 773-776.
40. Miyazawa, A., Fujiyoshi, Y., and Unwin, N. (2003) Structure and gating mechanism of the acetylcholine receptor pore, *Nature 423*, 949-955.
41. Cymes, G. D., Ni, Y., and Grosman, C. (2005) Probing ion-channel pores one proton at a time, *Nature 438*, 975-980.

42. Prince, R. J., and Sine, S. M. (1998) Epibatidine activates muscle acetylcholine receptors with unique site selectivity, *Biophys J 75*, 1817-1827.
43. Wang, H. L., Auerbach, A., Bren, N., Ohno, K., Engel, A. G., and Sine, S. M. (1997) Mutation in the M1 domain of the acetylcholine receptor α subunit decreases the rate of agonist dissociation, *J. Gen .Physiol. 109*, 757-766.
44. Milone, M., Wang, H. L., Ohno, K., Fukudome, T., Pruitt, J. N., Bren, N., Sine, S. M., and Engel, A. G. (1997) Slow-channel myasthenic syndrome caused by enhanced activation, desensitization, and agonist binding affinity attributable to mutation in the M2 domain of the acetylcholine receptor α subunit, *J Neurosci 17*, 5651-5665.
45. Walters, C. L., Brown, S., Changeux, J. P., Martin, B., and Damaj, M. I. (2006) The a2 but not a7 subunit of the nicotinic acetylcholine receptor is required for nicotine-conditioned place preference in mice, *Psychopharmacology (Berl) 184*, 339-344.
46. Grutter, T., and Changeux, J. P. (2001) Nicotinic receptors in wonderland, *Trends Biochem Sci 26*, 459-463.
47. Edelstein, S. J., and Changeux, J. P. (1998) Allosteric transitions of the acetylcholine receptor, *Adv Protein Chem 51*, 121-184.
48. Changeux, J. P., and Edelstein, S. J. (1998) Allosteric receptors after 30 years, *Neuron 21*, 959-980.
49. Colquhoun, D. (1987) Affinity, Efficacy, and Receptor Classification: Is the Classical Theory Still Useful?, In *Perspectives on Receptor Classification*, pp 103-114, Alan R. Liss, Inc.
50. Colquhoun, D. H., A. G. (1981) On the Stochastic Properties of Single Ion Channels, *Proceedings of the Royal Society of London. Series B, Biological Sciences. 211*, 205-235.
51. Penner, R., and Neher, E. (1989) The patch-clamp technique in the study of secretion, *Trends Neurosci 12*, 159-163.
52. Neher, E. (1988) The use of the patch clamp technique to study second messenger-mediated cellular events, *Neuroscience 26*, 727-734.
53. Dougherty, D. A. (2008) Physical organic chemistry on the brain, *J Org Chem 73*, 3667-3673.
54. Dougherty, D. A. (2008) Cys-loop neuroreceptors: structure to the rescue?, *Chem Rev 108*, 1642-1653.
55. Nowak, M. W., Kearney, P. C., Sampson, J. R., Saks, M. E., Labarca, C. G., Silverman, S. K., Zhong, W., Thorson, J., Abelson, J. N., Davidson, N., and et al. (1995) Nicotinic receptor binding site probed with unnatural amino acid incorporation in intact cells, *Science 268*, 439-442.
56. Noren, C. J., Anthony-Cahill, S. J., Griffith, M. C., and Schultz, P. G. (1989) A general-method for site-specific incorporation of unnatural amino-acids into proteins, *Science 244*, 182-188.
57. Dougherty, D. A. (2000) Unnatural amino acids as probes of protein structure and function, *Curr Opin Chem Biol 4*, 645-652.

58. Beene, D. L., Dougherty, D. A., and Lester, H. A. (2003) Unnatural amino acid mutagenesis in mapping ion channel function, *Curr Opin Neurobiol 13*, 264-270.
59. Nowak, M. W., Gallivan, J. P., Silverman, S. K., Labarca, C. G., Dougherty, D. A., and Lester, H. A. (1998) In vivo incorporation of unnatural amino acids into ion channels in Xenopus oocyte expression system, *Methods Enzymol 293*, 504-529.
60. Dougherty, D. A. (1996) Cation-π interactions in chemistry and biology: A new view of benzene, Phe, Tyr, and Trp, *Science 271*, 163-168.
61. Zacharias, N., and Dougherty, D. A. (2002) Cation-pi interactions in ligand recognition and catalysis, *Trends Pharmacol Sci 23*, 281-287.
62. Ma, J. C., and Dougherty, D. A. (1997) The cation-π interaction, *Chem. Rev. 97*, 1303-1324.
63. Dougherty, D. A., and Stauffer, D. A. (1990) Acetylcholine binding by a synthetic receptor. Implications for biological recognition, *Science 250*, 1558-1560.
64. Gallivan, J. P., and Dougherty, D. A. (1999) Cation-pi interactions in structural biology, *Proceedings of the National Academy of Sciences of the United States of America 96*, 9459-9464.
65. Zhong, W., Gallivan, J. P., Zhang, Y., Li, L., Lester, H. A., and Dougherty, D. A. (1998) From ab initio quantum mechanics to molecular neurobiology: a cation-pi binding site in the nicotinic receptor, *Proceedings of the National Academy of Sciences of the United States of America 95*, 12088-12093.

Chapter 2

Methods for Combined Single-Channel and Whole-Cell Recording of Ion Channels Expressing Unnatural Amino Acids

2.1 Introduction

Data from whole-cell electrophysiology can be used to compare the relative potencies of a series of agonists on a given ligand-gated ion channel (LGIC), or of a single agonist across multiple different mutated receptors. Frequently, the later process is accomplished by introducing a variety of conventional mutations at the site of interest(*1*) to determine how that perturbation impacts receptor function. Such functional changes can be measured by changes in agonist potency given in the functional metric EC_{50}, the effective concentration of agonist required for half-maximal response. In order to determine the relationship between amino acid side chain structure and receptor function with enhanced control, unnatural amino acids can be introduced in receptors to provide systematic, subtle perturbations of receptors' structural and electronic properties(*2*). Such studies can also help determine whether specific interactions between receptor and agonist(*3, 4*) or between side chains primarily impact the binding of agonist to the receptor or gating(*5-11*). Gating is the process by which a channel converts from a closed to an open conformation. A combination of whole-cell electrophysiology and nonsense suppression to introduce unnatural amino acids has been common in the Dougherty group for over a dozen years(*12-17*). This thesis describes a new methodology that combines the use of single-channel recording with semi-automated whole-cell recording in order to employ these methods synergistically and efficiently. This set of techniques was further developed to combine these two types of electrophysiology in combination with nonsense suppression. The techniques

described in this chapter, and applied throughout much of this thesis, make use of the rapid data collection that semi-automated whole-cell recording via the OpusXpress 6000A enables. At the same time, the techniques I develop here make use of the detailed kinetic information that is available from single-molecule experiments on ion channels. Whole-cell data can often demonstrate a compelling correlation in structure-function studies. However, on its own, whole-cell data offers an incomplete description of some key phenomena of ion channels because these equilibrium measurements cannot be used to unambiguously discriminate between binding and gating effects(*6, 18*).

In short, the method considered here involves screening mutants and conditions (concentration, agonist, etc.) with whole-cell recording, then performing single-channel recording on the most interesting mutants and conditions. This allows for characterization of changes in single-channel kinetics that correspond to changes seen in whole-cell data. This chapter describes the development of this efficient methodology, outlines types of studies where it has been particularly useful, and describes ways in which it expands the capabilities of the nonsense suppression methodology.

The receptors that were used in the studies described in this chapter are nicotinic acetylcholine receptors (nAChRs). The neuronal and muscle types introduced in Chapter 1 are both used, including rat $\alpha4\beta2$ receptors with and without L9'A in the $\beta2$ subunit and the mouse muscle nAChR. Of the muscle nAChRs, the fetal version is comprised of $2\alpha1$, $\beta1$, γ, and δ, while the adult version is comprised of $2\alpha1$, $\beta1$, ε, and δ subunits. L9'S mutations were also

used in the muscle nAChRs, in both the β1 and δ subunits(*14, 19, 20*). Most single-channel studies described in this chapter were performed in the presence of agonist in the cell-attached configuration. However, other patch configurations(*21, 22*), and some agonist-free recordings will be reported here and elsewhere in this thesis.

2.2 Results

In order to efficiently combine whole-cell and single-channel recording of nAChRs, the first step was to construct an electrophysiology rig capable of regularly obtaining seals with resistances of 20-100 gΩ and RMS noise of < 0.5 pA. Here I will briefly summarize the capabilities of the final rig, on occasion illustrating them with traces and data; more data will be presented in the remainder of the thesis chapters which applied the methods developed and described in this chapter. Details of the specific components and further description are provided in Materials and Methods.

2.2.1 Electrophysiology Rig Components

CV-5 100GU headstage (chosen for low noise—0.15 pA RMS with a 4-pole Bessel filter at 5 kHz bandwidth in optimal conditions)

GeneClamp 500B

Avens filter

Hum Bug noise eliminator

Tektronix TDS 210 oscilloscope

1320A Digidata

Gateway computer (Windows XP) with Clampex 9.2 for recording

Data sampler (Axon Instruments Digidata 1320A)

Vibration isolation workstation (Newport)

Faraday cage (Newport)

Lamp (Warner Instrument Corp., Sun-1)

Dissecting microscope (Leica, GZ4)

Fine manipulator with axial drive (Narishige Scientific Instrument Lab, MMO-203)

Manipulator (custom; x, y, and z range of several cm each)

Recording chamber (custom, volume ~ 2 ml; flow rate ~ 0.5–2 ml/min)

Recording software: Clampex 9.2

The components were arranged and connected as is described in **Figure 2.1** and the accompanying caption; see Materials and Methods for further description.

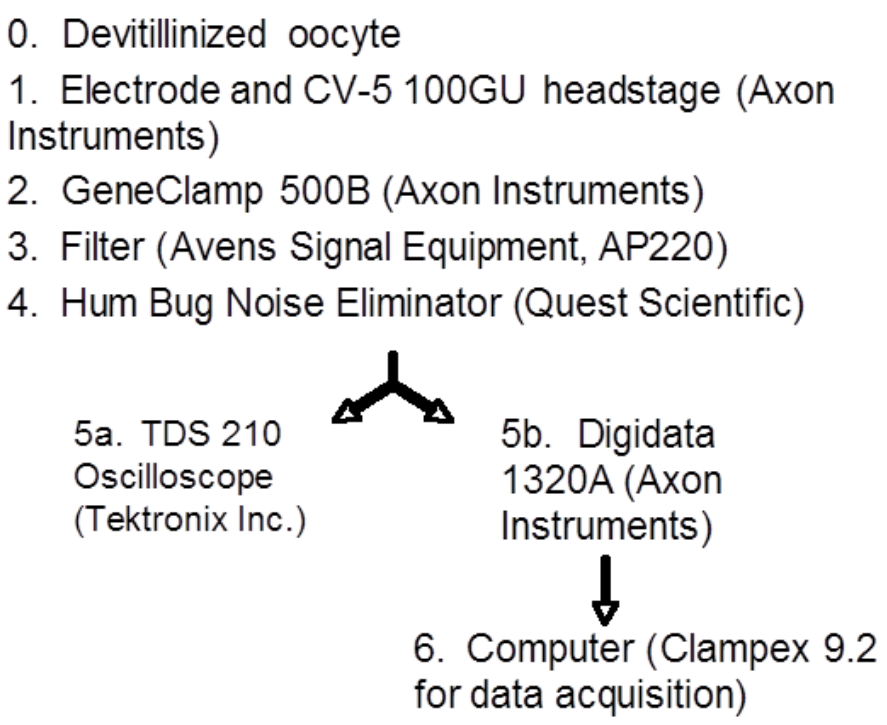

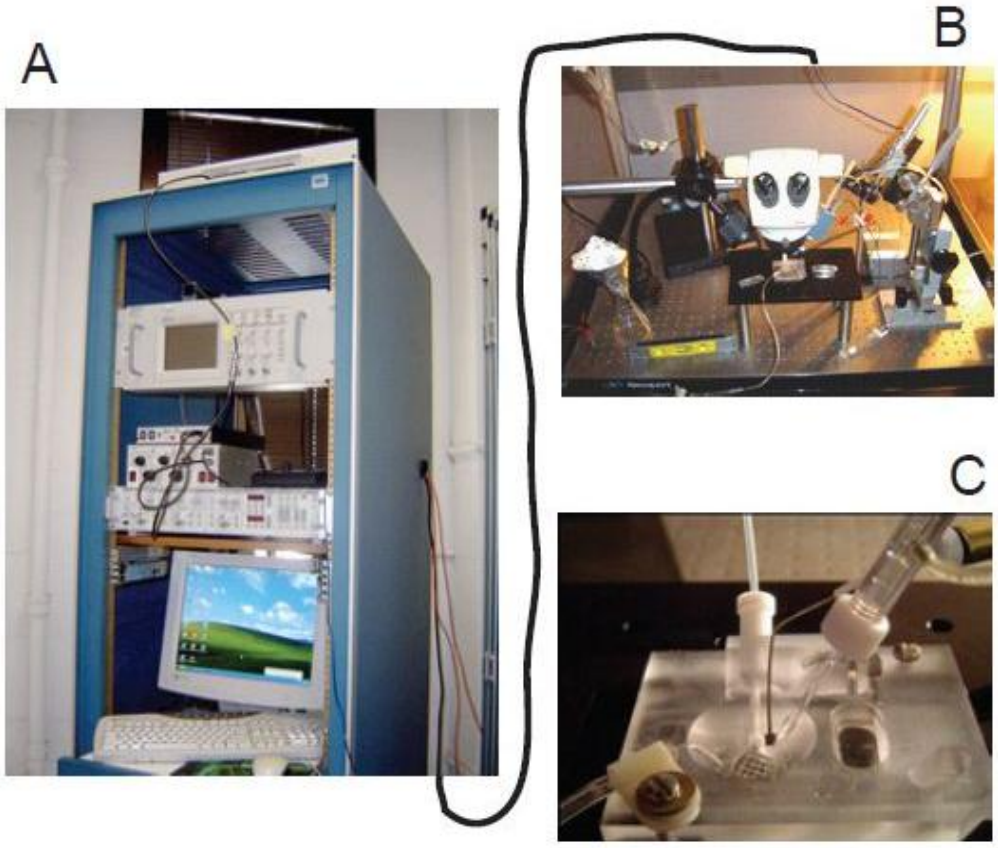

Figure 2.1. A schematic (upper, previous page) and pictorial (lower, A–C) overview of the electrophysiology rig (see Materials and Methods for details). A) (from bottom) computer with Clampex 9.2, GeneClamp 500B, Avens filter, Hum bug, and oscilloscope (TDS 210), all mounted in a rack. The Digidata 1320A is on top of the blue rack. B) Inside the Faraday cage: course manipulator, headstage, recording platform with recording chamber, dissecting microscope, and fine manipulator (at left, unpictured). The black line between A and B shows how the electrical signal is carried from the headstage out the top of the Faraday cage, then to the amplifier (GeneClamp 500B). C) Recording chamber with nylon mesh in the bottom, bath electrode (brown), recording pipette (clear), white perfusion system at top, and bent aspiration tube leading to tubing at bottom left

2.2.2 Overview of Experiments and Results

Using this rig in combination with the OpusXpress, single-channel and whole-cell data were obtained for several different agonists and partial agonists of nAChRs including: acetylcholine (ACh), choline (Ch), tetramethylammonium (TMA), epibatidine (Epi), nicotine (Nic), and varenicline (Var). Typical single-channel recordings had RMS noise of 0.3–0.4 pA and gave seals with

resistances between 10 and 50 gΩ. RMS noise as low as ~ 0.24 pA and a few seals with resistances of over 300 gΩ were obtained. Although several seals that lasted > 1 hour were obtained, and 10 minute seals were common, other gigaseals lasted less than a few minutes. As a whole, patch duration varied widely, though at the extremes, no seals could be formed on some oocytes, while others gave several successive high resistance seals (> 30 gΩ). There was no systematic relationship between these oocytes; not even necessarily by donor frog.

All of the single-channel traces displayed in this thesis are in the 'connect-the-dot' trace form. In these traces, the discrete sampled data points—20,000 to 100,000 per second (usually 50 kHz)—are not shown, but rather a continuous trace which represents the individually sampled data points is shown. **Figure 2.2** shows several examples of single-channel traces of various receptors with various agonists.

Specific examples of single-channel phenomena will be shown in the relevant chapters. These include: channel block (Chapter 4), desensitization (Chapters 3 and 4), partial agonism (Chapter 4), single-channel rectification behavior (Chapter 6), and patches obtained > 10 days post-injection (Chapter 6). Various methods and uses of characterizing the probability of a channel being open, P_{open}, will be presented throughout this thesis. A wide range of analyses of single-channel data can be performed. Examples of some of these analyses are given in **Figures 2.3 and 2.4** and the accompanying captions.

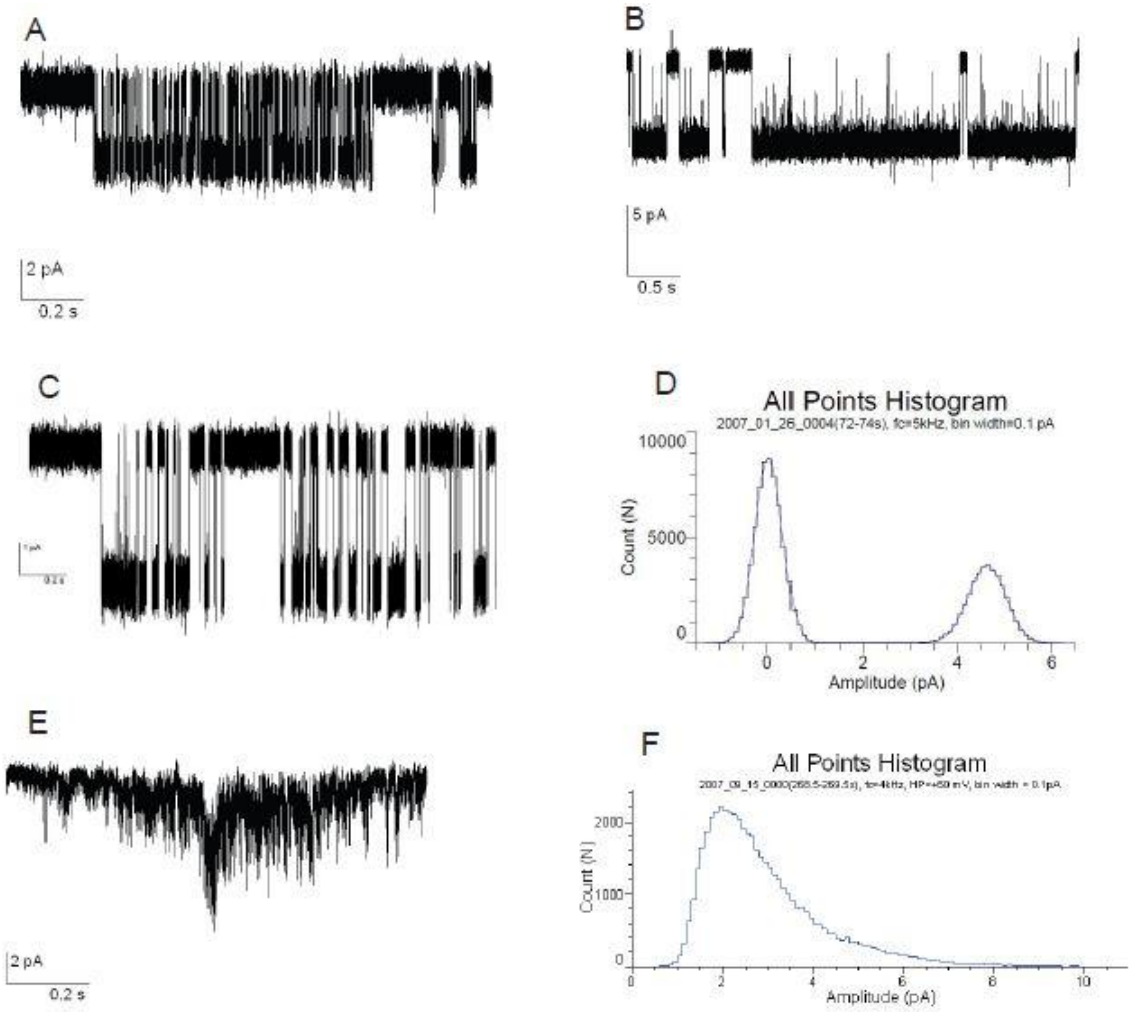

Figure 2.2. Examples of data collected using the electrophysiology rig shown in Figure 2.1. All data were collected in the cell-attached configuration, are filtered at 4 or 5 kHz (Gaussian) for display, and openings are shown as downward deflections. Recordings were made at pipette potentials of +50 to +70 mV. A) Wild type muscle (α12β1γδ) nAChR with 50 μM ACh (approximately EC50) in the pipette. B) α12β1L9'Sγδ nAChR at 1.2 μM ACh (approximately EC50). C) (α1W149F1W)2β1L9'SγδL9'S with 2.0 mM Ch in the pipette. D) All points histogram corresponding to the 2 seconds of data shown in C. The open-channel current is ~ 4.6 pA, which at the pipette potential (+70 mV) corresponds to a single-channel conductance of ~ 66 pS. E) An occasional type of channel activity seen in these recordings. This type of activity was most common after significantly changing the pipette potential (see discussion). It is clearly qualitatively different from nAChR activity. F) An all points histogram of the data shown in E can be used to further verify that this channel activity does not exhibit the discrete openings and closings typical of nAChRs.

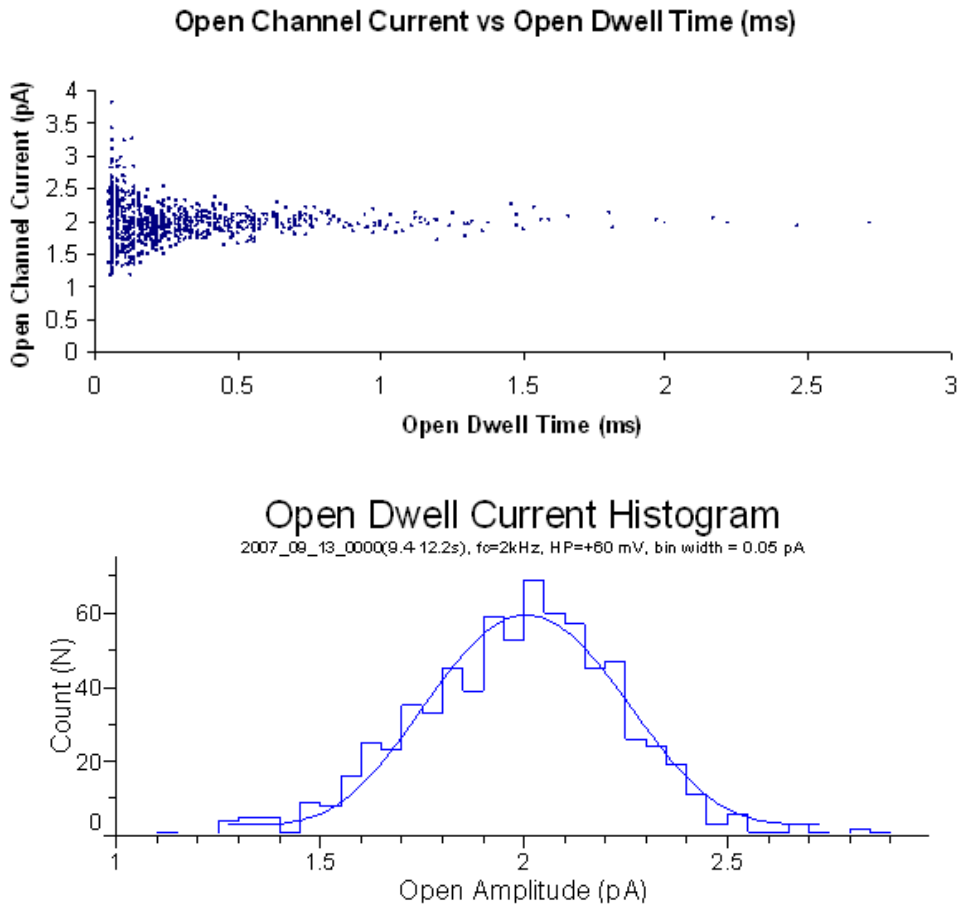

Figure 2.3. Upper) The relationship between open channel current and the open dwell time of single-channel events. If events of different open dwell time were of systematically different current, then the events may not be long enough to reach full conductance. A plot like this is used to identify whether the open dwell times are long enough to be properly resolved. The increased variability in the shorter events is expected since they represent only a few sampled data points each. Lower) This open dwell current histogram, which corresponds to the data in the upper graph, shows that all of the openings of this channel can be fit by a single Gaussian distribution centered at ~ 2 pA. This channel therefore does not have multiple conductances.

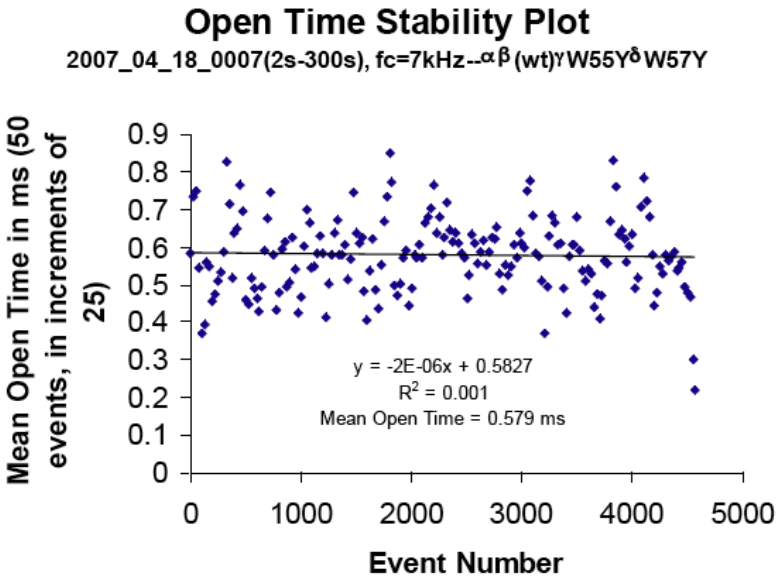

Figure 2.4. An open dwell time stability plot(*23*). Here, the average open dwell times of 50 consecutive events are represented as a single data point. Each subsequent data point then averages the open dwell time by moving over 25 events; for example, the first data point represents events 1–50, while the second data points represents events 26–76. Although the open dwell times do show some spread, this variation is over a fairly narrow range close to the mean of 0.58 ms. The fact that the best fit line has zero slope indicates that the open dwell times are stable over the course of the 298 seconds that this data represents.

Figure 2.5 is a set of single-channel recordings from a single pipette that represent some of the range of capabilities of these combined techniques and several types of data. First, data is obtained in the usual cell-attached configuration (**Figure 2.5A**). **Figure 2.5B** then shows all of the data for the formation of the outside-out configuration (see figure caption) and **Figure 2.5C** and **D** show channel activity that is induced when agonist (in this case, varenicline) is added to the bath solution. Additionally, the oocyte that was used to generate the cell-attached and outside-out patches shown in **Figure 2.5** was previously recorded on the OpusXpress to verify expression level in this specific oocyte.

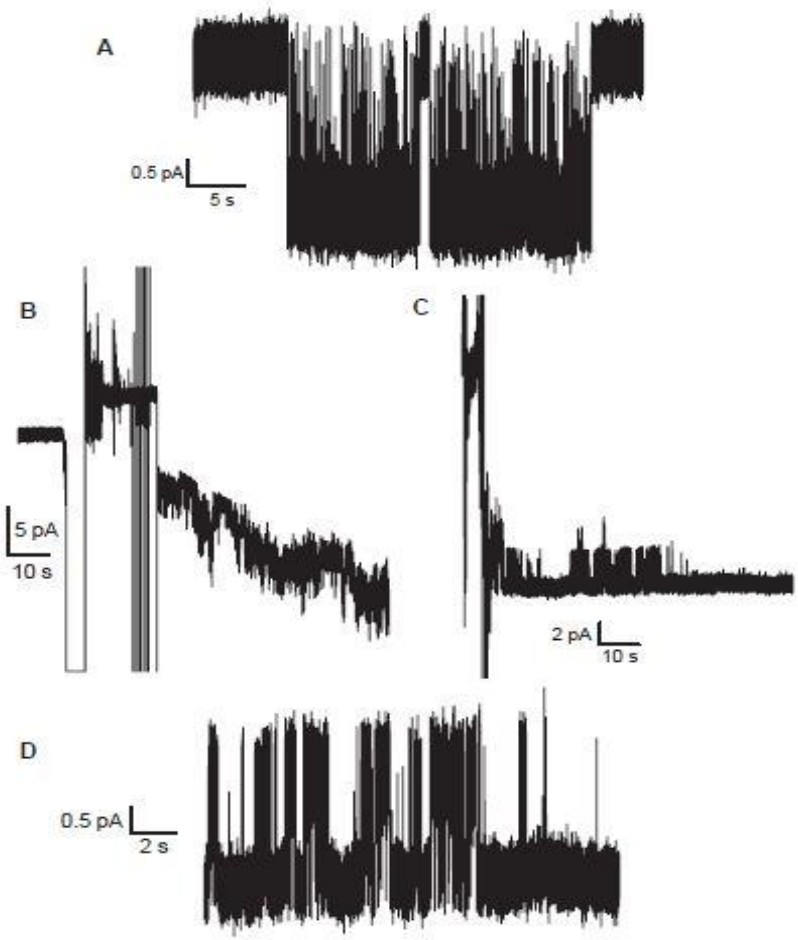

Figure 2.5. Single-channel traces from a single pipette in both the cell-attached (A) and outside-out (B–D) configurations for a 20:1 mRNA injection ratio of α4L9'A:β2 in the presence of varenicline. All data were filtered at 2 kHz for display. The oocyte used to collect these data was previously evaluated on the OpusXpress (whole-cell recording) to verify expression. A) Long-lived clusters of the channel are elicited by 9 nM varenicline in the pipette (this is approximately 10 times the macroscopic EC_{50} for this receptor); inward current is shown as downward deflections. B) A long trace showing the conversion of the cell-attached patch (first 10 seconds) to whole-cell mode with the application of significant suction to rupture the membrane. The pipette was then withdrawn from the oocyte and, over the course of ~ 10 seconds, a gigaseal forms, now in the outside-out configuration. The spikes that occur after this are an applied seal test to check the patch resistance. Shortly after that, the large baseline shift corresponds to the application of pipette potential (-60 mV). Some channel activations are seen here, despite the fact that no agonist has been applied directly in the bath. This is probably due to varenicline that leaked from the pipette prior to patch formation and during recording. C) Patch disruption and subsequent channel activity was then elicited by switching to a pipette potential of +60 mV and adding 30 µl of 120 nM varenicline to the bath. With an approximate chamber volume of 300 µl, this should produce roughly the same varenicline concentration that was in the pipette. D) A 22 second expansion of some of the channel activity in the outside-out configuration. It is qualitatively similar to the channel activity from the cell-attached patch in trace A. In C and D, the patch configuration is inverted, so channel openings at these pipette potentials are seen as upward deflections.

The whole-cell current for this oocyte at 0.5 μM ACh was > 10 μA. To my knowledge, this is the first time that such an experiment has been reported; the techniques that led to successfully performing both whole-cell and single-channel recording on the same oocyte are described later in this chapter.

2.2.3 Relationships Between Single-Channel and Whole-Cell Data

There are a number of ways in which the relationship between single-channel and whole-cell data can be illustrated(*24, 25*). In a sense, the relationship is very simple: whole-cell data represents the sum of thousands of active channels (in a typical mammalian cell) up to tens of millions of active channels (for some channels expressed in *Xenopus laevis* oocytes); see '*Number of Receptors for Whole-Cell and Single-Channel Recording'* in the Discussion section for more details.

One useful experiment that highlights this relationship is the measurement of an oocyte's membrane potentials on the OpusXpress (**Table 2.1**) and a corresponding current-voltage (I-V) relationship experiment at the single-channel level (**Figure 2.6**). The reversal potential for a given ion is the cell membrane potential at which, when a channel is open, no net flow of that ion occurs in either direction. Ideally, the single-channel recording solutions that are used should have a reversal potential of ~ 0 mV for devitellinized oocytes. That allows the membrane potential of the cell-attached patch to be estimated as being equal in magnitude and opposite in sign to the applied pipette potential.

Membrane potential (mV)

Frog	Pipette Solution	Ca^{2+}-free ND96	Bath Solution
45286AZE27	-4	-12	2
45286AZE27	-9	-15	-2
45286AZE27	2	-5	8
45286AZE27	-6	-11	3
45286AZE27	-5	-8	2
45286AZE27	-11	-10	0
4Z56367B50	-6	-8	3
4Z56367B50	-13	-22	2
4Z56367B50	-4	-13	1
4Z56367B50	-5	-11	0
4Z56367B50	-8	-20	-4
Averages	**-6**	**-12**	**1**

Table 2.1. Membrane potentials measured for devitellinized oocytes from two different donor frogs on the OpusXpress in three different solutions. The pipette solution is the one used in the pipettes for single-channel recording. Ca^{2+}-free ND96 is the usual buffer used during whole-cell experiments reported in this thesis. The bath solution is the solution that is used to fill the recording chamber during single-channel experiments. Thus, the observed average reversal potential for the oocytes in single-channel experiments in this bath solution is ~ 0 mV. The standard deviations in the solutions are 4 mV, 5 mV, and 3 mV, respectively. Therefore, in a typical single-channel experiment at an applied pipette potential of +60 mV, we expect the single-channel conductance to be ±5 – 10% based on oocyte-to-oocyte variation.

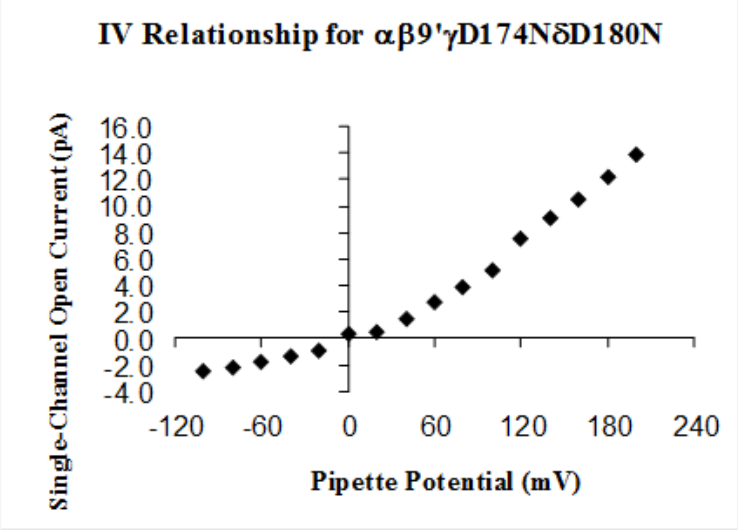

Figure 2.6. Graph of the relationship between current (I) and pipette potential (mV) for a single $(\alpha 1)_2\beta 1L9'S\gamma D174N\delta D180N$ channel in a cell-attached patch at its macroscopic EC_{50} value (160 μM ACh). The relationship is nonlinear—this channel passes current more readily inward (positive pipette potentials) than it does outward (negative pipette potentials). The least reliable values are at the pipette potentials that produce current values closest to 0 pA, since those open currents are the hardest to measure. Nevertheless, the reversal potential for the channel is very close to 0 mV.

2.2.4 Single-Channel Recording of Receptors Expressing Unnatural Amino Acids

I will now briefly summarize the results of several techniques and procedures I developed in order to maximize the probability of obtaining one active channel in a cell-attached patch during single-channel recording, including of receptors expressing unnatural amino acids. These include: control of pipette tip size, modulation of sylgard application to the pipette tip, the role of oocyte membrane health and leak currents, and the use of long incubation times.

2.2.4.1 Pipette Tip Size and Sylgard Application

Two methods of pulling pipettes were used: vertical puller and horizontal puller. In both cases, details of each pipette were kept, including length of pulls, the bubble numbers (see Materials and Methods for definition) before and after polishing the pipette tip, the qualitative distance between the edge of the applied sylgard and the pipette tip, the resistance of the pipette in the bath solution, the resistance and RMS noise of a seal (if one formed), the number of hours elapsed between when the pipette was polished and used, the drug concentration, and the oocyte. A number of relationships between these data may exist; I will now present one that I have evaluated: the relationship between bubble number and pipette resistance in solution (**Figure 2.7**). The data used to produce the two graphs in **Figure 2.7** correspond to several recording sessions in which the same pipette and bath solutions were used. The average bubble number was 4.39 before polishing and 4.13 after polishing. The average pipette resistance in

solution was 13 MΩ. 18 out of 29 of the patches in these recording sessions formed seals, with an average seal resistance of 37 gΩ. The average RMS noise for these 18 seals was 0.34 pA.

The distance between the pipette tip and edge of the applied sylgard was monitored for each pipette and recorded as either close or very close. There does not appear to be a relationship between the distance and quality of seal. The important factor is that at least a part of the pipette with sylgard is in the bath during recording. Pipettes with very close sylgard coatings had ~ 10–15% chance of becoming covered with sylgard and therefore completely unusable. Therefore, I recommend only covering pipettes to the qualitatively 'close' level.

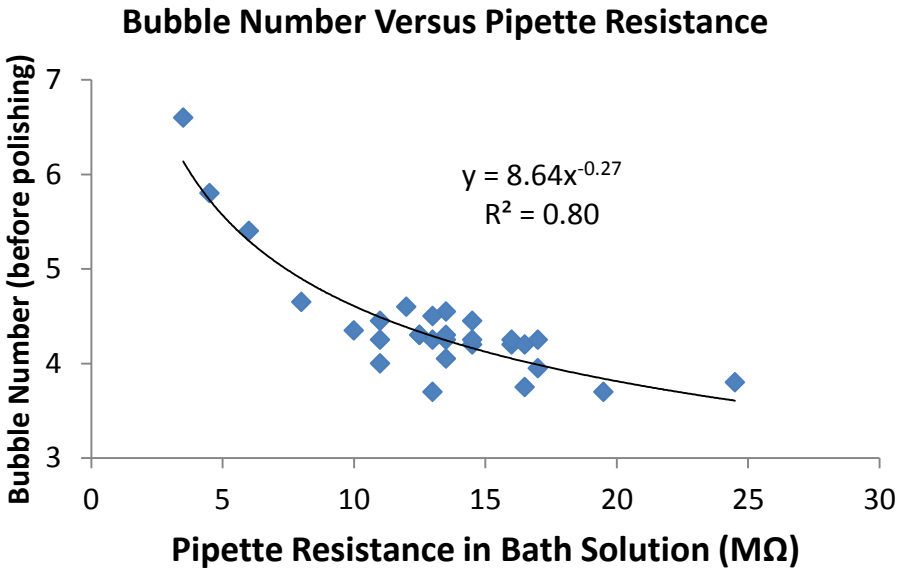

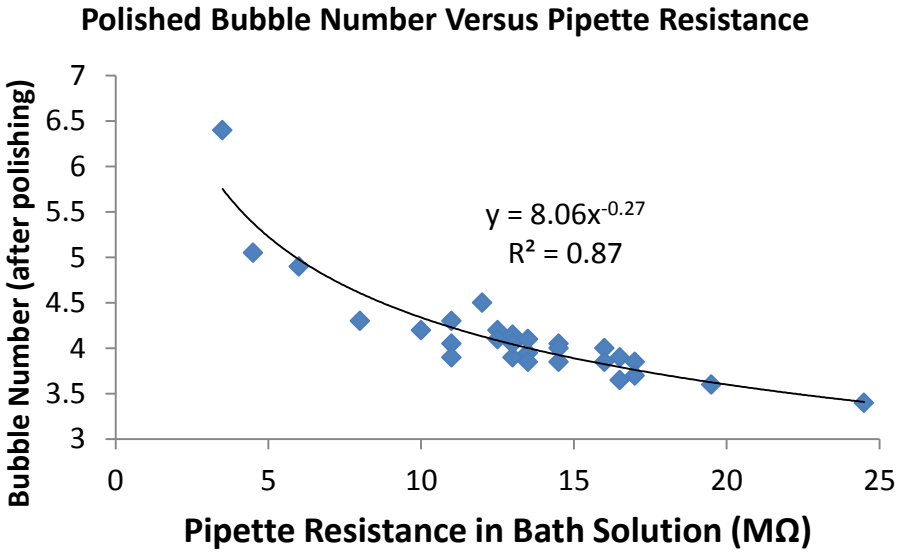

Figure 2.7. These two graphs show the relationship between measured bubble number during pipette fabrication, both immediately after pulling the pipette (upper graph, previous page) and after polishing the pipette tip in the microforge (lower graph). The fit gets better after polishing, which is not surprising, since it is the polished electrodes that are actually used in the recordings. Bubble numbers of ~ 4.5 before polishing and slightly over 4 after polishing correspond to pipette resistances of ~ 10–15, which was a useful range for these recordings. The specific fit and correlation on the graph are given solely as a guideline to show level of variation and the overall trend.

2.2.4.2 Oocyte Health and Expression Levels

In addition to control of the pipettes, the health and viability of oocytes was monitored in a variety of experiments. These included: comparison of the whole-cell leak current and resting potential (**Figure 2.8**), separation of oocytes to reduce collective maturation, injecting multiple batches of oocytes at the same time, and specific methods for keeping oocytes healthy for ≥ 10 days to increase expression level of some wild type channels.

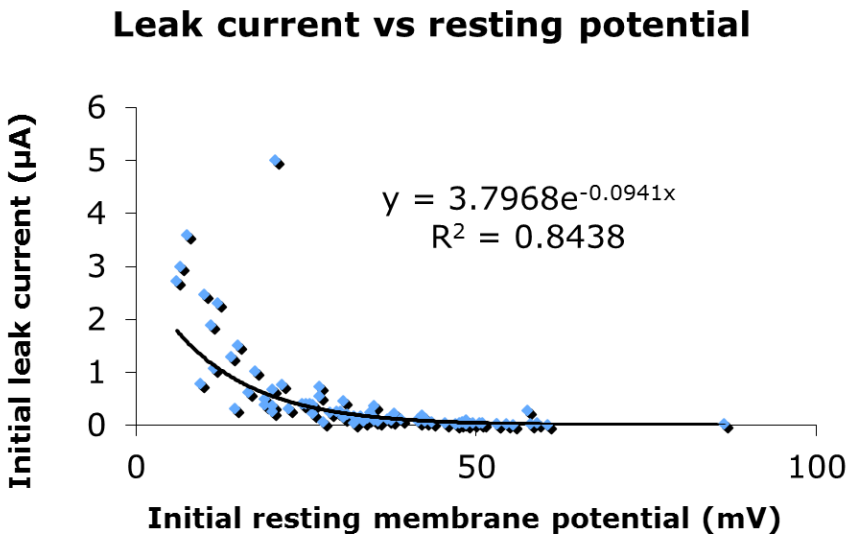

Figure 2.8. The relationship between the initial leak current (µA) of an oocyte after being voltage clamped at -60 mV on the OpusXpress and the initial resting membrane potential (mV) just prior to voltage clamping. Healthy oocytes generally had initial leak currents significantly lower than 1 µA. These oocytes with low initial leak currents had the largest probability of living through an opus run, while oocytes with large initial leak currents (> 1–2 µA) often had their leak currents increase throughout the run. In some cases, oocytes with leak currents > 1 µA were analyzed and gave reliable whole-cell dose response relations, but this was only attempted if the maximal agonist-induced response was > 10 times the leak current. The specific fit and correlation on the graph are given solely as a guideline to show level of variation and the overall trend.

In many experiments, equal numbers of oocytes (10–30) were injected at the same time with the same receptor (mRNA for wild type or mRNA/tRNA mix for nonsense suppression) then separated into 2 or more 35 mm dishes for incubation in fresh oocyte incubation media at 18° C. Sometimes, oocytes in one of the 2 or more dishes would be significantly less healthy than oocytes in the other dish(es). Due to significant donor-to-donor variability in oocyte health and expression, injection of 3 batches of oocytes at the same time was found to give a sufficiently high chance of having oocytes with high enough expression for single-channel recording. Ways to keep oocytes healthy for long periods of time are addressed in Materials and Methods.

2.3 Discussion

2.3.1 Development of Methodology for Combined Single-Channel and Whole-Cell Recording of Ion Channels Expressing Unnatural Amino Acids

One of the most important factors that had to be addressed in order to allow for single-channel recording on ion channels expressing unnatural amino acids was ensuring sufficient expression levels in *X. laevis* oocytes to find channels in cell-attached patches. Additionally, some receptors express at low enough levels that even single-channel recording on wild-type or conventional mutants can prove difficult. In order to optimize the control of whole-cell expression level for increasing efficiency of single-channel recording, I varied several parameters of the oocyte expression system, as is common in optimizing expression for new receptors in our research group: the amount of mRNA and tRNA injected, the relative amounts of each subunit (ratios), the number of injections and durations between them, the incubation time, and the incubation temperature. In addition to control of pipette properties, I found four factors to be important tools to providing good oocyte health that is necessary for combined whole-cell and single-channel recording.

The goal in these experiments was to obtain a whole-cell current that gives a probability of having one active channel in the patch of ~ 0.2 to 0.4; sometimes two or more channels will be present, while at other times, no active channels may be present in a given patch. Note that I err on the low side for expression because although QuB can analyze multiple channels in a single

patch, the analysis is necessarily more complex and less intuitive; also most analysis presented in this thesis was performed using Clampfit. Moreover, reducing expression was generally not difficult, so the data that are presented in this thesis generally emphasize periods during which only one channel was active. In the following discussion, I will summarize my experiences with optimizing oocyte health, pipette properties, recording configuration, the role of pure populations of receptors and the number of receptors on an oocyte, the determination of parameters such as P_{open} from single-channel data and their relationship to whole-cell data, and the development of a method to perform single-channel recording on oocytes that have specifically been identified as having significant expression. Several experimental controls will also be discussed in order to minimize the convoluting influence of endogenous channels in oocytes.

2.3.1.1 General Oocyte Health

The exact concentration of collagenase needed to achieve the desired level of defolliculation can vary significantly from lot-to-lot of collagenase, so it should be recalibrated for each lot. The optimal collagenase time balances sufficient degradation of the follicular membrane, which impedes sorting and efficient injection, and actual oocyte membrane integrity/rigidity, which can decrease with excessive collagenase treatment. If oocytes are slightly underdigested by collagenase, their follicular membranes will generally continue to separate over the subsequent 24 hours, in which case injecting the day after

frog surgery is often optimal. On some occasions, overdigestion by collagenase appeared to have a significantly detrimental impact on the ability to perform single-channel recording due to decreased membrane rigidity, which made stripping the oocytes difficult, decreased the probability of forming a gigaseal, and decreased the percentage of seals that were of sufficiently high resistance.

Oocytes injected at the same time and expressing the same receptor placed in separate dishes often displayed different levels of health. This supports the general observation that oocyte membrane degradation and maturation appear to be random processes, at least based on visual inspection of the outside of the oocyte. Once one oocyte in a dish begins to mature, others often follow quickly (personal communication from Bruce N. Cohen, consistent with personal observations). Once they begin maturing, oocytes can rarely be devitellinized. Therefore, for the purposes of this thesis, each media change was accompanied by careful inspection of oocytes. Here, regularly changing oocyte media means changing media at: 30–60 minutes post-injection and 6–12 hours post-injection, then every 12–24 hours based on oocyte health as determined by visual inspection of oocytes. At any media change, if oocytes in a given dish exhibited maturation (characteristic circular blemish developing on the cell membrane), those oocytes were discarded. The remaining oocytes were rinsed with fresh incubation media (2–10 minutes) before being placed in separate fresh incubation oocyte media. In addition, other oocytes that looked ‘dead’—as exhibited by disintegration/swirling of the membrane—were discarded at each media change.

Two other general factors that were found to effect oocyte health were: the type of incubation dish and the components of the incubation media. For incubation dishes, we've found that the 35 mm dishes from CELLSTAR extend oocyte viability and reduce oocyte adhesion to the dish (see Materials and Methods). In addition, 1–2 % equine serum was found to be the optimal level in incubation media. Values between 0 and 5% were incorporated. When oocyte incubation media was used without equine serum, significant oocyte adhesion to the dish bottoms was observed; these oocytes were generally not viable for recording. Faster orbital shaking sometimes offset this effect, but may decrease overall oocyte health and on many occasions led to oocytes clumping at the edge of the dish. 5% equine serum prevented oocyte adhesion to the dish no better than 2%, while 5% equine serum increased the probability that the oocyte incubation media would become contaminated and unusable.

2.3.1.2 Receptor-Dependent Effects on Oocyte Health

Two factors that impact oocyte health but can vary from receptor-to-receptor are constitutive activity and overexpression. Constitutive activity, sometimes called spontaneous opening for LGICs, occurs when the receptor enters the activated conformation even in the absence of agonist. As is the case with cells that have high leak currents, it is observed that oocytes expressing constitutively activated receptors, such as nAChRs with mutations of hydrophobic residues to hydrophilic residues in the pore (L9'S)(*14, 19, 26*), are generally less healthy. On the other hand, these oocytes sometimes display significantly larger

agonist-activated whole-cell currents as well (see Chapter 3 for further discussion). One strategy that can be employed to address oocyte health when expressing constitutively active receptors is to incubate the cells with a channel blocker that can be washed off prior to recording, such as QX314 or QX222(*27*). This may be advisable when two or more L9'S mutations are used in the muscle nAChR, but does not appear to be necessary for L9'A mutations in the α4β2 receptor.

For receptors that routinely express > 40 μA in oocytes, the current signal can reach saturating values for the opus for some oocytes. At these high whole-cell currents, the opus can struggle to maintain the voltage at the clamped voltage value, and so the opus traces show increased variability. 40 μA corresponds to ~ 17,000,000 channels for muscle nicotinic receptors (see calculation below); this is significantly more receptors than is needed for whole-cell recording, which can be accomplished with two orders of magnitude fewer channels, or single-channel recording, which can be accomplished with as few as ~ tenfold fewer channels. In these cases, decreasing the number of expressed receptors may both increase oocyte health and increase the fidelity of the recordings—both whole-cell and single-channel. Expression can be decreased by injecting less mRNA—sometimes 10- or 100- fold less, or by using significantly shorter post-injection incubations(*28*). However, additional methods for controlling the number of channels being monitored are available.

2.3.1.3 Number of Receptors for Whole-Cell and Single-Channel Recording

The *X. laevis* oocyte is ~ 1000 µm in diameter, thus if it were a perfect sphere, it would have surface area of $\pi*d^2$ = 3,142,000 μm^2. The oocyte membrane actually contains a significant number of invaginations, which greatly increase the surface area. Assuming a twofold increase in surface area from these invaginations, the oocyte surface is actually ~ 6,300,000 μm^2. Thus, for a pipette with tip diameter of 1.0 µm (A = 0.785 μm^2), there are ~ 8,000,000 pipette tip-sized patches per membrane. However, as was observed by Sigworth and Neher(*29*), the capacitance of the membrane in the gigaseal of a patch is actually about 5–10 times larger than that indicated by the area of the pipette tip. This may be due to a significant additional portion of oocyte membrane actually entering the pipette tip, as is often pictured (**Figure 2.12**, below)**.** Assuming a conservative estimate of 5 times the membrane, there are ~ 1,600,000 patches per oocyte.

We routinely observe whole-cell currents of 1 µA up to 50 µA at V_{memb} = -60 mV, which corresponds to a conductance (g) of 16.7 µS up to 830 µS (g = I/V). Since the embryonic muscle nAChR ($\alpha 1_2 \beta 1 \gamma \delta$) has a single-channel conductance of ~ 40 pS, a whole cell current of 6 µA (100 µS at -60 mV) corresponds to $1.0*10^{-4}$ S per cell / ($4*10^{-11}$ S per channel) = 2,500,000 channels. **Thus, there would be an average of 1 channel per patch if the whole cell current were ~ 4 µA.**

For $(\alpha 1)_2\beta 1\gamma\delta$, a signal-to-noise ratio of > ~ 3–5 can be achieved for receptors (or mutants/agonists) that produce I_{max} of ≥ ~ 100 nA; this is considered 'sufficient expression' for whole-cell expression, but will vary with a variety of properties. For these specific channels with single-channel conductance ($g_{channel}$) of ~ 40 pS (with Na^+ as the permeant ion), 100 nA at a potential of -60 mV corresponds to ~ 40,000 receptors on the ooycte's surface (g_{oocyte} = I/V = 100 nA/0.06 V = $1.7*10^{-6}$ S; $g_{oocyte}/g_{channel}$ = ~ 40,000). Receptors with a lower $g_{channel}$ may be defined as having sufficient expression for I_{max} values proportionally lower than 100 nA, provided that I_{max} can be determined, given the signal-to-noise ratio of the current responses. These calculations illustrate a significant difference in expression levels of channels for the two methods being combined in this thesis: single-channel and whole-cell recording.

A separate way to increase the probability of observing single-channel events is to increase the patch size. Two common ways to do this are: (1) to use larger pipette tips for the single-channel recordings and (2) to record in the outside-out configuration instead of the cell-attached configuration.

Throughout this thesis, several attempts were made to systematically vary the size of pipette tips, as measured by bubble number after pulling the pipette and pipette resistance. Although there is a clear relationship between the 'quick and dirty' bubble number and the pipette resistance in the final recording solution (**Figure 2.4**), the control of these parameters during the pipette pulling process proved more difficult. This was true for both of the pipette pulling procedures used: (a) a custom pipette puller (courtesy of Bruce N. Cohen), which allowed for

the position of the pipette glass during the second pull to be set manually, and (b) an automatic puller, a Flaming/Brown P-97. In many cases, larger pull-to-pull variation in bubble number was seen than variation observed after systematically varying the program parameters (pressure, heat, pull, velocity, and delay). The *Sutter Instrument Pipette Cookbook* (2010 Rev F.) provided useful information on designing programs for the P-97.

Several alternatives exist to the cell-attached patch recording configuration emphasized in this thesis, including: whole-cell, outside-out, inside-out, and perforated patch. The whole-cell method is not effective in oocytes given the electrical components of the electrophysiology rig; it also loses much kinetic information. The opus recordings provide whole-cell data as needed. On the other hand, each of the other pipette configurations offers distinct benefits, as have been previously summarized(*21, 30*). One of these configurations, outside-out, offers a method for increasing the area of oocyte membrane analyzed in single-channel recording. It also allows for multiple different concentrations to be readily applied to the same channel/patch of membrane, though this has also been done in the cell-attached configuration(*31*). See **Figure 2.5** for an example of how an outside-out patch was obtained and a description of the related channel events.

This data appear qualitatively similar to the data analyzed elsewhere for this receptor at similar concentrations; in this case the outside-out configuration did not appear to alter channel kinetics. Moreover, loss of cytosolic components—in the outside-out configuration the inside of the patch now faces

the pipette solution instead of the oocyte's cytosol—didn't qualitatively change channel activation. This rig was not designed to emphasize recording in the outside-out patch configuration; however, with modifications to the perfusion system, regular outside-out recording with various concentrations of agonist—or even multiple agonists—on a single channel is well within the capability of our rig.

For one key set of receptors that might be pursued in the Dougherty group, α4β2, some other experimenters have reported rundown and other experimental difficulties in single-channel recording of these neuronal receptors(*32*) (Cynthia Czajkowski and Joe Henry Steinbach, personal communications). Rundown is a phenomena in which the current being measured decreases over the course of an experiment. In some single-channel experiments, the channel activity can disappear completely. It is possible that under our specific recording conditions and with oocytes, these problems could be addressed. A single outside-out patch of α4L9'Aβ2 A3B2 (20:1) (**Figure 2.5)** seemed to show similar behavior to a cell-attached patch of the same channel and agonist, although detailed kinetic analysis was not performed.

Another specific type of experiment that could make use of cell-detached configurations is the investigation of the relationship between specific cytosolic molecules—such as the polyamine spermine—and inward rectification(*32, 33*). See Chapter 6 for further discussion.

A method of obtaining the inside-out configuration is exposure to: (a) air or (b) hexadecane(*21*). If using inside-out patches, I suggest avoiding introducing

hydrophobic molecules such as hexadecane, which may partition into the bilayer and thereby change the bilayer properties and impact channel kinetics.

2.3.1.4 Pure Populations of Receptors

When unnatural amino acids are used, read-through and reaminoacylation control experiments can be used to verify a sufficiently pure population of receptors if they show that the desired receptor is overwhelmingly or solely present after extended incubations (> 48 h–72 h). Such a determination is made by comparison of I_{max} values that show < 5% -- 10% current when oocytes are injected with, for example, 76mer tRNA.

The procedure developed and used here involves performing all single-channel recording within 48 h of the most recent tRNA injection (72 h if opus recording at 72 h showed < 5–10% read-through or reaminoacylation current). In some cases, in order to increase expression, oocytes were injected initially with mRNA + tRNA, then injected again 24 h–72 h later with mRNA + tRNA (on rare occasions, just tRNA was injected during the second injection). Data collected > 48 h (> 72 h) post-tRNA injection, were only used in the analysis when 2 or more patches recorded at < 48 h (or < 72 h) showed qualitatively and quantitatively similar single-channel activity. In these cases the low measured level of contamination, by read-through/reaminoacylation, indicates a high likelihood (> 90–95%) of getting the right channel in the patch. This is true except in the case that the single-channel conductance of the contaminating channel is significantly lower than the single-channel conductance of the desired channel. In addition to

being unlikely, this difference is readily monitored by quantitative comparison of the single-channel conductance of data collected pre- and post-48 h (or 72 h), and never interfered with data analysis. Moreover, channels with significantly lower conductance than the channels studied in this thesis are not problematic to analyze because the signal-to-noise ratio of those events is so low that they couldn't be analyzed, even if we wanted to.

2.3.1.5 Single-Channel and Whole-Cell Recording on the Same Oocyte

When a specific receptor being expressed in a given batch of oocytes (specific donor frog) gave primarily significant whole-cell responses, it was often true that any oocyte from that donor frog had a significant chance of producing patches with single-channel activity. Specifically, if ≥ 6 of 8 oocytes in a given opus expression test or run were expressing at sufficient levels, then chances of finding channels on any oocyte from that donor frog injected with the same mRNA/tRNA within the first few patches were high (>> 50%).

However, a limitation of this technique of modulating channel density on oocytes is that biological variation can be significant. During several recording sessions, I observed whole-cell I_{max} values that varied over at least 1 order of magnitude for a specific receptor, yet the cells gave similar EC_{50} values. Attempts to address this variability in the number of receptors expressed from oocyte-to-oocyte by separating injected oocytes that visibly 'leaked' more or less immediately after injection did not reveal an obvious correlation between the two

groups. Rather, the difference is more likely inherently at the biological level and varies oocyte-to-oocyte.

Although it was not the main purpose of any experiments reported here to perform *both* single-channel recording and whole-cell recording on *the same oocyte*, I began developing this technique in order to mitigate the frustrating impact of oocyte-to-oocyte variation in expression levels. This enhances our ability to combine the techniques of single-channel and whole-cell recording in a targeted, efficient way and reduced the frustration associated with performing single-channel recording on an oocyte that may—due essentially to bad luck—be expressing much less receptor than the average oocyte from that donor frog. Such enhanced targeting of resources is even more desirable when these techniques are additionally combined with incorporation of unnatural amino acids, since the tRNA required is used as a stoichiometric reagent. To my knowledge, no similar experiments have been reported for oocytes, so their execution is briefly summarized in the methods section.

Note that these experiments are far more likely to succeed if whole-cell recording precedes single-channel recording due to the significant membrane damage that is introduced by whole-cell recording and the fact that the oocyte must be devitellinized prior to single-channel recording. This damage is more extreme for whole-cell recording performed with the OpusXpress, even when physically smaller electrodes with resistances towards the high end of the permitted range on the OpusXpress (3 MΩ and 10 MΩ, for current and voltage electrodes, respectively) are used. In these cases, no obvious qualitative

difference in channel activity was seen between oocytes recorded on the OpusXpress and those not. I therefore conclude that whole-cell recording on the OpusXpress–and the corresponding large electrodes and significant changes to membrane potential—do not appear to significantly impact subsequent single-channel events or kinetics.

Note that in some cases even oocytes that showed expression on the opus did not give active channels in cell-attached patches. This effect appeared to increase with increasing time delay between opus recording and single-channel recording, yet oocytes must be given at least 1 hour after whole-cell recording for their membranes to heal. A recovery time of 2–10 hours post opus recording seemed ideal.

2.3.2 Applicability of the Technique to Various Receptors and Agonists

In order to demonstrate the broad applicability of combined single-channel and whole-cell recording, including on channels expressing unnatural amino acids, the various types of channel activations possible should be considered. Issues of single-to-noise, which may allow for measurements on channels with lower conductances, are addressed in the Methods section. Recording on channels with different levels of expression has been extensively addressed above. However, we must also consider recording onto channels with different level of activation or with agonists that activate channels to different extents. Some of these broad quantitative issues are addressed below, in addition to

specific discussion and analysis in the appropriate chapters. Note that I did *not* attempt to design single-channel experiments for the recording of GPCRs(*6, 34*).

2.3.2.1 Quantitative Relationships Between Whole-Cell and Single-Channel Data

As in most experiments on LGICs, information from macroscopic experiments is usually limited by the speed of the solution change. The solution exchange time for the OpusXpress has been estimated at ~ 1–2 seconds for flow rates similar to those used in the experiments reported here(*35*). These are much slower than nAChR kinetics at most concentrations I used, but faster than the kinetics of some receptors (i.e., ρ1 $GABA_A$). In the rare cases where activation/deactivation kinetics can be resolved by the OpusXpress, the sampling and filtering characteristics must first be optimized. Use of an analog-to-digital sample rate ≥ 2.5 times the analog filter's cut off frequency avoids aliasing(*36*). If low concentrations of agonist (nM or lower) are used, then one component of the opus trace activation is expected to be the association rate, assuming that this rate is diffusion limited.

2.3.2.2 NP_{open}, P_{open}, Efficacy, and the Possibility of Multiple Channels in a Patch

In the ideal single-channel experiment, there is one active channel in a patch, and for at least some concentrations, clusters of activity are seen with high enough NP_{open} to establish that those events are arising from the same channel and therefore represent P_{open} for the channel. In NP_{open}, N indicates that the

probability of being open being reported reflects an unknown number of channels, N. At concentrations where the binding equilibrium is saturated, a measured P_{open} value would be $P_{open,max}$ and is a measure of efficacy—the ability of the agonist to open the channel. Single-channel recording allows for direct determination of this parameter, while whole-cell recording allows for determination of the relative efficacy of two or more agonists. In addition, measurements of efficacy from single-channel data are often reported to 2–3 significant figures(*5, 10, 34, 37*), which is probably better resolution than is obtainable based on variation in whole-cell current measured on the OpusXpress. Chapter 4 describes the development of a proposed model for a mutated nAChR and a resulting measurement of efficacy by fitting single-channel data to multiple ACh concentrations using QuB(*38-41*).

In all cases, the assignment of which agonist(s) are full agonists requires single-channel measurement to verify, at a minimum, that $P_{open,max}$ is ~ 1. That is to say, clusters of activity—channel activations that end in desensitization—must occur in which the probability of the channel being open is nearly one if an agonist is a full agonist. A fact that appears to be underappreciated is that, in cases where desensitization is fast(*42, 43*) or the rate of exit from the desensitized state back to the open channel is very slow, it may be difficult to unambiguously assign full or partial agonism at either the whole-cell or single-channel level. Until recently a partial agonist has been defined as a molecule that produces a relatively lower gating equilibrium constant, Θ, where Θ is the channel opening rate (β) divided by the channel closing rate (α). In these cases,

Θ must be < ~ 10–30 for an agonist to be considered a partial agonist(*44*). Recently, different models, invoking a pre-opening conformational change, have been proposed to explain why some molecules are only able to partially activate receptors(*45-47*).

Some analysis software, such as QuB, can be used to analyze single-channel recordings even when multiple channels are simultaneously active. However, unambiguous assignment of the number of channels in a patch is difficult and even with such analysis, it is impossible except in regions of extended very high P_{open} for full agonists at saturated binding. This ambiguity is summarized in the representation of many measured P_{open} values as NP_{open}. Indeed, calculations of NP_{open} for 1–40 channels show that a measured NP_{open} value of ~ 0.01, was consistent with many different numbers of channels present, with P_{open} getting correspondingly smaller to represent larger—but still very small—values of NP_{open}.

On the other hand, when P_{open} is significantly greater than 0.5, overlapping channel events may readily be seen if multiple channels are active. **Figure 2.9** shows what these overlapping events would look like when artificially superimposed on a trace with very high P_{open} (> 0.9) and compares them to observed brief current deflections from the open state.

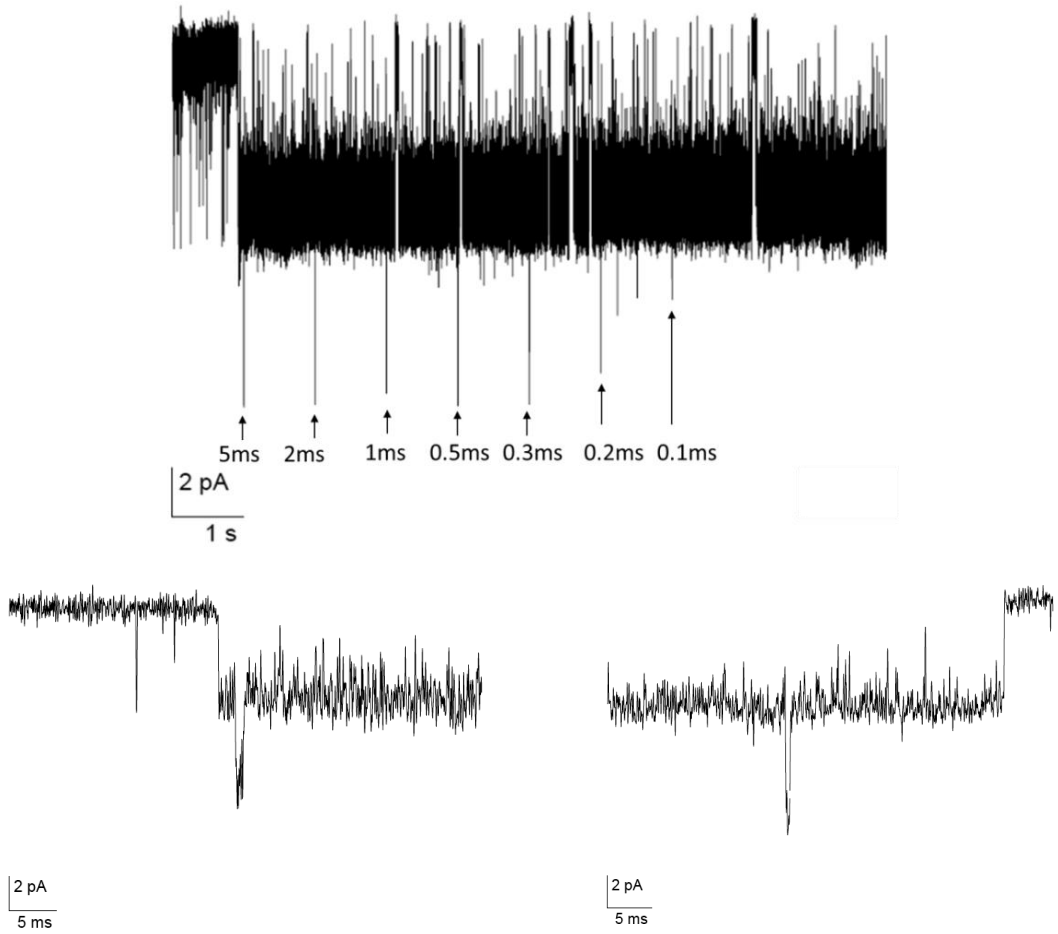

Figure 2.9. Upper) A single-channel record in which downward deflections represent an open channel. At the start, the channel is mostly closed, with brief openings, then the channel is primarily open. In order to examine the resolution limit for brief openings that my analysis can detect from the open state, current transitions (baseline shifts) of 5 ms, 2 ms, 1 ms, 0.5 ms, 0.3 ms, 0.2 ms, and 0.1 ms have been added. Both qualitatively and quantitatively, openings > 0.3 ms can clearly be discerned from noise. The result is that this record appears to have a single channel that switches between low and high Popen, rather than multiple channels, since they don't appear to open as overlapping events. Lower Left) A high resolution trace of a separate record with actual brief openings from both the closed and open state. Lower Right) For comparison, a high resolution trace of a 0.5 ms current transition added to the open state. Comparison of the real opening (left) and added one (right) once again demonstrate that 0.5 ms openings overlaid on the high Popen sections of data can readily be assigned.

A minimum number for N can be assigned based on the largest number of overlapping (simultaneous) channel openings. For data analyzed in this thesis, I confine my analysis to patches with either no or very few (<< 5%) overlapping channel events. In the few cases where records with overlapping channel events

were analyzed, patches exhibiting this behavior were quantitatively compared to those with that displayed only opening of a single channel at any given time. The resulting data were only included in the analysis if they quantitatively agreed with patches that displayed no overlapping openings. Further discussion of multiple channels and analysis of NP_{open} is given in Chapter 5. As is described there, other parameters, such as the length of time that a channel spends open, τ_{open}, can often be used to clarify results(*48*), though a full treatment of overlapping events is complex(*49*).

2.3.3 Control Experiments for Single-Channel Recording in Oocytes

Channels that are believed to be endogenous to oocytes were observed in some single-channel recordings. These channels generally exhibited kinetics that were different from nAChRs kinetics, a different current (at the recording pipette potentials), and were often mechanosensitive(*50, 51*). Although these parameters generally made the identification and separation of these events from channel activity from the desired, exogenously expressed channel of interest, possible, it took some skill to do so. Therefore, and in order to ensure the applicability of characterization of unnatural amino acids expressed in oocytes by single-channel recording to a broad range of receptors, a method was developed, in conjunction with Shawna Frazier (Lester lab), that seemed to decrease the occurrence of these extraneous current events.

In addition to the obvious controls of recording on uninjected oocytes and recording on channels with no agonist in the pipette, three variables were

investigated to identify and/or eliminate endogenous channel activity: the time between stripping an oocyte and recording on it, the use of suction during recording to identify mechanosensitive channels, and the use of glass dishes to incubate oocytes. In early experiments, recording on oocytes began as soon as the stripped oocyte was placed in the recording chamber. Reasoning that the transition from incubation media to hypertonic solution to bath solution, as well as removal of the vitelline membrane, all caused significant stress to the oocyte, we decided to delay recording of the stripped oocyte after being placed in the chamber in order to allow it to equilibrate.

A second method, which allowed for the identification of the presence of mechanosensitive channels, was to apply suction to the oocyte after a few minutes of recording on the channel of interest. When suction is applied, the channel is probably not mechanosensitive if its activity (P_{open}, τ_{open}, conductance, etc.) continues at the same level. The presence of a mechanosensitive channel in the patch could often be identified if activity could be induced by suction in a record with no activity (or a desensitized channel). P_{open} for these mechanosensitive channels varied with applied suction: ~ 0.5 with light suction and nearly 1 with moderate suction. In addition to this characteristic, these channels were generally easy to distinguish from exogenously expressed channels due to their raggedy openings and closings. On several occasions, light suction was applied during channel openings; nAChRs did not display a qualitatively different P_{open} or conductance when suction was applied in this way.

Anecdotally, I do not notice that oocytes that spend 30 or more minutes in the stripping solution exhibit more endogenous channel activity, especially when this procedure was followed. Nevertheless, the time in the stripping solution should be no more than is necessary to exhibit significant separation between the oocyte membrane and the vitelline membrane.

The third variable we considered, incubation of oocytes in glass dishes instead of plastic dishes, did not appear to significantly decrease the occurrence of these extraneous channel events.

In addition to endogenous oocyte channels, it is important to be aware of other potential contaminants of the single-channel signal. These include: receptor heterogeneity (such as a receptor with an omitted subunit), spontaneous openings, voltage-gated channels, and patching to something other than the cell.

Channels with omitted subunits can form functional receptors, and these have been characterized, including at the single-channel level(*52, 53*). The relationship between receptors lacking a subunit and spontaneous openings has been at least partially explored(*53*). One type of subunit omission experiment is fairly straightforward: one (or more) of the mRNAs coding for a subunit of the receptor is simply not included in the mRNA mix. If subsequent whole-cell experiments reveal no agonist-induced activation, or only activation at several orders of magnitude higher concentration than the channel's EC_{50}, then it is unlikely that the signal from this receptor will impact whole-cell data or single-channel analysis. If the whole-cell leak currents for these channels are systematically higher than for oocytes expressing receptors with all subunits, this

could indicate that a receptor is being expressed that can open spontaneously, even though it may not bind agonist with nearly as high affinity as the full receptor. Thus, in order to quantitatively examine any potential impact on single-channel analysis, recording should be performed on several patches from multiple oocytes from different donor frogs. Both agonist-induced and spontaneous single-channel events from receptors lacking a subunit can then be quantitatively analyzed and compared to single-channel recording of the receptor of interest. Events with characteristics of the undesired receptor can then be analyzed separately in subsequent analysis.

The only time that nAChRs gave significant single-channel currents in the absence of agonist was when 2 or more L9'S mutations were included (Chapter 4). As with the subunit omission experiments, understanding the spontaneous openings of a channel is valuable because some mutations (such as the L9' mutations) may increase the rate of spontaneous opening. If they increase it significantly, then any kinetic analysis should take into account these unliganded (usually brief) openings(*54*).

Channels that were likely voltage-gated were only present in records on rare occasions. They most often appeared after significant changes to the applied pipette potential and at high voltage (> +120 mV applied pipette potential). These events were of variable, but generally high conductance (> 100 pS) and irregularly shaped as opposed to the square, discrete openings of nAChRs.

A previous report demonstrated that it was possible to obtain current transitions when patching onto sylgard(*55*). Although the recording conditions are significantly different (higher salt and larger pipette potential), on a few occasions I did deliberately patch onto sylgard. High resistance seals did form readily, but I did not observe current transitions or channel-like activity.

2.3.4 Miscellaneous Recording Advice for Single-Channel Recording

My success rate for obtaining gigaseals of ~ 40% is similar to the 40–50% success rate that more experienced labs have reported (Bruce Cohen, personal communication). Several of the key factors in obtaining high rates of gigaseals are outlined in the Materials and Methods section. At one point, I had several consecutive recording sessions where the probability of obtaining a gigaΩ seal went down significantly (to < 20%) and when seals did form, they were of significantly lower resistance. At this point, I implemented the additional step of refiltering the pipette solutions at the start of each recording session as well as additional rinsing of the recording chamber at the end and beginning of each session. These measures restored the gigaseal rate and resistances.

Oftentimes, a patch, particularly with high resistance (> 50 gigaΩ), will not contain any channels. This may be disproportionately true for high resistance seals, since they are more likely to result from smaller pipettes, which in turn are less likely to contain a large enough section of membrane to have an ion channel.

As has been previously reported(*21*), I find that unpolished pipettes do not form seals nearly as readily as polished pipettes, though unpolished pipettes can be used in a pinch. The role of glass cleaned with chromic/sulfuric acid versus uncleaned glass was not investigated.

Sometimes (~ 20% of the time), when stripping an oocyte, the vitelline membrane was significantly thicker and less translucent than usual. This was usually true of most/all or none of the oocytes from a particular donor frog. The recording sheets contain a note when oocytes with this property were used for single-channel recording, though qualitatively I did not observe differences in the records from these oocytes. As always, these oocytes were only used for single-channel recording if the vitelline membrane could be completely removed.

2.4 Conclusions

Calculations shown in the discussion section of this chapter and data collected and reported throughout the rest of this thesis indicate that the oocyte expression system can be used for single-channel characterization of many receptors in which the DAD group has incorporated unnatural amino acids. The unique aspects and control experiments developed to perform single-channel recording on ion channels expressing unnatural amino acids were discussed above.

When a dozen or more rates are measured in a single-channel experiment, one or more are almost invariably seen to vary between mutants or agonists. By developing a technique in which we first perform whole-cell

recording, we verify that the changes to these receptor properties are ones that meaningfully impact overall receptor function, as opposed to minor and/or potentially compensating changes in binding and gating. We consequently advance the view that screening receptors by whole-cell recording, followed by targeted single-channel recording of high expressing wild type receptors, conventional mutants, unnatural mutants, or partial agonists, is a particularly efficient way to obtain kinetic information on key mutants while minimizing the tendency towards over interpretation of detailed single-channel kinetic analysis. Specific examples of the various ways in which we productively combined these techniques are described throughout this thesis.

2.5 Future Studies

It is perhaps underappreciated, but important to understand, that analysis of single-channel data can rarely be considered ‘complete’. So, for much of the single-channel data presented in this thesis, the analysis is necessarily partial. An exhaustive detailing of future studies available just by analyzing data that I’ve already collected could occupy an entire additional thesis. I have left some of these ideas with the group separate from my thesis. In the future studies sections of each chapter, I will generally restrict myself to the most interesting *experimental* single-channel studies. In this chapter, I outline analysis of the data I’ve collected about pipettes that could be done in order to continue optimizing this important and time-consuming process (see **Table 2.2**), as well as control experiments on endogenous and mechanosensitive channels.

	Singles	**Opus**
Pipette preparation		
Clean glass	0.25	NA
Prepare sylgard	0.25	NA
Pull pipettes	0.5	0.5
Sylgard pipettes	2	NA
Polish pipettes	2.5	NA
Fill pipettes	2	0.25
Pipettes per session	36	20
Attrition rate (estimated)	40%	10%
TOTAL pipette preparation	**378**	**17**
Solution preparation	15	40
Rig/Opus set up	30	15
Plate drugs, impale oocytes	NA	15
Strip oocyte and rinse for recording	40	NA
TOTAL Preparation Time	**463**	**87**
Recording		
Average per patch/run	30	60
Patches/runs per mutant	20	5
Clean up	20	20
TOTAL recording	**620**	**320**
Analysis (opus)		30
SCR analysis		
Initial screen of file	10	
Filtering	3	
Remove Electrical Interference	2	
Baseline correction	10	
All points histograms	5	
Event detection (automatic)	0.5	
Analysis of preliminary statistics	10	
Manual event detection	30	
Fit dwell time histograms	20	
τ_{crit}(s)	15	
# of interations per file	2.5	
Analysis time per file	**264**	
Analysis time per mutant	**2110**	**150**

Table 2.2. This table gives estimates for the amount of time spent on several of the main aspects of preparing for, executing and analyzing data for single-channel and whole-cell (opus) experiments. All values are in minutes.

When pulling pipettes on the custom vertical pipette puller, detailed notes were kept on the heat used and the duration of each pull. This could be compared to the final solution resistance of pipettes to determine which parameters or combination thereof, if any, correlate to achieving pipettes of the desired size. As of yet, this data from the manual, vertical puller have not been converted to electronic form for analysis because the P-97 provides much more rapid pipette production, with only slightly higher—and sometimes lower—pipette attrition rates (e.g. pulled glass that does not make it to the recording stage, in this case due to being significantly too small or big based on bubble number). In the case that particularly expensive pipette glass is used, a more efficient method based on analysis of existing data may be warranted. Additional dependencies may be worth considering. For example, there may be dependence on other factors, such as the lot of KG-33 glass used and/or how long the glass is cleaned in chromic/sulfuric acid. Since pipette resistance and seal quality (RMS noise and seal resistance) were also recorded for each pipette, analysis of the full, broader data set would allow for comparison of the probability of getting a seal, as well as seal quality, to the above parameters. Examination of these data could provide useful information going forward concerning combined optimization of pipette characteristics to maximize probability of getting a high resistance seal with the desired number of active channels. Another parameter that could be analyzed to optimize seal resistance and probability of formation is the time delay between polishing the pipette tip and using that pipette to form a patch. I hypothesize that as the length of this time delay increases (average was a few

hours), the probability of forming a gigaseal will decrease, but the effect could be on the quality of the seal and may be non-linear versus time.

A standard error for the seal resistances and RMS noise for patches I obtained is not available, but could be calculated from existing data by transcribing all lab notes (recording files) into electronic files.

In dozens, and perhaps hundreds, of single-channel records, suction was applied at the end of the record—and in some cases during active channel events. This suction rarely impacted P_{open} (see Materials and Methods); however, in some cases it induced new channel events. These were often raggedy events that were qualitatively different from the channel of interest, but they were not quantitatively characterized. However, qualitatively, the P_{open} of these mechanosensitive, presumably endogenous, channels often appeared to increase with increasing suction(*50*). Using data I've already collected, this behavior could be further characterized, along with the impact on channel kinetics.

2.6 Materials and Methods

The combined single-channel and whole-cell recording of *X. laevis* oocytes expressing LGICs with unnatural amino acids requires several distinct steps and significant preparation. This Materials and Methods section will describe: (2.1) general molecular biology methods, (2.2) site-directed mutagenesis and transcription, (2.3) preparation of tRNA for incorporation of unnatural amino acids, (2.4) expressing LGICs in *X. laevis* oocytes, (2.5) whole-

cell recording with the OpusXpress 6000A, (2.6) single-channel recording on a custom-built electrophysiology rig, (2.7) combined single-channel and whole-cell recording performed on a single oocyte, and (2.8) analysis of the resulting single-channel and whole-cell data. Note that, in practice, several steps are often completed in parallel.

2.6.1 Molecular Biology Methods; Preparations and Precautions

2.6.1.1 General Materials and Methods

Throughout these studies, unless otherwise stated, the water used was Millipore-filtered water with resistivity ≥ 17.5 MΩ-cm. The 0.2 µm filters used are Nalgene (Cat # 450-0020, Thermo Fisher Scientific, Inc., Wilmington, DE). For all molecular biology reactions, reagents were combined in an appropriately sized Eppendorf tube (usually > ~ 3 times the reaction volume), mixed by pipetting for 30 s, vortexed for 3 s, then microcentrifuged for 1–3 s, unless otherwise specified. Whenever possible, all RNA (here mRNA and tRNA) was handled at a dedicated RNA lab bench that was cleaned with ethanol before each use and kept clear of RNAses at all times. The RNA was pipetted with a set of pipettes that were never used with RNAses. Unless otherwise noted, mRNA and tRNA were kept up to ~ 1 year at -80° C, and stored in aliquots for a few injections (~ 2–8 µl) in order to minimize freeze-thaw cycles.

All agarose gels were 1%, generally made by dissolving 0.60 g agarose (Cat #15510-019, Invitrogen, Carlsbad, CA) in 60 mL of 1x Tris/acetic acid/EDTA (from 1 part 50x TAE, Cat #161-0743, Bio-Rad Laboratories, Hercules, CA,

diluted with 49 parts water). Gels were prepared as needed by boiling the 1% agarose in 1x TAE (heated for 1 minute in a microwave in an Erlenmeyer flask with a Kimwipe to prevent boiling over) and pouring the solution into a gel mold with a comb with the desired number of lanes (typically 8–16 lanes). This was stored at 4° C for 1–12 hours until use. The running buffer for the gel was 1x TAE; typically gels were run for ~50 minutes at 110 V, 400 milliamperes. Gels were visualized by bathing in ethidium bromide (0.1%) for 15 minutes followed by UV imaging (AlphaImager 3400, Alpha Innotech/Cell Biosciences, Santa Clara, CA). Typical exposure times were 1–2 seconds.

2.6.1.2 Buffers and Oocyte Incubation Media

The compositions of commonly used solutions are briefly defined here; all recording solutions were stored at 4° C with parafilm around the cap. Whole-cell drug solutions were stored up to 14 days at 4° C, while single-channel drug solutions were stored up to several months at -20° C, while attempting to minimize the number of freeze thaw cycles. ND96 solution consisted of 96 mM NaCl, 2 mM KCl, 1 mM $MgCl_2$, 1.8 mM $CaCl_2$, 5 mM HEPES, with pH set to 7.5 with NaOH. Ca^{2+}-free ND96 solution consisted of 96 mM NaCl, 2 mM KCl, 1 mM $MgCl_2$, 5 mM HEPES, with pH set to 7.5 with NaOH. The resulting solutions were filtered with a 0.2 µm filter and stored at 4° C. Usually, 1–4 liters were made at a time. Frequently, it was convenient to prepare a concentrated (20x) stock solution of ND96 and Ca^{2+}-free ND96 in order to quickly prepare the large volume of buffers used in semi-automated electrophysiology. These solutions

can be kept for 6–12 months at 4° C if parafilmed, as long as no solid is found in the bottle. I strongly recommend filtering all recording solutions (0.2 µm), including stock solutions, every few months, especially for cell-attached single-channel recording (where it is desirable to perform all of a given set of experiments with a given batch of pipette solution so that single-channel conductances are more comparable—same osmolarity, pH, etc.).

To obtain oocyte incubation media from ND96, 138 mg sodium pyruvate (Sigma; P2256-25G; final concentration 2.5 mM) and 60 mg theophylline (Sigma T1633-50G; final concentration 0.67 mM) was added to 500 ml of 1x ND96 solution and filtered with a 0.2 µm filter. 500 µl of 10 mg/ml gentamicin solution (Sigma G1397-10 ml; final concentration ~ 0.021 mM) was added. 1–2% equine serum (Hyclone, #SH30074.03, 500 ml) was added, and stored at 4° C, then used within 10 days. The osmolarity of the resulting incubation media was tested on a freezing point osmometer (Precision Instruments, Inc.; Osmette) and should be in the range of 190–230 osmol/L. I prefer values on the lower end of this range (190–200), especially for whole-cell experiments on the OpusXpress 6000A (Molecular Devices Axon Instruments, Sunnyvale, CA), as it seems to increase oocyte health during the runs. It is especially important that parafilm be used to seal the cap of the bottle containing the oocyte incubation media.

Oocyte stripping solution consisted of: 196 mM NaCl, 2 mM KCl, 1 mM $MgCl_2$, 5 mM HEPES, pH to 7.5. Note that this high salt solution was found to be preferable to an alternative hypertonic solution that contained a high concentration of sucrose; the later solution quickly became moldy even at 4° C.

Bath solution consisted of: 120 mM KCl, 5 mM HEPES, 1 mM $MgCl_2$, and 2 mM $CaCl_2$, pH to 7.4. In our experiments, this solution gives a reversal potential for agonist-induced currents of devitellinized oocytes of ~ 0 mV (see **Table 2.1**). Therefore, with an applied pipette potential of +100 mV, the transmembrane potential of a cell-attached patch is ~ -100 mV. Pipette solution consisted of: 100 mM KCl, 10 mM HEPES, 1 mM $MgCl_2$, 10 mM K_2EGTA, pH = 7.4.

2.6.2 PCR-Based Site-Directed Mutagenesis and mRNA Transcription

Mutagenic primers of 25–45 bases were designed with 50–55% GC content and $T_m \geq 78°$ C. They were terminated with one or more C/G at the 3' end and designed to avoid primer dimers. For each conventional mutation described here, forward and reverse (complementary sequence) primers were ordered (Integrated DNA Technologies). For each mutation, polymerase chain reaction (PCR) was performed using the Stratagene QuickChange method. 50 μl reaction mixtures containing 5 μl 10x polymerase buffer, 1 μl circular dsDNA template (5–50 ng), 1.25 μl of both mutagenic primers (~ 125 ng each), 1 μl 25 mM dNTP mix, 39.5 μl RNAse-free H_2O (Ambion Nuclease-Free Water, Cat #AM9932), and 1 μl Pfu Turbo Hotstart DNA polymerase were used with a 10 minute extension time in each thermocycle. Annealing temperatures were modified as required for successful incorporation of the mutation (iCycler, Bio-Rad Laboratories, Hercules, CA). 10 μl of each PCR reaction mixture were removed for a gel screen against the corresponding circular DA (control) in neighboring lanes to verify amplified linear product.

1.5–3 hour digestions of the remaining PCR reaction were performed with *Dpn*I to eliminate methylated template DNA from the PCR product, leaving the desired mutated DNA. The PCR products were amplified by electroporation (Electroporator 2510, Eppendorf, Hamburg, Germany) of Super Competent Top 10 *Escherichia coli* cells at 1800 V, followed by ~ 12 hours of growth on agar/Luria broth/ampicillin plates in an incubator with orbital shaking at 37° C. Single colonies were selected and amplified separately in 4 ml liquid Luria broth (Difco, #240230) + 4 μl ampicillin (Sigma, A9518-25G) or 4 ml liquid 2xYT Medium (Difco, #244020) + 4 μl ampicillin with orbital shaking (300 rpm) at 37° C for ~ 12 hours.

Using a QIAPrep Miniprep kit (Cat #27106, Quiagen, Valencia, CA), DNA from each bacterial sample was isolated as follows. DNA was pelleted by centrifuging at 2100 g for 5 minutes at 4° C and resuspending in 250 μl chilled buffer P1 in a 1.5 ml Eppendorf tube. 250 μl buffer P2 were added and mixed by inverting 6 times; 350 μl buffer N3 were then added and mixed immediately by inverting 6 times. Following 10 minutes of microcentrifuging at 13,000 rpm, the supernatant was pipetted onto a QIAprep spin column, centrifuged 1 minute and the flow-through discarded. The QIAprep spin column was washed with 0.5 ml buffer PB, centrifuged for 1 minute and the flow-through was discarded. This rinse was repeated with 0.75 ml Buffer PE. Residual buffer was removed with an additional 1 minute microcentrifuging. DNA was then eluted with 30–50 μl water into a fresh 1.5 ml Eppendorf tube with 1 minute microcentrifuging. The amount of DNA solution recovered from the spin column was tracked by drawing a line

on the Eppendorf tube at a level corresponding to volume of water used in the final DNA elution step. In some cases, several additional 1–2 minute microcentrifugations were needed to recover this total volume from the column. The concentration of the resultant DNA was quantified by measurement either on a UV-vis (SQ2802; Daigger) or NanoDrop-1000 (Thermo Scientific, Inc., Wilmington, DE).

DNA was then sequenced to verify the successful incorporation of the mutation at the selected site. The α1-subunit cDNAs used in these experiments encode an HA epitope in the M3-M4 cytoplasmic loop for Western blot studies (not described). The HA epitope provides an independent way of determining if a mutation(s) giving no current is not functional or is not being assembled, transported, and inserted into the cell membrane. Control experiments show that this epitope does not significantly alter EC_{50}.

DNA for each of the muscle and neuronal nAChR subunits (wild type or mutated) in expression vector pAMV were individually linearized by adding 50 μg (~ 50–100 μl) to 20 μl 10x buffer, 20 μl *Not*I (New England Biolabs, Ipswich, MA). RNAse-free water was added to a final reaction volume of 200 μl, followed by incubation for 8–16 hours in a 37° C water bath. Complete linearization was verified by running an agarose gel of ~ 2 μl reaction mixture against 2 μl of circular DNA. If the linearization reaction was not complete, additional *Not*I enzyme was added for up to an additional 24 hours of incubation. Once fully linearized, the DNAs were then transcribed using mMESSAGE mMACHINE T7 kits (Cat #AM1344M, Applied Biosystems, Foster City, CA) individually for each

subunit required for the receptor to be expressed. Typically transcription was performed by combining, in the following order: 6 μl 10x transcription buffer, 30 μl 2x NTP mix, 8 μl RNAse-free water, 10 μl (~ 10 μg) linearized plasmid DNA, 6 μl T7 enzyme mix. The resulting transcription reaction mixture was incubated for 3–4 hours in a 37° C water bath. Transcription was stopped by adding 3 μl DNAse and incubating at 37° C for an additional 1 hour.

The resulting mRNA was purified using an RNeasy Mini kit (Cat #74104, Quiagen, Valencia, CA). First, the reaction volume was adjusted to 100 μl by adding 37 μl RNase-free water, then 350 μl buffer RLT (with 1% β-mercaptoethanol previously added to buffer RLT), was added, vortexed 5 seconds and microcentrifuged 10 seconds. 250 μl of 100% ethanol were added and the resulting solution was mixed with gentle pipetting. The entire 700 μl sample was then applied to an RNeasy column placed in a 2 ml collection tube and microcentrifuged for 15 seconds at 14,000 rpm. The flow-through was discarded and the column was placed in a new 2 ml collection tube where it was washed with 500 μl diluted buffer RPE (4:1, 100% ethanol: RPE concentrate) by 15 seconds of microcentrifuging at 14,000 rpm. The flow-through was discarded and the washing process repeated with 500 μl diluted buffer RPE and 2 minutes microcentrifuging. The column was then transferred to a new 2 ml collection tube and microcentrifuged for 1 minute at 14,000 rpm to ensure dryness and minimize ethanol carryover. The column was then transferred to a final 1.5 ml Eppendorf tube, and, depending on desired final concentration, 30–60 μl RNase-free water were pipetted directly onto the silica-gel membrane of the column, followed by

elution with 1 minute microcentrifuging at 14,000 rpm. The eluent was reapplied to the silica-gel of the column and re-eluted to increase concentration. On some occasions, a second re-elution was performed, which appeared to further increase concentration. As above with DNA, the final volume of eluted RNA solution recovered here was roughly verified by drawing a line on the Eppendorf tube at a level corresponding to the volume of water used in the final elution step. Additional spins were used after final reapplication of eluent, if necessary, to recover approximately this total volume from the column. The concentration of mRNA was determined as described above for DNA (UV-vis or NanoDrop).

2.6.3 Preparation of tRNA Ligated with Unnatural Amino Acids for Incorporation by Nonsense Suppression

The nitroveratryloxycarbonyl (NVOC)-protected cyanomethyl ester forms of unnatural amino acids were used as previously synthesized by various Dougherty group members. These were coupled to the dinucleotide dCA, and enzymatically ligated to 74-mer THG73 $tRNA_{CUA}$ as previously described(*2*). Successful ligation was verified by MALDI-MS.

2.6.4 Expression of Ligand-Gated Ion Channels in X. Laevis oocytes

2.6.4.1 Preparation of Solutions and Injection Needles

Drug solutions were prepared in Ca^{2+}-free ND96 by supplementing with the desired concentration of drug within 12 hours prior to recording. For acetylcholine (ACh) chloride (A6625, Sigma), typical stock solution concentration

was 1.00 M in water and was immediately stored at -80° C in aliquots of 100–500 µl for ≤ 3 freeze-thaw cycles. Stock concentration varied for other agonists. Drug solutions for recording were prepared from stock solutions by first making the highest 3–4 concentrations—however, many concentrations were to be used per order of magnitude in concentration. Serial dilutions of these upper concentrations were performed by adding 5.00 ml to a final volume of 50 ml in Ca^{2+}-free ND96. ~ 10 doses over ~ 3 orders of magnitude of agonist concentration centered on the anticipated EC_{50} value is a good starting point. However, if the receptor was known or suspected to have a low Hill coefficient, n_H, (< ~ 1.2), then concentrations over 4 orders of magnitude were appropriate for initial runs in order to maximize the chance of seeing low concentrations with no response and a plateau in the dose-response at the highest concentrations. In addition, 4 doses per order of magnitude were used if there was reason to suspect multiple populations of receptors may have been present in a single oocyte in order to more definitively detect and characterize a possible biphasic dose-response behavior in which each component represents a different receptor population.

Injection needles were pulled from 8-inch-long glass with an outer diameter of 1.14 mm and an inner diameter of 0.53 mm (Cat #3-000-210-G8, Drummond Scientific, Broomall, PA) in groups of 10 or more on a Flaming/Brown P-97 horizontal pipette puller (Sutter Instrument Co., Novato, CA).

2.6.4.2 Isolation of X. Laevis Oocytes

Oocytes were isolated from *X. laevis* frogs by lab technicians in Professor Henry Lester's lab according to their standard operating procedure. Briefly, female *Xenopus laevis* frogs were purchased from Nasco (Cat # LM00535MX) and shipped during non-extreme temperatures. Frogs were allowed > 28 days to acclimate to their new environment, which consisted of charcoal-filtered tanks at 17° C ± 1° C with a light cycle of 12 hours full spectrum fluorescent light (8:00 am–8:00 pm) and 12 hours dark. After anesthetizing the frog for surgery (12–15 minutes in a solution of 1 g tricaine methanesulfonate and 1.7 g sodium bicarbonate in 1 l of frog tank water), a number of oocytes proportional to the number ordered for that day were removed from one side of the frog. No more than two-thirds of the oocytes were removed in any given surgery and surgeries for a given frog were performed on alternating sides. The harvested oocytes were separated into clumps of ~ 30 oocytes each and transferred into solution of 0.03% collagenase (Sigma, Cat#: C9891) in OR-Mg (2 mM KCl, 20 mM $MgCl_2$, 82 mM NaCl, 5 mM HEPES, pH = 7.4) in 15 ml tubes for ~ 80–100 minutes with slow, gentle partial inversion (~ 20 cycles per minute). The oocytes were then visually inspected. Healthy, spherical, stage V–VI oocytes of ~ 1 mm diameter were sorted into 60 mm dishes (Greiner Bio-One, CELLSTAR), rinsed twice with OR-Mg, then placed in fresh 60 mm dishes in oocyte incubation media. Subsequent to the first surgery for a given frog, the frog was allowed to recover for 14 days in an individual cage with 0.01 % gentamycin. A maximum of six surgeries per donor frog, 3 on each side, were performed, after which the frog

was euthanized.

2.6.4.3 Injection of Xenopus laevis *Oocytes*

Immediately prior to working in the injection station, all surfaces—including gloves—were sprayed with 95% ethanol and allowed to dry. The injection station consisted of: a microscope (Leica S6E, Spectra Services, Ontario, NY) with 20x eyepiece and adjustable objective (~ 0.5x–4 x), a flexible light source that had multiple lighting levels (Dolan-Jenner Industries, Inc., #3100, Lawrence MA), and x, y, z manipulator on a stable base (Nanoject Support Base, Cat #3-000-025-SB, Drummond Scientific, Broomall, PA). A 10 µl microdispenser (Cat #3-000-510-X, Drummond Digital Microdispenser) was used to control volume of injected solutions to within a few nl.

Wild type or mutant receptors were expressed by preparing solutions of mRNA with a total mRNA concentration of ~ 1–2 ng/nl for the desired ion channel subunits. In order to incorporate unnatural amino acids with the nonsense suppression technique, the unnatural amino acid-conjugated tRNA was deprotected with ~ 5–7 minutes photolysis using a 1 kW Hg(Xe) arc lamp with WG-335 and UG-11 filters. Within 15 minutes of deprotection, this tRNA was mixed with ~ 5–25 ng mRNA of the desired mRNA containing the UAG mutation at the site of interest and ~ 25 ng deprotected tRNA-amino acid and the two were co-injected as described below.

Injection of wild type receptors, receptors with conventional mutations, and receptors expressing unnatural amino acids then proceeded in similar ways, as follows. Freshly flame-sterilized Inox forceps (No. 5, Dumont, Foster City, CA)

were used to break a previously pulled injection needle to a tip diameter of ~ 10–20 μm at the injection station. This injection needle was then *completely* back filled with mineral oil, loaded onto the 10 μl microdispenser, and placed in the injection manipulator. mRNA (or mRNA + tRNA) solution, typically 1–3 μl, was placed on a clean coverslip and drawn into the injection needle. Once the mRNA (or mRNA + tRNA) solution was placed on the coverslip, and especially under the light source, the amount of time that these small volumes were left on the coverslip was minimized since evaporation could rapidly change the RNA concentration. The amount of solution actually drawn up into the injection needle was compared to the amount deposited on the coverslip in order to verify that the volume had not been significantly altered.

Defolliculated stage V–VI *X. laevis* oocytes (Nasco, Fort Atkinson, WI) were injected by lining them up in a custom made dish with ridged bottom, pressing the injection needle through the cell membrane until the membrane visibly bounced back, then expelling ~ 50–70 nl of the combined mRNA (or mRNA + tRNA) solution into the cell. The overall injection volume was kept to less than 10% of the oocyte (e.g. < ~ 100 nl) in order to avoid damaging the oocyte membrane. Injected oocytes were placed in 35 mm dishes (Cat #627160, Greiner Bio-One, CELLSTAR) with fresh incubation media. 10–40 oocytes were stored per 35 mm dish. The oocyte incubation media was changed 30–60 minutes after injection, and oocytes were incubated at 17±2° C with orbital shaking. Subsequently oocytes were examined 6–12 hours later, then every 12–24 hours. During these checks, oocytes that were damaged or had begun the

maturation process (showing an expanding circle of degenerating membrane) were discarded and the media was changed. In some cases, the health of injected oocytes was improved by using a new 35 mm dish each time the oocyte incubation media was changed.

2.6.4.4 Controlling Expression Levels

Several ways to control the number of receptors on the oocyte surface were covered in the discussion section. For receptors which commonly exhibited very low expression level (especially wild type α4β2), long incubation times were employed in order to obtain sufficiently high expression for single-channel recording. Oocytes were carefully examined at each media change as described above, which allowed them to be kept healthy and viable for successful recording (single channel and whole cell) for 6–10 days post-injection and 8–15 days after surgical removal from the donor frog. Since expression can vary significantly between oocytes from different donor frogs and waiting ~ 1 week before knowing expression levels is inefficient, multiple batches of oocytes were frequently injected in parallel. Injecting 3 batches of oocytes was found to be the optimal number, though if a given receptor or mutant is reliably expressing, fewer batches may be sufficient for high chance of successful single-channel recording.

2.6.5 Whole-Cell Recording with the OpusXpress

Semi-automated whole-cell voltage clamp recordings of *X. laevis* oocytes expressing LGICs were performed with the OpusXpress 6000A (Molecular

Devices Axon Instruments, Sunnyvale, CA). Varying types and levels of maintenance procedures were developed in the group in order to accommodate the high level of regular use of our OpusXpress 6000A (60–100 hours per week). The key aspects of the most common maintenance procedures are briefly summarized here; keep in mind that the timeline is not exact and, in many cases, specific aspects of the maintenance listed below were also performed as needed.

2.6.5.1 Maintenance of the OpusXpress

Weekly maintenance: The electrode holders are cleaned by completely disassembling and rinsing in water with stirring for 30–60 minutes. The brass pin, threaded Teflon collar, and electrode wire with nylon sleeve and silicone seal were not rinsed. Each piece is then dried thoroughly and carefully inspected for any use-related wear. Damaged or overly worn pieces are replaced at this time; the most common are: electrodes losing their chloride coating, broken or missing AgCl pellets, cracks in the electrode holder threading, and corroded brass pins. Electrodes are then reassembled. Debris is removed from solution filters by sonicating them in water for 10 minutes. Headstages are inspected for corrosion and chambers are inspected for damage; chambers are rinsed individually by pipetting several ml of water to remove debris. The liquid handler nozzles and headstages are wiped with a moistened Kimwipe, then allowed to dry before use.

Monthly maintenance: In addition to the weekly maintenance, the headstage are sprayed tracks with Inox lubricant and fluorocarbon gel (Cat #911–1, The SmartGrease Co., Fairhaven, MA) is applied to the driving

assembly shafts; gloves are required. Also approximately each month, all peristaltic tubing on pumps A, B, and the aspirator pump are replaced. The new peristaltic tubing is primed by rinsing with 70% isopropanol for 10 minutes, followed by rinsing with water for 10 minutes. In each case a flow rate of ≥ 1 ml/minute is used for pump A and B and ≥ 4 ml/minute for the aspirator pump. It is important that the aspirator pump rate be large enough to ensure that there is no overflow of isopropanol or water in the chambers. It is crucial that such overflow be avoided because several electrical circuit boards for the opus are located directly under the chambers and there is not a water-tight seal between the chambers and electronics. This type of overflow generally results from insufficient aspiration, which can arise for several different reasons even if the aspiration rate is larger than the sum of pump A + pump B flow rates. Obstruction of the aspirator (in chamber) can be overcome by removing the aspirator and blowing air through it to remove any physical debris, such as decomposing oocyte membrane; light should be visible through the aspirator in order for it to function effectively. The lines that lead from the chambers to the aspirator tubing can become disconnected even during normal usage; these should be checked and all appropriate washers should be used at each junction. A third issue affecting aspiration is that the aspirator pump itself may not efficiently grip the tubing. In many cases, the ability of the pump to efficiently grip the peristaltic tubing to pump buffer can be greatly enhanced by the use of a material with moderate static friction (e.g., lab tape).

2.6.5.2 OpusXpress Recording Session

A typical OpusXpress recording session is now described. Recording electrodes were pulled on a Flaming/Brown P-97 horizontal puller starting with borosilicate glass with length 15 cm, outer diameter of 1.5 mm, and inner diameter of 1.17 mm (Cat #BF 150–117–15, Sutter Instrument Co., Novato, CA). 20–30 electrodes are generally pulled in a batch before the puller filament is allowed to cool for 10–30 minutes.

In order to begin preparation for a recording session, these electrodes, which may be pulled days or weeks in advance, were back filled with 3.0 M KCl. Bubbles in the electrode tip were removed by flicking and the electrodes were placed in electrode holders. One of each of these holders with electrode was placed on each of the 16 OpusXpress headstages. The electrodes were then lowered into Ca^{2+}-free ND96 solution in the recording chambers. Electrodes with resistances initially in the ranges: 0.3–3 MΩ for current (I) electrodes and 0.3–10 MΩ for voltage (V) electrodes, were used for repeated experiments (multiple runs) as long as their resistances were still in range, they did not show drift, and they continued to be free of significant oocyte membrane (as indicated by visual inspection). Electrodes were usually replaced every 1–2 days. 96 well drug plates were filled with increasing concentrations of agonist in Ca^{2+}-free ND96 buffer, starting with 0 and continuing to concentrations of > 10 times EC_{50}, or where channel block was evident in the opus waveforms (traces) for receptors with Hill coefficients of ~ 2. If the Hill coefficient of the receptor being studied is significantly less than 2, then the highest agonist concentration may need to be

closer to ~ 100 times EC_{50}. In all cases it is important that the dose-response relation when plotted on a semi-log scale (normalized current response on the y-axis and log of concentration of agonist on the x-axis) 'turns over', meaning that there are at least a few data points at the upper concentrations that exhibit a normalized response of ~ 1. Similarly, it is important that at two or more of the lower concentrations no activation above baseline is seen in the opus waveforms; one of these should be the 0 concentration.

One oocyte was placed in each of the 8 recording chambers and impaled individually. In order to maximize oocyte health, and especially if subsequent single-channel recording on a given oocyte is desired, oocytes should be impaled to the least extent, and shortest duration, possible (see Section 2.7 for further details). Common recording parameters were: capacitance neutralization (0.0), output gain (1), ultra-high DC gain (on), and initial recording gain (1500). Recording gain was then optimized by increasing or decreasing gain individually on each impaled oocyte to achieve maximally square current responses to test pulses with minimal ringing (usually gain values of 3000–6000 for healthy oocytes). Oocytes were then voltage clamped at a holding potential between -40 mV and -80 mV, most typically at -60 mV. Larger holding potentials were used when necessary to increase I_{max}. This can be used to increase the signal-to-noise ratio if it is too low in order to regularly and consistently determine the maximal response at each concentration from the opus trace. However, this should be balanced against the observation that higher holding potentials often decrease oocyte viability over the course of an entire run. I_{max} comparisons, for

example for relative efficacy experiments, are made at the same holding potentials and after similar incubation times, temperatures, and parallel treatment of oocytes.

A typical opus run was performed by applying each concentration of drug solution (1 ml) for 15 seconds followed by a 130 second wash with Ca^{2+}-free ND96 solution between each applied drug concentration. During drug application, oocytes were superfused with a flow rate of 4 ml/min; during wash, a flow rate of 3 ml/min was used. Data were sampled at 125 Hz and filtered at 50 Hz. The run was initiated and dose-response data for all prepared agonist concentrations was collected for ≥ 5 oocytes with sufficient expression for each mutant. It is advisable to apply at least two control doses (Ca^{2+}-free ND96 with no added agonist) during each run to verify non-response as well as to differentiate from leak current, spontaneous openings, and fluidics effects (such as oocyte shearing and other membrane damage that can occur during recording). For each mutant, recordings were performed on oocytes from ≥ 3 different donor *X. laevis* frogs.

2.6.5.3 Control Experiments for Unnatural Amino Acid Incorporation

The fidelity of unnatural amino acid incorporation at each new site was verified with a 'wild type recovery' experiment and 'read-through/reaminoacylation' tests. In the 'wild type recovery' experiment, UAG mutant mRNA and tRNA charged with the amino acid that is present at this site in the wild type receptor are co-injected. Generation of receptors that are

functionally indistinguishable from the wild type receptor (similar EC_{50} and n_H) indicates that the residue carried by the suppressor tRNA was successfully and exclusively integrated into the receptor. For the 'read-through/reaminoacylation' tests, the UAG mutant mRNA was introduced with (1) no tRNA, (2) tRNA THG73 that is not charged with any amino acid, or (3) tRNA THG73 enzymatically ligated with dinucleotide dCA, but not coupled to any amino acid. Lack of currents in these experiments validates the reliability of the nonsense suppression experiments for the corresponding specific sites.

2.6.6 Single-Channel Recording (Patch Clamp)

2.6.6.1 Building an Electrophysiology Rig for Single-Channel Recording (with Bruce N. Cohen)

The electrophysiology rig was designed and built with emphasis on single-channel recording of *X. laevis* oocytes in the cell-attached configuration. Mechanical stabilization, high signal-to-noise, and minimal electrical interference (noise) were important design factors, while the rig was not designed for fast perfusion. The components listed in the results section were assembled as described for data acquisition, conditioning, sampling, and data storage. Some of the key considerations and resulting approach are summarized here and in the next section.

The CV-5 100GU headstage (gain 100 mV/pA) was equipped with a pipette holder that was modified with a small hole (~ 1 mm) into which a metal tube was inserted. This tube was connected to a manual pressure modulator

(mouth pipette)—ideally the tube of a 3 ml plastic syringe with bypass valve. Since many components were extra, unused components (HAL lab, or sometimes DAD lab), each part was thoroughly dusted (Kimwipes and can of air) prior to use. Dirt in the recording solutions or in the pipette tip can be fatal to single-channel experiments. Additionally, all components were cleaned of any salt residue. Electrical components for the rig were purchased at the Caltech Electrical Engineering shop (i.e., BNC cables, soldering iron and solder, heat-activated insulator, Q-dope, etc.) or C&H Supply in Pasadena (i.e., capacitor, pump, miscellaneous hardware, etc.). All other materials were obtained from the Caltech Biology stockroom (i.e., syringes, beakers, glass vials, tygon tubing, etc.), were custom made by the instrument shop (fine manipulator holder, rod to mount solution bottles), or purchased from commercial suppliers.

2.6.6.2 Minimizing Electrical and Mechanical Noise; Grounding (with Bruce N. Cohen and Pam Fong)

In order to ensure that each component has the same electrical frame of reference, we connected all of these to a single power strip, which is preferably configured with no resistors in-between outlets. Shorter cables with minimal looping were emphasized since extraneous current flow is more easily induced in looped cables. Monitors sometimes produce high frequencies, so an LCD was used for the computer display. Care was taken to route the video cable well away from other cables and electrical components. Whenever possible, the computer hard drive is defragmented once per month. The doors to the Faraday cage were grounded to the vibration isolation workstation. In order to inhibit salt

accumulation from disrupting the solder connections used for grounding, these connections were coated with Q-dope.

Certain configurations of the rig components resulted in increased noise. These were generally found and corrected by trial and error. For example, when the Hum Bug was directly touching the GeneClamp 500B, a significant noise transient was observed. Placing the Hum Bug on top of the filter eliminated this noise. Several modifications and additions were required in order to obtain the level of mechanical stability and low noise required for cell-attached single-channel recording. A faraday cage, which is open on one side (for the vibration isolation workstation) and has hinged doors on one other side for general access, encased the following items: the recording chamber (on raised platform; Newport), course manipulator (for initial positioning of pipette), light, and dissecting microscope—which were all mounted on a leveled Newport vibration isolation workstation. The fine manipulator (Narishige) was mounted separately in the cage, but not connected directly to the table. No cables (headstage to GeneClamp 500B), grounding wires, bath electrode, or power cable for light were allowed to touch the table—they were either suspended from the top of the cage, or connected to the side of the cage. Where possible, the overall center of mass of the components on the table was kept as low as possible. To enhance this goal, and to generally dampen vibrations caused by motions in the rig room or nearby, 2 30-pound lead bricks were added to the table top.

2.6.6.3 Single-Channel Electrophysiology Rig Maintenance

Similar maintenance was implemented for this electrophysiology rig as the above described for the opus, as applicable. Also important are rinsing the perfusion lines and chamber after each use with water, regular maintenance of electronics, and frequent checking of the wiring/cables for salt buildup, fraying, and proper grounding. Additionally, every few months the pipette holder was cleaned with ethanol and sonicated for 15 minutes to remove oil and dirt buildup that can increase noise. Annual maintenance included deconstruction of the majority of the components on the table, cleaning, and reassembly.

2.6.6.4 Preparation of Solutions for Single-Channel Recording

Within 12 hours prior to recording, the recording pipette solution with the desired concentration of agonist was made from pipette solution. For extended recording sessions, drug solutions were stored at 4° C (or on ice) if not being used for extended periods of time. These solutions were moved to room temperature ~ 1 hour prior to use.

2.6.6.5 Preparing Pipettes for Single-Channel Recording

2.6.6.5.1 Cleaning the Pipette Glass

KG–33 glass with I.D. = 0.80 mm +/- 0.05 mm, O.D. = 1.60 mm +/- 0.05 mm, length = 75.0 mm +/- 3 mm (Garner Glass Company; lots: 2544, 5596, 7687, and 8286) was cleaned by complete submersion in chromic-sulfuric acid (Fisher, SC88-1) for ~ 12–36 hours, followed by rinsing ≥ 4 times each with

alternating water and methanol, then bathing ≥ 16 hours in methanol and drying ≥ 12 hours at ~ 110° C. Cleaned glass was stored for ~ 6–12 months in an airtight container.

2.6.6.5.2 Pulling Pipettes

Pipettes with final resistances of ~ 8–25 MΩ, were pulled from cleaned KG-33 glass in two stages. Pipettes were made using two different pullers: a vertical puller and a horizontal Flaming/Brown P-97 electrode puller (Sutter Instrument Company, Novato, CA); the latter, once available, proved significantly more efficient.

Vertical puller (**Figure 2.10A**): This custom-built puller had a variable-current power supply. The filament used was a nichrome heater coil (David Kopf, #710). The first pull was used to thin the glass over a length of several mm to a width of ~ 200 µm, this was achieved with heat of ~ 24 amperes through a nichrome wire looped 2.5 times with diameter of ~ 10 mm. The glass was then repositioned so that the middle of the thinned portion was approximately centered in the filament. Pipette tip size can be controlled by varying the precise positioning after the first pull and the current during the second pull. The current for the second pull was adjusted—generally between 13.5 and 14.0 amperes—to yield pipette openings of the desired size. A crude estimate of pipette tip size was regularly made and recorded for each pipette after pulling and again after polishing (see below).

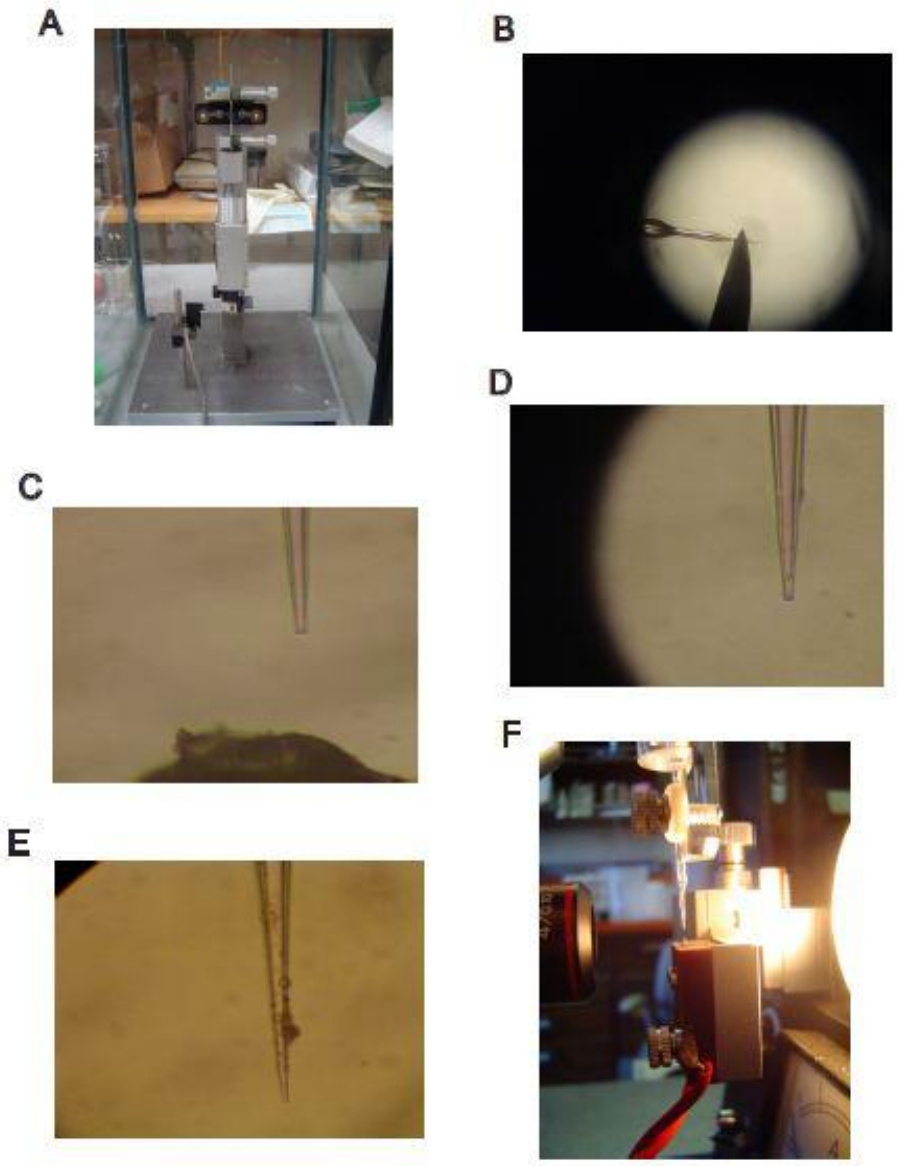

Figure 2.10. Preparation of pipettes for single-channel recording. A) The custom vertical puller on which some pipettes were pulled. B) The process of applying sylgard to the pipette tip after pulling electrodes at 80x magnification. The picture shows the use of the tip of a small needle to apply the sylgard, which is visible as globs over the entire visible pipette shaft. This coating with a material of high dielectric constant increases the electrical isolation of the pipette tip. The sylgard coating is also hydrophobic, so it prevents water from creeping up the tip when in solution. Pictures C, D, and E are shown at 900x magnification. C) A "good" pipette tip (shown near a filament). D) A pipette tip that has been covered in sylgard; it is unusable. E) A pipette tip that has significant dirt near the tip. If polishing on the microforge in the subsequent step doesn't remove this dirt, then the pipette should not be used. F) Microforge used for polishing the pipette tip. The pipette tip is lowered near the filament, and current is passed through the filament to polish the pipette tip.

The tip size was estimated as follows: A 10 ml syringe was fitted with silicon tubing (here the silicon piece from Drummond Microcaps and Tygon tubing was used) and the back end of the pipette was placed firmly in the tubing. The pipette tip was then submerged in 95–100% ethanol and the plunger depressed slowly until bubbles were seen coming from the pipette tip. The syringe reading at this time was recorded and is termed the bubble number. Depression until the reading is ~ 4.0 to 4.5 ml (i.e. depression of ~ 5.5 to 6.0 ml) typically corresponded to pipettes of ~ 10–20 MΩ in our recording solutions. The size was never directly measured, but based on viewing at high magnification and the resistances, the pipette tips in this range were probably ~ 0.5–3 µm in diameter.

Horizontal puller: The ramp value was determined, and the program developed, as outlined in the *Sutter Instrument Pipette Cookbook* (2010 Rev F.). The most recently used parameters were: P = 500, heat = 510 (ramp = 520), pull = 000, velocity = 24, delay =1.

For either puller, it was generally easiest to obtain a pipette tip with the desired size by systematically adjusting the appropriate parameters for the second pull. Because, unlike whole-cell opus recording, these single-channel pipettes will not be inserted into the oocyte, the overall pipette morphology is less important than the pipette tip size and physical characteristics (such as defects) immediately in the vicinity of the pipette tip. Thus, the main pipette morphology concern was to make pipette tips that could be filled with recording pipette solution as easily as possible. Consequently, one of the key benefits of the

horizontal puller was that the pipettes it produced were symmetrical and almost always both could be used, while for the vertical puller, the pipettes were asymmetrical and the lower pipettes generally had long, thin tips that made them nearly impossible to remove bubbles from for recording. Also, for both the vertical and horizontal pullers, significant variation in pipette-to-pipette tip size was common, even when identical settings were used. In order to maximize filament life, and diminish pipette-to-pipette size variation, no more than several successive pulls were performed on either puller, generally corresponding to 5–10 pipettes at a time. A break of 10–30 minutes of non-use of the puller was generally sufficient to prevent overheating and increase consistency in pipette tip size.

2.6.6.5.3 Applying Sylgard and Polishing the Pipette Tip

Sylgard (World Precision Instruments, SYLG184) was then applied to within ~ 20–100 µm of the pipette tip using the tip of a 23 gauge needle (Becton Dickinson & Co). The Sylgard was cured by ~ 10–20 seconds of gentle rotation of the pipette, with freshly coated tip up, in a stream of hot air from a heat gun. Pipettes at this stage can be stored for ~ 14 days in an air-tight container. Pipette tips were polished for ~ 15–30 seconds on a microforge with a compound microscope providing 900x magnification (15 x eyepieces, 60 x objective, NA 0.70), usually immediately before recording and preferably no more than several hours before use. At this magnification, openings in tips of pipettes with bubble number ~ 4.4 or larger are clearly discernible. After polishing the pipette tip, the

bubble number was again tested and recorded. The bubble number should be measurably lower than it was after being initially pulled; in my experience, a decrease of ~ 0.2 to 0.5 ml best facilitates gigaseal formation. This level of decrease in bubble number is often accompanied by a visible change in the pipette tip morphology—the tip becomes slightly darker and tapers to a narrower diameter. If there was no change in the bubble number or no change in the pipette tip, the pipette tip was polished a second time. Pipettes were then stored, coated tip up, in a closed plastic box (Biology stockroom) affixed in clay to prevent contamination. The high magnification of the microforge allowed for unsuitable pipettes to be identified and discarded before attempting to record with them. For example, in some cases, sylgard accidentally covered the pipette tip making it unusable (**Figure 2.10D**). In other cases, dirt near the tip was readily visible (**Figure 2.10E**). If this dirt did not disappear with polishing, then the pipette was discarded. These factors, in addition to the occasional breakage of the pipette tip and small pipettes/overpolishing (which lead to pipette tips that cannot be filled) contributed to the overall 40% attrition rate (**Table 2.2**).

2.6.6.6 Single-Channel Recording

2.6.6.6.1 Preparing the Oocyte for Single-Channel Recording

One to three oocytes were placed in hypertonic solution (oocyte stripping solution) for 15–30 minutes. After this incubation, the oocyte(s) were visually inspected to determine if the vitelline membrane (**Figure 2.11**) had separated from at least part of the oocyte. Since the hypertonic solution doesn't cause the

vitelline membrane to swell, but rather causes the oocyte's cell membrane to shrink, the oocyte generally appeared dimpled or slightly creased in one or more regions when it was ready to have its vitelline membrane stripped. When this was the case, the vitelline membrane was generally visible as a translucent, colorless membrane that was separated from the oocyte membrane by up to ~50–100 µm.

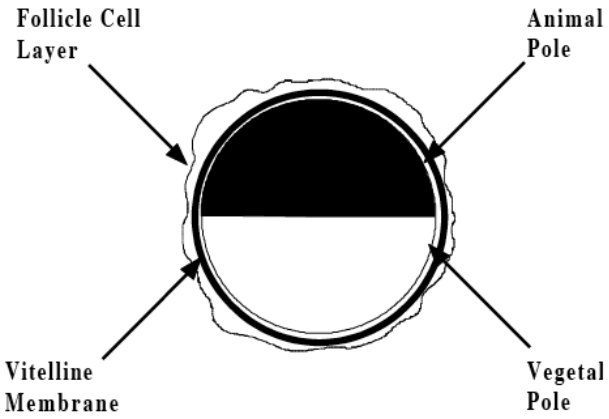

Figure 2.11. A schematic of a stage V or VI oocyte from a *Xenopus laevis* frog ovary. This cell has an approximate diameter of 1 mm. The outermost, irregular follicular cell layer is removed during the initial oocyte preparation by digestion with collagenase and subsequent orbital shaking for 12–24 hours. Here the vitelline membrane is shown as a thick black layer that surrounds the entire oocyte. In hypertonic solution, the oocyte's membrane shrinks away from the vitelline membrane allowing the vitelline membrane to be manually stripped from the oocyte. The oocyte is bipolar with a darker animal pole (upper) and lighter vegetal pole (lower). This is of practical application in single-channel recording because it is often easier to record on the animal pole, since positioning of the pipette over this pole allows for maximal contrast between the pipette tip and easy pipette manipulation while minimizing the chances of accidentally touching the oocyte prematurely. Some oocytes also display a lighter color band around the hemisphere between the animal and vegetal poles. (From *The Axon CNS Guide, 3rd Edition*)

The oocyte's vitelline membrane was then gently stripped using 2 pairs of jeweler's forceps (Dumont, No. 5). This step takes some practice; it was usually easier to strip the vitelline membrane from oocytes that had been allowed to recover 1–2 hours after whole-cell recording (see discussion section on '*Single*-

Channel and Whole-Cell Recording on the Same Oocyte' for details). Oocytes should not be left in the hypertonic solution for more than ~ 1 hour because the oocytes osmoregulate over time and return to their normal volume, at which point stripping the vitelline membrane becomes very difficult.

I developed the following procedure for stripping the vitelline membrane with a high level of success (80–90%). It involved gripping the vitelline membrane with one pair of sharp-tipped jeweler's forceps (Dumont No. 5) and pulling slightly (~ 200 µm, or 1/5th the diameter of the oocyte) away from the oocyte; only the vitelline membrane should move. Using a second pair of jeweler's forceps, part of the vitelline membrane that was now being pulled away from the oocyte was grasped. The two forceps were then slowly pulled away from each other. In the ideal case, the oocyte rolls out of the vitelline membrane, which comes off in a single piece. But, in some cases, the vitelline membrane comes off the oocyte in a few separate pieces, so it is important to keep track of the vitelline membrane to ensure that all of it has been removed. Vitelline membrane that remains on the oocyte can interfere with gigaseal formation and recording. The devitellinized oocyte was then transferred to a separate 35 mm dish with bath solution for 1-2 minutes, then transferred to the recording chamber which was filled with bath solution (~ 1 ml). Once devitellinized, it is important to avoid contact with the air-water interface, which can cause the oocyte membrane to rupture. The two forceps are wiped gently with a moistened Kimwipe after each use and not used for any other purpose in order to ensure that the tips stay sufficiently sharp for grasping and removing the vitelline membrane.

2.6.6.6.2 Final Pipette and Rig Preparation for Single-Channel Recording

The tips of sylgarded, polished pipettes were filled by submerging them in the drug pipette solution and applying suction to the back of the pipette for ~ 30–60 seconds. The same 10 ml syringe used to test the 'bubble number' can be used to apply this suction, provided that it is kept dry. During this time, the progress of filling the pipette tip was monitored by viewing the pipette against a strong light source for contrast. The back end of the pipette was then fire polished for ~ 3–5 seconds in the flame of a small butane torch (~ 2-cm-long flame) until the back end of the pipette ass visibly smooth and rounded. This step is important to reduce the extent to which the pipette scratches chloride off of the AgCl wire for the pipette (see below). Once cooled to room temperature, the pipette is then back filled with the same drug solution as was used to fill the tip, using a 28 gauge syringe needle (World Precision Instruments, MF28G-5) and 1 ml syringe with attached 0.2 µm nylon filter and flicked until all bubbles have been removed from the tip. This sometimes took up to a few minutes of intermittent flicking and vertical standing (in clay), especially for smaller pipette tips—with polished bubble number < 4.0—that may not have been significantly filled with the suction step for tip filling. Since sylgard applied near the pipette tip sometimes made it hard to unambiguously identify bubbles as opposed to uneven sylgard distribution, as pipettes were filled they were again viewed against a strong light source to aid in identification of bubbles. A single-channel pipette with a bubble cannot be used for recording.

Once prepared, the pipette was loaded into the electrode holder with AgCl wire. I re-chlorided the silver wire prior to each recording session and any time that silver is visible on the wire (shiny as opposed to dull brown) by submersion in household bleach for 15–30 minutes, until dull brown in color. Do not chloride the entire length of the wire, as the non-pipette end must make electrical contact with the brass pin that connects to the headstage in the pipette holder. Ag wires can generally be re-chlorided 3–5 times. Sometimes, Ag wires were cleaned in a flame, but these often proved difficult to re-chloride evenly. Once the pipette is secured on the headstage, positive pressure is applied and the solution level in the chamber is reduced to ~ 1–2 mm above the oocyte by gently sucking off the top layer of solution with a Pasteur pipette. In our rig, this leaves ~ 300 µl of bath solution in the chamber. It is important not to disrupt the oocyte membrane at all at this stage to minimize the occurrence of events from mechanosensitive channels (see Section 2.6.6.6.4 for further details). The application of positive pressure to the pipette and aspiration of the top layer of solution are important steps to prevent clogging of the pipette tip before a gigaseal is formed with the oocyte. An additional precaution taken was to refilter the drug solutions (0.2 µm nylon filter) before each recording session, especially if gigaseal formation was problematic.

The pipette was introduced into the recording bath at a steep angle of 60–70°. This, in addition to prior reduction of the bath solution volume, minimized the length of the pipette in contact with the solution and the resultant noise. The course and fine manipulators were then adjusted to place the tip of the pipette

within ~ 200 µm of the oocyte without touching it. All unnecessary AC electronics (especially lights) were then turned off and the pipette resistance was tested and recorded as the solution resistance. Final approach to the oocyte occurred with the fine manipulator (Narishige) while applying a 100 µV seal test. Contact with the oocyte was recognized as a small baseline deflection on the oscilloscope accompanied with a 1.5- to 3-fold increase in the pipette resistance.

2.6.6.6.3 Obtaining the Cell-Attached Configuration for Single-Channel Recording

Once the pipette was in contact with the oocyte membrane, data acquisition was initiated, then gentle suction was applied by mouth as soon as possible in order to minimize channel activity that might be missed as channels desensitize (**Figure 2.12**). Often, gigaseal formation occurred nearly instantaneously, but sometimes took as many as several minutes with intermittent gentle suction. In other cases, success in forming a gigaseal was achieved after additional advancement of the pipette and application of moderate suction. In some cases, small negative pipette potentials (-5 to -50 mV) facilitated gigaseal formation, though this process was often slow. Once a gigaseal of several to hundreds of gΩ was formed, the desired pipette potential was applied.

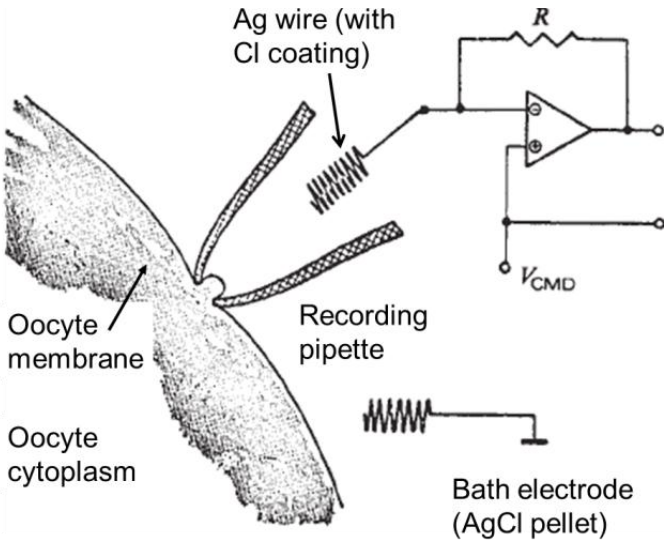

Figure 2.12. A diagram of the physical and electrical connection between the recording pipette and the oocyte membrane. As is described in text, the gigaseal is formed by pressing the pipette tip against the oocyte, then applying suction. This process results in an electrically isolated patch of membrane that is believed to be partially sealed to the inside of the pipette in addition to the rim, producing an 'omega'-like shape in the pipette tip. VCMD controls the applied pipette potential through the AgCl wire. (Adapted from Sigworth and Neher, 1980(*29*))

Data were collected using a GeneClamp 500B amplifier (Axon Instruments) at full bandwidth (50 kHz; 4-pole Bessel, -3 dB) with a CV-5 100GU headstage. The signal was then low-pass filtered (Avens Signal Equipment, AP220, 20 kHz; 8-pole Bessel, -3 dB), sampled with a Digidata 1320A (50 kHz), and acquired in Clampex 9.2 (Axon Instruments). Channel openings and closings were observed as nearly discrete changes in the measured current when the signal was large enough with respect to the noise (usually ~ 3–10-fold). Once the gigaseal was lost, sufficient data (number of events) were collected, or further channel activity seemed unlikely due to channel desensitization or inactivation, the data acquisition was stopped. In some cases, recordings were performed at multiple pipette potentials on a single patch in single or multiple recording files (see **Figure 2.6**).

2.6.6.6.4 Controls for Single-Channel Recording

Where appropriate, several single-channel controls, whose purpose was described in more detail in the discussion section, were performed. These included: recording in the cell-attached configuration in the absence of agonist, recording with and without agonist on uninjected oocytes, recording after deliberately patching onto an oocyte-sized blob of sylgard, and applying gentle, moderate, and significant suction to the patch during recording.

The key additional step that we added, which seemed to significantly reduce the occurrence of endogenous channel events, was to allow the oocyte to sit in the recording chamber for 15 minutes after stripping the oocyte's vitelline membrane. 15 minutes in the chamber was generally sufficient, though this time length can readily be extended if endogenous activity is still seen.

2.6.6.6.5 Outside-Out Configuration for Single-Channel Recording

Attempts were made to achieve the outside-out patch configuration using both common methods to obtain the intermediate whole-cell configuration: significant suction and large voltage pulses(*21*). Though development of this recording configuration was not pursued extensively, my qualitative observation from trying each method a few times was that the suction method gave a better chance of obtaining the necessary intermediate whole-cell mode. Subsequent withdrawl of the pipette from the oocyte produced the outside-out patch configuration on some occasions. One of the best examples was shown in **Figure 2.5.** Since the outside-out configuration allows for multiple

concentrations, or even multiple agonists, to be applied to the same channel(s), it may be worth pursuing for single-channel dose-response studies. Also, the outside-out patch configuration could prove useful for receptors that are low expressing, since it often monitors a larger patch of membrane than the cell-attached method.

A useful overview and tutorial for many aspects of single-channel recording of ligand-gated ion channels is available(*56*).

2.6.7 Combined Single-Channel and Whole-Cell Recording of Single X. Laevis Oocytes

Oocytes were first recorded, as described in Section 2.5, on the OpusXpress. Extra care was taken to use opus electrodes that were as small as possible (toward the high ends of the respective resistance ranges) and the amount of time that oocytes spent impaled and voltage clamped was minimized. Immediately at the conclusion of the run, the electrodes were slowly removed (*not* using the 'home' function; instead by slowly backing the electrodes out). The oocytes were then gently removed from the opus chambers and transferred to individual wells of 12 well plates with fresh oocyte incubation media. Each well was labeled to indicate which recording chamber the oocyte came from for future correlation of the whole-cell and single-channel data. The oocytes were allowed to heal for 1–10 hours at 18° C with orbital shaking; usually a minimum of 3 hours was necessary before the next step.

Once visual inspection of the oocytes revealed that the membrane appeared to have healed—no remaining gashes from the whole-cell electrodes—an oocyte was transferred to hypertonic stripping solution. These previously opus-recorded oocytes were monitored carefully when they were in the hypertonic stripping solution. In some cases, oocyte health rapidly declined leading to disintegrating oocytes, especially if the oocyte membrane had not completely recovered after the whole-cell recording. In other cases, opus-recorded oocytes appeared not to display the characteristic shrinking in hypertonic stripping solution. Nevertheless, in several cases, cells that were opus recorded (often after expression tests—one or two high doses of agonist—and/or voltage ramps; see Chapters 5 and 6 for methods description) were successfully stripped and single-channel recording was performed as described in Section 2.6.6.6. One example was shown in **Figure 2.5**, in both the cell-attached and outside-out configurations for an oocyte that was previously recorded on the OpusExpress. With proper attention to the above details, success rates of ~ 30–50% should be possible.

2.6.8 Data Analysis

2.6.8.1 Analysis of Whole-Cell Data

Each opus data file (trace) was opened in Clampfit (Axon Instruments, Union City, CA) and the baseline was defined. A baseline current that is non-zero can be of two different categories: (1) leak current and (2) constitutive activity. Leak current occurs when current that is not flowing through ion

channels is measured. This is correlated to the property of initial membrane potential at the start of an opus run, as was shown in **Figure 2.8,** and so appears to be related to general oocyte health. Constitutive activity was addressed in the discussion. Baseline was defined as the average current of a 10 second period before the drug was applied and was corrected for significant slope, as necessary. Peak response was measured as the largest current deflection from baseline. This process was carried out in parallel for all oocytes in a given run, then repeated for the current traces at each concentration. EC_{50} and the Hill coefficient (n_H), with standard errors for each, were determined by fitting the normalized current responses versus agonist concentration to the Hill equation (**Equation 2.1**)(*57*). In this equation, I is the measured current at a given agonist concentration, [A], I_{max} is maximal response, EC_{50} is the effective concentration that produces the half-maximal current response, and n_H is the Hill coefficient. Briefly, each oocyte's normalized current response and corresponding drug concentration were plotted on a semi-log scale. The absence of current response to control dose (no drug) was verified. When oocytes could live through long runs the control doses were done as both the first dose and last dose to ensure reversibility. Larger standard error values were frequently observed for the regions of the dose-response curve that are near EC_{50}.

$$I/I_{\max} = 1/\left(1+\left(\frac{(EC_{50})}{[A]}\right)^{n_H}\right)$$

(**Equation 2.1**)

To determine whether or not a dose-response relation has multiple components, as opposed to having a low n_H, the F-test was used to determine

whether 1 component (monophasic) or 2 components (biphasic) best fits the dose-response data, while accounting for the fact that increasing the number of components increases the degrees of freedom and so necessarily produces a better fit.

On occasion, additional analysis of opus traces was performed. For example, whole-cell activation and deactivation kinetics were sometimes determined by fitting the rising and falling currents in opus traces, as previously described(*35*).

2.6.8.2 Analysis of Single-Channel Data

A wide variety of different analyses of single-channel data was performed, as dictated by the goals of each project in this thesis. Details for each are given in the appropriate chapters. In each case, methods are presented for the combined analysis and interpretation of single-channel and whole-cell data, often including channels expressing unnatural amino acids. Most analysis was done in Clampfit 9.2 using the single-channel search function (event detection); some analysis was done in QuB. Key parameters analyzed were: single-channel conductance, NP_{open}, τ_{open}, and τ_{closed} (especially to determine τ_{crit} and allow for estimation of P_{open}). In favorable cases, and when using QuB to fit single-channel data across multiple concentrations(*38-41*), I made some progress towards determining specific rate constants, such as the channel closing rate (α) and apparent opening rate (β').

A general method for 'cleaning up' single-channel data prior to analysis has been proposed(*58*). We feel that the addition of the steps presented in the discussion section on '*Controls for Single-Channel Recording'* and **Appendix B** make our data clean up and subsequent analysis more robust and reproducible. The extent to which our analysis is robust is demonstrated in many ways, including that on two occasions when a single-channel record was analyzed separately by two members of the lab (Shawna Frazier and Jai Shanata in one case; Ximena Da Silva and Jai Shanata in the other), quantitatively indistinguishable results were achieved for P_{open} calculations.

2.7 References

1. Hutchison, C. A., 3rd, Phillips, S., Edgell, M. H., Gillam, S., Jahnke, P., and Smith, M. (1978) Mutagenesis at a specific position in a DNA sequence, *J Biol Chem 253*, 6551-6560.
2. Nowak, M. W., Gallivan, J. P., Silverman, S. K., Labarca, C. G., Dougherty, D. A., and Lester, H. A. (1998) In vivo incorporation of unnatural amino acids into ion channels in Xenopus oocyte expression system, *Methods in enzymology 293*, 504-529.
3. Papke, R. L., Millhauser, G., Lieberman, Z., and Oswald, R. E. (1988) Relationships of agonist properties to the single channel kinetics of nicotinic acetylcholine receptors, *Biophys J 53*, 1-10.
4. Blum, A. P., Lester, H. A., and Dougherty, D. A. (2010) Nicotinic pharmacophore: the pyridine N of nicotine and carbonyl of acetylcholine hydrogen bond across a subunit interface to a backbone NH, *Proc Natl Acad Sci U S A 107*, 13206-13211.
5. Chakrapani, S., Bailey, T. D., and Auerbach, A. (2004) Gating dynamics of the acetylcholine receptor extracellular domain, *The Journal of general physiology 123*, 341-356.
6. Colquhoun, D. (1998) Binding, gating, affinity and efficacy: the interpretation of structure-activity relationships for agonists and of the effects of mutating receptors, *Br J Pharmacol 125*, 924-947.
7. Gleitsman, K. R., Shanata, J. A., Frazier, S. J., Lester, H. A., and Dougherty, D. A. (2009) Long-range coupling in an allosteric receptor revealed by mutant cycle analysis, *Biophys J 96*, 3168-3178.

8. Grosman, C., Salamone, F. N., Sine, S. M., and Auerbach, A. (2000) The extracellular linker of muscle acetylcholine receptor channels is a gating control element, *The Journal of general physiology 116*, 327-340.
9. Grosman, C., Zhou, M., and Auerbach, A. (2000) Mapping the conformational wave of acetylcholine receptor channel gating, *Nature 403*, 773-776.
10. Lee, W. Y., and Sine, S. M. (2005) Principal pathway coupling agonist binding to channel gating in nicotinic receptors, *Nature 438*, 243-247.
11. Xiu, X., Hanek, A. P., Wang, J., Lester, H. A., and Dougherty, D. A. (2005) A unified view of the role of electrostatic interactions in modulating the gating of Cys loop receptors, *J Biol Chem 280*, 41655-41666.
12. Dougherty, D. A. (2008) Physical organic chemistry on the brain, *J Org Chem 73*, 3667-3673.
13. Hanek, A. P., Lester, H. A., and Dougherty, D. A. (2008) A stereochemical test of a proposed structural feature of the nicotinic acetylcholine receptor, *J Am Chem Soc 130*, 13216-13218.
14. Kearney, P. C., Zhang, H., Zhong, W., Dougherty, D. A., and Lester, H. A. (1996) Determinants of nicotinic receptor gating in natural and unnatural side chain structures at the M2 9' position, *Neuron 17*, 1221-1229.
15. Lummis, S. C., Beene, D. L., Lee, L. W., Lester, H. A., Broadhurst, R. W., and Dougherty, D. A. (2005) Cis-trans isomerization at a proline opens the pore of a neurotransmitter-gated ion channel, *Nature 438*, 248-252.
16. Xiu, X., Puskar, N. L., Shanata, J. A., Lester, H. A., and Dougherty, D. A. (2009) Nicotine binding to brain receptors requires a strong cation-pi interaction, *Nature 458*, 534-537.
17. Zhong, W., Gallivan, J. P., Zhang, Y., Li, L., Lester, H. A., and Dougherty, D. A. (1998) From ab initio quantum mechanics to molecular neurobiology: a cation-pi binding site in the nicotinic receptor, *Proc Natl Acad Sci U S A 95*, 12088-12093.
18. Colquhoun, D., and Hawkes, A. G. (1982) On the stochastic properties of bursts of single ion channel openings and of clusters of bursts, *Philosophical transactions of the Royal Society of London 300*, 1-59.
19. Filatov, G. N., and White, M. M. (1995) The role of conserved leucines in the M2 domain of the acetylcholine receptor in channel gating, *Mol Pharmacol 48*, 379-384.
20. Leonard, R. J., Labarca, C. G., Charnet, P., Davidson, N., and Lester, H. A. (1988) Evidence that the M2 membrane-spanning region lines the ion channel pore of the nicotinic receptor, *Science 242*, 1578-1581.
21. Hamill, O. P., Marty, A., Neher, E., Sakmann, B., and Sigworth, F. J. (1981) Improved patch-clamp techniques for high resolution current recording from cells and cell-free membrane patches, *Pflugers Arch. 391*, 85-100.
22. Dascal, N. (1987) The use of the *Xenopus* oocyte system for the study of ion channels, *CRC Crit. Rev. Biochem. 22*, 317-387.
23. Weiss, D. S., and Magleby, K. L. (1989) Gating scheme for single GABA-activated Cl- channels determined from stability plots, dwell-time

distributions, and adjacent-interval durations, *The Journal of neuroscience: the official journal of the Society for Neuroscience 9*, 1314-1324.

24. Hille, B. (2001) *Ion channels of excitable membranes*, 3rd ed., Sinauer, Sunderland, Mass.
25. Mathie, A., Cull-Candy, S. G., and Colquhoun, D. (1987) Single-channel and whole-cell currents evoked by acetylcholine in dissociated sympathetic neurons of the rat, *Proceedings of the Royal Society of London. Series B, Containing papers of a Biological character 232*, 239-248.
26. Labarca, C., Nowak, M. W., Zhang, H., Tang, L., Deshpande, P., and Lester, H. A. (1995) Channel gating governed symmetrically by conserved leucine residues in the M2 domain of nicotinic receptors, *Nature 376*, 514-516.
27. Charnet, P., Labarca, C., Cohen, B. N., Davidson, N., Lester, H. A., and Pilar, G. (1992) Pharmacological and kinetic properties of a4b2 neuronal nicotinic acetylcholine receptors expressed in *Xenopus* oocytes, *J Physiol 450*, 375-394.
28. Gleitsman, K. R., Kedrowski, S. M., Lester, H. A., and Dougherty, D. A. (2008) An intersubunit hydrogen bond in the nicotinic acetylcholine receptor that contributes to channel gating, *J Biol Chem 283*, 35638-35643.
29. Sigworth, F. J., and Neher, E. (1980) Single Na+ Channel Currents Observed in Cultured Rat Muscle-Cells, *Nature 287*, 447-449.
30. Molleman, A. (2003) *Patch clamping: an introductory guide to patch clamp electrophysiology*, J. Wiley, New York.
31. Auerbach, A. (1991) Single-channel dose-response studies in single, cell-attached patches, *Biophys J 60*, 660-670.
32. Haghighi, A. P., and Cooper, E. (2000) A molecular link between inward rectification and calcium permeability of neuronal nicotinic acetylcholine a3b4 and a4b2 receptors, *J Neurosci 20*, 529-541.
33. Nishino, A., Baba, S. A., and Okamura, Y. (2011) A mechanism for graded motor control encoded in the channel properties of the muscle ACh receptor, *Proc Natl Acad Sci U S A 108*, 2599-2604.
34. Colquhoun, D. (2006) Agonist-activated ion channels, *British journal of pharmacology 147 Suppl 1*, S17-26.
35. Wang, J., Lester, H. A., and Dougherty, D. A. (2007) Establishing an ion pair interaction in the homomeric rho1 gamma-aminobutyric acid type A receptor that contributes to the gating pathway, *J Biol Chem 282*, 26210-26216.
36. Sakmann, B., and Neher, E. (1995) *Single-channel recording*, 2nd ed., Plenum Press, New York.
37. Mukhtasimova, N., and Sine, S. M. (2007) An intersubunit trigger of channel gating in the muscle nicotinic receptor, *J Neurosci 27*, 4110-4119.
38. Qin, F., and Li, L. (2004) Model-based fitting of single-channel dwell-time distributions, *Biophys J 87*, 1657-1671.

39. Qin, F. (2004) Restoration of single-channel currents using the segmental k-means method based on hidden Markov modeling, *Biophys J 86*, 1488-1501.
40. Qin, F., Auerbach, A., and Sachs, F. (2000) Hidden Markov modeling for single channel kinetics with filtering and correlated noise, *Biophys J 79*, 1928-1944.
41. Qin, F., Auerbach, A., and Sachs, F. (2000) A direct optimization approach to hidden Markov modeling for single channel kinetics, *Biophys J 79*, 1915-1927.
42. Changeux, J. P., and Edelstein, S. J. (2005) Allosteric mechanisms of signal transduction, *Science 308*, 1424-1428.
43. Rayes, D., Spitzmaul, G., Sine, S. M., and Bouzat, C. (2005) Single-channel kinetic analysis of chimeric alpha7-5HT3A receptors, *Mol Pharmacol 68*, 1475-1483.
44. Kalbaugh, T. L. (2004) Ligand-binding residues integrate affinity and efficacy in the NMDA receptor, *Mol Pharmacol 66*, 209-219.
45. Lape, R., Colquhoun, D., and Sivilotti, L. G. (2008) On the nature of partial agonism in the nicotinic receptor superfamily, *Nature 454*, 722-727.
46. Lape, R., Krashia, P., Colquhoun, D., and Sivilotti, L. G. (2009) Agonist and blocking actions of choline and tetramethylammonium on human muscle acetylcholine receptors, *J Physiol 587*, 5045-5072.
47. Sivilotti, L. G. (2010) What single-channel analysis tells us of the activation mechanism of ligand-gated channels: the case of the glycine receptor, *J Physiol 588*, 45-58.
48. McManus, O. B., Blatz, A. L., and Magleby, K. L. (1987) Sampling, log binning, fitting, and plotting durations of open and shut intervals from single channels and the effects of noise, *Pflugers Arch 410*, 530-553.
49. Fredkin, D. R., and Rice, J. A. (1991) On the Superposition of Currents from Ion Channels, *Philos T Roy Soc B 334*, 347-356.
50. Reifarth, F. W., Clauss, W., and Weber, W. M. (1999) Stretch-independent activation of the mechanosensitive cation channel in oocytes of Xenopus laevis, *Biochim Biophys Acta 1417*, 63-76.
51. Silberberg, S. D., and Magleby, K. L. (1997) Voltage-induced slow activation and deactivation of mechanosensitive channels in Xenopus oocytes, *The Journal of physiology 505 (Pt 3)*, 551-569.
52. Charnet, P., Labarca, C., and Lester, H. A. (1992) Structure of the gamma-less nicotinic acetylcholine receptor: learning from omission, *Mol Pharmacol 41*, 708-717.
53. Jackson, M. B., Imoto, K., Mishina, M., Konno, T., Numa, S., and Sakmann, B. (1990) Spontaneous and agonist-induced openings of an acetylcholine receptor channel composed of bovine muscle alpha-, beta- and delta-subunits, *Pflugers Archiv: European journal of physiology 417*, 129-135.
54. Jackson, M. B. (1984) Spontaneous openings of the acetylcholine receptor channel, *Proc Natl Acad Sci U S A 81*, 3901-3904.

55. Sachs, F., and Qin, F. (1993) Gated, Ion-Selective Channels Observed with Patch Pipettes in the Absence of Membranes - Novel Properties of a Gigaseal, *Biophysical Journal 65*, 1101-1107.
56. Mortensen, M., and Smart, T. G. (2007) Single-channel recording of ligand-gated ion channels, *Nat Protoc 2*, 2826-2841.
57. Weiss, J. N. (1997) The Hill equation revisited: uses and misuses, *Faseb J 11*, 835-841.
58. Elenes, S., and Auerbach, A. (2002) Desensitization of diliganded mouse muscle nicotinic acetylcholine receptor channels, *J Physiol 541*, 367-383.

Chapter 3

Long-Range Coupling in an Allosteric Receptor Revealed by Mutant Cycle Analysis

Sections 3.1 through 3.8 of this chapter are reprinted from *Biophysical Journal*, 96. Kristin Rule Gleitsman, Jai A.P. Shanata, Shawnalea J. Frazier, Henry A. Lester, and Dennis A. Dougherty. *Long-Range Coupling in an Allosteric Receptor Revealed by Mutant Cycle Analysis,* 3168–178.

3.1 Abstract

The functional coupling of residues that are far apart in space is the quintessential property of allosteric proteins. For example, in Cys-loop receptors the gating of an intrinsic ion channel is allosterically regulated by the binding of small molecule neurotransmitters 50–60 Å from the channel gate. Some residues near the binding site must have as their primary function the communication of the binding event to the gating region. These gating pathway residues are essential to function, but their identification and characterization can be challenging. The present work introduces a simple strategy, derived from mutant cycle analysis, for identifying gating pathway residues using macroscopic measurements alone. In the exemplar Cys-loop receptor, the nicotinic acetylcholine receptor, a well-characterized reporter mutation (βL9'S) known to impact gating was combined with mutations of target residues in the ligand-binding domain hypothesized or previously found to be functionally significant. A mutant cycle analysis of the macroscopic EC_{50} measurements can then provide insights into the role of the target residue. This new method—elucidating long-range functional coupling in allosteric receptors (ELFCAR)—can be applied to a number of reporter mutations in a wide variety of receptors to identify both previously characterized and novel mutations that impact the gating pathway. We support our interpretation of macroscopic data with single-channel studies. ELFCAR should be broadly applicable to determining functional roles of residues in allosteric receptors.

3.2 Introduction

Cys-loop receptors mediate fast synaptic transmission throughout the central and peripheral nervous systems.[2-5] These pentameric, ligand-gated ion channels are prototypical allosteric receptors,[6] in that the activation (gating) of an intrinsic ion channel is allosterically regulated by the binding of small molecule neurotransmitters (acetylcholine (ACh), serotonin, GABA, or glycine). While valuable structural insights for Cys-loop receptors have appeared in recent years,[1, 7] detailed conformational mechanisms linking neurotransmitter binding to channel gating remain elusive.

Structurally, Cys-loop receptors have two principal functional domains (**Figure 3.1**). The extracellular domain, rich in β-sheet structure, contains the agonist binding sites. Each subunit also contains a transmembrane domain comprised of four membrane-spanning helices, one of which (M2) lines the ion channel. While the precise location of the channel gate has been debated, the consensus positions it at or below the middle of the M2 helix. This puts the channel gate some 50–60 Å away from the agonist binding sites. Neurotransmitter binding events must therefore be communicated over this distance to the channel gate.

In terms of function, such a clear demarcation of domains is less evident. For a given residue, if a mutation at the site leads to a change in receptor function, this could be because the binding of agonist or the gating of the channel (or both) has changed. It seems safe to say that residues in the middle of the

transmembrane domain do not contribute directly to agonist binding, and so residues in the transmembrane domain that contribute to function are typically described as ‘gating’ residues. In contrast, one expects to find residues in the extracellular domain with varying functional roles. Some residues will primarily facilitate agonist binding, either by directly contacting the agonist or by refining the shape or electronic properties of the agonist binding site. However, to achieve the long-range communication that is fundamental to Cys-loop receptor function, other extracellular domain residues must be involved in communicating the binding event to the channel gate, serving an instrumental role in the gating pathway. These gating pathway residues are in some ways the most interesting, but their identification and characterization can be challenging.

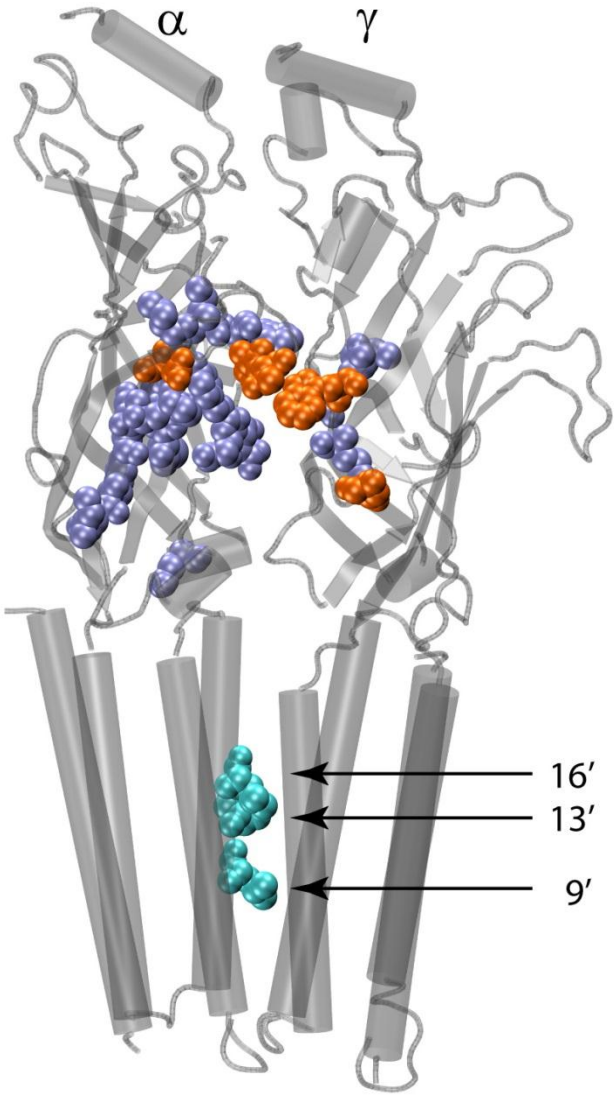

Figure 3.1. Residues considered here. Shown are two adjacent subunits of the cryo-EM structure of the *Torpedo* nAChR (pdb 2BG9).[1] The reporter residues in the transmembrane domain are shown as cyan and are labeled. Residues in the extracellular domain are in two classes: those with no long-range coupling (purple) and the five residues that show significant long-range coupling (orange). One non-coupling residue (γE168) is not defined in the EM structure and so is not shown.

One strategy for determining whether a given residue primarily contributes to agonist binding or channel gating involves single-channel recording on appropriate mutants, followed by kinetic analysis. However, in some Cys-loop

receptors (such as 5-HT_3)[8], single-channel conductances are too small for reliable kinetic analyses;[9, 10] in many other Cys-loop receptors, single-channel kinetics are complex or nonstationary, again vitiating single-channel kinetic analysis.[11, 12] Also, in other ion channels[13] and in allosteric receptors in general, single-channel studies are often not possible.

A more broadly applicable approach, allowing one to efficiently evaluate a number of mutants in search of unusual behavior, is to measure macroscopic currents across multiple concentrations. This produces the EC_{50} value, the concentration that induces half-maximal current in response to applied agonist, along with comparative measurements of maximal agonist-induced currents. In the case of ligand-gated ion channels, EC_{50} is a composite value, being responsive to both changes in agonist binding and channel gating behaviors. As such, it can be challenging to interpret shifts in EC_{50}. Here we describe an approach to use the readily obtained EC_{50} values to identify residues that substantially impacting receptor gating. We refer to the method as ELFCAR (elucidating long-range functional coupling of allosteric receptors). The basic tool involves mutant cycle analysis of EC_{50} values for distant pairs of mutation sites. Complementary observations concerning mutational effects on receptor efficacy and the effects of partial agonists support the basic methodology. Thus, ELFCAR provides an efficient strategy for identification of key gating pathway residues that may otherwise evade detection, without performing single-channel studies.

Key to the approach is the definitive feature of allosteric proteins–action at a distance. When a mutation in the transmembrane domain that is unambiguously associated with channel gating is paired with various mutations in the extracellular domain, the observation of non-multiplicative EC_{50} shifts for the two mutations signals a functional coupling between the two residues, and thus identifies the extracellular domain mutation as influencing gating. We show that this behavior derives from the typical allosteric kinetic scheme for Cys-loop receptors, suggesting the approach could provide a general probe of allosteric receptors.

3.3 Results

The prototypical and most-studied Cys-loop receptor, the muscle nicotinic acetylcholine receptor (nAChR), was used in this study. It is important to appreciate that the method is directly applicable to other Cys-loop receptors, and, in favorable cases, to other allosteric proteins as well. Here we have employed the muscle-type nAChR as a well-established system that allows us to evaluate the methodology.

The muscle nAChR is a heteropentamer with subunit composition ($\alpha_2\beta\gamma\delta$). Two non-equivalent binding sites are located in the extracellular domain at the αδ and αγ subunit interfaces. Nearly all Cys-loop receptors, including all nAChRs, contain a conserved leucine residue in the hydrophobic, pore-lining M2 helix of

each subunit (**Figure 3.1**). Mutating this residue, termed L9', to serine lowers the EC_{50}.[14, 15] Structural studies place L9' near the middle of the M2 helix, in the region of the occlusion of the closed channel, and while it can be debated whether L9' constitutes a literal gate of the channel, there can be no doubt that it is a crucial gating residue. In the present work, the L9'S mutation in the β subunit was used as a *reporter* to evaluate mutations of residues in the extracellular domain that may function as binding residues or as gating pathway residues.

3.3.1 βL9'S as a Reporter of Functional Role for Extracellular Residues

Agonist occupancy at both binding sites is required for efficient opening of the channel pore. **Scheme 3.1** shows a simplified kinetic model for activating the nAChR, leading to an expression for EC_{50} (**Equation 3.1**; see **Appendix A** for derivation),[16] where A is the agonist; R^C and R^O denote the closed and open states of the receptor; k_1 and k_{-1} are forward and reverse rate constants for agonist binding; K_D is the dissociation constant for the agonist; and Θ is the gating equilibrium constant, given by the ratio of the channel opening rate, β, to the channel closing rate, α. It is well understood that the actual kinetic model for the nAChR is likely more complicated, and that different Cys-loop receptors may show kinetic schemes that differ in detail. In addition, a strong gating mutation could enable spontaneous openings of the channel when no agonist is bound.

This could compromise the kinetic model discussed here. However, the βL9'S mutation alone does not lead to extensive spontaneous openings, and the types of mutations emphasized here, if they impact gating at all, discourage channel opening (decrease Θ), suggesting that spontaneous openings will not produce a major perturbation to the system. **Scheme 3.1** is typical for an allosteric receptor, capturing the essence of the situation: function depends on binding of an allosteric effector as well as signal transduction (gating). For ligand-gated ion channels, this means that EC_{50} depends on both K_D and Θ, where Θ is a measure of receptor efficacy. The graphical representation of the relationship between EC_{50} and Θ, based on **Equation 3.1**, is shown in **Figure 3.2**. Simulations of more complex kinetic schemes produce qualitatively similar plots. For full agonists (FAs), that is, those that produce a large Θ, the plot is linear with a negative slope. We will refer to this as the 'high slope' region of the plot. For smaller values of Θ, such as would be associated with partial agonism, the plot approaches an asymptote. We will refer to this as the 'plateau' region.[17]

$$A + R^{c} \underset{k_{-1}}{\overset{2k_1}{\rightleftharpoons}} A + AR^{c} \underset{2k_{-1}}{\overset{k_1}{\rightleftharpoons}} A_2R^{c} \underset{\alpha}{\overset{\beta}{\rightleftharpoons}} A_2R^{o} \quad , \qquad \textbf{Scheme 3.1}$$

where, $K_D = k_{-1}/k_1$ and $\Theta = \beta/\alpha$

$$EC_{50} = \frac{K_D}{(\Theta + 2)^{1/2} - 1} \qquad (\textbf{Equation 3.1})$$

A defining feature of allosteric proteins is that an allosteric effector shifts the equilibrium between two states, historically termed tensed and relaxed. However, binding of the allosteric effector itself does not define the exact state as tensed or relaxed, rather it produces a shift in the equilibrium *distribution* between these states. Consequently, once the allosteric signal is saturated, this equilibrium distribution depends only on the equilibrium constant governing tensed-relaxed interconversion. In the case of ligand-gated ion channels, such as the nAChR studied here, different allosteric effectors—i.e., different ligands for ligand-gated ion channels—produce different closed-open equilibria, characterized by Θ. Thus, while FAs ($\Theta >> 1$) cause the channel to be mostly open when agonist is bound, partial agonists influence this allosteric transition to a lesser extent, resulting in a smaller perturbation of the gating equilibrium. It is the varying extent to which ligand binding can bias the equilibrium that produces the general shape of the relationship between EC_{50} (function) and Θ, seen in **Figure 3.2**.

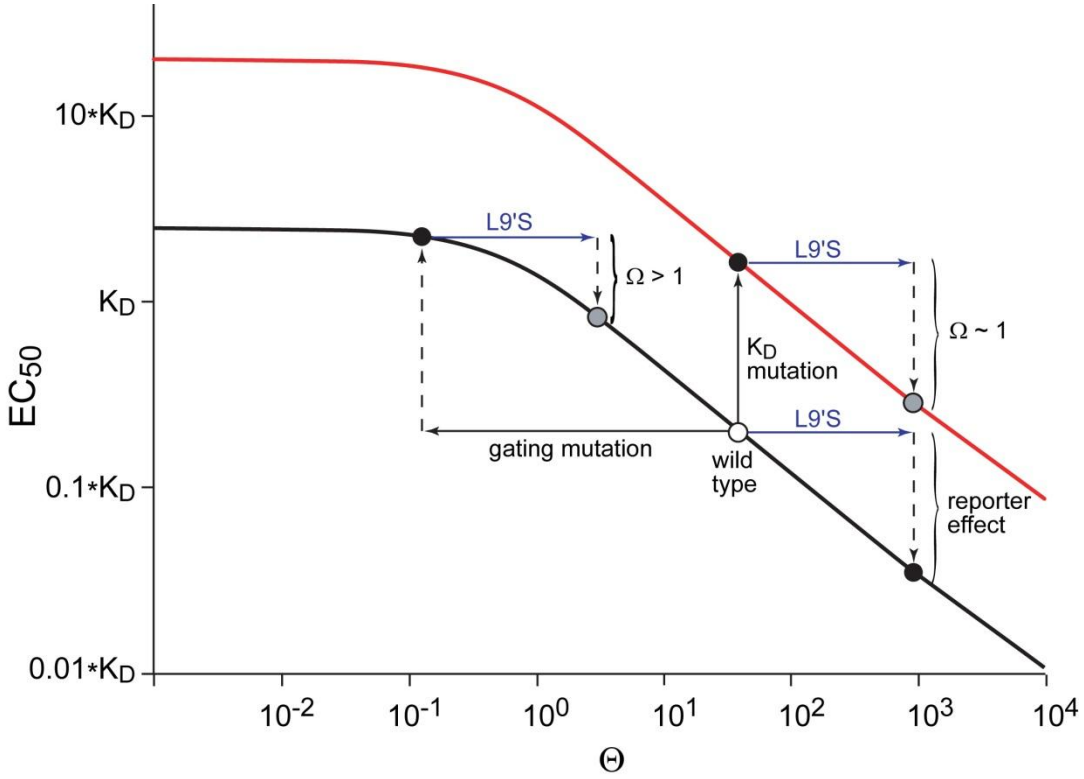

Figure 3.2. Black line: the relationship between EC_{50} and Θ as given in Equation 3.1. Red line: the same equation, but with a larger K_D. For both plots, in the negative slope region changes in Θ produce significant changes in EC_{50}, as shown when the reported effect is added to the wild type receptor. However, when beginning with Θ in the low slope region, a much smaller shift in EC_{50} occurs for equivalent shifts in Θ.

Previous studies[15, 18-20] have shown that polar mutations at L9' substantially increase Θ, causing a corresponding drop in EC_{50}. Our goal was to determine whether it was possible to use a *reporter* mutation such as βL9'S to evaluate whether the shift in EC_{50} from mutation at a *target* residue is primarily a result of changes in binding (K_D) or gating (Θ) (see the Supporting Material, **Figure 3.8**). Consider such a target mutation in the extracellular domain that only increases K_D, i.e., a pure binding mutation. This has the effect of raising the EC_{50} versus Θ curve, but maintaining its shape (**Figure 3.2, red line**). Addition

of the βL9'S mutation then causes a comparable increase in Θ, lowering EC_{50} by the same factor as in the wild type. The pairing of an extracellular domain binding mutation with the reporter transmembrane domain mutation results in a multiplicative shift in EC_{50}; the two mutations are independent.

Now, consider the consequences of an extracellular domain target mutation that affects gating, and not binding. Deleterious mutations (increase in EC_{50}) will cause a drop in Θ, and if the effect is large enough, the agonist employed will now be a partial agonist. The EC_{50} versus Θ relationship for this mutant will now lie in the plateau region of **Figure 3.2**. As a result, the subsequent increase in Θ caused by adding the βL9'S mutation will induce a much smaller drop in EC_{50}. The pairing of these mutations will no longer give a multiplicative shift in EC_{50}, and therefore the two mutations are functionally coupled. Thus, the βL9'S gating mutation acts as a reporter to identify a target mutation that is substantially loss-of-function (decreasing Θ). It is clear from **Figure 3.2** that a gain-of-function gating mutation (lower EC_{50}; increasing Θ) will still be in the high slope region and so will be additive with the βL9'S mutation. This method cannot detect gain-of-function gating mutations.

For many mutations in the extracellular domain, the βL9'S mutation is indeed multiplicative, producing a consistent 40-fold shift to lower EC_{50} (**Table 3.1**).[15, 21, 22] We now report the first examples of mutations closely associated with the agonist binding site for which the effect of βL9'S is substantially less than 40-fold, indicating non-multiplicative behavior (**Figure 3.1**). Four of these are

conventional mutants: αY190F, γD174NδD180N, γW55YδW57Y, and αD200N. Others have probed these sites, and they are generally considered to primarily influence gating.[23-29] As such, these studies validate the ELFCAR method. The fifth, a novel mutant, replaces αS191 with its α-hydroxy analogue, which we abbreviate Sah (for serine α-hydroxy), converting the backbone amide that links αY190 and αS191 to a backbone ester.[30, 31]

3.3.2 Mutant Cycle Analysis Suggests Long-Range Coupling

The typical way to analyze a system in which two mutations are evaluated, both individually and in tandem, is by mutant cycle analysis (**Figure** 3.3). Briefly, if a mutation at one site has no structural or energetic impact at a second site, then the effect of simultaneous mutations at both sites will simply be multiplicative (**Figure 3.3**). In the parlance of mutant cycle analysis, the coupling parameter, Ω, will be unity. In contrast, if two residues interact, the simultaneous mutation at both sites will lead to an effect that is either greater or less than the product of their individual effects, producing an Ω value that significantly deviates from unity. This approach has been broadly applied to a wide range of systems, including Cys-loop receptors, where several investigators have used mutant cycle analysis of EC_{50} values to determine functional coupling between neighboring residues of the extracellular domain.[32-34]

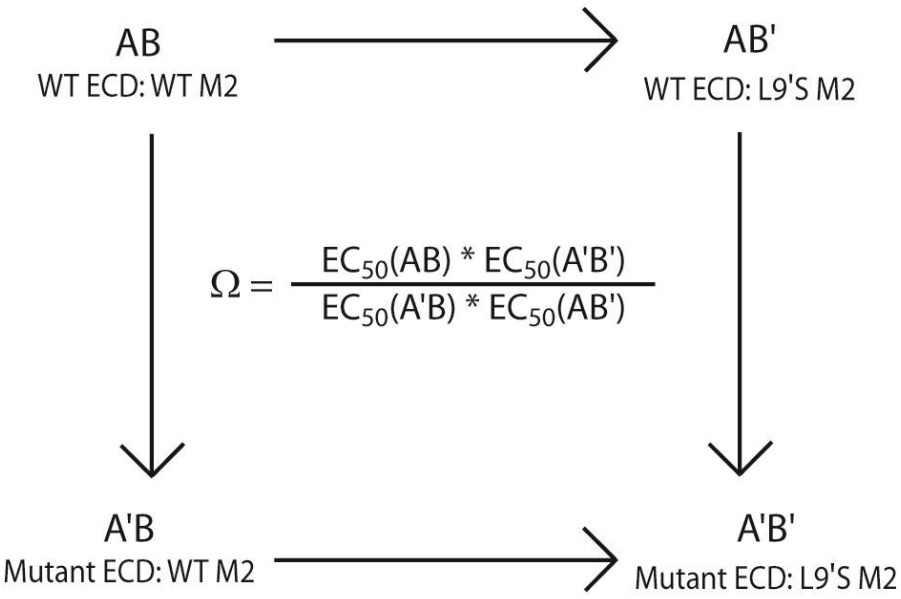

Figure 3.3. Scheme for double mutant cycle analysis where A and B represent amino acid positions and A' and B' represent mutations at these sites. The coupling parameter, Ω, is calculated from the given equation.

As could be anticipated from the EC_{50} values in **Table 3.1**, the vast majority of mutations made in the extracellular domain of the nAChR produce an Ω for coupling to βL9'S of ~ 1, indicating the functional independence of these residues. However, the five mutations noted above—αY190F, γD174NδD180N, γW55YδW57Y, αD200N, and αS191Sah—produced larger Ω values. We consider a value of Ω > 2 to signify a meaningful coupling (**Figure 3.4**). Phenomenologically, this establishes a long-range coupling between these extracellular domain sites and the βL9' site, as one would expect for an allosteric receptor. Typically, an Ω that deviates significantly from a value of 1 is interpreted to indicate a direct interaction between the residues, such as a hydrogen bond or a salt bridge.

Target Mutation	WT EC_{50}	EC_{50} with Reporter Mutation	Ratio	Ω
		βL9'S		
wild type	46	1.2	38	1.00
γD174NδD180N	590	160	3.7	11
αY190F	1200	520	2.3	17
γW55YδW57Y	180	24	7.5	5.1
αD200N	130	29	4.5	8.6
αS191Sah	300	50	6.0	6.4
αE45W	120	3	40	0.96
αY93Yah	39	1	39	0.98
αN94Nah	87	2.2	40	0.97
αD97E	3.3	0.09	37	1.0
αM144L	15	0.37	41	0.95
αM144Lah	50.4	1.3	39	0.99
αK145Q	170	8.1	21	1.8
αL146Lah	26	0.5*	52	0.74
αT148Tah	33	1.3	25	1.5
αW149Wah	36	0.72	50	0.77
αW149 5-F-Trp	200	4.7	43	0.90
αW149 5-Br-	88	2	44	0.87
αL199Lah	11	0.18	61	0.63
αT202Tah	24	0.48	50	0.77
αY203Yah	39	0.62	63	0.61
αF205Yah	67	1.4	48	0.80
αF205Y	90	1.5	60	0.64
αV206Vah	170	3.1	55	0.70
γL36δL39Lah	28	0.63	44	0.86
γI56δI58Iah	33	0.83	40	0.96
γA121δA124Aah	25	0.66	38	1.0
γE168QδE175Q	42	1.2	35	1.1
		γL9'S		
wild type	46	4.5	10	1.0
γD174NδD180N	590	244	2	4.2
αY190F	1200	650	2	5.5
γW55YδW57Y	180	74	2	4.2
		δL9'S		
wild type	46	1	46	1.0
γD174NδD180N	590	140	4	11
αY190F	1200	370	3	14
γW55YδW57Y	180	16	11	4.1
		αL9'S		
wild type	46	0.35	131	1.0
γD174NδD180N	590	65	9	14
αY190F	1200	223	5	24
γW55YδW57Y	180	7.5	24	5.5
		αV13'S		
wild type	46	0.1	460	1.0
γD174NδD180N	590	8.9	66	7
αY190F	1200	32	38	12
γW55YδW57Y	180	1.5	120	3.8
		αL16'S		
wild type	46	0.47	98	1.0
γD174NδD180N	590	59	10	10
αY190F	1200	190	6	15
γW55YδW57Y	180	8.5	21	4.6

Table 3.1. (Previous page). EC_{50} values with and without βL9'S reporter mutation for coupled and non-coupled residues. Values for the 3 coupled residues are also given for reporter mutations in all other subunits (γ, δ, and α) and positions (9', 13', and 16'). The ratio of EC_{50}s: target/(target with reporter) and resultant calculated Ω values are also reported. The standard error for all EC_{50} values was < 10%, except for *, which had standard error of 20%. Data at sites α148(51), α149(22), and αS191(45) have been reported previously.

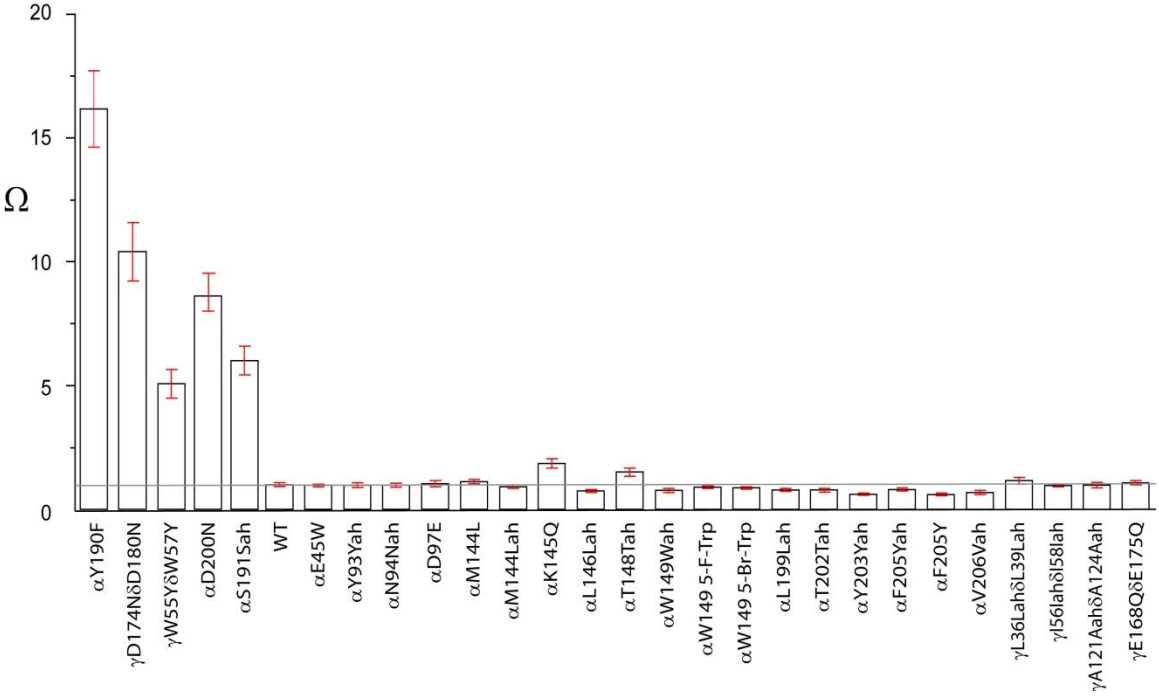

Figure 3.4. Values of Ω (coupling to βL9'S) for mutations considered here. The standard 40-fold shift expected for a βL9'S mutation produces an Ω value of one (horizontal gray line). 5-F-Trp is 5-fluorotryptophan and 5-Br-Trp is 5-bromotryptophan. For α-hydroxy acids (Yah, Nah, Lah, Tah, Wah, Vah, Iah, and Aah), a 3-letter abbreviation is used: the 1-letter code for the parent amino acid is followed by ah; thus Yah is the α-hydroxy acid of tyrosine.

In the present case, though, such a direct interaction is clearly impossible. We feel the interpretation of **Figure 3.2** is much more palatable. Significant coupling is seen because both the βL9'S mutation and the particular extracellular domain mutation disrupt the gating pathway.

3.3.3 Single-Channel Recording Supports Whole-Cell Mutant Cycle Analysis Conclusions

The most convincing way to evaluate the impact of a particularly interesting mutation is by single-channel analysis. To test our interpretation of the mutant cycle analyses using EC_{50} values, we chose three extracellular domain mutants which ELFCAR identified as gating pathway residues (αY190F, γD174NδD180N, and γW55YδW57Y) for single-channel studies. From these recordings, the open probability in the patch, NP_{open} was obtained. N is the number of channels in the patch, which often cannot be precisely determined. P_{open} is derived from **Scheme 3.1** and depends only on Θ at equivalent points on the dose-response relation. The NP_{open} measurements reported were obtained using the macroscopic EC_{50} concentration of ACh, and thus represent $0.5(NP_{open,max})$. Each of the three target mutations produces a very large decrease in NP_{open} (**Figure 3.5; Table 3.2**) compared to the wild type value of ~0.5 (data not shown); they are substantially deleterious gating pathway mutations. Also consistent with the model, adding the βL9'S mutation substantially increases NP_{open}. The single-channel analysis thus supports the interpretation of the macroscopic EC_{50} data.

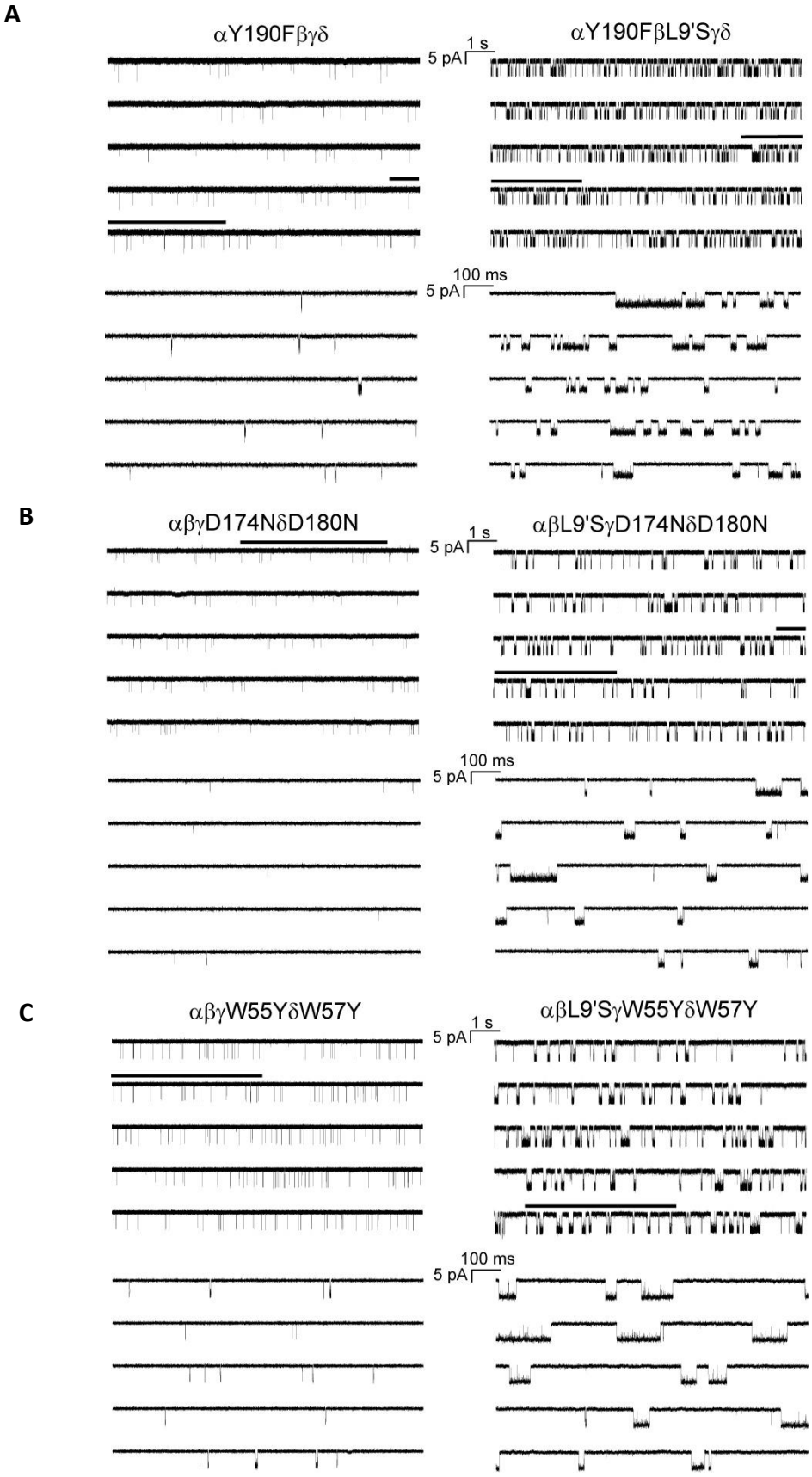
A
αY190Fβγδ
αY190FβL9'Sγδ
1 s
5 pA
100 ms
5 pA
B
αβγD174NδD180N
αβL9'SγD174NδD180N
1 s
5 pA
100 ms
5 pA
C
αβγW55YδW57Y
αβL9'SγW55YδW57Y
1 s
5 pA
100 ms
5 pA

Figure 3.5. (Previous page). Single-channel currents for select mutants. In each case, ACh is applied at the macroscopic EC_{50} value (Table 3.1), and the left panel has no reporter mutation while the right panel is for receptors with the βL9'S reporter mutation. For each of the 6 receptors, the lower trace (5s) depicts an expansion of the section of the upper trace indicated with a line. Records were obtained in the cell-attached configuration with a pipette potential of + 100 mV and are shown at 5 kHz bandwidth. Channel openings are shown as downward deflections. (A) αY190F. (B) γD174NδD180N. (C) γW55YδW57Y.

Mutant	Ω	I_{max} ratio	NP_{open}	NP_{open} βL9'S
αY190F	17	11	0.0026 ± 0.0006	0.18 ± 0.04
γD174NδD180N	11	13	0.0007 ± 0.0005	0.08 ± 0.06
γW55YδW57Y	5	12	0.018 ± 0.005	0.26 ± 0.06

Table 3.2. Coupling parameter, Ω, and I_{max} ratio from whole-cell data. NP_{open} values (± SEM) at respective macroscopic EC_{50} values (Table 3.1) from single-channel data

3.3.4 Other Reporter Mutations Support Gating Pathway Assignments

An implication of this experimental strategy is that other residues in the transmembrane domain that substantially increase Θ could act as reporters for extracellular domain residues; we are not limited to the β subunit or the well-characterized L9' position. To test this notion, L9'S mutations were made in the α, γ, and δ subunits, and two other Ser mutations were made in the M2 helix of the α subunit at positions V13' and L16' (**Figure 3.1**). All of these mutations lower EC_{50} significantly, and all positions are confidently ascribed to be gating residues. As shown in **Figure 3.6**, the extracellular domain mutations that give significant Ω values with βL9'S also show significant Ω values with L9'S mutations present in the other subunits. Recalling that there are two α subunits,

we find that there is a general coupling parameter sequence of $\beta \approx \delta > \alpha > \gamma$. Thus, subtle asymmetries between subunits exist regarding the L9' residues' contribution to gating, which are also reflected in the EC_{50} values of the various L9'S mutants (**Table 3.1**). If one considers positions other than 9', all the mutated gating pathway residues again produce meaningful Ω values, and the magnitude of their effect is consistently α9' > α16' > α13' (**Figure 3.6**).

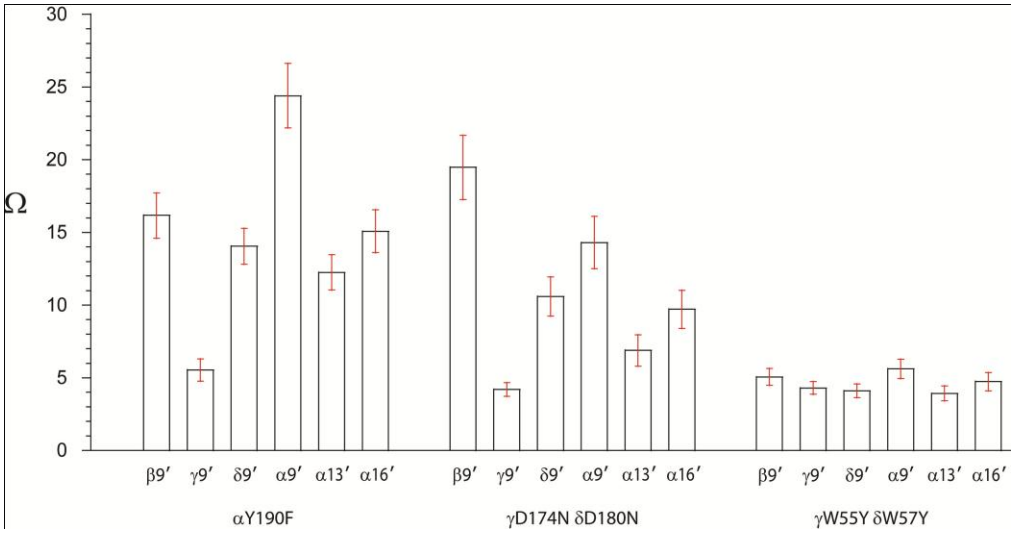

Figure 3.6. Values of Ω for various reporter mutations. For each of the three extracellular domain mutations, results for six different reporter mutations are shown. Reporter mutations are identified by their location; in each case, the mutation is of a hydrophobic residue to serine.

3.3.5 The Reporter Mutation βL9'S Systematically Increases I_{max} for Gating Pathway Residues

This interpretation of the mutant cycle analysis data predicts other behaviors for extracellular gating pathway residues. For example, to produce a significant mutant cycle analysis coupling to L9' (Ω > 2), the mutation in the

extracellular domain must convert ACh to a partial agonist, such that the target mutation is now in the plateau region of **Figure 3.2**. Due to this decrease in Θ, the maximal current observed in response to saturating concentrations of ACh (I_{max}) should diminish. In general, interpreting differences in I_{max} can be challenging due to variations in whole-cell current among oocytes, which can stem from a variety of sources that may or may not relate to the actual mutation in question. However, use of a reporter mutation can assist in the interpretation of I_{max} differences. For mutations that render ACh a partial agonist, increasing efficacy through a reporter mutation produces a significant systematic increase in I_{max}. We find that these increases are larger and more consistent than the typical variability in I_{max} in conventional mutagenesis studies. Thus, if a receptor with a target mutation shows a large increase in mean I_{max} on introduction of a reporter mutation, the mutation likely affects gating. This is shown in **Figure 3.7** for mutations with large Ω values, along with several examples with Ω near one. Recovery of I_{max} by introduction of the reporter mutation confirms the gating pathway residue assignments made by mutant cycle analysis. Moreover, the single-channel observations support this interpretation, in that the increase in NP_{open} is the microscopic correlate of the macroscopic observation of recovery of I_{max} (**Table 3.2**).

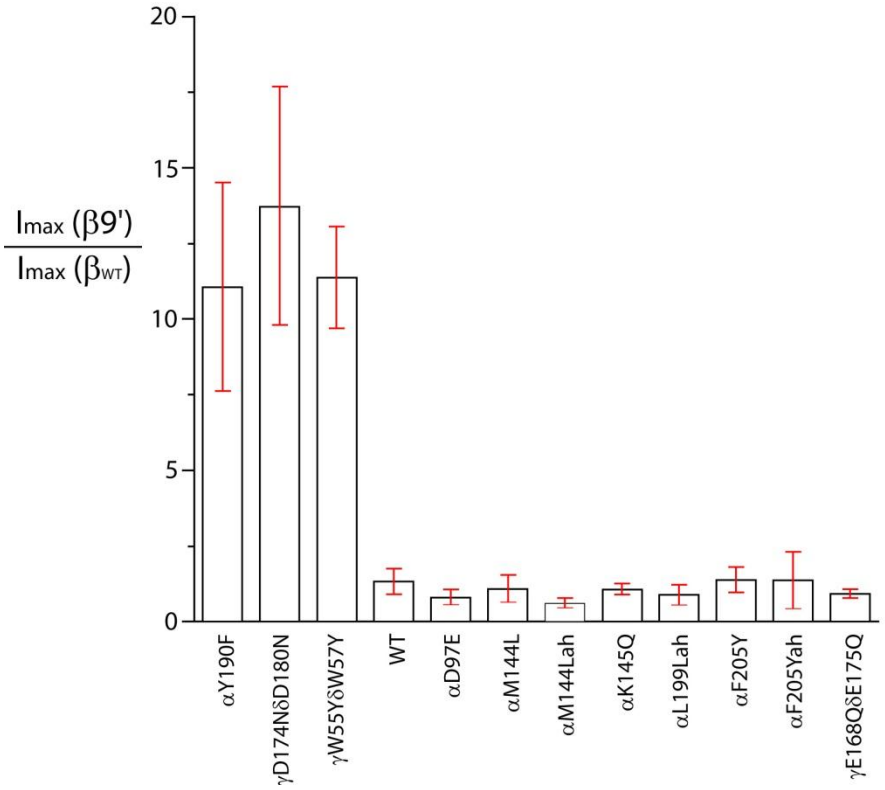

Figure 3.7. Variation in I_{max} in response to introduction of a βL9'S reporter mutation

3.3.6 Experiments with the Partial Agonist Succinylcholine Support Gating Pathway Assignments

Given the argument that a substantially deleterious mutation of a gating pathway residue converts the full agonist ACh to a partial agonist, which manifests as a diminished I_{max}, it is interesting to consider the behavior of an inherent partial agonist, such as succinylcholine (SuCh).[35] The relative efficacy, ε, of a partial agonist can be defined as the ratio of the maximal current elicited by a partial agonist (PA) to the maximal current elicited by a full agonist (FA; **Equation 3.2**). At saturating doses of agonist, all the receptors are presumed to

be in a diliganded state (A_2R), meaning that differences in I_{max} for the two agonists are due to differences in the probability that a single channel is open when the binding equilibrium is saturated, $P_{open,max}$. For wild type muscle nAChR, SuCh is a partial agonist with ~ 4% efficacy relative to ACh.

$$\varepsilon = \frac{I_{max,PA}}{I_{max,FA}} = \frac{P_{open,max,PA}}{P_{open,max,FA}}, \qquad P_{open,max} = \frac{\beta}{\alpha+\beta} = \frac{\Theta}{\Theta+1} \quad \textbf{(Equation 4.2)}$$

In the presence of an αL9'S mutation alone, SuCh becomes a full agonist. Three of the five gating pathway residues were characterized using the partial agonist SuCh. Unlike what is observed for binding mutations, when αY190F, γD174NδD180N, and γW55YδW57Y contained a L→S mutation at either the 9' (α or β), 13' (α), or 16' (α) site, the recovery of SuCh toward full agonism is blocked. As before, the magnitude of the effect follows the trend α9' > α16' > α13' (data not shown). This is interpreted as further evidence that mutation of these extracellular domain residues drastically impairs normal gating function. Note that the efficacies of SuCh for the gating pathway mutants without the L9'S reporter mutation are not dramatically different from that of wild type (0.04 ± 0.02 for wild type, 0.04 ± 0.01 for αY190F, 0.02 ± 0.01 for γD174NδD180N, and 0.01 ± 0.0009 for γW55YδW57Y).

3.4 Discussion

In this work we propose that appropriately designed double mutant studies can provide valuable insights into the mechanism of action of an allosteric receptor. We begin with a mutation at a site whose function is unambiguous. Here, this reporter residue can be one of several sites in the transmembrane region of a ligand-gated ion channel, far removed from the agonist binding site. It is assumed that mutations at this site primarily, if not exclusively, perturb the gating of the receptor, and this view is supported by detailed studies of the reporter mutations. A second site, the target site, can then be probed by combining mutations there with a reporter mutation. Here we consider a number of target sites that are far removed from the reporter residue. Analysis of the results can proceed along several lines. The classical tool is a mutant cycle analysis. Indeed we find that, while most pairings of remote residues produce independent behavior ($\Omega \sim 1$), for select target residues a mutant cycle analysis produces strong coupling parameters. Typically, such coupling is interpreted to indicate a direct interaction between the residues. However, in all cases here the residues are much too far apart to accommodate a direct structural interaction. As such, we have an allosteric coupling between remote residues, which manifests in a mutant cycle analysis just as if the two were structurally coupled. Of course, such action at a distance is the definitive feature of an allosteric system, but there are few cases where such pairwise interactions have been seen. Since the reporter mutation influences gating, coupling requires that the target residue also impact gating, allowing an apparent long-range interaction to

be revealed in the mutant cycle analysis. We have labeled such residues as being on the 'gating pathway', with the understanding that any mutation that preferentially stabilizes one state of the receptor could produce a positive result in ELFCAR, regardless of its location in the receptor. The particular residues studied here, however, do lie in regions of the receptor that have been considered to be part of the primary structural transduction from binding site to channel gate.

A less phenomenological analysis can be made with reference to **Figure 3.2**. The key here is that if the mutation at the target site perturbs gating by decreasing Θ, moving the system to the left along the EC_{50} versus Θ curve, and if the effect is large enough, the system will now be in the plateau region. Then, when the reporter mutation is added, its effect on EC_{50} will be diminished relative to what is seen in the receptor that is wild type at the target site. To be informative, the mutation at the target site must be loss-of-function (diminished Θ) and must have a substantial effect on gating. If Θ is diminished only slightly by the target mutation, or if Θ is increased (gain-of-function) the system will remain in the region of high slope, and the reporter mutation will have its normal effect. Also, when we do see significant coupling, that does not rule out the possibility that K_D has changed in addition to Θ; ELFCAR can only establish that a significant decrease in Θ has occurred. At the same time, when a target mutation produces a large shift in EC_{50} but a conventional 40-fold additional shift on adding the βL9'S reporter mutation, it is tempting to conclude that the target

mutation exclusively impacted K_D. However, changes in Θ that are significant but not large enough to move the system into the plateau region of **Figure 3.2** could be involved in addition to or instead of a K_D change. For example, the K145Q mutation has been reported to impact gating,[26] but without moving Θ into the plateau region. In the present work, K145Q shows a marginal functional coupling with L9'S, with an Ω value near the cut off for significance (1.8 ± 0.2). As such, ELFCAR is best suited to identifying mutations that strongly perturb gating ($\Omega > 2$); negative results should be interpreted cautiously. Note that in receptors for which the wild type Θ is smaller than in the muscle-type nAChR, ELFCAR would be expected to be more sensitive to small changes in Θ.

Several additional observations support our analysis of the results seen here. First, in a typical mutant cycle analysis, Ω values less than 1 can be observed and are functionally significant. However, in the present context, the model of **Figure 3.2** allows only for $\Omega > 1$, which is consistent with our data. Importantly, three mutations shown here to impact gating by the ELFCAR approach have been confirmed to be gating mutations by single-channel analyses. The single-channel values we report are NP_{open}. The true probability that a single channel is open at these concentrations, P_{open}, is increased by a factor of N, where N is the number of channels in the patch. Because the measured probability that the channel is open is very low ($\leq$ 2%) for the gating pathway mutations without the reporter mutation, the number of channels in the patch cannot be exactly determined. However, if there are actually multiple

channels in these patches, our NP_{open} values would be overestimates of P_{open}. The measured NP_{open} values are substantially diminished upon addition of each of the three target residues we tested (αY190F, γD174NδD180N, and γW55YδW57Y), such that the modest perturbation of EC_{50} associated with the target mutations can be primarily ascribed to dramatic changes in the gating pathway. Other single-channel studies of residues considered here are also consistent with our findings.

Other observations support our general model. If a target mutation substantially reduces Θ, then ACh should become a PA at the receptor. This should lead to reduced maximal currents from whole-cell recordings, and just such an effect is seen. Also, an inherent PA should be sensitive to the consequences of the target mutation, and we find that is indeed the case for SuCh.

It is interesting to consider the residues that have been probed here; **Figure 3.1** highlights them all. The considerable distance between the reporter residues and the target residues is clear from this image. Concerning the target residues, those with no strong coupling (purple) are dispersed throughout the extracellular domain, and, although only five have been identified so far, the same is true of the gating pathway residues (orange). There is no simple pattern that distinguishes the two classes.

The agonist binding site of the nAChR is an ‘aromatic box’, shaped by five, conserved aromatic residues: αY93 (A), αW149 (B), αY190 (C1), αY198 (C2),

and γW55/δW57 (D).[7, 36] The letter designations signify the 'loop' of the extracellular domain that contains the particular residue[37]. Because all the natural agonists of Cys-loop receptors have a cationic group, the presence of the aromatic box suggested that a cation-π interaction contributes to agonist binding.[38, 39] Indeed, αW149 (B) and the aligning residues have been shown to contribute to agonist binding through a cation-π interaction in both the nAChR and the 5-HT_3 receptors.[22, 40] We find Ω ~ 1, consistent with a binding role for this residue. Note that subtle mutations have been employed at this site, taking advantage of the power of unnatural amino acid mutagenesis. We cannot rule out the possibility that more disruptive mutations at this and other sites would impact receptor gating. Indeed, the αW149F mutation has been probed, and it impacts both binding and gating.[41] Most of the mutations in **Table 3.1** are, by conventional standards, relatively subtle, and we would argue that some caution must be employed in interpreting the consequences of more severe mutations.

The residue analogous to αY198 (C2) has been shown to bind serotonin through a cation-π interaction in the MOD-1 receptor[42]. Previous studies in the nAChR show that mutations at this site exhibit normal coupling to L9'S mutations.[43] Single-channel studies of the αY198F mutant indicate only modest changes in gating[24] that would be outside the limits of detection for ELFCAR.

The residue αY93 (A) has been extensively probed. In the $GABA_A$ receptor the analogous residue makes a cation-π binding interaction to the native agonist.[44] In the nAChR, side chain mutations at this site strongly impact

channel gating. However, the mutation studied here—αY93Yah—is a *backbone* mutation. Our finding of Ω ~ 1 indicates no strong perturbation of gating by a backbone mutation in this region. This conclusion is supported by the similar result at the adjacent residue (αN94Nah).

The remaining two box residues, αY190 (C1) and γW55/δW57 (D), have never been shown to make a cation-π interaction with an agonist. Both are clearly assigned as gating pathway residues according to the ELFCAR method. αY190 has been extensively studied. That αY190F strongly impacts gating is unambiguously established by the single-channel records of **Figure 3.5A**. Other workers have also found strong perturbations to gating for mutations at this site.[25, 26] Some studies have also found a contribution to binding, but, as discussed above, the present work does not address this issue. The important point is that the finding of a large Ω value in ELFCAR is fully supported by single-channel studies. In addition, a backbone mutation at the adjacent residue, αS191Sah, also produces a large Ω value in ELFCAR. We have recently shown that this residue makes a strong hydrogen bond to a side chain from the complementary subunit (γ/δ), and that the hydrogen bond contributes significantly to gating.[45] Most gating models for the nAChR invoke considerable movement of loop C,[7, 46, 47] and the finding of large Ω values for these two loop C residues is consistent with these models.

The final binding box residue, γW55/δW57 (D), shows a large Ω value for the Tyr mutant. Our single-channel studies (**Figure 3.5C**) clearly establish an

impact on gating for this mutation. Previous single-channel studies of the Phe mutant show a small effect on binding (3.4-fold) and a very large effect on gating (50-fold),[48] consistent with the present results. There is reason to anticipate that loop D may also undergo significant rearrangements during gating. In Unwin's image of the *Torpedo* nAChR,[1] with no agonist bound, TrpD is flipped out away from the box that is so well formed in AChBP (with or without agonist bound). This again suggests that movement of TrpD occurs on ligand binding, consistent with it being a gating pathway residue.

The fifth gating pathway residue we identified, αD200, is not part of the aromatic binding box, but appears to lie outside the box. However, it is part of a triad of residues that includes αY190 and αK145 and that has been suggested to undergo significant rearrangement on gating.[26] Previous single-channel studies have shown that mutation at this site perturbs gating.[23, 26] As such, the large Ω seen here with ELFCAR is fully consistent with other studies.

3.5 Conclusions

In this work, we have developed an efficient strategy for identifying mutations that impact receptor function by significantly impeding the gating pathway. The method involves combining mutations of extracellular domain residues proposed to be functionally important with a known gating pathway (reporter) mutation. For interesting sites, ELFCAR can provide guidance for more focused, advanced studies, such as detailed unnatural amino acid

mutagenesis of putative binding residues or single-channel analysis, where possible, for gating residues (**Figure 3.8**).

The kinetic model of **Scheme 3.1** refers to the nAChR, but it contains the essential features of any allosteric system. There is a binding interaction with an allosteric effector and an intrinsic conformational change associated with the signaling event. The former is a bimolecular association, and so is saturable at high ligand concentration. However, the conformational change is unimolecular, and so it is an intrinsic property of the system. It is the combination of these two processes that produces the curvature of **Figure 3.2** and thus allows for the specific application of mutant cycle analysis presented here. As such, we anticipate that the same approach could be applied to other allosteric systems, allowing a facile means to identify the roles of particular residues in a complex protein system. Thus, while this study has focused exclusively on a single Cys-loop receptor, we believe the approach is broadly applicable to other Cys-loop receptors and to allosteric receptors in general. Certainly, comparable reporter residues can be found in the other Cys-loop receptors; the L9' residue is highly conserved and it seems likely to play an important gating role throughout the family. We emphasize that, although all members of the Cys-loop family are genetic orthologs, functional paralogs, and structural homologs, there is growing evidence that the detailed mechanisms of action will vary from system to system.[39] Thus, the present approach, based on the readily obtained EC_{50} measure, offers a robust and efficient way to search for such variations in gating mechanism.

3.6 Materials and Methods

3.6.1 Site-Directed Mutagenesis

Fetal mouse muscle nicotinic acetylcholine receptor (nAChR) α-, β-, γ-, δ-subunits were utilized in the experiments. Each subunit was expressed in pAMV vectors. Mutations were made at the site of interest using a standard Stratagene QuikChange protocol. For the incorporation of unnatural residues, the site of interest was mutated to the amber stop codon. In addition, the α-subunits contain an HA epitope in the M3-M4 cytoplasmic loop for Western blot studies. Control experiments show that this epitope does not detectably alter EC_{50}. Primers were designed to fulfill the established criteria and were ordered from Integral DNA technologies. Polymerase chain reactions (PCRs) reactions were carried out using a high fidelity Pfu DNA polymerase, and a 10 min extension time was used in each thermocycle. Annealing temperatures were modified as required for successful incorporation of the mutation. DpN1 digestion was used to eliminate methylated template DNA from the PCR products. After PCR purification (Qiagen standard protocol), amplification of the PCR product was conducted by electroporation with Super Competent Top 10 *E. coli,* followed by 12 h of growth on agar/LB/ampicillin plates. Single colonies were selected and amplified in liquid LB/ampicillin culture. The DNA was isolated from the bacteria (Qiagen, miniprep kit), and sequenced to verify the successful incorporation of the mutation at the selected site.

The circular bacterial plasmid of the mutation-containing DNA was linearized using a Not1 restriction enzyme. Linearized plasmids were used as the DNA template for *in vitro* transcription using T7 mMessage mMachine enzyme kits (Ambion) to make mRNA. Quantification of mRNA was determined using a NanoDrop spectrophotometer (NanoDrop Technologies, Thermo Scientific, Wilmington, DE).

For conventional mutations, the stoichiometry of subunits was 2:1:1:1 of α:β:γ:δ by mass with a total mRNA concentration of ~ 2 μg/μL. For unnatural mutations,[49] a total of 40 ng of mRNA in a 10:1:1:1 α:β:γ:δ subunit ratio was coinjected with the synthetic α-hydroxy acids conjugated to the dinucleotide dCA and ligated to truncated 74-nucleotide tRNA, as previously described. Ratios of mRNA to tRNA were typically 1:1.

Stage V–VI oocytes of *Xenopus laevis* (Nasco, Fort Atkinson, WI) were injected with 50 nL of the mRNA or mRNA/tRNA mixture. The oocytes were incubated in culture media containing 1–2% horse serum at 18 ˚C.

3.6.2 Whole-Cell Electrophysiology

Whole-cell electrophysiological recordings were performed on injected *Xenopus laevis* oocytes after 12–36 h incubation. Recording was done in two-electrode voltage clamp mode using the OpusXpress 6000A (Axon Instruments, Union City, CA). Oocytes were superfused with Ca^{2+}-free ND96 solution (in mM:

96 NaCl, 2 KCl, 1 $MgCl_2$, 5 HEPES) at flow rates of 4 mL/min during drug application (15 s) and 3 mL/min during wash (130 s). Macroscopic agonist-induced currents were recorded in response to bath application of the indicated agonist concentrations at -60 mV or -80 mV. Data were sampled at 125 Hz and filtered at 50 Hz. ACh chloride and SuCh chloride were purchased from Sigma/Aldrich/RBI (St. Louis, MO). Agonist solutions ranging from 0.0100 to 5000 µM were prepared in Ca^{2+}-free ND96 from a 1.00 M stock solution. Dose-response relations were constructed for each mutation using data from $\geq$ 5 oocytes. Dose-response relations were fitted to the Hill equation (**Equation 3.3**) to determine the EC_{50} and the Hill coefficient.

$$I/I_{max} = 1/(1+(EC_{50}/[A])^{n_H}) \qquad \textbf{(Equation 3.3)}$$

Here, I is the current for agonist concentration [A], I_{max} is the maximum current, EC_{50} is the concentration to elicit half maximal response, and n_H is the Hill coefficient. The dose-response relations of individual oocytes were examined and used to determine outliers. The reported EC_{50} values are from the curve fit of the averaged data.

3.6.3 Single-Channel Characterization of Selected Gating Pathway Residue Mutants

Single-channel recording was performed in the cell-attached configuration on devitellinized oocytes 24–60 h after injection at 20 ± 3°C with an applied pipette potential of +100 mV, as described previously.[50] Pipettes were fabricated from thick-walled (I.D. = 0.80 mm, O.D. = 1.60 mm) KG-33 glass (Garner Glass Company, Claremont, CA) and coated with sylgard (World Precision Instruments, Sarasota, FL); they had resistances of 8–25 MΩ. The bath solution contained, in mM, 120 KCl, 5 HEPES, 1 $MgCl_2$, 2 $CaCl_2$, pH = 7.4, so that the transmembrane potential of the patch was -100 mV and the reversal potential for agonist-induced currents was ~ 0 mV. The pipette solution contained, in mM, 100 KCl, 10 HEPES, 1 $MgCl_2$, 10 K_2EGTA, pH = 7.4 and was supplemented with the indicated concentrations of ACh using a 1.00 M stock solution.

Before single-channel recording, whole-cell expression levels were determined with 100–1000 μM ACh doses using the whole-cell recording conditions on each mutant. When whole-cell expression exceeded ~ 300 nA for receptors with the target mutation alone and ~ 3 μA for receptors with both a target mutation and a reporter mutation, oocytes were typically incubated 4–10 additional h prior to single-channel recording. Data were collected using a GeneClamp 500B amplifier (Axon Instruments, Union City, CA) with a CV-5 GU headstage at full bandwidth (4-pole Bessel, -3 dB, 50 kHz). The signal was then low-pass filtered (8-pole Bessel, -3 dB, 20 kHz) and sampled with a Digidata

1320A and Clampex 9.2 (Axon Instruments, Union City, CA) at 50 or 100 kHz. Only recordings that showed no simultaneous activations were included in NP_{open} analysis. In this manner ≥ 3 patches at EC_{50} were analyzed for all mutants, except for the αβγD174NδD180N and αβL9'SγD174NδD180N mutants for which 2 patches each were obtained. Data were filtered offline (Gaussian, -3 dB, 5 kHz) and electrical interference at harmonics of 60 Hz was removed, if necessary. Event transitions were detected with Clampfit 9.2 (single-channel search). A dead time, τ_d, of 40 μs was applied to all events. The time-average probability that exactly one channel in the patch is open (NP_{open}) was calculated as the total open time divided by the total closed time.

Acknowledgements

We thank B.N. Cohen for advice on single-channel recording and analysis. This work was supported by the NIH (NS 34407; NS 11756). J.A.P.S. was partially supported by an NRSA training grant. K.R.G. was partially supported by an NSF Graduate Research Fellowship.

3.7 REFERENCES

1. Unwin, N. Refined structure of the nicotinic acetylcholine receptor at 4 angstrom resolution. *Journal of Molecular Biology* **346**, 967-989 (2005).
2. Connolly, C.N. & Wafford, K.A. The Cys-loop superfamily of ligand-gated ion channels: the impact of receptor structure on function. *Biochemical Society Transactions* **32**, 529-534 (2004).

3. Grutter, T. & Changeux, J.P. Nicotinic receptors in wonderland. *Trends Biochem Sci* **26**, 459-63 (2001).
4. Lester, H.A., Dibas, M.I., Dahan, D.S., Leite, J.F. & Dougherty, D.A. Cys-loop receptors: new twists and turns. *Trends in Neurosciences* **27**, 329-336 (2004).
5. Sine, S.M. & Engel, A.G. Recent advances in Cys-loop receptor structure and function. *Nature* **440**, 448-455 (2006).
6. Changeux, J.P. & Edelstein, S.J. Allosteric mechanisms of signal transduction. *Science* **308**, 1424-1428 (2005).
7. Sixma, T.K. & Smit, A.B. Acetylcholine binding protein (AChBP): a secreted glial protein that provides a high-resolution model for the extracellular domain of pentameric ligand-gated ion channels. *Annu Rev Biophys Biomol Struct* **32**, 311-34 (2003).
8. Peters, J.A., Hales, T.G. & Lambert, J.J. Molecular determinants of single-channel conductance and ion selectivity in the Cys-loop family: insights from the 5-HT3 receptor. *Trends Pharmacol Sci* **26**, 587-94 (2005).
9. Chang, Y. & Weiss, D.S. Channel opening locks agonist onto the GABAC receptor. *Nat Neurosci* **2**, 219-25 (1999).
10. Davies, P.A. et al. The 5-HT3B subunit is a major determinant of serotonin-receptor function. *Nature* **397**, 359-63 (1999).
11. Keramidas, A. & Harrison, N.L. Agonist-dependent single channel current and gating in alpha4beta2delta and alpha1beta2gamma2S GABAA receptors. *J Gen Physiol* **131**, 163-81 (2008).
12. Legendre, P. The glycinergic inhibitory synapse. *Cell Mol Life Sci* **58**, 760-93 (2001).
13. Li, G. & Niu, L. How fast does the G1uR1Q(flip) channel open? *Journal of Biological Chemistry* **279**, 3990-3997 (2004).
14. Filatov, G.N. & White, M.M. The role of conserved leucines in the M2 domain of the acetylcholine receptor in channel gating. *Mol Pharmacol* **48**, 379-84 (1995).
15. Labarca, C. et al. Channel gating governed symmetrically by conserved leucine residues in the M2 domain of nicotinic receptors. *Nature* **376**, 514-6 (1995).
16. Kalbaugh, T.L. Ligand-binding residues integrate affinity and efficacy in the NMDA receptor. *Molecular pharmacology* **66**, 209-219 (2004).
17. Edelstein, S.J., Schaad, O. & Changeux, J.P. Single binding versus single channel recordings: a new approach to study ionotropic receptors. *Biochemistry* **36**, 13755-60 (1997).
18. Mitra, A., Cymes, G.D. & Auerbach, A. Dynamics of the acetylcholine receptor pore at the gating transition state. *Proc Natl Acad Sci U S A* **102**, 15069-74 (2005).
19. Kosolapov, A.V., Filatov, G.N. & White, M.M. Acetylcholine receptor gating is influenced by the polarity of amino acids at position 9' in the M2 domain. *J Membr Biol* **174**, 191-7 (2000).

20. Sigurdson, W., Chen, J., Akabas, M., Karlin, A. & Auerbach, A. Single-Channel Kinetic-Analysis of Mouse Achr M2 Mutants Alpha-L251c and Alpha-S248c. *Biophysical Journal* **66**, A212-A212 (1994).
21. Kearney, P.C. et al. Dose-response relations for unnatural amino acids at the agonist binding site of the nicotinic acetylcholine receptor: tests with novel side chains and with several agonists. *Mol Pharmacol* **50**, 1401-12 (1996).
22. Zhong, W. et al. From ab initio quantum mechanics to molecular neurobiology: a cation-pi binding site in the nicotinic receptor. *Proc Natl Acad Sci U S A* **95**, 12088-93 (1998).
23. Akk, G., Sine, S. & Auerbach, A. Binding sites contribute unequally to the gating of mouse nicotinic alpha D200N acetylcholine receptors. *J Physiol* **496 (Pt 1)**, 185-96 (1996).
24. Akk, G., Zhou, M. & Auerbach, A. A mutational analysis of the acetylcholine receptor channel transmitter binding site. *Biophys J* **76**, 207-18 (1999).
25. Chen, J., Zhang, Y., Akk, G., Sine, S. & Auerbach, A. Activation kinetics of recombinant mouse nicotinic acetylcholine receptors: mutations of alpha-subunit tyrosine 190 affect both binding and gating. *Biophys J* **69**, 849-59 (1995).
26. Mukhtasimova, N., Free, C. & Sine, S.M. Initial coupling of binding to gating mediated by conserved residues in the muscle nicotinic receptor. *J Gen Physiol* **126**, 23-39 (2005).
27. O'Leary, M.E. & White, M.M. Mutational analysis of ligand-induced activation of the Torpedo acetylcholine receptor. *J Biol Chem* **267**, 8360-5 (1992).
28. Sine, S.M. et al. Naturally occurring mutations at the acetylcholine receptor binding site independently alter ACh binding and channel gating. *J Gen Physiol* **120**, 483-96 (2002).
29. Xie, Y. & Cohen, J.B. Contributions of Torpedo nicotinic acetylcholine receptor gamma Trp-55 and delta Trp-57 to agonist and competitive antagonist function. *J Biol Chem* **276**, 2417-26 (2001).
30. Chapman, E., Thorson, J.S. & Schultz, P.G. Mutational Analysis of Backbone Hydrogen Bonds in Staphylococcal nuclease. *J. Am. Chem. Soc.* **119**, 7151-7152 (1997).
31. England, P.M., Zhang, Y., Dougherty, D.A. & Lester, H.A. Backbone mutations in transmembrane domains of a ligand-gated ion channel: implications for the mechanism of gating. *Cell* **96**, 89-98. (1999).
32. Kash, T.L., Jenkins, A., Kelley, J.C., Trudell, J.R. & Harrison, N.L. Coupling of agonist binding to channel gating in the GABA(A) receptor. *Nature* **421**, 272-5 (2003).
33. Price, K.L., Millen, K.S. & Lummis, S.C. Transducing agonist binding to channel gating involves different interactions in 5-HT3 and GABAC receptors. *J Biol Chem* **282**, 25623-30 (2007).

34. Venkatachalan, S.P. & Czajkowski, C. A conserved salt bridge critical for GABAA receptor function and loop C dynamics. *Proc Natl Acad Sci U S A* **105**, 13604-9 (2008).
35. Xiu, X., Hanek, A.P., Wang, J., Lester, H.A. & Dougherty, D.A. A unified view of the role of electrostatic interactions in modulating the gating of Cys loop receptors. *J Biol Chem* **280**, 41655-66 (2005).
36. Brejc, K. et al. Crystal structure of an ACh-binding protein reveals the ligand-binding domain of nicotinic receptors. *Nature* **411**, 269-76 (2001).
37. Corringer, P.J., Le Novere, N. & Changeux, J.P. Nicotinic receptors at the amino acid level. *Annu Rev Pharmacol Toxicol* **40**, 431-58 (2000).
38. Dougherty, D.A. & Stauffer, D.A. Acetylcholine binding by a synthetic receptor. Implications for biological recognition. *Science* **250**, 1558-1560 (1990).
39. Dougherty, D.A. Cys-loop neuroreceptors: structure to the rescue? *Chem Rev* **108**, 1642-53 (2008).
40. Beene, D.L. et al. Cation-pi interactions in ligand recognition by serotonergic (5-HT3A) and nicotinic acetylcholine receptors: The anomalous binding properties of nicotine. *Biochemistry* **41**, 10262-10269 (2002).
41. Akk, G. Aromatics at the murine nicotinic receptor agonist binding site: mutational analysis of the alphaY93 and alphaW149 residues. *J Physiol* **535**, 729-40 (2001).
42. Mu, T.W., Lester, H.A. & Dougherty, D.A. Different binding orientations for the same agonist at homologous receptors: a lock and key or a simple wedge? *J Am Chem Soc* **125**, 6850-1 (2003).
43. Kearney, P.C., Zhang, H., Zhong, W., Dougherty, D.A. & Lester, H.A. Determinants of nicotinic receptor gating in natural and unnatural side chain structures at the M2 9' position. *Neuron* **17**, 1221-9 (1996).
44. Padgett, C.L., Hanek, A.P., Lester, H.A., Dougherty, D.A. & Lummis, S.C.R. Unnatural amino acid mutagenesis of the GABA(A) receptor binding site residues reveals a novel cation-pi interaction between GABA and beta(2)Tyr97. *Journal of Neuroscience* **27**, 886-892 (2007).
45. Gleitsman, K.R., Kedrowski, S.M.A., Lester, H.A. & Dougherty, D.A. An Intersubunit Hydrogen Bond in the Nicotinic Acetylcholine Receptor that Contributes to Channel Gating *J Biol Chem* **283**, 35638-43 (2008).
46. Gao, F. et al. Agonist-mediated conformational changes in acetylcholine-binding protein revealed by simulation and intrinsic tryptophan fluorescence. *J Biol Chem* **280**, 8443-51 (2005).
47. Miyazawa, A., Fujiyoshi, Y. & Unwin, N. Structure and gating mechanism of the acetylcholine receptor pore. *Nature* **423**, 949-55 (2003).
48. Akk, G. Contributions of the non-alpha subunit residues (loop D) to agonist binding and channel gating in the muscle nicotinic acetylcholine receptor. *J Physiol* **544**, 695-705 (2002).

49. Nowak, M.W. et al. *In vivo* incorporation of unnatural amino acids into ion channels in a *Xenopus* oocyte expression system. *Methods Enzymol* **293**, 504-529 (1998).
50. Hamill, O.P., Marty, A., Neher, E., Sakmann, B. & Sigworth, F.J. Improved patch-clamp techniques for high resolution current recording from cells and cell-free membrane patches. *Pflugers Arch.* **391**, 85-100 (1981).
51. Cashin, A. L., E. J. Petersson, H. A. Lester, and D. A. Dougherty. 2005. Using physical chemistry to differentiate nicotinic from cholinergic agonists at the nicotinic acetylcholine receptor. *J. Am. Chem. Soc.* 127:350-356.

3.8 Supporting Material

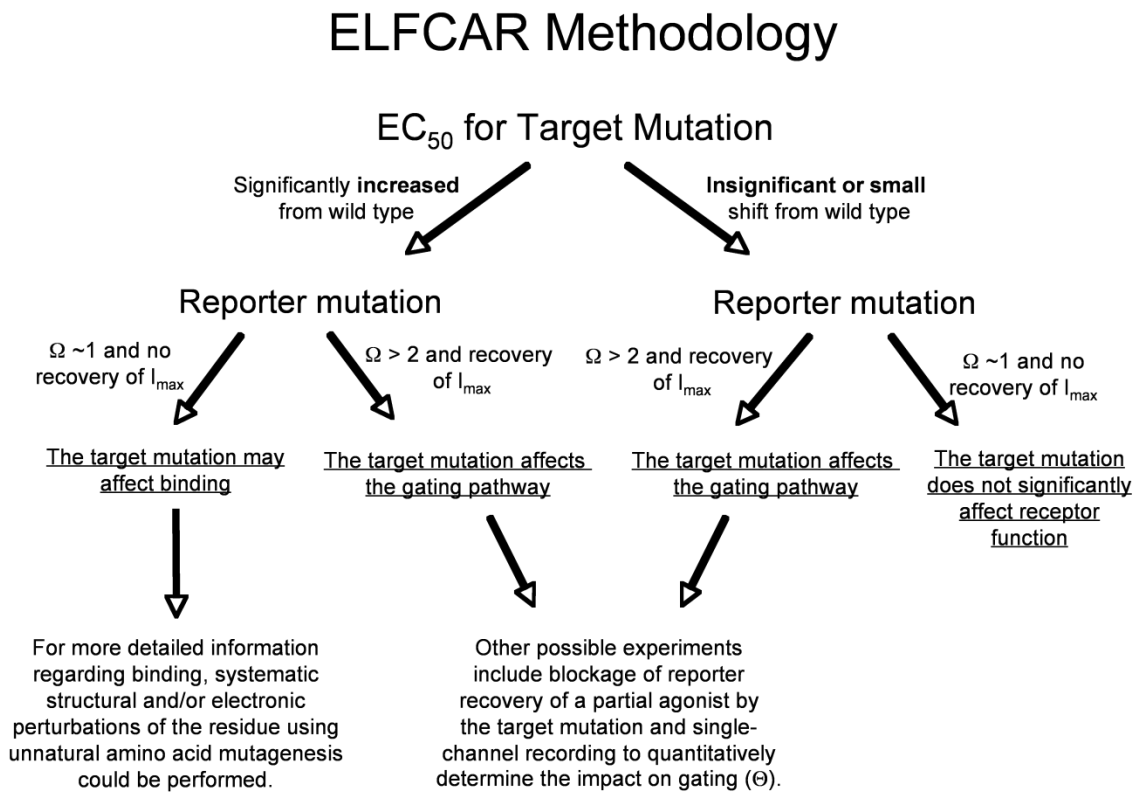

Figure 3.8. Experimental outline for applying the ELFCAR methodology introduced here to identify mutations that affect the gating pathway

3.8.1 The relationship between Ω, I_{max}, and NP_{open}

In < 10% (2 of > 20) of patches obtained for single-channel recordings of the three target mutations shown in **Table 3.2**, a higher P_{open} mode was seen as part of the channel activity. Since this mode accounted for << 50% of events even when it was present, it accounts for a small minority (<< 10%) of total events. Moreover, its rare occurrence indicates that this P_{open} is clearly not

representative of the functional behavior of these mutations. Rather, it appears to be an infrequently visited mode of the channel. We thus report NP_{open} values ignoring this rare mode.

The macroscopic and microscopic data display correlating shifts for the target mutations versus target + reporter mutations. However, there are apparent quantitative differences between the following comparisons (in the background of a target mutation): I_{max}9'/I_{max} wild type (11–17) and NP_{open}9'/NP_{open} wild type (14–116, reflecting a similar shift in Θ over the range of our measured NP_{open} values). These differences are accounted for by our observation of a high P_{open} mode. If channels are in this mode ~ 1% of time, then that effectively limits the range over which I_{max} can shift—adding a fixed ~ 0.01 to each NP_{open} value would limit the maximal possible I_{max} shift to 50 since $P_{open,max}$ at EC_{50} is 0.5. The present results for I_{max} shifts accord with this observation well: the drastic gating pathway mutations that ELFCAR identifies display a near-maximal 11–17-fold increase in I_{max} when a reporter mutation is added. On the other hand, EC_{50} increases are 4–26-fold, corresponding to Θ decreases of 15-680-fold which are quantitatively similar to the microscopic NP_{open} results. Since the high P_{open} mode would account for, at most, a small minority of the total open conductance, it is not reflected in the EC_{50} shifts. Thus, the macroscopic (I_{max} and EC_{50}) data are in accordance with the drastic change in function obvious in microscopic data (**Figure 3.5**).

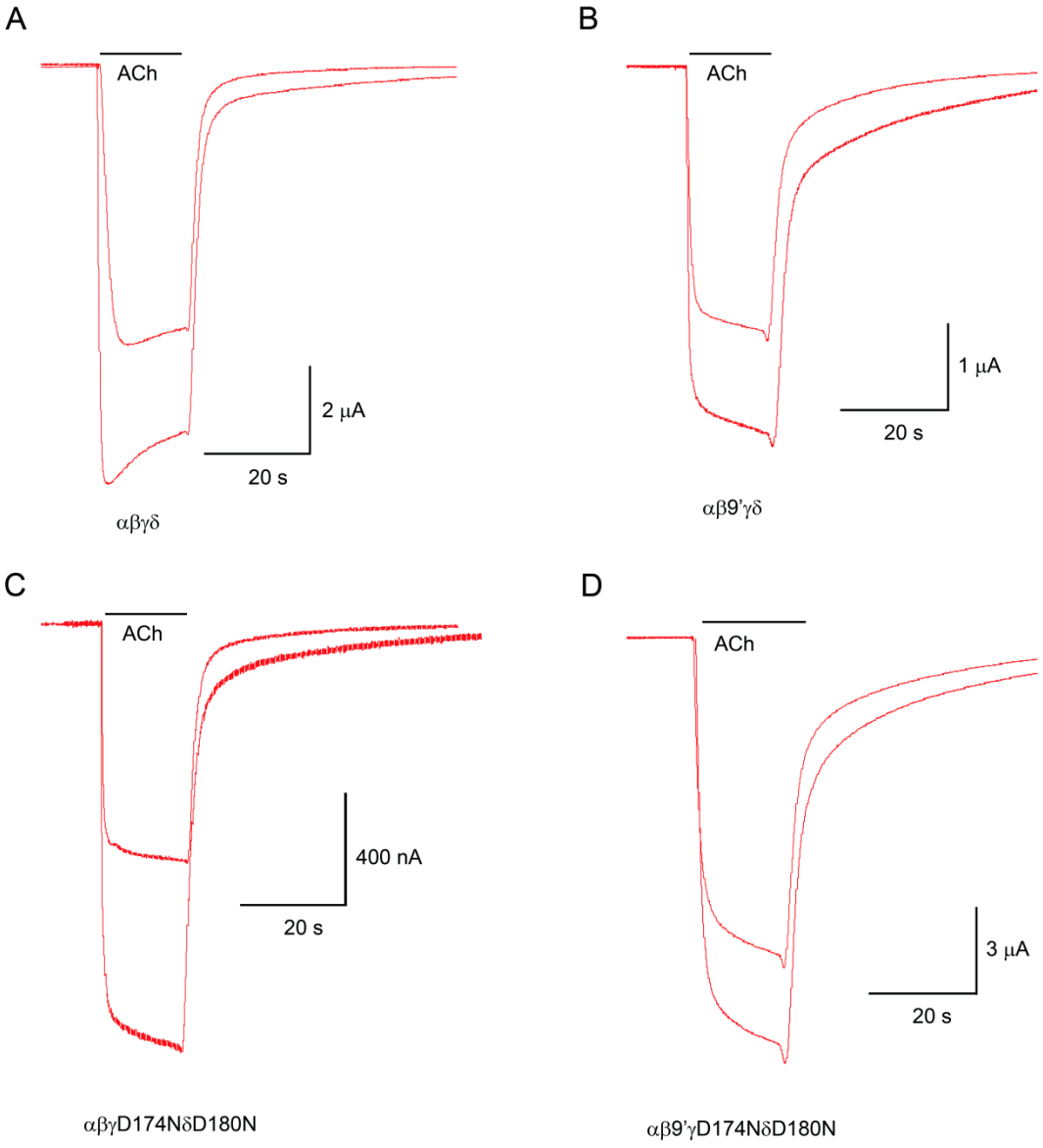

Figure 3.9. Agonist-induced voltage-clamp currents. Each panel shows the inward macroscopic current elicited near EC_{50} (Table 3.1) and at a saturating concentration as downward deflections for one of 4 receptors: A) αβγδ, B) αβ9'γδ, C) αβγD174NδD180N, D) αβ9'γD174NδD180N. Note that I_{max} is similar for αβγδ and αβ9'γδ, but that I_{max} increases significantly when the L9'S mutation is introduced in the background of the target mutation (γD174NδD180N).

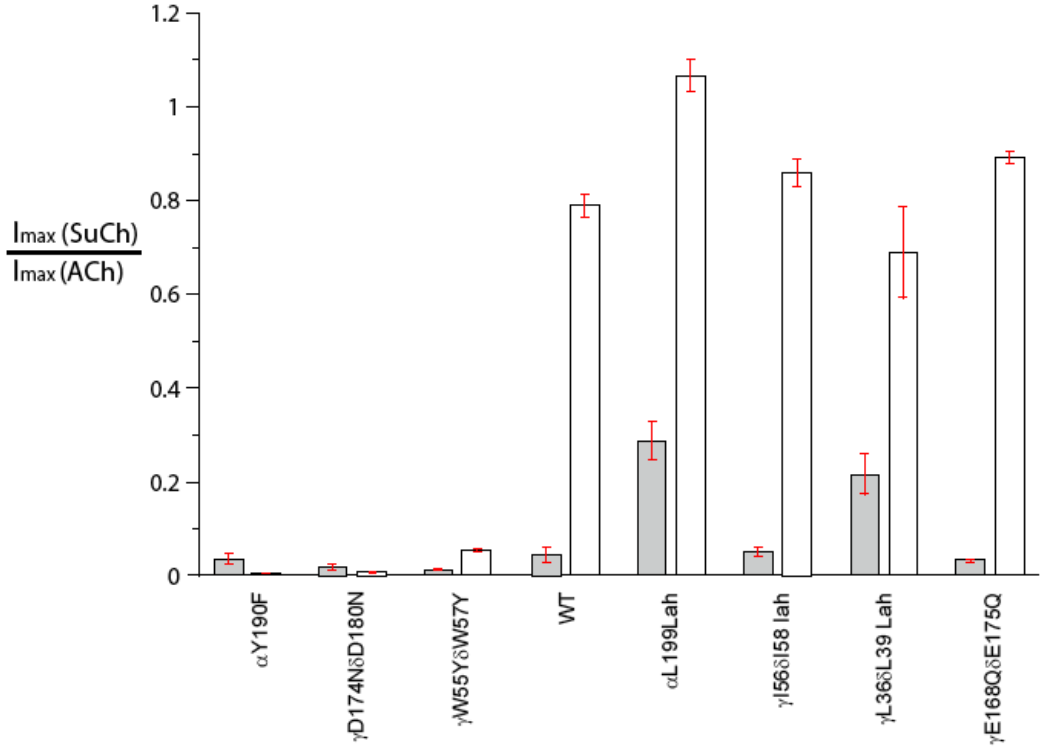

Figure 3.10. For extracellular domain mutations with Ω > 2, the normal recovery of SuCh towards full agonism in the presence of an L9'S reporter mutation is blocked. The gray bars represent receptors with a wild type pore domain, while the white bars represent receptors with a βL9'S mutation. The wild type receptor and four mutations to the right all show the characteristic increase in efficacy in the presence of the L9'S pore mutation, while the three mutations on the far left do not.

3.9 Additional Discussion

As with mutant cycle analysis for short-range interactions, ELFCAR reveals if two probed perturbations are functionally independent ($\Omega = 1$) or interacting ($\Omega \neq 1$). In the case of interaction (functional dependence), $\Omega > 2$ or < 0.5 are possible. The main utility of the ELFCAR procedure is to identify mutations that significantly decrease the ability of an allosteric receptor to be activated. For LGICs, this corresponds to significant decreases in the gating parameter (Θ). When EC_{50}s are used as the functional assay, a result of $\Omega = 1$ indicates that the residues are non-interacting. However, in this case, if there is no recovery of maximal activation, and the initial target did impact receptor function, then ELFCAR can be used to suggest a likely impact on binding to the receptor. Further experiments, such as incorporation of a series of fluorinated aromatic unnatural amino acids, can then be pursued to determine the residue's impact on binding for perturbations that do not functionally couple to allosteric activation (**Figure 3.8**).

Biological variation in oocyte experiments can be significant. Thus, in ELFCAR a reporter is introduced to produce an unambiguous, systematic increase in I_{max} that is significantly larger than normal oocyte-to-oocyte variation (see error bars in **Figure 3.7**). In fact, the ~ tenfold increase in I_{max} upon adding a reporter in the presence of a strongly functionally coupled target is a definitive indication—from whole-cell data alone—of the significance and functional role of the target residue. The functional change corresponding to the increase in I_{max}

we describe could, in theory, happen for any allosteric receptor. However, the relatively similar I_{max} values for the wild type receptor with and without the reporter βL9'S mutation (**Figure 3.9B** and **A**, respectively) show that the significant qualitative difference in whole-cell current isn't immediately evident for all receptors. Consequently, the use of reporter mutations with larger Θ shifts than the target mutation should allow ELFCAR to be used to identify more subtle deleterious gating mutations, especially for LGICs with lower Θ values (such as $1 < \Theta < 20$). It is also worth noting that I_{max} is only one of several components of the whole-cell data, beyond the EC_{50}, that can be used to assess a target's functional role. Some of these were covered in Chapter 2, such as analysis of whole-cell activation and deactivation kinetics where applicable. Here I'll briefly highlight that, in addition to any systematic changes in expression level (I_{max}), the Hill coefficient (n_H) contains information about channel activation.

ELFCAR is also a valuable tool for application to targets that do not yield a significant functional change, some of which may still play significant roles in allosteric function. Specifically, because Ω is large in some cases, the EC_{50} shift caused by the target alone can be quite small; it is barely over twofold in the case of αY190F. Such a small shift in EC_{50} can be hard to interpret. ELFCAR thereby expands the utility of whole-cell recording to identify functionally significant residues that may not be identified based on EC_{50} shift alone. ELFCAR also enables the identification of a broader range of residues than merely those which lie directly along the pathway of the gating structural transduction. Any mutated

target that leads to a change in the relative stabilization of the closed and open states can produce a positive ELFCAR result. ELFCAR can therefore enable the identification of important inter-residue functional interactions—even at a distance—anywhere in the receptor.

3.9.1 ELFCAR Methodology

Based on the results and analysis presented in this chapter, we developed a specific set of protocols in order to efficiently implement the core component of ELFCAR. This use of mutant cycle analysis is summarized in **Figure 3.11**, which distills the essence of **Figure 3.8**.

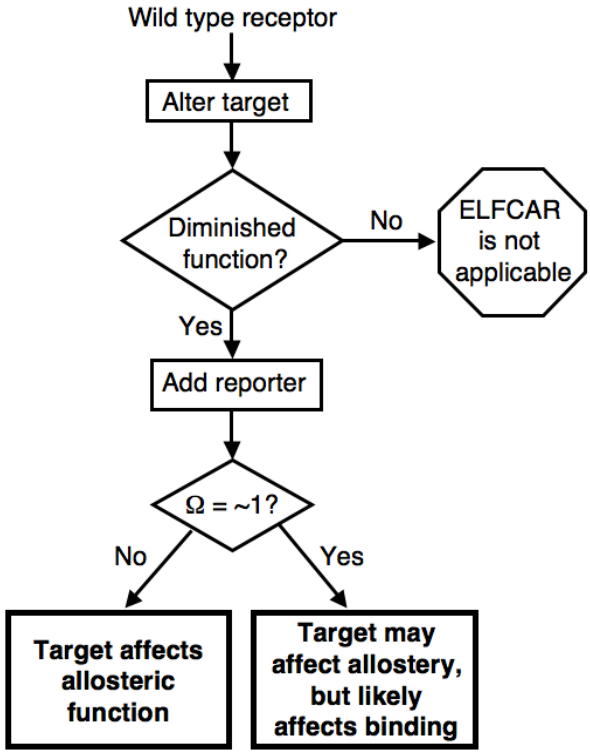

Figure 3.11. (Previous page). The application of ELFCAR involves: (a) identification of a gain-of-function reporter mutation, (b) making the mutated allosteric receptors, (c) expressing them in a heterologous system or some other system for functional assay, (d) obtaining functional data for the allosteric receptors, and (e) analyzing this data to calculate Ω. For many allosteric receptors, once all necessary mutants are made, steps c–e can be performed rapidly (< 1 week) and in parallel. For each target to be evaluated, 4 receptor sets are needed for mutant cycle analysis: wild type, target, reporter, and target + reporter. But, in practice, the reporter and wild type will be the same for any given receptor, so each new Ω value requires 2 functional measurements: target and target + reporter.

See our book chapter: '*Using Mutant Cycle Analysis to Elucidate Long-Range Functional Coupling in Allosteric Receptors'* in *Methods in Molecular Biology Allostery: Methods and Protocols* for more details and notes regarding applying this methodology.

Several other acronyms were considered before we ultimately selected ELFCAR; some of the other acronyms we considered are included in **Appendix C**.

3.9.2 Single-Channel Data and Its Correlation to Whole-Cell Data

Since the single-channel recordings were performed at the midpoint of the macroscopic dose-response relation (EC_{50}), analysis of closed dwell time histograms did not provide a way to readily distinguish non-conducting closed or unbound dwells from the desensitized states of the channel. As a result, detailed modeling was difficult. However, if we take the longest closed component in each mutant as the desensitized state, all NP_{open} values are shifted to larger values in such a way that the substantial increase in NP_{open} upon addition of

βL9'S is preserved. On the other hand, what is readily evident from the closed dwell time histograms and single-channel traces is that the decrease in NP_{open} is caused largely by a shift in the closed dwell times (**Figure 5**). In the 3 extracellular domain targets for which single-channel data were obtained here, these long closings account for > 80% of the total closed dwell time. Also, consistent with previous reports, addition of a βL9'S mutation increases open dwell time, generally ~ 3–5-fold for the primary component (under the present analysis parameters). This primary open dwell time component constitutes at least 80% of the total time that the channel spends open in each case.

For reasons discussed in the supporting information, we were unable to find a specific correlation between the single-channel measurement of NP_{open} and the whole-cell measurement of I_{max}. However, based on a combined interpretation of single-channel NP_{open} of the receptors without the reporter mutation and Ω from ELFCAR, we estimate that, of the three receptor sets that we studied via single-channel recording, the γD174NδD180N mutation is the most functionally perturbing, while the γW55YδW57Y mutation is the least. The single-channel traces in the left panels of **Figure 3B** and **C** demonstrate this qualitatively.

Analysis of single-channel records isn't possible for all LGICs, some of which have complex kinetics or single-channel conductances that are too small for systematic study. Thus, ELFCAR provides some of the information previously accessible primarily by single-channel recording in more straightforward and readily implemented whole-cell dose-response measurements. As a whole,

ELFCAR is most powerful as one tool in a broader toolbox of approaches to understanding how allosteric receptors, such as LGICs, function at the molecular level.

3.10 Future Studies

Several applications and expansions of ELFCAR may be of interest. I will briefly outline them here.

A) It is worth reiterating that, for some receptors, functional changes are difficult to assess by single-channel recording alone. Several reasons exist for this, such as: low single-channel conductance, larger numbers of subconductances, and difficulty in achieving a sufficiently pure population of receptors. The 5-HT_{3A}, GABA(C)R, and possibly GlyR are just some of several allosteric receptors for which ELFCAR may prove particularly useful.

B) Along these lines, it would be interesting to directly show the broad applicability of ELFCAR to other allosteric receptors—even beyond LGICs. This would likely require alternative functional assays beyond electrophysiology. In the selection of other allosteric receptors to pursue, the implications of **Figure 3.2** should be considered for both the wild type receptor and the reporter.

C) Several aspects of the binding sites of allosteric receptors could be probed with ELFCAR.

   a. The possibility of different functional interactions of the different binding sites with the channel pore could be examined. For the fetal muscle-type receptor ($\alpha_2\beta\gamma\delta$) that was the focus of these studies, the two binding site affinities are significantly different for ACh. It would be interesting to compare the functional coupling of various agonists to the channel pore, including agonists with more similar binding affinities, such as epibatidine. These data could be compared to data from experiments in receptors that contain more nearly equivalent binding sites, such as the adult muscle-type nAChR ($\alpha_2\beta\varepsilon\delta$) or 5-$HT_{3A}$. This could produce a correlation between the ability of agonists to activate (gate) receptors and their ability to bind to the receptor.

   b. The long-range functional coupling of mutations in (or near) two different binding sites could be probed in receptors where one of the binding region mutations can act as a reporter. The results of such studies could be used to address the functional coupling between binding sites that leads to the phenomena of cooperativity in some allosteric receptors.

D) The fact that the β and δ subunit pores seem to be more strongly functionally coupled to the binding site than the α and γ subunit pores is of

interest. A more detailed ELFCAR study of these subunit asymmetries could be pursued.

Chapter 4

Activation of Wild Type and Mutant Muscle-Type Nicotinic Acetylcholine Receptors by Acetylcholine, Choline, and Tetramethylammonium

4.1 Introduction

In Chapter 1, I introduced an experiment that the Dougherty group did with unnatural amino acids to demonstrate a cation-π binding interaction to TrpB (α1Trp149) (**Figure 4.1**) of the muscle-type nicotinic acetylcholine receptor (nAChR)(*1*). I also discussed the fact that the functional measurements in those experiments were EC_{50} values that are combined measures of binding and gating. In order to unambiguously assign all rates of a kinetic scheme, even one as simple as **Model 4.1**, single-channel data are required.

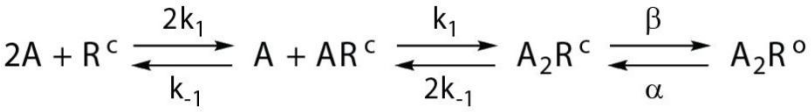

(**Model 4.1**)

A previous study showed that mutation of TrpB to phenylalanine had a significant impact on channel function, primarily by diminishing the ability of the channel to gate. Specifically, the channel opening rate, β, was decreased nearly 100-fold(*2*). Given that TrpB is unambiguously in the aromatic binding box (**Figure 4.1**) we hypothesized that the different functional roles assigned by these two studies were based on the fact that mutating tryptophan to phenylalanine produces a substantial change of both size and electrostatics, while the fluorinated tryptophans used in the Dougherty group study are subtle perturbations in which essentially only the residues' ability to form a cation-π interaction is systematically altered.

In this chapter, I will describe attempts to find and optimize a set of mutants and agonists to facilitate measuring detailed kinetics, including the channel opening rate, β, for the muscle-type nAChR.

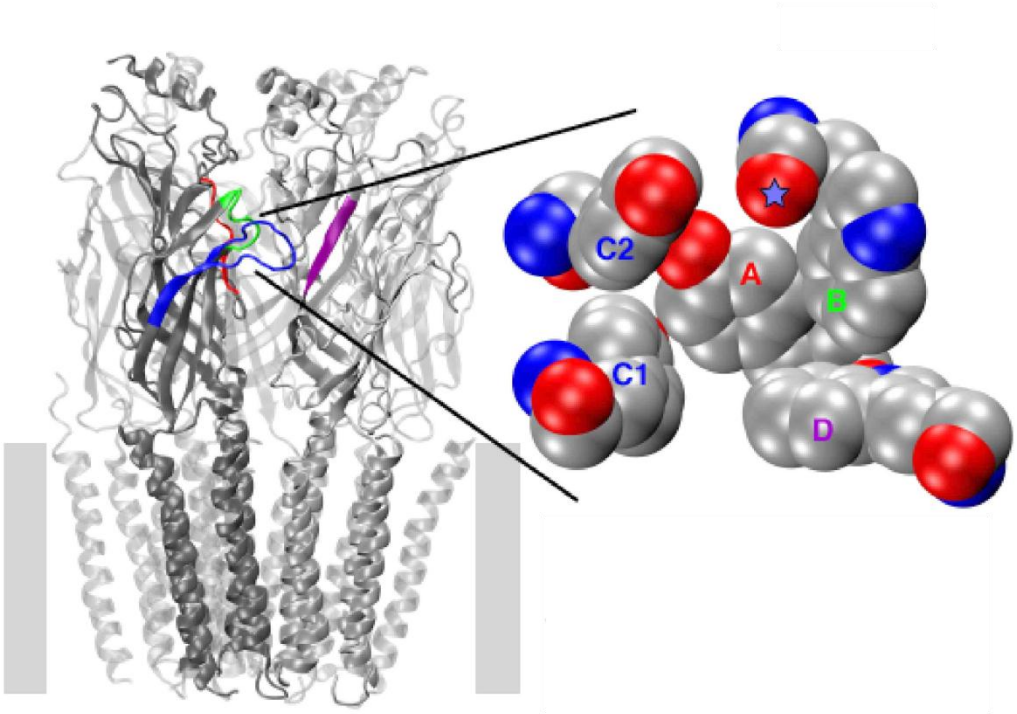

Figure 4.1. Left: An image of the nAChR from Torpedo, pdb file 2BG9(*3*). The approximate position of the membrane is shown as thick grey bars. Right: The "aromatic box" of AChBP, pdb file 1I9B(*4*). Residues are labeled according to the "loop" convention(*5*). TrpB (green) is the key residue for many of the studies reported in this chapter and Chapter 5.

4.1.1 Experimental Design

Before starting work on assembling the equipment necessary for single-channel recording (Chapter 2), we considered several aspects of the recording process in order to ensure that isolation of 1 to a few ion channels in a patch of membrane was statistically and technically feasible for nAChRs being heterologously expressed in *X. laevis* oocytes using nonsense suppression. Based on whole-cell currents routinely observed for mono-fluorinated tryptophan introduced by nonsense suppression at TrpB of a few μA(*1*), heterologous

expression of muscle nAChR in *X. laevis* oocytes is a system well-suited for the isolation of a patch of membrane with a single ion channel, even when this unnatural amino acid is introduced by nonsense suppression (see Chapter 2 for supporting calculation).

A separate, but overlapping, consideration is that the number of events (openings and closings) that can be collected in time periods on the order of minutes (1 to 30 minutes) must be ~ 500 to 50,000. Thus, a channel that desensitizes very quickly (< 10 ms), or which has very slow opening and closing rates (i.e., ~ 1 s^{-1})(*6*) may not produce enough data for statistical analysis. However, muscle nAChR has relatively fast rate constants and does not desensitize this quickly(*7, 8*).

On the other hand, some rates, such as the channel opening rate, β, for the muscle-type nAChR are at the upper end of resolution for most single-channel recording. Several tools to control the rates in **Model 4.1** include: introduction of mutations, varying agonists, varying voltage, and varying temperature. Of these tools, mutating receptors and use of varying agonists are some of the most widely used, probably because they can achieve the largest effects on rates. Changes to voltage and temperature-dependent studies have also been used (*9–12*).

In order to obtain seals of the resistances shown in the experiments discussed here (10–100 gigaΩ) and a resultant signal-to-noise ratio of > 3 (for f_c ~ 10 kHz or smaller), several aspects of the electrophysiology recording apparatus must be optimized. Since the ultimate goal is to be able to measure

current fluctuations on the order of one trillionth of an ampere (pA), sources of extraneous noise must be meticulously eradicated and/or compensated.

In addition to the techniques for reducing the several types of noise discussed in Appendix B, Section 2.1 (careful electrode design, proper tip immersion in the bath, and appropriate low-pass filtering), physical (macroscopic) disruptions may impact the ability to measure small current variations. For example, vibrations present in the building are damped by mounting the recording chamber, manipulator, dissecting scope, and light on a vibration isolation table with heavy table top. Additionally, the integrity of the cell membrane is important and membrane disruptions introduced during the stripping process must be minimized. Moreover, recording at lower temperatures, 18–20 °C, increases chances that the oocyte membrane will remain intact. Lastly, we use potassium as the permeant ion, since it has the largest conductance, thereby increasing the signal-to-noise ratio.

With these considerations in mind, we designed and built (see Chapter 2 for description) an electrophysiology rig capable of detecting current fluctuations of ~3 pA with durations of just ~ 50 µs, at bandwidths of up to 10 kHz (when f_s = 50 kHz to 100 kHz). In order to obtain reliable event detection in this range, the typical precautions for creating electrodes with proper physical characteristics must be carefully observed(*13*)—in some cases they were even enhanced, as described in Chapter 2.

4.2 Results and Discussion

All single-channel data presented in this chapter are in the cell-attached configuration and at positive pipette potentials. Thus, channel openings here will always be shown as downward deflections.

4.2.1 Early Single-Channel Studies: Acetylcholine (with Bruce Cohen; Some Data Were Collected on Bruce Cohen's Single-Channel Rig)

Single-channel recording of the wild type, fetal mouse muscle nAChR ($(\alpha1)_2\beta1\gamma\delta$) produced the following traces (**Figure 4.2**).

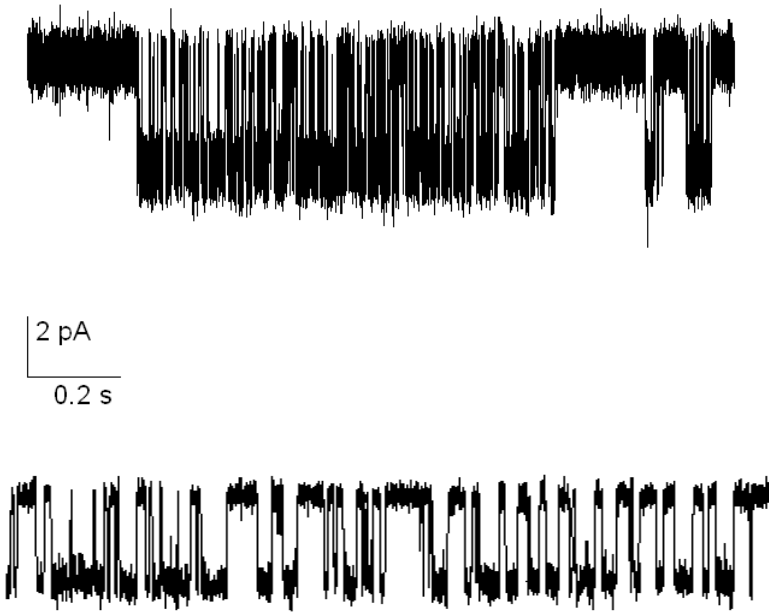

Figure 4.2. Wild type mouse muscle nAChR single-channel records at macroscopic EC_{50} (50 μM ACh), shown at f_c = 5 kHz. The applied pipette potential was + 60 mV. The specific receptor here is $(\alpha1)_2\beta1\gamma\delta$. Upper: 1 second trace, with scale bar. Lower: 100 ms expansion of upper trace

5-F-W (F_1W) was introduced in the $(\alpha1)_2\beta1\gamma\delta$ receptor at αW149 (TrpB) by nonsense suppression. **Figure 4.3** compares wild type and $(\alpha1_{W149F1W})_2\beta1\gamma\delta$

single-channel traces.

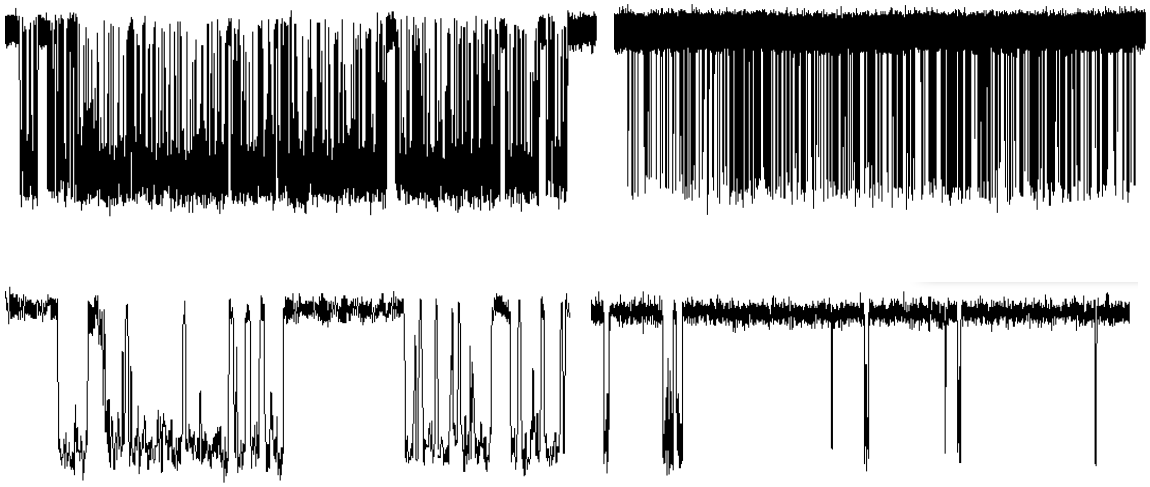

Figure 4.3. Single-channel recording of $(\alpha 1)_2\beta 1\gamma\delta$ and $(\alpha 1_{W149F1W})_2\beta 1\gamma\delta$. In each case, ACh is applied in the pipette at 300 μM. Upper traces show several seconds of data of $(\alpha 1)_2\beta 1\gamma\delta$ (at left) and $(\alpha 1_{W149F1W})_2\beta 1\gamma\delta$ (at right), while lower traces show ~ 100 ms. Less activation of the $(\alpha 1_{W149F1W})_2\beta 1\gamma\delta$ is qualitatively evident. The channel open currents were 5–6 pA at an applied pipette potential of + 100 mV.

The primary impact of the fluorination effect that we observed was a sevenfold decrease in apparent agonist binding rate (k_1) using acetylcholine as the agonist (**Figure 4.4**). The channel opening rate, β, was not significantly impacted by fluorination of TrpB (40,000 s^{-1} versus 45,000 s^{-1} for wild type at 300 μM ACh). However, the ability of the experiment to resolve rate constants that are fast (> ~40,000 s^{-1}) was in question—if fluorination was decreasing β, we might not be able to see this effect. Indeed, the channel opening rate of ACh has been much discussed, and is usually estimated at 60,000 s^{-1}, or even faster(*14, 15*).

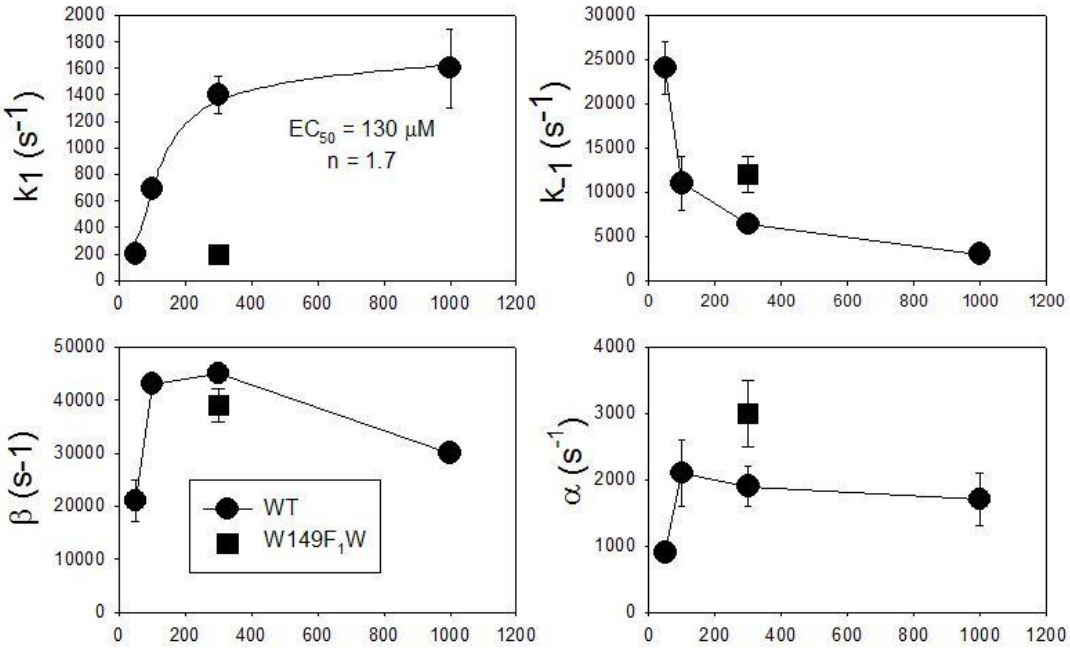

Figure 4.4. Measured rate constants for the WT ($(\alpha 1_{W149F1W})_2\beta 1\gamma\delta$; filled circles) and $(\alpha 1_{W149F1W})_2\beta 1\gamma\delta$ (filled squares). Data for the mutant was obtained at a single concentration (300 µM ACh). In each of the four graphs, rates (y-axis) are given in s^{-1} and concentrations (x-axis) are given in µM ACh.

Summary of rate constants		
	$\alpha_2\beta\gamma\delta$	$(\alpha_{W149F1W})_2\beta\gamma\delta$
β	34,000 s^{-1}	39,000 s^{-1}
α	1,700 s^{-1}	2,800 s^{-1}
k_+	4 $\mu M^{-1}s^{-1}$	0.7 $\mu M^{-1}s^{-1}$
k_-	10,000 s^{-1}	12,000 s^{-1}

Table 4.1. A table summarizing the rate constants from the previous figure. By far the largest change is in k_+, the association rate of the agonist with the receptor.

4.2.2 The L9'S Mutation

In the wild type receptor from the previous section ($(\alpha 1)_2\beta 1\gamma\delta$), a mutation in the channel pore at β1L9'S has been widely studied(*16–19*). In the nAChR,

the highly conserved M2 channel pore lining helix (dark gray in **Figure 4.1**) is often numbered starting with 1' at the cytoplasmic end. Thus, the 9' location is roughly in the middle of the membrane. When mutations are made to more hydrophilic residues, such as Leu→Ser, the receptor becomes much more sensitive to agonist and the EC_{50} decreases. This has proven useful in many experiments that probe mutations that otherwise increase EC_{50}. Thus, in the experiments in the previous section, recording on the $(\alpha1_{W149F1W})_2\beta1\gamma\delta$ receptor at concentrations significantly above EC_{50} was not possible due to the fact that channel block prevented reliable current sizes and events. For example, **Figure 4.5** is a single-channel trace of the $(\alpha1)_2\beta1L9'S\gamma\delta$ channel at its EC_{50} of 1.2 μM ACh. This mutation—and in some cases multiple L9' mutations, which have been shown to have a cumulative effect(*18*)—are used in several studies in this chapter as well as the next chapter.

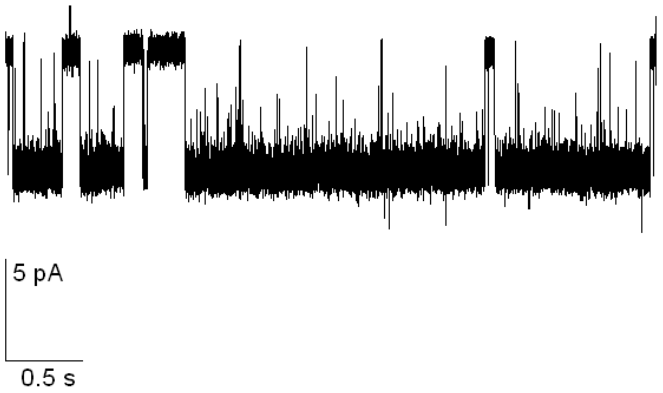

Figure 4.5. Single-channel record of $(\alpha1)_2\beta1L9'S\gamma\delta$. Openings are shown as downward deflections. This recording was at a pipette potential of +100 mV and 1.2 μM ACh, which is the macroscopic EC_{50} for this receptor.

4.2.3 Single-Channel Recording on $(\alpha1)_2\beta1L9'S\gamma\delta L9'S$ at 300 μM TMA

Given that we could not be sure that the channel opening rate was

completely resolved, we sought a system with a significantly lower channel opening rate, preferably no larger than 5,000 s^{-1}-10,000 s^{-1}, so that this rate would be within the resolution of our single-channel rig. One such partial agonist, which also displays a cation-π interaction with TrpB is tetramethylammonium (TMA)(*20*). The kinetic parameters for activation of $(\alpha1)_2\beta1\gamma\delta$ by TMA have been previously reported(*21*): $\beta = 3023\ s^{-1}$ and $\alpha > 150\ s^{-1}$ ($\Theta = \beta/\alpha = \sim 20$). The EC_{50} is 868 μM, so P_{open} doesn't saturate until several mM TMA. Thus, the right shift (increase) in EC_{50}, which the introduction of the fluorinated tryptophans we wish to study would cause, may make the concentrations of TMA required untenably large. Thus, we chose a specific pair of pore mutations that have been previously characterized with TMA and the fluorinated tryptophan series: Leu→Ser at β9' and δ9'. Since the impact of 9' mutations (Leu→Ser) is hypothesized to be an increase the in channel open time (i.e., a decrease in the channel closing rate)(*16, 22*), combining them should result in clusters of the channel being predominantly open, punctuated with brief closures. These should be of an easily resolvable average duration: $1/(3023\ s^{-1}) = 330\ \mu s$). The EC_{50} of TMA on $(\alpha1)_2\beta1L9'S\gamma\delta L9'S$ was reported as 48 μM(*20*). Thus, we chose an initial concentration of TMA well above this (300 μM) for our single-channel experiments (**Figures 4.6 and 4.7**).

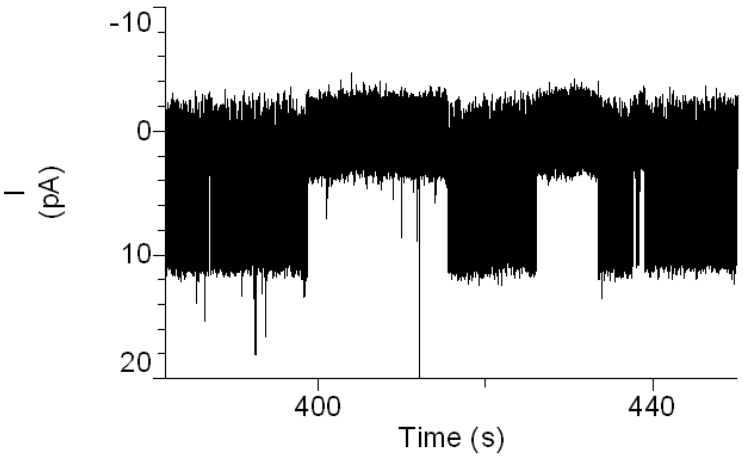

Figure 4.6. Approximately 1 minute of single-channel activity of $(\alpha 1)_2\beta 1L9'S\gamma\delta L9'S$ with 300 μM TMA in the pipette. Unlike other traces in this chapter, this is shown at full bandwidth (cut-off frequency, f_c, of 20 kHz).

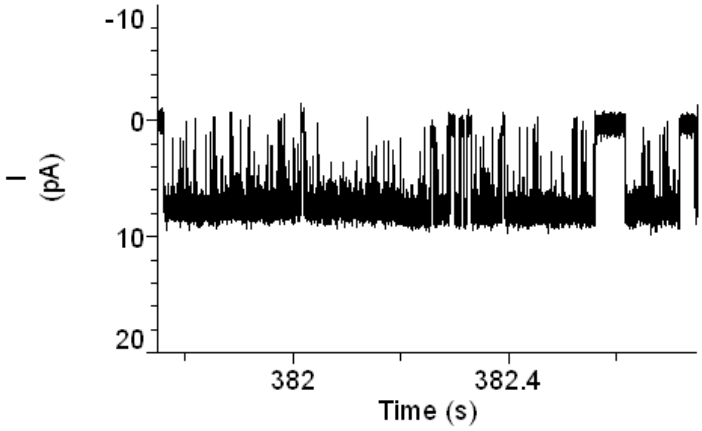

Figure 4.7. One second of single-channel activity of $(\alpha 1)_2\beta 1L9'S\gamma\delta L9'S$ with 300 μM TMA in the pipette. Shown at f_c = 5 kHz.

As expected for a concentration above the previously reported macroscopic EC_{50}, the channel is mostly open. Many brief channel closures (< 100 μs), several less brief closures (~ 10 ms), and 2 long closures (> 30 ms) are visible. Now, using the clean-up procedure described in **Appendix B**, we

replace sections of data that were poorly idealized with baseline, as in **Figure 4.8**.

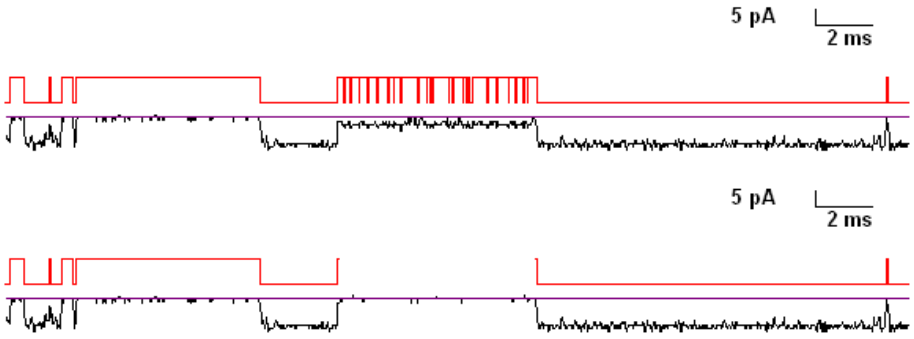

Figure 4.8. A 30 ms section of $(\alpha 1)_2\beta 1L9'S1\gamma\delta L9'S$ at 300 μM TMA. The data (black) and corresponding detected events (red) are shown before (upper) and after (lower) clean up. In both cases, channel openings are shown as downward deflections. In the upper trace there is clearly a region of many misdetected brief openings.

On the other hand, some segments have brief openings from the closed state. These appear well resolved, and are left unaltered for the analysis—as in the two brief openings in **Figure 4.9**.

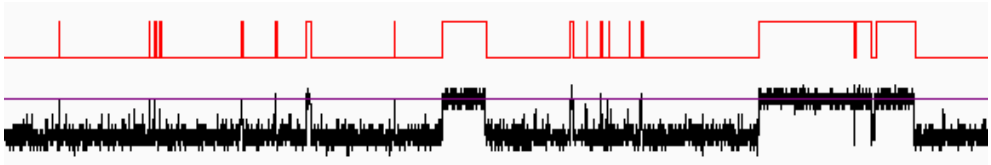

Figure 4.9. A 160 ms section of $(\alpha 1)_2\beta 1L9'S\gamma\delta L9'S$ at 300 μM TMA. Channel openings are shown as downward deflections. Two brief openings from the longer of the two closed states (right) are evident.

We then define clusters as being delimited by closed states longer than 100 ms (i.e., 100 ms is the critical time, τ_{crit}, for cluster duration); if the channel is closed for longer than this amount of time, then it is likely in a desensitized state. Additionally, clusters were required to exhibit at least 8 events: 4 cycles of

opening and closing. This clean-up and cluster definition yielded a record of 12,584 events when a dead time, τ_d, of 20 μs was imposed. As discussed in **Appendix B**, the number of states in each class was determined by adding states (closed states first) until the LL reached a plateau (**Table 4.1**).

# of closed states	LL	ΔLL
1	56107.22	NA
2	75945.95	19838.73
3	76339.57	393.62
4	76388.21	48.64
5	76646.14	257.93

Table 4.2. Variation of LL with number of closed states. LL increases as the number states (in this case, closed states) are added to a model. The increase between 4 and 5 states is discussed in the text.

The large increase upon addition of a fifth state (red) is not physically meaningful. This highlights an important admonition in building kinetic models from single-channel data—the statistical fits (maximizations of the log likelihood) must be viewed critically. In the case of adding a fifth closed state above, the resultant rates (and histogram when fitted to the corresponding number of components, below (**Figure 4.10**)) have no basis in the observed data. In particular, one component (corresponding to a rate constant of > 100,000 s^{-1}, the channel opening rate), is grossly exaggerated (see histogram). In addition to the use of the histogram to eliminate models such as the one with 5 closed states, I demonstrated that the aberrant LL value was specifically caused by the mis-estimation of the channel opening rate. When I fixed the channel opening rate constant at 22,000 s^{-1}, the LL increased only slightly (~ twofold) when a fifth closed state was added.

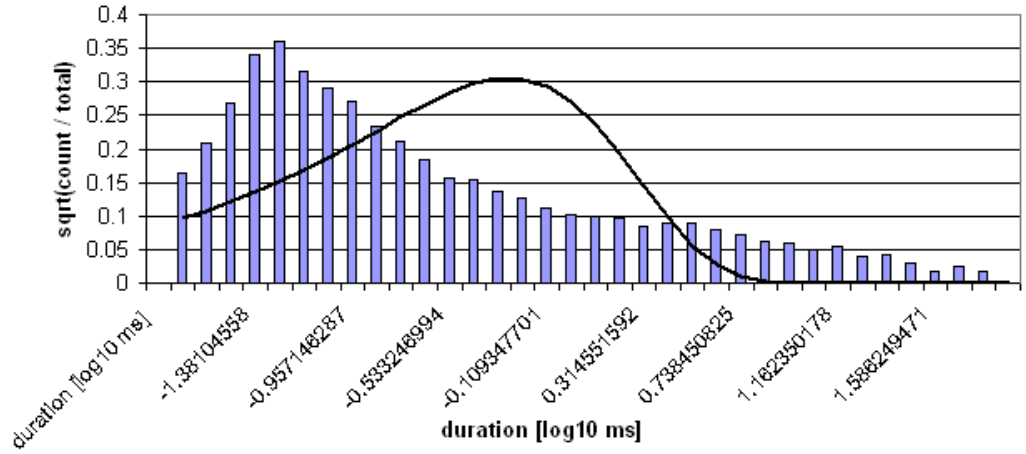
sqrt(count / total)
0.4
0.35
0.3
0.25
0.2
0.15
0.1
0.05
0
duration [log10 ms]
-1.381045581
-0.957146287
-0.533246994
-0.109347701
0.3145515921
0.7384508251
1.1623501781
1.5862494711
duration [log10 ms]

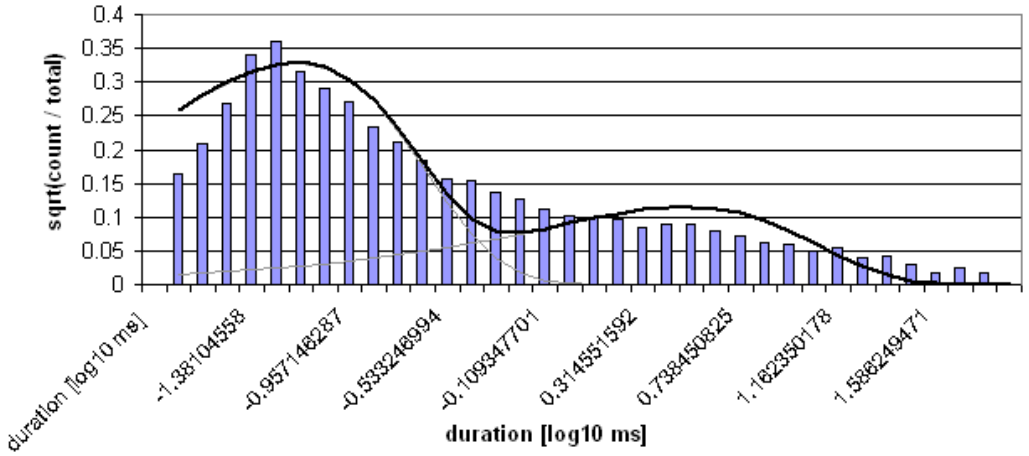
sqrt(count / total)
0.4
0.35
0.3
0.25
0.2
0.15
0.1
0.05
0
duration [log10 ms]
-1.381045581
-0.957146287
-0.533246994
-0.109347701
0.3145515921
0.7384508251
1.1623501781
1.5862494711
duration [log10 ms]

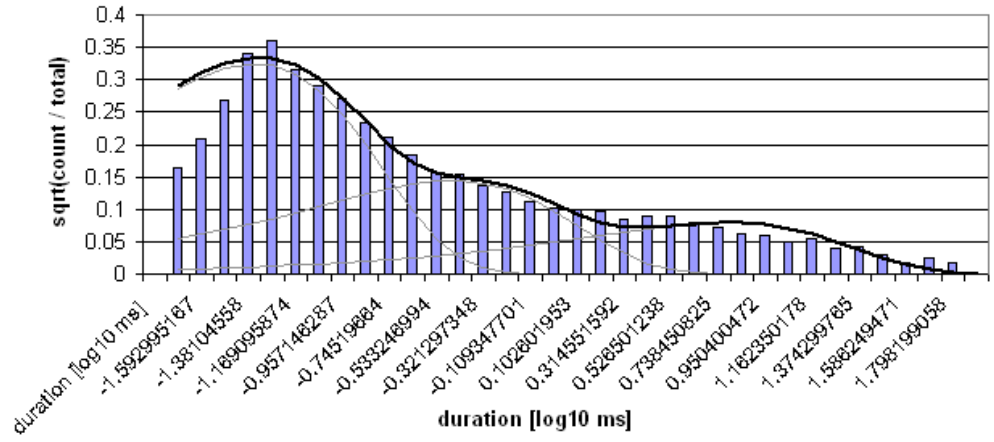
sqrt(count / total)
0.4
0.35
0.3
0.25
0.2
0.15
0.1
0.05
0
duration [log10 ms]
-1.592995167
-1.381045581
-1.169095374
-0.957146287
-0.745196994
-0.533246994
-0.321297348
-0.109347701
0.1026019531
0.3145515921
0.5265012381
0.7384508251
0.9504004721
1.1623501781
1.3742997651
1.5862494711
1.7981990581
duration [log10 ms]

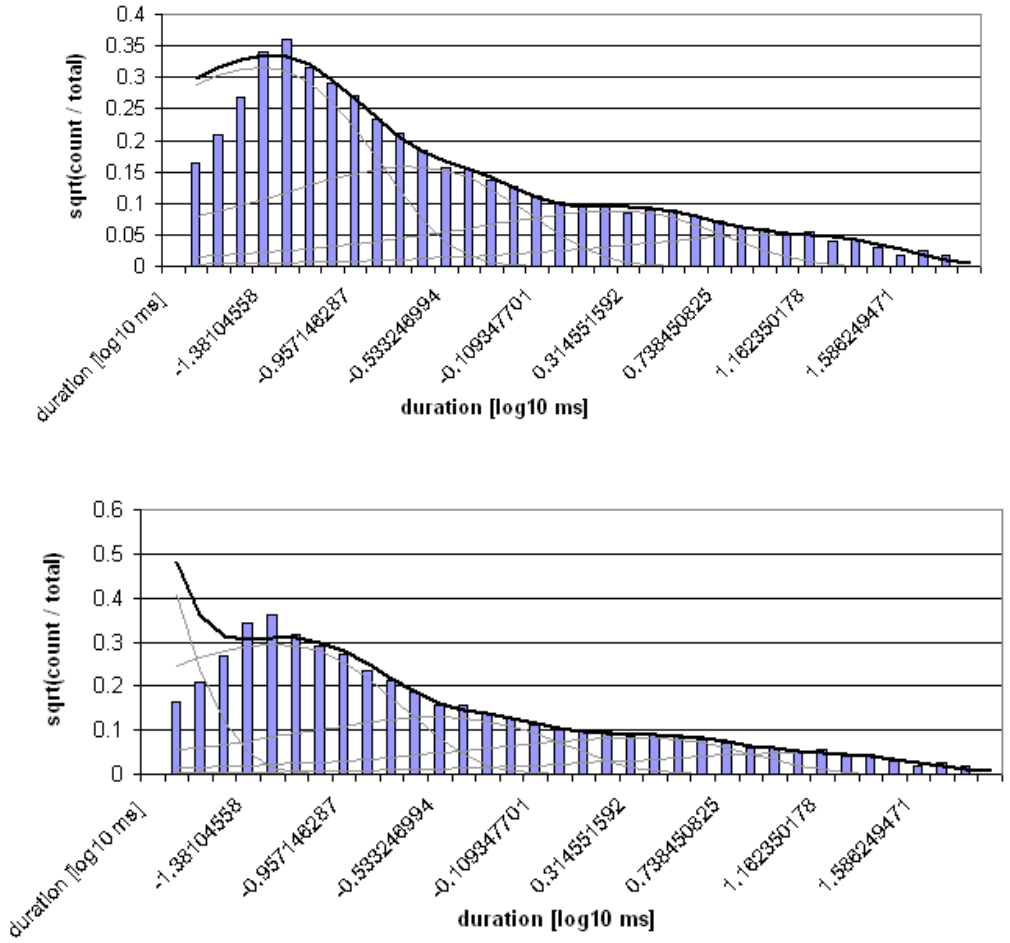

Figure 4.10. Closed dwell time histograms with successively additional components from QuB. 5 different fits are shown. From top (previous page) to bottom: 1, 2, 3, 4, and 5 components. When more than one component is shown, the dark black line is the sum of the components and a light gray line shows the specific contribution of each component. These 5 histograms correspond to the LL values given in Table 4.1.

The number of open states was determined in a similar manner, but was more straightforward, as there was only one component in the open histogram (**Table 4.2**).

# of open states	LL	ΔLL
1	76388.21	NA
2	75909.54	-478.67

Table 4.3. Variation of LL with number of open states. LL *decreases* upon the addition of a second open state. There is clearly only one open state.

The final model should thus have 4 closed states (black) and 1 open state (red), as shown in **Model 4.2**.

Figure 4.11. Model 4.2, a 5 state model of the nAChR. Each number above or below a line corresponds to a rate (units: s^{-1}) for the corresponding forward or reverse transition. The numbering of the states corresponds to the order that they were input into QuB. One possible physical interpretation of this data is that the first two steps (4→3 and 3→1) are binding steps, 1→2 is the gating step, and 2→5 is desensitization.

In order to verify the validity of this model (beyond the use of statistics and fits to histograms), we simulate data, with the final model above as input in QuB. The result (**Figure 4.12**) is compared qualitatively to what actual data looked like (**see Figure 4.9, above**). Indeed, the simulated data are quite similar to the original, another piece of support that this model fits the observed data.

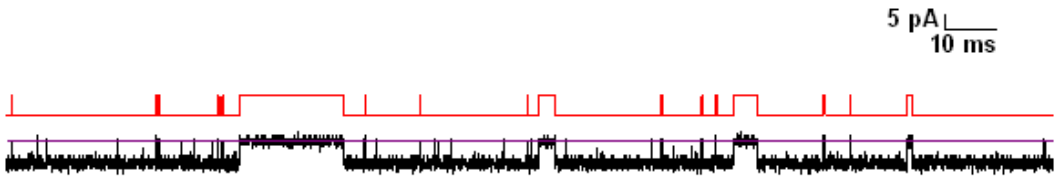

Figure 4.12. A 160 ms section of simulated data based on the final TMA model 2, above. Channel openings are shown as downward deflections.

The rate constant in this final model that corresponds to the channel opening rate (β) is from state 1→2 and is 22,700 s^{-1}, nearly eightfold higher than

expected (3,023 s^{-1}). Although we have not collected data with TMA on $(\alpha1)_2\beta1\gamma\delta$, compared to previous studies' findings(*20*), we see that the β9', δ9' mutant seems to have significantly increased the channel opening rate. Based on the gating rates in the above mechanism, β = 22,700 s^{-1} and α = 260 s^{-1}. Thus P_{open} = 22,700 s^{-1}/(22,700 s^{-1} + 260 s^{-1}) = 0.989 and Θ = β/α = 87.

Comparing our P_{open} to the previously reported value of P_{open} for $(\alpha1)_2\beta1\gamma\delta$ (0.886)(*21*) we find that TMA on $(\alpha1)_2\beta1L9'S\gamma\delta L9'S$ has a high open probability. Indeed, as the value of Θ = 87 indicates, TMA acts essentially as a full agonist on $(\alpha1)_2\beta1L9'S\gamma\delta L9'S$.

Unfortunately, this value for the channel opening rate is still near the resolution of our single-channel rig (see Chapter 2). Thus, we may still not be completely resolving this rate constant. Consequently, we sought an agonist with an even lower opening rate constant. Choline is a nAChR partial agonist with reported β = 50 s^{-1}, α = 1400 s^{-1}, and Θ = 0.035 (for the adult mouse muscle type, $(\alpha1)_2\beta\varepsilon\delta$(*23*)).

4.2.4 Initial Single-Channel Recording on $(\alpha1_{W149F1W})_2\beta1L9'S\gamma\delta L9'S$ at 2.0 mM Choline

I have obtained a single patch with data from $(\alpha1_{W149F1W})_2\beta1L9'S\gamma\delta L9'S$ at 2.0 mM choline and recorded at multiple pipette potentials (**Figure 4.13**).

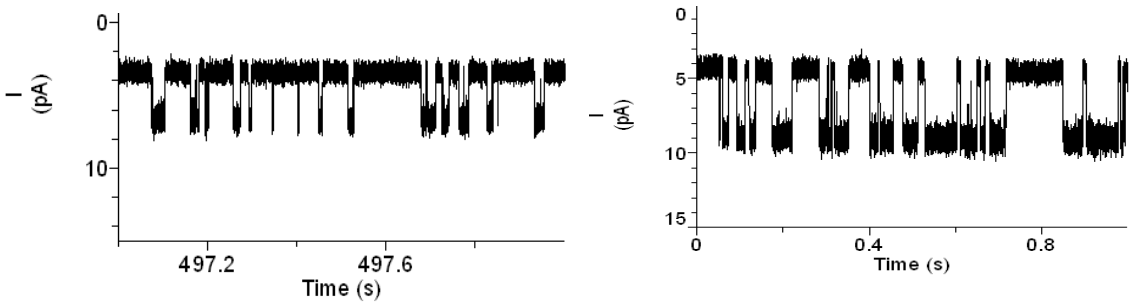

Figure 4.13. $(\alpha 1_{W149F1W})_2\beta 1L9'S\gamma\delta L9'S$ single-channel activity at 2.0 mM choline. Each trace is 1 second of channel events at f_c = 5 kHz. Left: Pipette potential of +50 mV. Right: Same patch at a pipette potential of +70 mV

Note that increasing the pipette potential (HP) from +50 mV to +70 mV creates a noticeable increase in the both the open channel current and the baseline (leak current). From this information (as well as the current at HP = + 30 mV (results not shown)) we have **Table 4.4**.

HP (+) in mV	Channel I (pA)
30	2.5
50	3.8
70	4.5

Table 4.4. The variation of open channel current amplitude with varying applied pipette potentials applied to $(\alpha 1_{W149F1W})_2\beta 1L9'S\gamma\delta L9'S$ with 2.0 mM choline

A plot of the current-voltage relationship (I-V) is shown in **Figure 4.14**. This line has R^2 = 0.971 and slope = 0.05 pA/mV = 50 pS. This is the slope conductance. The reversal potential was -22 mV, a result that warranted further consideration since, based on the solutions we are using (see Materials and Methods, Chapter 2), we expect a reversal potential of 0 mV. Indeed, other single-channel experiments across positive and negative pipette potentials (Chapter 6) as well as whole-cell measurements of the reversal potential of

devitellinized oocytes (Chapter 2) indicate that for the recording solutions used throughout my thesis, the single-channel reversal potentials for nAChRs are ~ 0 mV. The low reversal potential estimated for this patch was probably due to the fact that no rectification behavior could be estimated since recordings were only performed at positive pipette potentials.

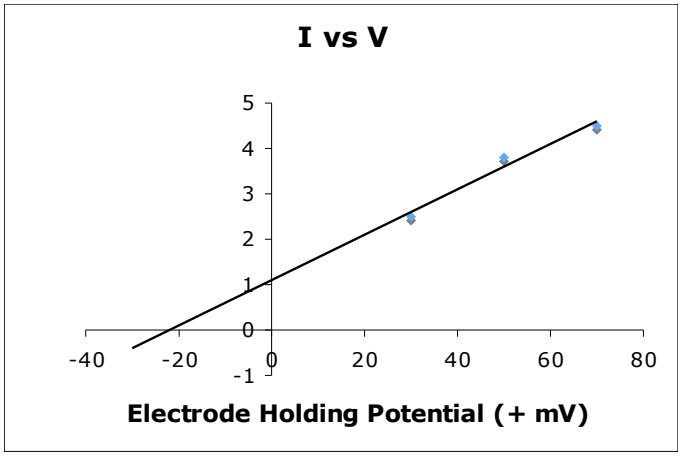

Figure 4.14. An I-V plot of the data in Table 4.4. The black line (linear regression) was extrapolated to negative pipette potentials in order to estimate the reversal potential.

4.2.5 Single-Channel Recording on $(\alpha 1)_2\beta 1L9'S\gamma\delta L9'S$ Using 5 mM Choline

Figure 4.15, Upper shows data from a gigaseal that lasted just over an hour. In this case, 5 mM choline was applied in the pipette to $\alpha 1_2\beta L9'S9'\gamma\delta L9'S$ and there was significant channel activity during the entire record. Interestingly, the macroscopic phenomenon of desensitization (state 5 of **Model 2**) seems to manifest itself here at the single-channel level—the number of active channels decreases until, at the end, only a single channel is active (though presumably the other channels are still in the patch, and ligand bound). It is worth keeping in

mind that over the course of this file, over 180,000,000 samples were taken (the sampling frequency was 50 kHz). A one second section of data at the end of the recording is shown (**Figure 4.15, Lower**).

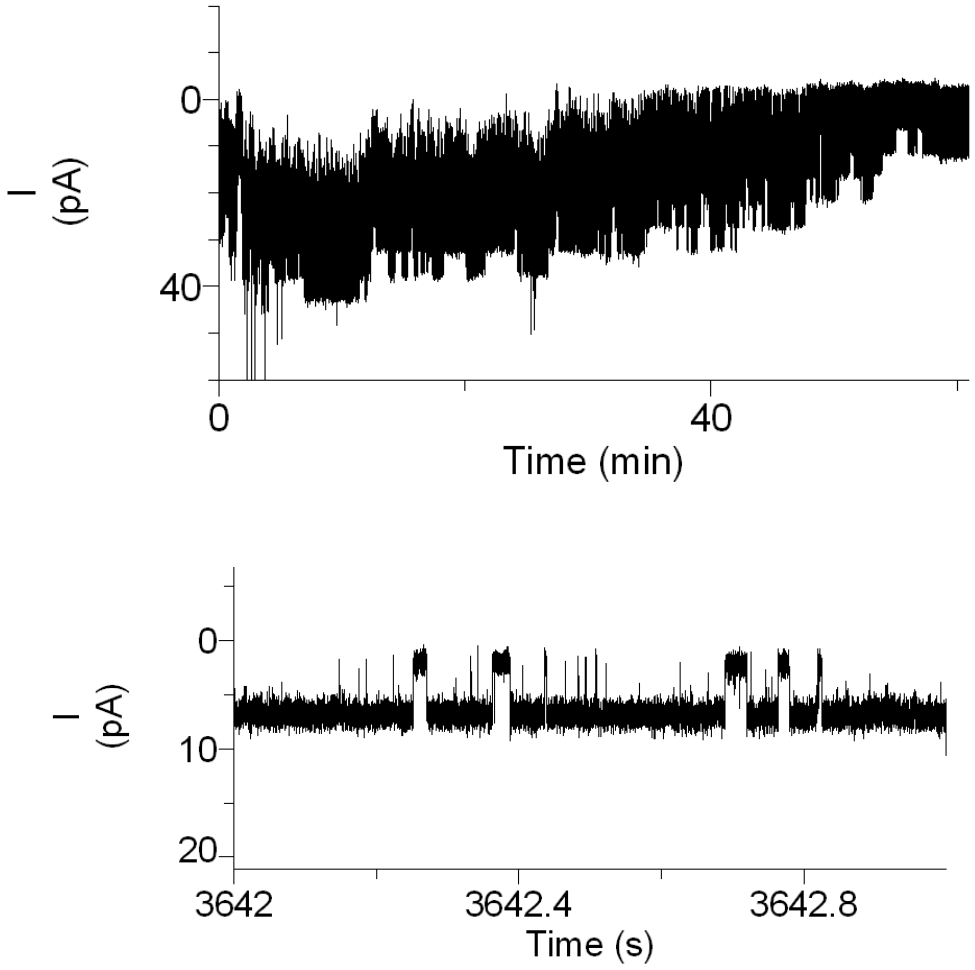

Figure 4.15. Single-channel recording of $(\alpha 1)_2\beta 1L9'S9'\gamma\delta L9'S$ at 5 mM choline. Recordings were performed at a pipette potential of +70 mV. Upper: > 1 hour of recording. Lower: 1 second of data showing that the channel is mostly open, but has some brief closures

An all points histogram can be used to evaluate the number of active channels in a patch as well as their relative conductances (**Figure 4.16**).

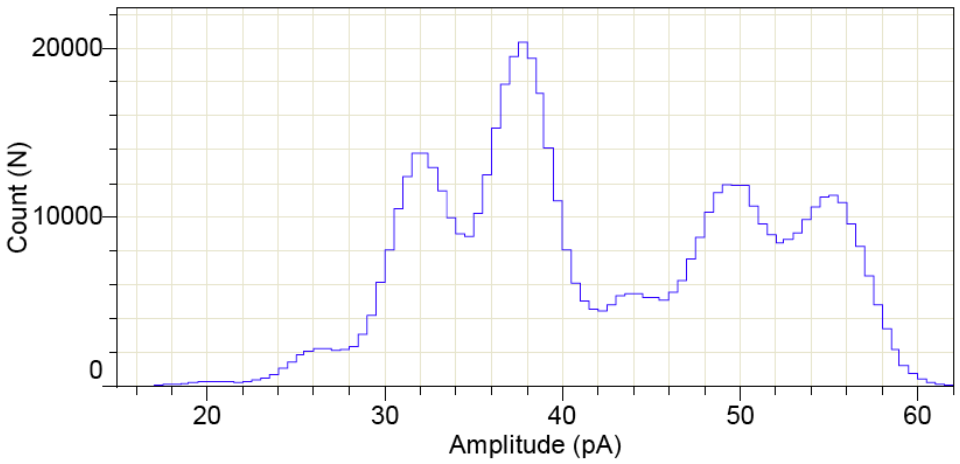

Figure 4.16. An all points histogram for a single-channel recording with multiple simultaneously active channels. When the component at ~ 20 pA is included (the effective baseline in this case) 7 components are visible, corresponding to at least 6 different open channels.

This choline data appear to still have some brief closures like the ACh and TMA data shown above, but those closures are generally of longer durration. Thus, we expect the channel opening rate to be slower than the 22,000 s^{-1} for TMA. A three-state model fit to a small portion of data with 5 mM choline indicates that β ~ 3,000 s^{-1}. However, it does not appear that 5 mM choline was a high enough concentration to saturate the binding equilibrium. In this case, this measurement of β is actually the apparent channel opening rate, β'. Higher concentrations of choline will be needed in order to accurately measure β (such as the concentration dependent data shown in **Figure 4.4**). However, these higher concentrations of choline cause increasing levels of open channel block that will convolute analysis and themselves introduce further brief closures.

In summary, I have performed single-channel recording with multiple agonists on $(\alpha1)_2\beta1L9'S\gamma\delta L9'S$ and $(\alpha1_{W149F1W})_2\beta1L9'S\gamma\delta L9'S$. The ultimate goal

of this project is to develop a model for receptor activation of a wild type nAChR and compare this to rates that we measure for the receptor when a fluorinated tryptophan is substituted by nonsense suppression at TrpB. Since accurate measurement of β proved difficult, we ultimately picked a different nAChR to characterize. In the next chapter (5), I will present single-channel data for the neuronal α4β2 receptor that, in combination with whole-cell data, establish a cation-π interaction to TrpB of that receptor. Those experiments are performed with the highly relevant agonists nicotine and a smoking cessation drug, Chantix® (varenicline).

If further experiments on the muscle-type nAChR are desired in which the channel opening rate (β) can be resolved, the TMA data I've gathered thus far on $(\alpha1)_2\beta1L9'S\gamma\delta L9'S$ suggest another system that might work. The channel opening rate increased ~ eightfold relative to previously reported channel opening rates with TMA on $(\alpha1)_2\beta\gamma\delta$. Thus, since choline is probably not viable without further receptor perturbations, the channel opening rate for TMA on $(\alpha1)_2\beta1\gamma\delta$ could be measured. If it is ~ 3,000 s^{-1}, as has been previously reported, then perhaps using TMA with a single 9' mutation (either βL9'S or δL9'S) will produce a sufficiently low EC_{50}, while still reducing the channel opening rate (relative to ACh) to a resolvable rate (< 10,000 s^{-1}).

The use of the epsilon subunit (in place of gamma) in future studies offers two distinct advantages: (1) it produces receptors with a larger single-channel conductance, which increases SNR, and (2) it produces receptors with nearly equivalent binding sites, which should simplify the kinetic analyses. It was

therefore characterized at the whole-cell and single-channel levels with ACh.

4.2.6 Whole-Cell Characterization of $(\alpha1)_2\beta1\varepsilon\delta$

I have performed whole-cell characterizations of the mouse adult nAChR ($(\alpha1)_2\beta1\varepsilon\delta$) (**Figures 4.17 and 4.18**).

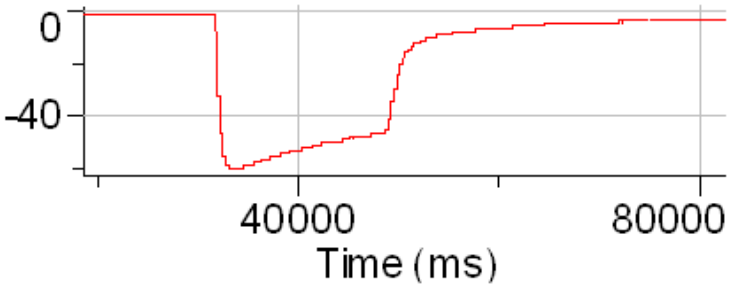

Figure 4.17. Sample opus trace on the receptor $(\alpha1)_2\beta1\varepsilon\delta$. At 215 μM ACh (above the EC_{50} of 70 μM; see next figure), significant whole-cell currents are observed, 60 μA in this case (y axis). Also, a moderate amount of whole-cell desensitization is evident.

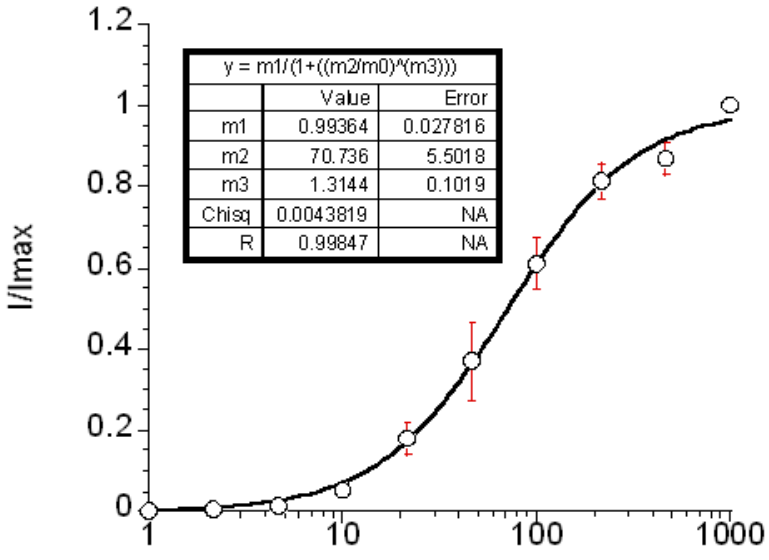

Figure 4.18. Whole-cell dose response curve for $(\alpha1)_2\beta1\varepsilon\delta$. The x-axis is concentration of agonist (ACh). The EC_{50} (70 μM ACh, m2) and Hill coefficient (1.3, m3) are given in the inset.

4.2.7 Single-Channel Characterization of $(\alpha 1)_2\beta 1\varepsilon\delta$ (with Bruce Cohen)

The mouse adult receptor ($(\alpha 1)_2\beta 1\varepsilon\delta$) was also characterized by single-channel recording (**Figure 4.19, and 4.20, Right**). Like the fetal receptor (**Figure 4.19, and 4.20, Left**), it exhibited some channel block at 300 µM ACh that manifest as a combination of brief closures and a reduction in single-channel conductance.

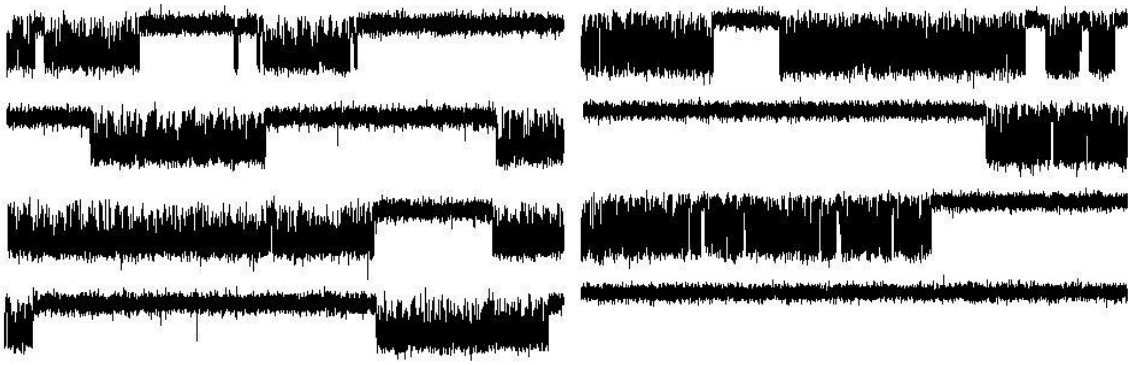

Figure 4.19. Single-channel recording of nAChRs at 300 µM ACh. The applied pipette potential was + 100 mV in each case and 8 seconds of data (2 seconds per line) are shown for each at f_c = 2 kHz. Left: $(\alpha 1)_2\beta 1\gamma\delta$. Right: $(\alpha 1)_2\beta 1\varepsilon\delta$

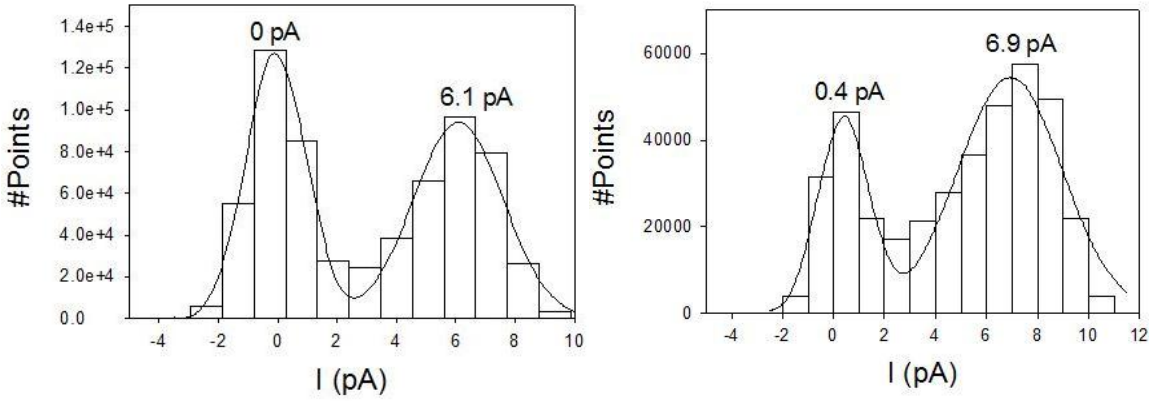

Figure 4.20. All points histograms of the data points corresponding to the single-channel data shown in the previous figure. The corresponding chord conductances are 61 pS ($(\alpha 1)_2\beta 1\gamma\delta$) and 65 pS ($(\alpha 1)_2\beta 1\varepsilon\delta$). This increase in conductance for $(\alpha 1)_2\beta 1\varepsilon\delta$ is less than expected, perhaps due to increased channel block.

More detailed kinetic analysis of the $(\alpha1)_2\beta1\varepsilon\delta$ receptor was performed using QuB; the results are presented in **Figure 4.21**. These kinetics should be considered in light of the fact that they were performed for data at a single concentration (300 µM ACh). Ideally a minimum of 3 concentrations are used and fitted simultaneously (see next section).

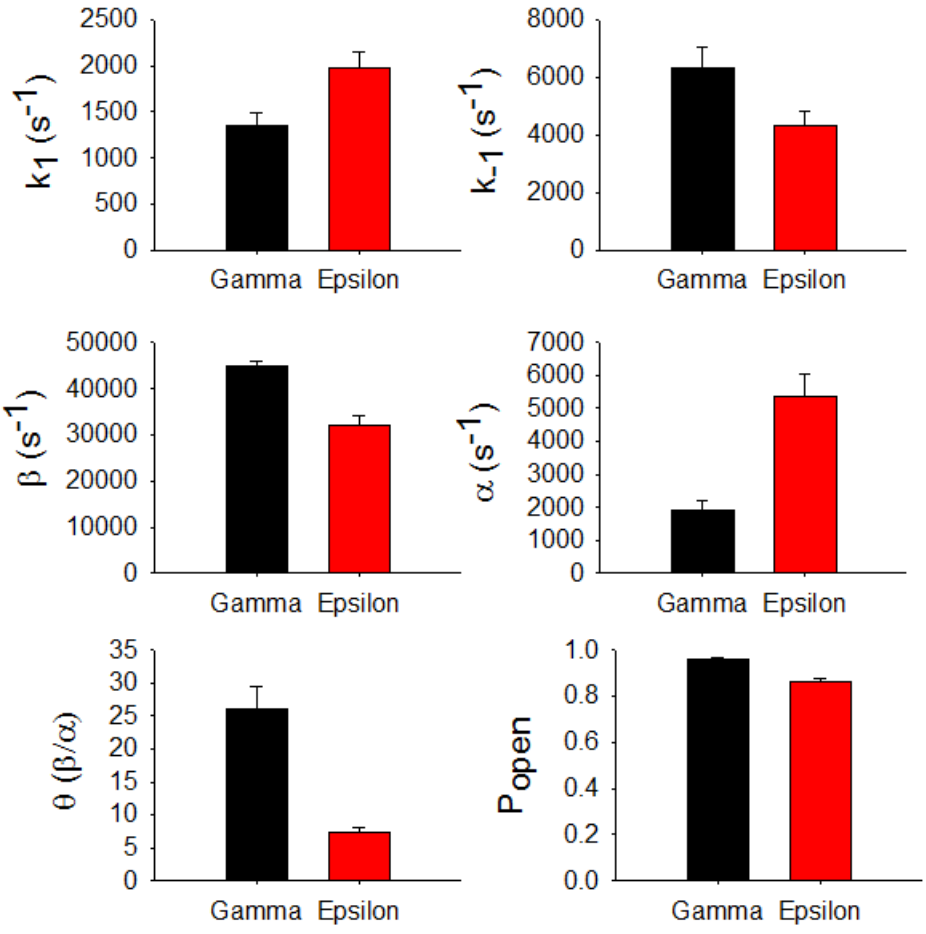

Figure 4.21. Summary comparison of rate constants, Θ, and P_{open} for the $((\alpha1)_2\beta1\gamma\delta)$ (black) and $((\alpha1)_2\beta1\varepsilon\delta)$ (red) receptors. The relationship between Θ and P_{open} for full agonists is highlighted by the fact that a significant reduction in Θ for the full agonist ACh only produces a small decrease in P_{open}. The relationship is different for partial agonists, especially for Θ < 1. In the case of the epsilon-containing receptor, the main difference that these kinetic studies revealed was an increase in the channel closing rate, α. This change was also largely responsible for the decrease in Θ.

4.2.8 Progress Towards a Kinetic Model for $(\alpha 1)_2\beta 1L9'S\gamma D174N\delta D180N$

We were interested in producing a kinetic model for $(\alpha 1)_2\beta 1L9'S\gamma D174N\delta D180N$ for reasons covered in detail in Chapter 3. Briefly, it is one of a few receptors that exhibit a significant coupling between the channel pore mutation (βL9'S) and the extracellular domain mutations in the complementary subunits ($\gamma D174N\delta D180N$). Single-channel data were recorded at EC_{50} (160 μM ACh) as well as 500 μM ACh and 2000 μM ACh (**Figure 4.22**).

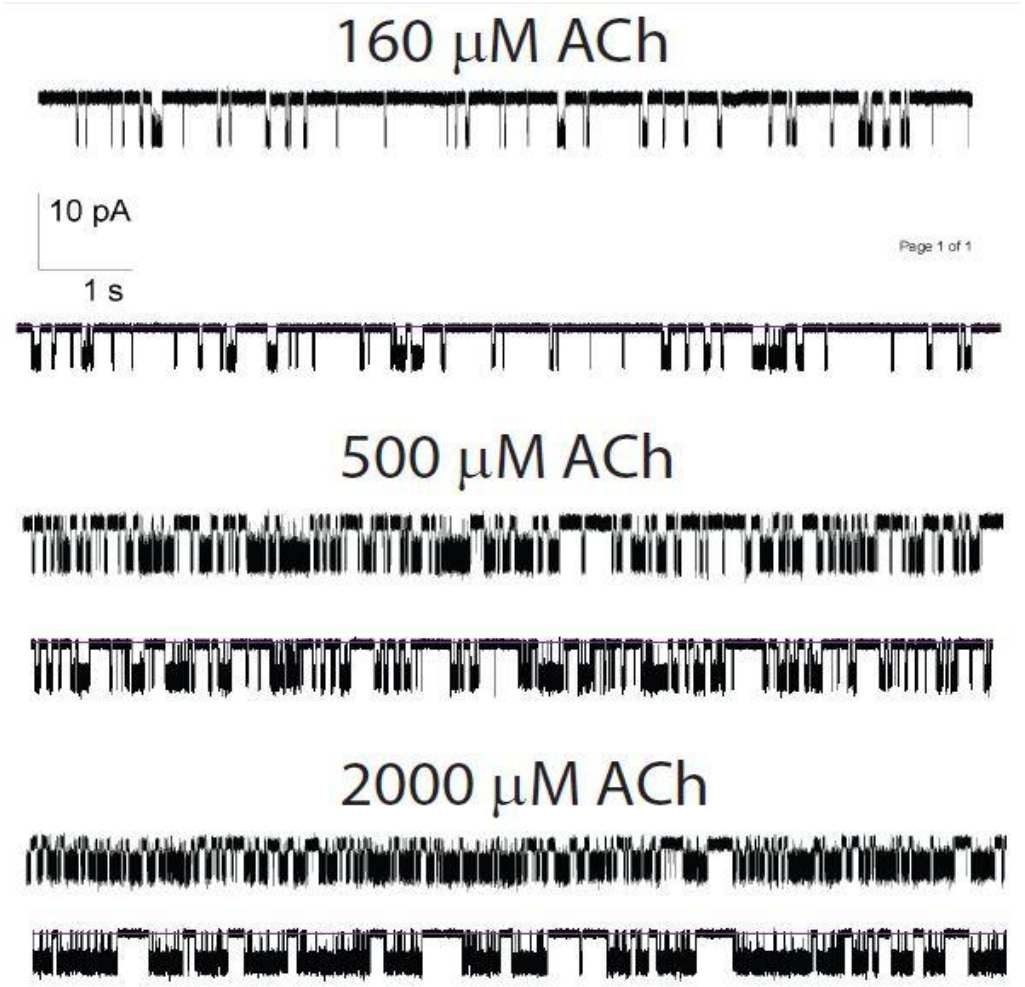

Figure 4.22. 3 pairs of single-channel traces for ACh activation of $(\alpha 1)_2\beta 1L9'S\gamma D174N\delta D180N$ at indicated concentrations. In each pair, the upper trace is the actual data collected and the lower trace is simulated data based on the model. The scale bar in the top trace applies to all traces.

Based on the data collected across these 3 concentrations and the approach to data analysis outlined in Appendix B, a kinetic model was developed using QuB (**Model 4.3**). As suggested by **Model 4.1**, the models here were fixed so that the rate of 5→4 (first binding) was twice that of 4→1 (second binding) and 1→4 (second unbinding) was twice that of 4→5 (first unbinding). The extra closed state (3) was added to account for long closed periods that are

qualitatively evident in the traces in **Figure 4.22** and generally characteristic of nAChRs. This is the probably the desensitized state. The result was **Model 4.3**:

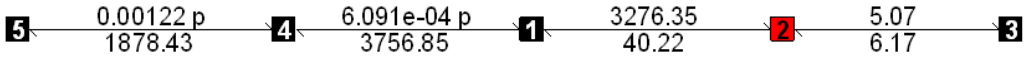

.

The simulated data in **Figure 4.22** were then refit to a 5 state model, producing the three models in **Figure 4.23.**

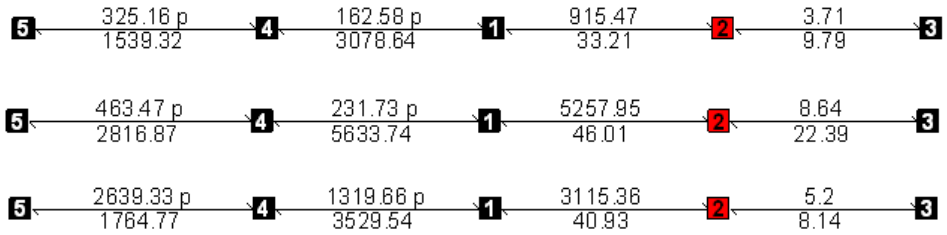

Figure 4.23. The 3 models for re-fitting simulated data at the concentrations given in Figure 4.22. Varying p values in the first two steps correspond to the different concentrations.

The combined qualitative agreement of the traces in **Figure 4.22** and the quantitative similarities of the rates for the models in **Figure 4.23** indicate that a reasonably stable model for these data has been obtained. These data are further in agreement with the fact that the γD174NδD180N mutation on its own drastically diminishes the channel's ability to gate, while βL9'S restores some of this (Chapter 3). Based on this single-channel data and QuB modeling, I estimate Θ for $(\alpha 1)_2\beta$L9'SγD174NδD180N to be ~ 10. The channel opening rate, β, is ~ 3000 s^{-1}, and this is the first receptor for which I can confidently report an estimate of β.

4.2.9 Agonist-Free Single-Channel Recording of $(\alpha 1)_2\beta 1L9'S\gamma\delta L9'S$

An alternative approach to learning about the impact of mutations, including pore domain mutations such as L9'S and L9'A, is to study the openings of the channels in the absence of agonist. The gating equilibrium constant (Θ) for these spontaneous openings in the wild type nAChR has been estimated at ~ 10^{-6}(*24, 25*). However many mutations, including L9'S, significantly increase Θ, making it feasible to study spontaneous openings of mutated nAChRs. **Figure 4.24** shows single-channel data for $(\alpha 1)_2\beta 1L9'S\gamma\delta L9'S$ and a corresponding open dwell time histogram is given in **Figure 4.25**.

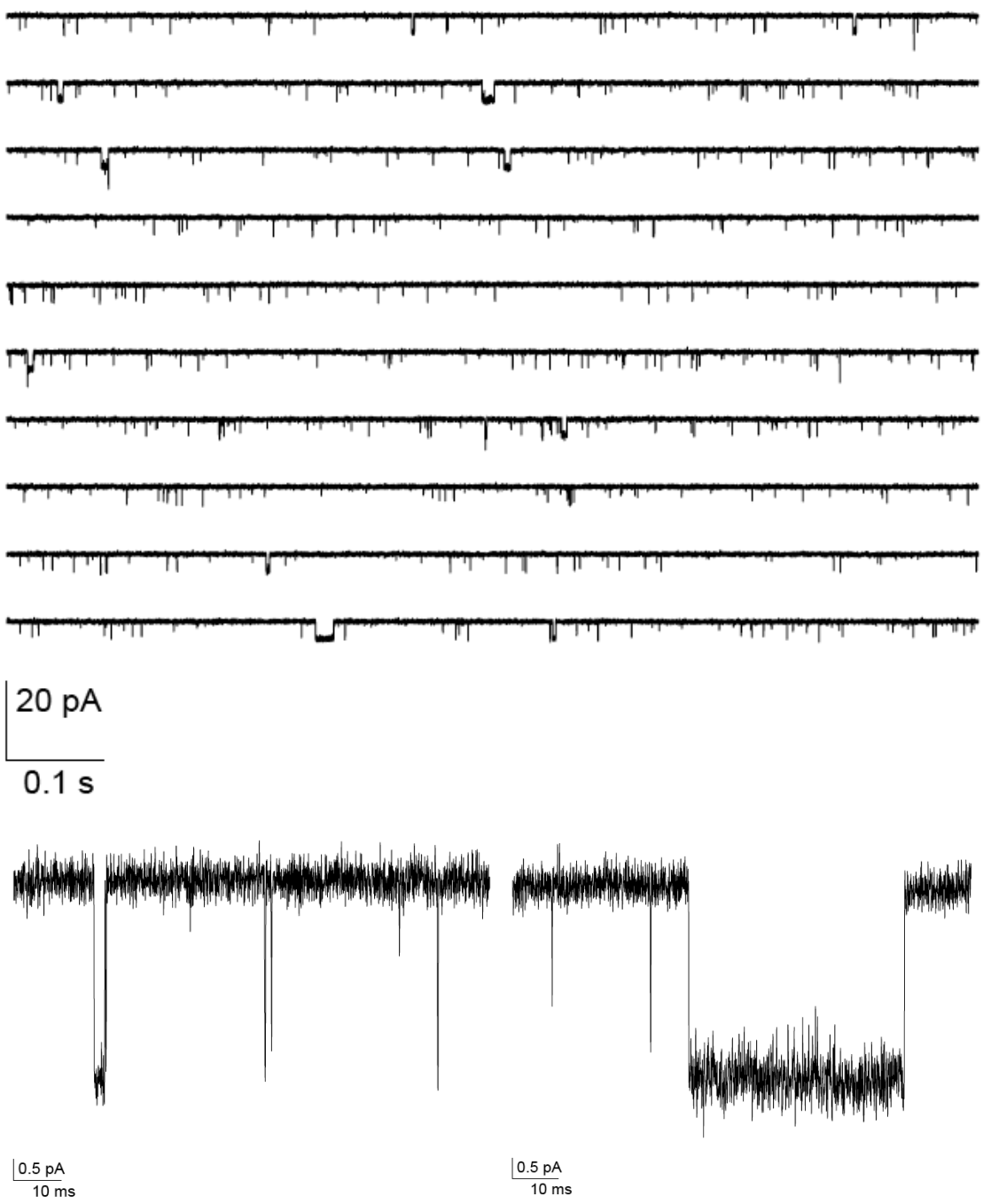

Figure 4.24. Single-channel records of $(\alpha 1)_2\beta 1L9'S\gamma\delta L9'S$ with no agonist applied. A special pipette holder that had never been exposed to agonist was used for these experiments. Upper: 10 seconds of spontaneous openings, 1 second per line. At least a few overlapping channel openings are present, so we know that there are multiple channels in this patch. Lower: examples of the three different open durations apparent in the single-channel data. Brief (~ 100 μs), intermediate (several ms), and long (> 10 ms). See the open dwell time histogram below.

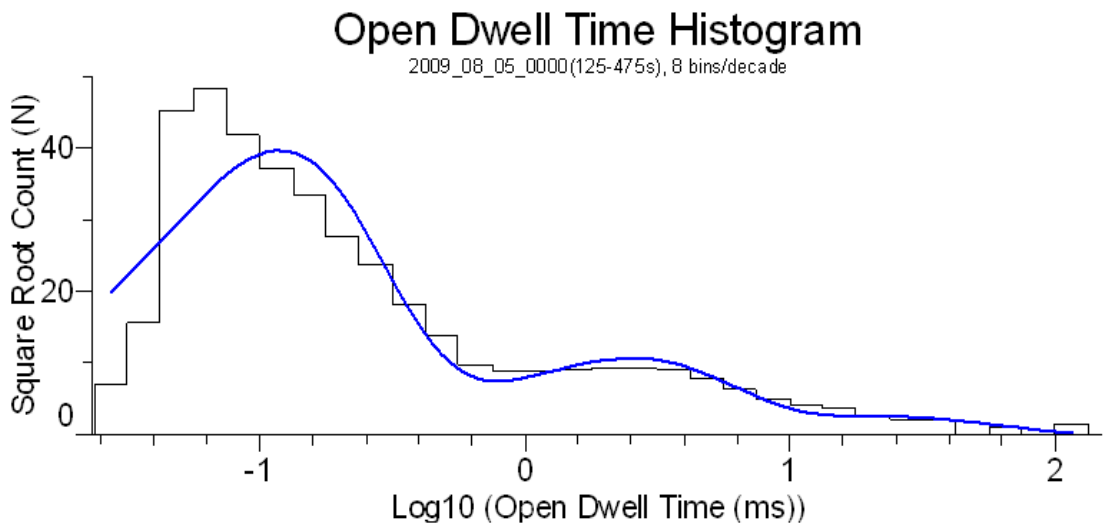

Figure 4.25. Open dwell time histogram of spontaneous openings of $(\alpha 1)_2\beta 1$L9'SγδL9'S. Over 10,000 events are represented in this histogram, which was fitted to 3 components. High resolution, qualitative examples of these openings are shown in the previous figure.

Given high whole-cell agonist-induced currents (20–50 μA), I expect multiple channels per patch. Indeed, **Figure 4.24** indicates that there are at least two channels in the patch analyzed here. While this has essentially no impact on analysis of the channel's open dwell time, multiple channels in a patch make a detailed analysis of the closed dwell times in terms of the kinetics of the receptor difficult. One or more component may be reduced by a factor of N, where N is the number of channels in the patch. Nevertheless, the following three-component fit of the closed dwell times suggests multiple distinct components (**Figure 4.26**).

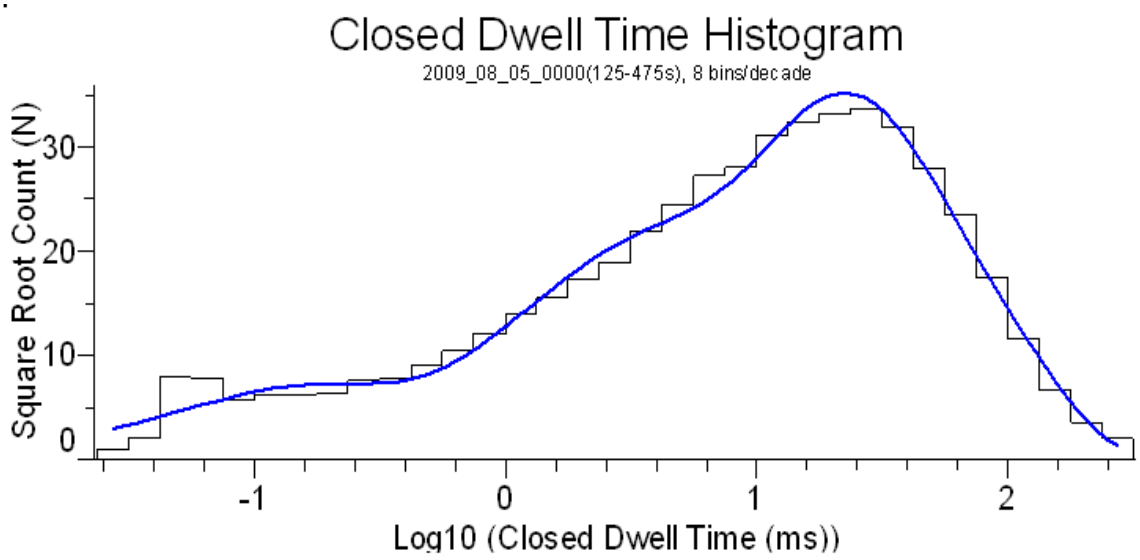

Figure 4.26. Closed dwell time histogram of spontaneous openings of $(\alpha 1)_2\beta 1L9'S\gamma\delta L9'S$. Over 10,000 events are represented in this histogram, which was fitted to 3 components.

I've found that spontaneous openings of $(\alpha 1)_2\beta 1L9'S\varepsilon\delta$ also show multiple different open dwell times (data not shown). Further characterization of spontaneous openings of receptors containing one or two L9'S pore mutations could prove interesting in developing gating models of the nAChR.

4.3 Materials and Methods

The materials and methods used for whole-cell and single-channel recording in this chapter were described in Chapter 2. All conventional mutants were made by site-directed mutagenesis (Section 2.2). As in the past, for incorporation of unnatural amino acids, we inject the subunit(s) to be suppressed in excess. In some experiments, the α1 subunit was suppressed at TrpB (α1Trp149), so the injected mRNA ratios were 10:1:1:1. This solution was mixed in a 1:1 ratio with F_1W-tRNA and 50 nl of the resulting solution were injected per

oocyte. Note that single-channel experiments at multiple concentrations on the $(\alpha 1)_2\beta$L9'SγD174NδD180N receptor were all performed in the cell-attached pipette configuration. Thus, each concentration was collected on a different patch. Data analysis is described in **Appendix B**. The ε subunit was provided by Purnima Deshpande.

4.4 References

1. Zhong, W., Gallivan, J. P., Zhang, Y., Li, L., Lester, H. A., and Dougherty, D. A. (1998) From ab initio quantum mechanics to molecular neurobiology: a cation-pi binding site in the nicotinic receptor, *Proc Natl Acad Sci U S A 95*, 12088-12093.
2. Akk, G. (2001) Aromatics at the murine nicotinic receptor agonist binding site: mutational analysis of the alphaY93 and alphaW149 residues, *The Journal of physiology 535*, 729-740.
3. Unwin, N. (2005) Refined structure of the nicotinic acetylcholine receptor at 4 angstrom resolution, *Journal of Molecular Biology 346*, 967-989.
4. Brejc, K., van Dijk, W. J., Klaassen, R. V., Schuurmans, M., van Der Oost, J., Smit, A. B., and Sixma, T. K. (2001) Crystal structure of an ACh-binding protein reveals the ligand-binding domain of nicotinic receptors, *Nature 411*, 269-276.
5. Corringer, P. J., Le Novere, N., and Changeux, J. P. (2000) Nicotinic receptors at the amino acid level, *Annu Rev Pharmacol Toxicol 40*, 431-458.
6. Chang, Y., and Weiss, D. S. (1999) Channel opening locks agonist onto the $GABA_C$ receptor, *Nat Neurosci 2*, 219-225.
7. Auerbach, A., and Akk, G. (1998) Desensitization of mouse nicotinic acetylcholine receptor channels. A two-gate mechanism, *The Journal of general physiology 112*, 181-197.
8. Elenes, S., and Auerbach, A. (2002) Desensitization of diliganded mouse muscle nicotinic acetylcholine receptor channels, *The Journal of physiology 541*, 367-383.
9. Gupta, S., and Auerbach, A. (2011) Mapping heat exchange in an allosteric protein, *Biophys J 100*, 904-911.
10. Gupta, S., and Auerbach, A. (2011) Temperature dependence of acetylcholine receptor channels activated by different agonists, *Biophys J 100*, 895-903.

11. Charnet, P., Labarca, C., Cohen, B. N., Davidson, N., Lester, H. A., and Pilar, G. (1992) Pharmacological and kinetic properties of a4b2 neuronal nicotinic acetylcholine receptors expressed in *Xenopus* oocytes, *The Journal of physiology 450*, 375-394.
12. Auerbach, A., Sigurdson, W., Chen, J., and Akk, G. (1996) Voltage dependence of mouse acetylcholine receptor gating: different charge movements in di-, mono- and unliganded receptors, *The Journal of physiology 494 (Pt 1)*, 155-170.
13. Hamill, O. P., Marty, A., Neher, E., Sakmann, B., and Sigworth, F. J. (1981) Improved patch-clamp techniques for high-resolution current recording from cells and cell-free membrane patches, *Pflugers Arch 391*, 85-100.
14. Liu, Y., and Dilger, J. P. (1991) Opening rate of acetylcholine receptor channels, *Biophys J 60*, 424-432.
15. Maconochie, D. J., and Steinbach, J. H. (1998) The channel opening rate of adult- and fetal-type mouse muscle nicotinic receptors activated by acetylcholine, *The Journal of physiology 506 (Pt 1)*, 53-72.
16. Filatov, G. N., and White, M. M. (1995) The role of conserved leucines in the M2 domain of the acetylcholine receptor in channel gating, *Mol Pharmacol 48*, 379-384.
17. Gleitsman, K. R., Shanata, J. A., Frazier, S. J., Lester, H. A., and Dougherty, D. A. (2009) Long-range coupling in an allosteric receptor revealed by mutant cycle analysis, *Biophys J 96*, 3168-3178.
18. Kearney, P. C., Zhang, H., Zhong, W., Dougherty, D. A., and Lester, H. A. (1996) Determinants of nicotinic receptor gating in natural and unnatural side chain structures at the M2 9' position, *Neuron 17*, 1221-1229.
19. Xiu, X., Puskar, N. L., Shanata, J. A., Lester, H. A., and Dougherty, D. A. (2009) Nicotine binding to brain receptors requires a strong cation-pi interaction, *Nature 458*, 534-537.
20. Beene, D. L., Brandt, G. S., Zhong, W., Zacharias, N. M., Lester, H. A., and Dougherty, D. A. (2002) Cation-pi interactions in ligand recognition by serotonergic (5-HT3A) and nicotinic acetylcholine receptors: the anomalous binding properties of nicotine, *Biochemistry 41*, 10262-10269.
21. Zhang, Y., Chen, J., and Auerbach, A. (1995) Activation of recombinant mouse acetylcholine receptors by acetylcholine, carbamylcholine and tetramethylammonium, *J Physiol 486*, 189-206.
22. Labarca, C., Nowak, M. W., Zhang, H., Tang, L., Deshpande, P., and Lester, H. A. (1995) Channel gating governed symmetrically by conserved leucine residues in the M2 domain of nicotinic receptors, *Nature 376*, 514-516.
23. Akk, G., Milescu, L. S., and Heckmann, M. (2005) Activation of heteroliganded mouse muscle nicotinic receptors, *The Journal of physiology 564*, 359-376.
24. Jackson, M. B. (1984) Spontaneous openings of the acetylcholine receptor channel, *Proc. Natl. Acad. Sci. U.S.A. 81*, 3901-3904.

25. Jackson, M. B. (1985) The kinetics of unliganded acetylcholine receptor channel gating, *Biophys. J. 49*, 663-672.

Chapter 5

Nicotine Binding to α4(L9'A)$_2$(β2)$_3$ and Varenicline (Chantix®) Binding to (α4L9'A)$_2$(β2)$_3$ and (α4L9'A)$_3$(β2)$_2$

Sections 5.2 through 5.4 of this chapter are reprinted from *Nature*, 458. Xinan Xiu, Nyssa L. Puskar, Jai A. P. Shanata, Henry A. Lester, and Dennis A. Dougherty. *Nicotine Binding to Brain Receptors Requires a Strong Cation-π Interaction,* 354–357. Copyright (2009) with permission from *Nature*.

5.1 Introduction

In Chapter 4, I used a variety of agonists and mutants in an attempt to learn about the rate at which ion channels open, as well as to build kinetic models of a mutant nicotinic acetylcholine receptor. However, as the name implies, the *nicotinic* acetylcholine receptors (nAChRs) bind nicotine in addition to their endogenous agonist acetylcholine. This binding is particularly strong in brain nAChRs (**Figure 5.1**). The resultant activation of these receptors from nicotine binding triggers dopamine release that initiates and sustains nicotine dependence mediated by mesolimbic reward(*1, 2*).

The muscle-type nAChRs were the focus of Chapters 3 and 4; previous studies of binding to these receptors showed a cation-π interaction between acetylcholine (ACh) and TrpB(*3*). However, similar studies showed no similar binding pattern to nicotine(*4*). Moreover, the binding mode of nicotine to *neuronal* nAChRs was not known, despite its key role in nicotine addiction and resultant therapeutic strategies for smoking cessation (see Section 5.6, below). This chapter explores the binding of nicotine, a highly addictive, yet widely available drug, and varenicline (Chantix®), a smoking cessation treatment, to the α4β2 neuronal nAChRs.

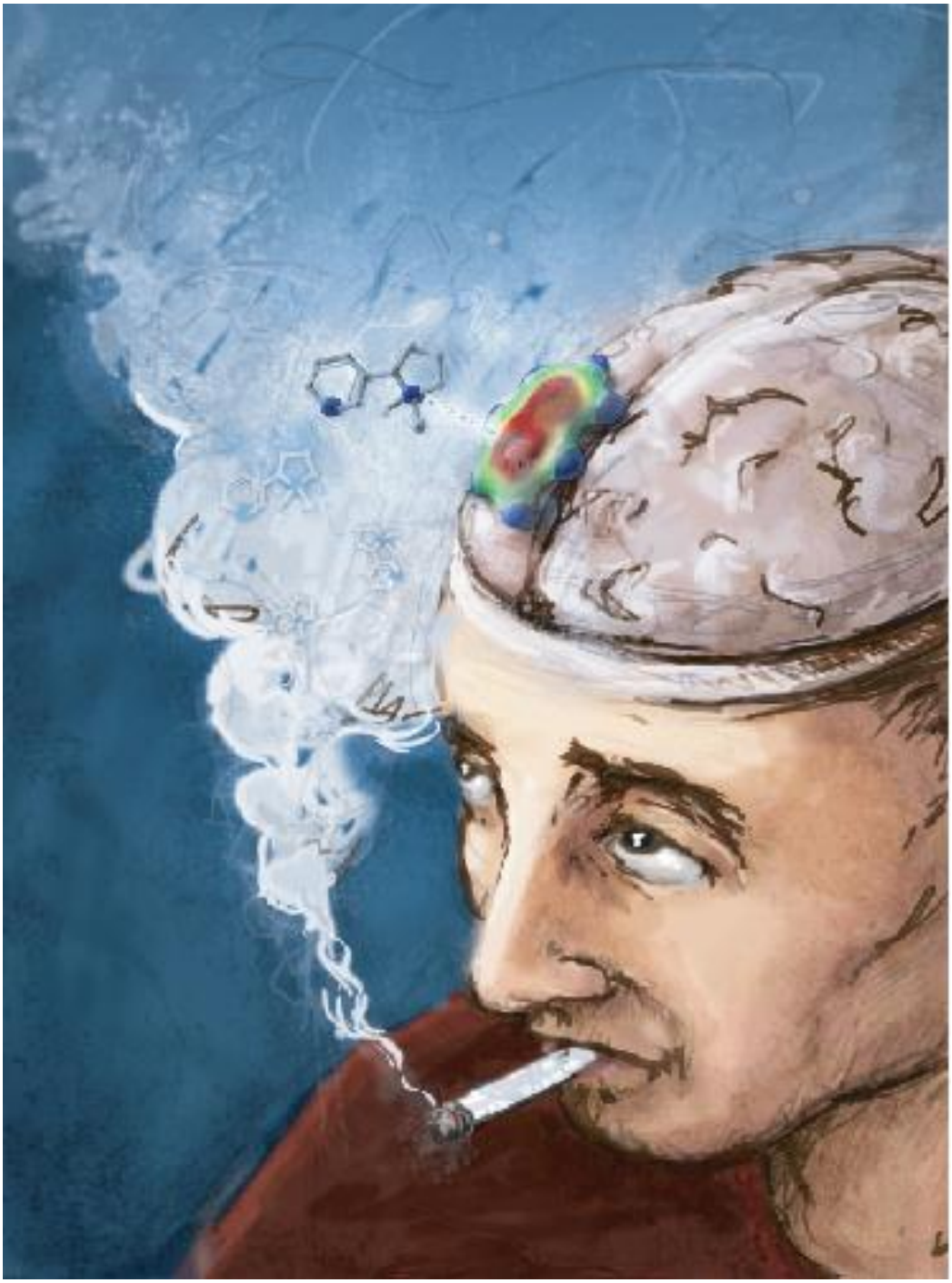

FIgure 5.1. An artists' rendition of the interaction of nicotine and brain receptors. Nicotine from cigarette smoke gets to the brain quickly, where it has a wide range of cognitive effects. Figure courtesy of Wolfe Gleitsman

5.2 Nicotine Binding to Brain Receptors Requires a Strong Cation-π Interaction

Nicotine addiction begins with high-affinity binding of nicotine to acetylcholine (ACh) receptors in the brain. The end result is over 4,000,000 smoking-related deaths annually worldwide and the largest source of preventable mortality in developed countries. Stress reduction, pleasure, improved cognition, and other CNS effects are strongly associated with smoking. But, if nicotine activated ACh receptors found in muscle as potently as those in the brain, smoking would cause intolerable and perhaps fatal muscle contractions. Despite extensive pharmacological, functional, and structural studies of ACh receptors, the basis for the differential action of nicotine on brain versus muscle ACh receptors has not been determined. Here we show that at the α4β2 brain receptors thought to underlie nicotine addiction, the high affinity of nicotine is the result of a strong cation-π interaction to a specific aromatic amino acid of the receptor, TrpB. In contrast, the low affinity of nicotine at the muscle-type receptor is largely due to the fact that this key interaction is absent, even though the immediate binding site residues, including the key TrpB, are identical in the brain and muscle receptors. At the same time a hydrogen bond from nicotine to the backbone carbonyl of TrpB is enhanced in the neuronal receptor relative to the muscle-type. A point mutation near TrpB that differentiates α4β2 and muscle-type receptors appears to influence the shape of the binding site, allowing nicotine to

interact more strongly with TrpB in the neuronal receptor. ACh receptors are established therapeutic targets for Alzheimer's disease, schizophrenia, Parkinson's disease, smoking cessation, pain, attention deficit-hyperactivity disorder, epilepsy, autism, and depression(*5*). Along with solving a chemical mystery in nicotine addiction, our results provide guidance for efforts to develop drugs that target specific types of nicotinic receptors.

Nicotinic acetylcholine receptors (nAChR) comprise a family of ≥ 20 homologous subtypes that mediate fast synaptic transmission throughout the central and peripheral nervous systems(*6*). The neuronal receptors are found in the central nervous system (CNS) and autonomic ganglia. Of these, the subtype most strongly associated with nicotine addiction and the target of recently developed smoking cessation drugs is termed α4β2(*7-11*). The high nicotine affinity of α4β2 receptors, when combined with the ability of nicotine to cross the blood-brain barrier and its favorable pharmacokinetics, allows nicotine at the submicromolar concentrations in tobacco smoke to acutely activate these receptors, providing reward, cognitive sensitization, and perhaps other effects. In addition, the high-affinity interaction allows smoked nicotine to act as an intracellular pharmacological chaperone of α4β2 receptors, leading to the upregulation of receptors thought to underlie effects of chronic exposure(*10, 12*).

In previous studies of the nAChR of the neuromuscular junction (muscle-type), we showed that an important contributor to ACh binding is a cation-π interaction to a specific tryptophan (TrpB, residue 149, **Figure 5.2**)(*13*). These results were subsequently supported by the important series of crystal structures of ACh binding proteins (AChBP)(*14, 15*). These structures revealed the 'aromatic box' structural motif of **Figure 5.2**, and the aligning residues are predominantly aromatic throughout the Cys-loop family of neurotransmitter-gated ion channels. In other Cys-loop receptors, a cation-π interaction between the natural agonist and one of the aromatics is always seen, although its precise location varies(*16*). Interestingly, when nicotine activates the muscle-type nAChR, there is no cation-π interaction(*17*), consistent with its relatively low affinity for this receptor. This suggested that a cation-π interaction could discriminate between high affinity neuronal receptors and low affinity muscle-type receptors. However, subtle effects must be involved, as the nAChRs of the CNS and neuromuscular junction are homologous throughout most regions of sequence and are essentially identical in the immediate vicinity of the agonist binding site (**Figure 5.7**).

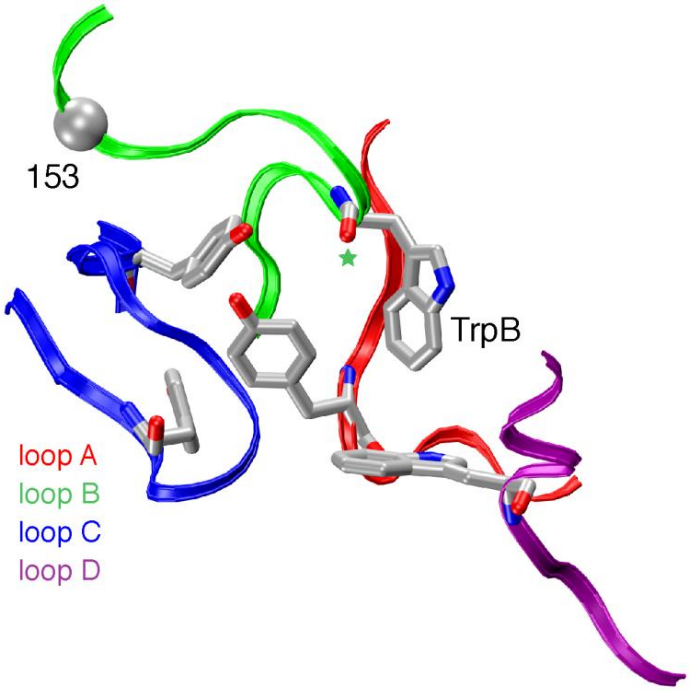

Figure 5.2. The binding site of AChBP, thought to resemble that of nAChRs. Shown are the four principal 'loops' that define the binding site(*6*). Also highlighted are TrpB (149) studied here; its backbone carbonyl (green star); and the α carbon on position 153, which has also been mutated here. Note that loop C contributes two aromatic residues; the other loops each contribute one. The image is of Protein Data Bank file 1I9B(*14*).

Here we describe studies of the α4β2 neuronal receptor. We find a remarkable alteration of binding behavior: *both* ACh and nicotine make a strong cation-π interaction to TrpB. In addition, a hydrogen bond from nicotine to the backbone carbonyl of TrpB that is weak in the muscle-type is much stronger in the α4β2 receptor. Taken together, these two noncovalent interactions fully rationalize the differential affinity of nicotine in the brain versus the neuromuscular junction.

A cation-π interaction between a drug and a receptor can be revealed by incorporation of a series of fluorinated amino acid analogues (**Figure 5.3**); a consistent trend in receptor response indicates a binding interaction. Such an experiment is enabled by the nonsense suppression methodology for incorporation of unnatural amino acids into receptors and channels expressed in *Xenopus* oocytes. While we have found the nonsense suppression methodology to be broadly applicable(*18, 19*), implementing the methodology for study of the α4β2 neuronal nAChRs proved to be especially challenging, requiring new strategies. The α4β2 receptors express in *Xenopus* oocytes at inadequately low levels for nonsense suppression experiments. However, recent studies showed that the Leu9'Ala (L9'A) mutation in the M2 transmembrane helix of the α4 subunit greatly improves expression without altering the pharmacological selectivity of the receptor(*20*). Therefore, all studies of α4β2 described here included this mutation. As with other mutations of L9', the L9′A mutation lowers EC_{50} by influencing receptor gating in ways that are fairly well understood and that do not distort the present analysis of the binding site (some 60 Å from the 9' position)(*21, 22*). In addition, previous studies of the muscle-type receptor used a comparable mutation at L9', and control experiments established that it did not alter binding trends(*13, 23*).

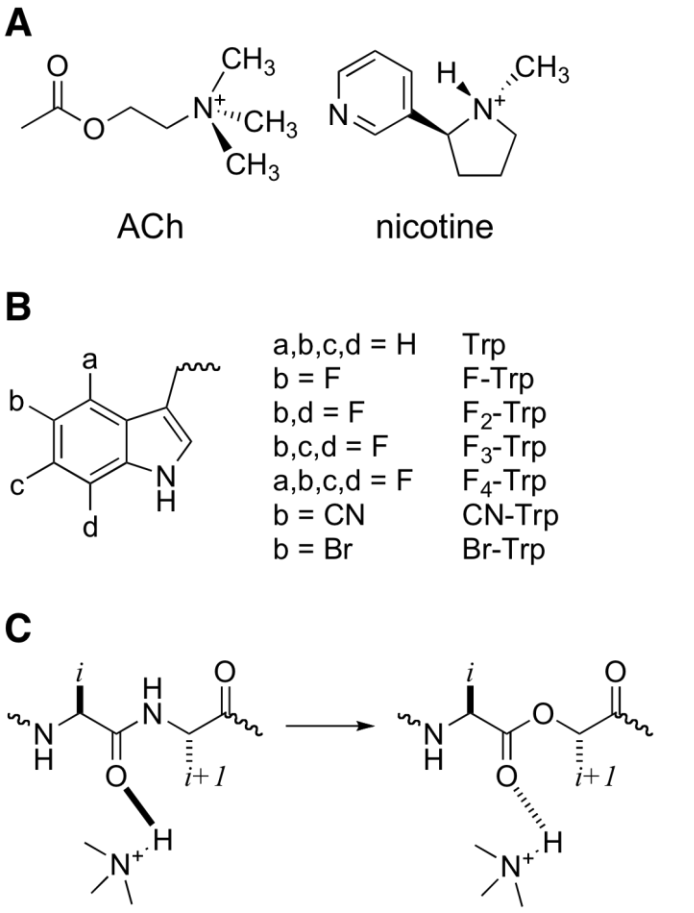

Figure 5.3. Agonists and unnatural amino acids considered here. a) Structures of ACh and nicotine. b) Unnatural amino acids considered here. If not otherwise indicated, an a, b, c, or d group is H. Br, bromo group; CN, cyano group. c) The backbone ester strategy for modulating a hydrogen bond

The nAChRs are pentameric. The muscle-type receptor has a precise stoichiometry of $(\alpha1)_2\beta1\gamma\delta$. However, the α4β2 receptor can have variable stoichiometry. In particular, there are two forms of α4β2, $(\alpha4)_2(\beta2)_3$ and $(\alpha4)_3(\beta2)_2$, which we will refer to as A2B3 and A3B2(*12, 24, 25*), respectively. Agonist binding sites are at the appropriate α-β interfaces. The A2B3 form has higher sensitivity for nicotine and may be upregulated during chronic exposure to nicotine; our studies have focused on it. Controlling the ratios of mRNAs injected into the oocyte can reliably control subunit stoichiometry in the wild type receptor.

However, in a nonsense suppression experiment, the subunit that contains the stop codon where the unnatural amino acid has been incorporated can exhibit low and variable expression levels. Therefore we sought a second, independent indicator of the stoichiometry of the α4β2 receptor. We now report that the A2B3 and A3B2 forms of the α4(L9'A)β2 receptor show markedly different rectification behaviors. As indicated by either voltage ramp or voltage jump experiments, A2B3 is substantially more inward rectifying than A3B2 (**Figure 5.8**). Thus, in all our experiments with unnatural amino acids, the stoichiometries of mutant receptors are monitored by measuring I-V relations with voltage jumps. For each mutant receptor studied, we determined the fraction, (outward current at +70 mV/inward current at –110 mV), and a value ≤ 0.1 establishes the desired A2B3 stoichiometry (**Table 5.1**, Supplementary Discussion). With these methodological developments in hand, incorporation of unnatural amino acids into the α4β2 receptor becomes feasible (**Figure 5.4**).

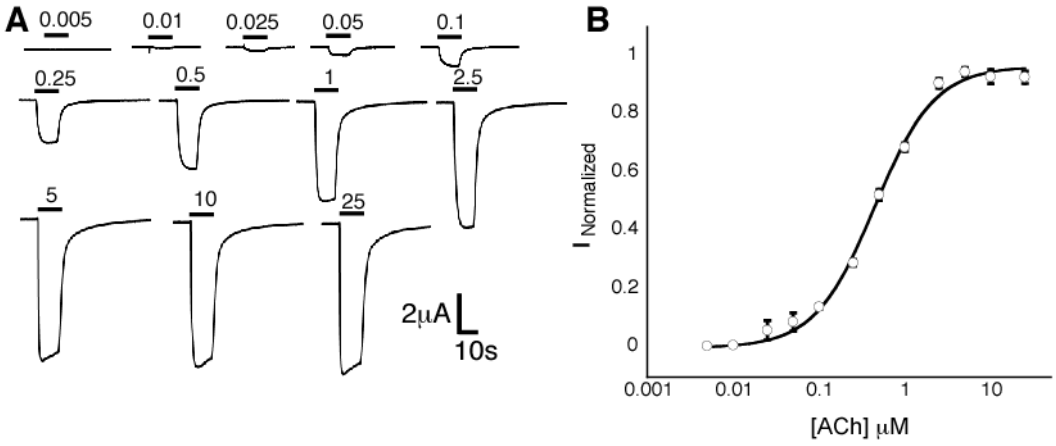

Figure 5.4. Nonsense suppression in the α4β2 receptor. Shown is a wild-type recovery experiment, in which Trp is incorporated at the TrpB position. a) Representative traces of

voltage-clamp currents. Bars represent application of ACh at concentrations noted. b) Fit of data in a to the Hill equation. Error bars indicate s.e.m; *n* = 6–8.

As shown in **Table 5.1** and **Figure 5.5**, a compelling “fluorination” trend is seen for both ACh and nicotine at TrpB of the α4β2 receptor. This is in sharp contrast to the results at the muscle-type receptor, in which no such trend is seen for nicotine activation. Further support for an important cation-π interaction for both agonists is provided by the large perturbation induced by a cyano (CN) group—which is strongly deactivating in a cation-π interaction—compared to a bromo (Br) group, which is roughly isosteric to CN but much less deactivating.

We have also evaluated other residues that constitute the aromatic box of the ACh binding site (**Table 5.1**). The results for α4β2 very much parallel our previous findings for the muscle-type receptor (Supplementary Discussion). This indicates that it is specifically the interaction with TrpB that discriminates the two receptor subtypes.

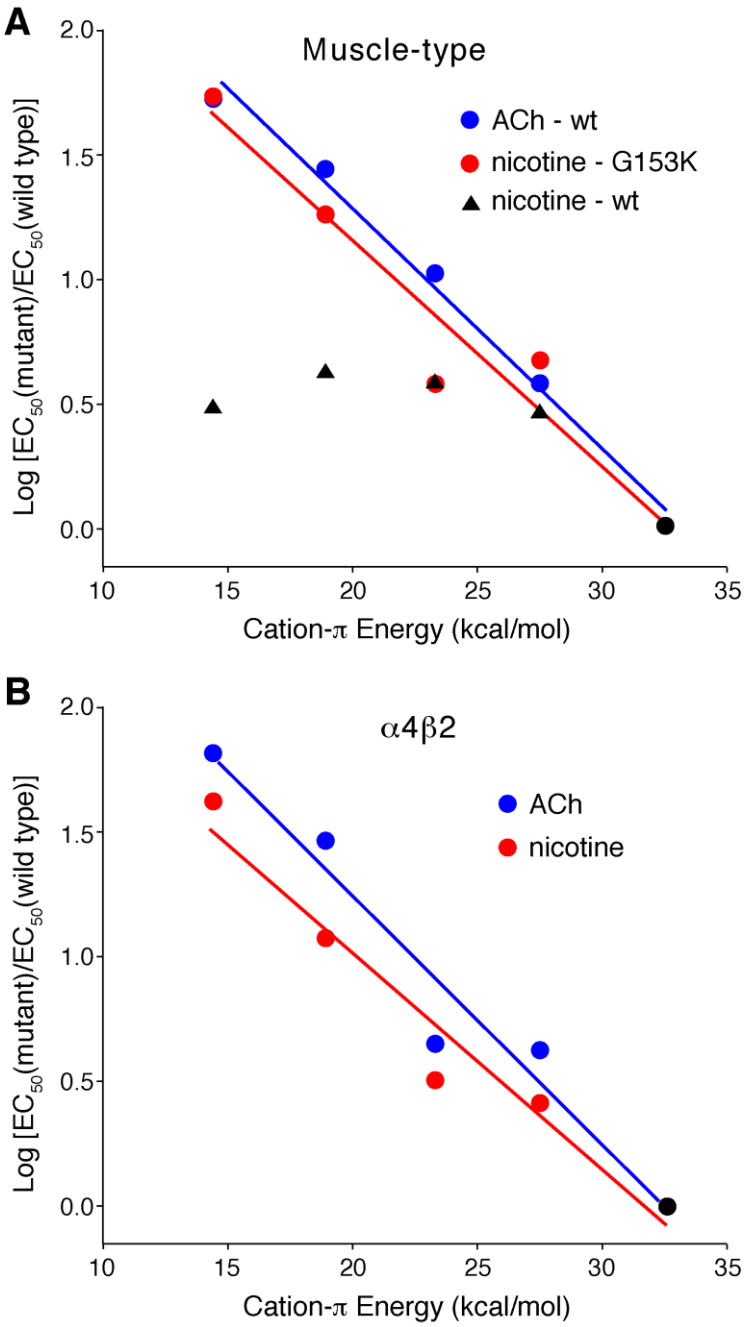

Figure 5.5. Fluorination plots. Note that in both plots, all data sets share the point at *x* = 32.6 kcal mol^{-1} (cation-π energy for Trp); y = 0 (black circle). Moving to the left then corresponds to monofluoro-, difluoro-, trifluoro-, and tetrafluoro-TrpB. Cation-π binding energies (x-axes) are from (*13*). a) Muscle-type receptor. The designation WT indicates Gly at position 153. b) α4β2 receptor

The EC_{50} values reported here represent a measure of receptor function; shifts in EC_{50} can result from changes in ligand binding and/or receptor gating

properties. By ascribing the results to attenuation of a cation-π interaction, we are effectively concluding that it is ligand binding that is being modulated by fluorination, but that conclusion is not incontrovertible. To resolve this ambiguity, we evaluated the gating behaviors of key receptors using single-channel recording. For the wild type and the receptor with F_3-Trp at TrpB, we compared the probabilities that the channel is open (P_{open}) at nicotine concentrations that evoke half-maximal macroscopic steady-state currents (EC_{50} = 0.08 μM and 1.2 μM, respectively). Any differences between the two P_{open} values must result from differences in gating behaviors. As suggested by **Figure 5.6** and as confirmed by further single-channel analysis (**Figure 5.9** and Supplementary Discussion), the wild type and mutant receptors have P_{open} values that are essentially indistinguishable. Thus, the shift in EC_{50} for F_3-Trp is primarily, if not exclusively, a consequence of changes in binding. We conclude that fluorination of TrpB of the α4β2 (A2B3) receptor primarily impacts sensitivity to nicotine by decreasing nicotine's cation-π interaction with this residue.

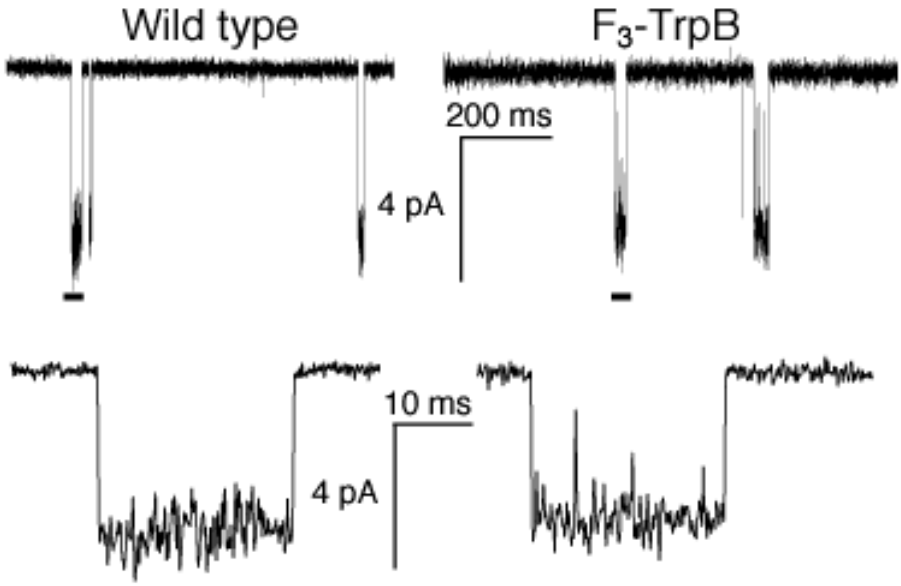

Figure 5.6. Single-channel recordings from wild type α4β2 (conventional expression) and the F_3-Trp mutant (nonsense suppression) at site B, with nicotine applied at EC_{50} values (0.080 and 1.2 μM, respectively). Lower traces are expansions of the regions marked by a bar in the upper traces. Records were obtained in the cell-attached configuration with a pipette potential of +100 mV and are shown at 2 kHz bandwidth. Channel openings are shown as downward deflections.

These results indicate that nicotine is positioned more closely to TrpB in the α4β2 agonist binding site than in the muscle-type. This suggested that another nicotine binding interaction could also be altered. An important chemical distinction between ACh and nicotine is that only the latter can act as a hydrogen bond donor, through the pyrrolidine N^+-H (**Figure 5.3A**). Examination of the AChBP crystal structures (**Figure 5.2**)(*26*) suggested that the backbone carbonyl associated with TrpB could act as the hydrogen bond acceptor, and several groups have shown the importance of this interaction(*26-28*). Previously, we probed this potential hydrogen bond in the muscle-type receptor by replacing the *(i+1)* residue with its α-hydroxy analogue (**Figure 5.3C**). This converts the backbone amide to a backbone ester, which is well-established to be a

substantially poorer hydrogen bond acceptor. In the muscle-type receptor, this change raised the nicotine EC_{50} by a modest factor of 1.6(*29*). We now find that for precisely the same change in the α4β2 receptor, the nicotine EC_{50} increases 19-fold, a relatively large effect for such a subtle mutation(*30-32*). Recall that the backbone ester substitution does not destroy the hydrogen bond, it simply attenuates it. Importantly, ACh, which cannot make a conventional hydrogen bond to the carbonyl, shows no shift in EC_{50} in response to this mutation (**Table 5.1**). This establishes that the ester mutation does not globally alter the binding/gating characteristics of the receptor.

The differential affinity of nicotine for α4β2 versus muscle-type receptors results from stronger interactions in the former with TrpB–both cation-π and hydrogen bonding. Since the two receptors are identical with regard to the five residues that make up the aromatic box, a factor 'outside the box' must be influencing its precise geometry, such that nicotine can approach TrpB more closely in α4β2 than in muscle-type nAChR. Pioneering work has identified residues responsible for the fact that α4β2 receptors show consistently higher affinity than the homopentameric α7 neuronal receptors(*33*). At a particular residue in loop B–position 153, only four residues from TrpB–mutations strongly influence affinity. In high affinity α4β2 receptors this residue is a Lys, and is proposed to form a backbone hydrogen bond between loops B and C that helps shape the aromatic box (**Figure 5.2**). In the lower affinity α7 neuronal receptor, residue 153 is a Gly, and molecular dynamics simulations of α7 suggest that a

Gly at 153 discourages the formation of the hydrogen bond between loops B and C. Interestingly, the aligned residue in the muscle-type receptor is also a Gly, and a naturally occurring G153S mutation is gain-of-function and associated with a congenital myasthenic syndrome(*34*). We now report that the muscle-type α1 G153K mutant shows much higher affinity for nicotine, and that, when this mutation is present, the cation-π interaction to TrpB is strong. The data are summarized in **Table 5.1** and **Figure 5.5**. As expected, the ACh cation-π interaction is maintained in the muscle-type receptor with the G153K mutation. These data indicate that the loop B-loop C hydrogen bond that is naturally present in α4β2 shapes the aromatic box such that nicotine can make a closer contact to TrpB, and that this structural feature is absent or weaker in the muscle-type receptor.

Taken together, the present results indicate that the higher affinity of nicotine in the brain relative to the neuromuscular junction is a consequence of enhanced interactions with TrpB. A cation-π interaction that is absent in the muscle-type receptor is quite strong in α4β2. In addition, a hydrogen bond to a backbone carbonyl that is weak in the muscle-type is enhanced in α4β2. Both effects are quite substantial, and in combination they are more than adequate to fully account for the differential sensitivity to nicotine of the two receptors. The side chain of residue 153 in loop B distinguishes the two receptor types and apparently influences the shape and/or electronic properties of the binding site

aromatic box, allowing a stronger interaction between nicotine and TrpB in high affinity receptors.

Methods Summary

Whole-cell electrophysiological characterization of agonist-induced responses. Rat α4β2 and mouse $(\alpha1)_2\beta1\gamma\delta$ ion channels were expressed in *Xenopus laevis* oocytes. For α4β2 receptors, subunit stoichiometry was controlled by varying the α4:β2 subunit ratio and verified by voltage jump experiments. Dose-response measurements for these channels were performed with a holding potential of -60 mV.

Unnatural amino acid/α-hydroxy acid incorporation. Unnatural amino acids and α-hydroxy acids were prepared, coupled to dCA and ligated to 74-mer THG73 as described previously(*19*).

Single-channel characterization of α4β2. Single-channel recording was performed in the cell-attached configuration with a pipette potential of +100 mV. P_{open} values were calculated from event-detected data using Clampfit 9.2 single-channel search.

Full methods and any associated references are available in the online version of the paper at www.nature.com/nature.

Acknowledgements. We thank B.N. Cohen for advice on single-channel recording and analysis. This work was supported by the NIH (NS 34407; NS 11756) and the California Tobacco-Related Disease Research Program of the University of California, Grant No. 16RT-0160. J.A.P.S. was partially supported by an NRSA training grant.

5.3 Online Methods

5.3.1 Whole-Cell Electrophysiological Characterizations of the Agonist-Induced Responses

Rat α4 and α2 mRNAs as well as mouse α1, β1(L9'S), γ, and δ mRNAs were obtained from NotI linearizations of the expression vector pAMV, followed by *in vitro* transcription using the mMessage mMachine T7 kit (Ambion, Austin, TX). The mutations for each subunit were introduced according to the QuikChange mutagenesis protocol (Stratagene).

To express wild type neuronal ion channels, α4L9'A mRNA was co-injected with β2 mRNA at various ratios (total mRNA 10‑25 ng/cell). Stage V-VI *Xenopus laevis* oocytes were injected and incubated at 18° C for 24‑48 h (whole-cell recording) or 60–90 h (single-channel recording).

Agonist-induced currents were recorded in two-electrode voltage clamp mode using the OpusXpress 6000A (Molecular Devices Axon Instruments) at a holding potential of -60 mV. Agonists were prepared in Ca^{2+}-free ND96 solution

and applied for 12 s followed by a 2 min wash with Ca^{2+}-free ND96 solution between each agonist application. Acetylcholine chloride and (-)-nicotine tartrate were purchased from Sigma/Aldrich/RBI (St. Louis, MO). Dose-response data were obtained for ≥ 6 concentrations of agonist and for ≥ 5 oocytes. Mutants with I_{max} of ≥ 100 nA were defined as functional. EC_{50} and Hill coefficient were calculated by fitting the dose-response relation to the Hill equation. All data are reported as mean ± SEM.

Voltage jump experiments were performed in the absence of ACh and also at EC_{50} concentration of ACh. The membrane potential was held at -60 mV, and stepped to 10 test potentials at 20 mV increments between +70 mV and -110 mV for 400 ms each. The voltage was then held for 600 ms at -60 mV holding potential between each episode. To isolate the ACh-induced currents, control traces ([ACh] = 0) were subtracted from the steady-state amplitudes of the ACh-induced currents of the test pulses. Normalized I-V curves were generated using current amplitudes normalized to that at -110 mV. For each α4L9'Aβ2 mutant, normalized $I_{+70\ mV}$ ± s.e.m. from ≥ 5 cells was reported.

5.3.2 Unnatural Amino Acid/α-Hydroxy Acid Incorporation

Nitroveratryloxycarbonyl (NVOC)-protected cyanomethyl ester forms of unnatural amino acids and α-hydroxythreonine cyanomethyl ester were synthesized, coupled to the dinucleotide dCA, and enzymatically ligated to 74–mer THG73 $tRNA_{CUA}$(*19*). The unnatural-amino-acid–conjugated tRNA was deprotected by photolysis immediately prior to co-injection with mRNA containing

the UAG mutation at the site of interest. Approximately 10–25 ng mRNA and 25 ng tRNA-amino acid or tRNA-hydroxy acid were injected into stage V–VI oocytes in a total volume of 70 nL. For unnatural amino acid mutagenesis experiments in the muscle-type receptor, the α1, β1, γ, and δ subunits were co-injected in a 10:1:1:1 ratio. All muscle-type receptors contained a L9'S mutation in the β subunit.

The fidelity of unnatural amino acid incorporation was confirmed at each site with a 'wild type recovery' experiment and a 'read-through/ reaminoacylation' test. In the 'wild type recovery' experiment, UAG mutant mRNA was co-injected with tRNA charged with the amino acid that is present at this site in the wild type protein. Generation of receptors that were indistinguishable from the wild type protein indicated that the residue carried by the suppressor tRNA was successfully and exclusively integrated into the protein. In the 'read-through/ reaminoacylation' test, the UAG mutant mRNA was introduced with (1) no tRNA, (2) tRNA THG73 that was not charged with any amino acid, or (3) tRNA THG73 enzymatically ligated with dinucleotide dCA. Lack of currents in these experiments validated the reliability of the nonsense suppression experiments.

5.3.3 Single-Channel Characterization of α4β2

Single-channel recording was performed in the cell-attached configuration on devitellinized *Xenopus laevis* oocytes at 20 ± 2°C with a pipette potential of +100 mV, as described previously(*31, 35*). Pipettes were fabricated from thick-walled (I.D. = 0.80 mm, O.D. = 1.60 mm) KG-33 glass (Garner Glass Company,

Claremont, CA) and coated with sylgard (World Precision Instruments, Sarasota, FL); they had resistances of 10–20 MΩ. The bath solution contained 120 mM KCl, 5 mM HEPES, 1 mM $MgCl_2$, and 2 mM $CaCl_2$, pH = 7.4, so that the reversal potential for agonist-induced currents of devitellinized oocytes was ~ 0 mV, and the transmembrane potential of the patch was ~ -100 mV. The pipette solution contained 100 mM KCl, 10 mM HEPES, 1 mM $MgCl_2$, 10 mM K_2EGTA, pH = 7.4, and was supplemented with the indicated concentrations of nicotine. Data were collected using a GeneClamp 500B amplifier (Axon Instruments, Union City, CA) at full bandwidth (50 kHz; 4-pole Bessel, -3 dB) with a CV-5 100 GU headstage. The signal was then low-pass filtered (Avens Signal Equipment, AP220, 8-pole Bessel, -3 dB 20 kHz) and sampled with a Digidata 1320A and Clampex 9.2 (Axon Instruments, Union City, CA) at 50 kHz. Only patches that showed no simultaneous activations were analyzed. For each mutant, this was ≥ 3 patches from oocytes from 2 different donor frogs. Data were filtered offline (Gaussian, -3 dB, 5 kHz) and electrical interference at harmonics of 60 Hz was removed if necessary. Event transitions were detected with Clampfit 9.2 (single-channel search). A dead time, τ_d, of 100 μs was applied to all events. Open and closed dwell time histograms were generated as described previously(*36*) and fitted using the predefined log-transformed exponential probability density function in Clampfit 9.2. To delineate clusters, a critical closed duration, τ_{crit}, was defined using two separate methods (Supplementary Discussion); in both cases closed dwell times longer than τ_{crit} were excluded from further analysis. Sojourns to a subconductance state (< 85% of the full conductance level) were treated as

closed and accounted for < 10% of the total openings in all records. The time-average probability that the channel is open (P_{open}) was calculated as the total open time divided by the revised total closed time.

5.4 Supplementary Information

5.4.1 Supplementary Figures

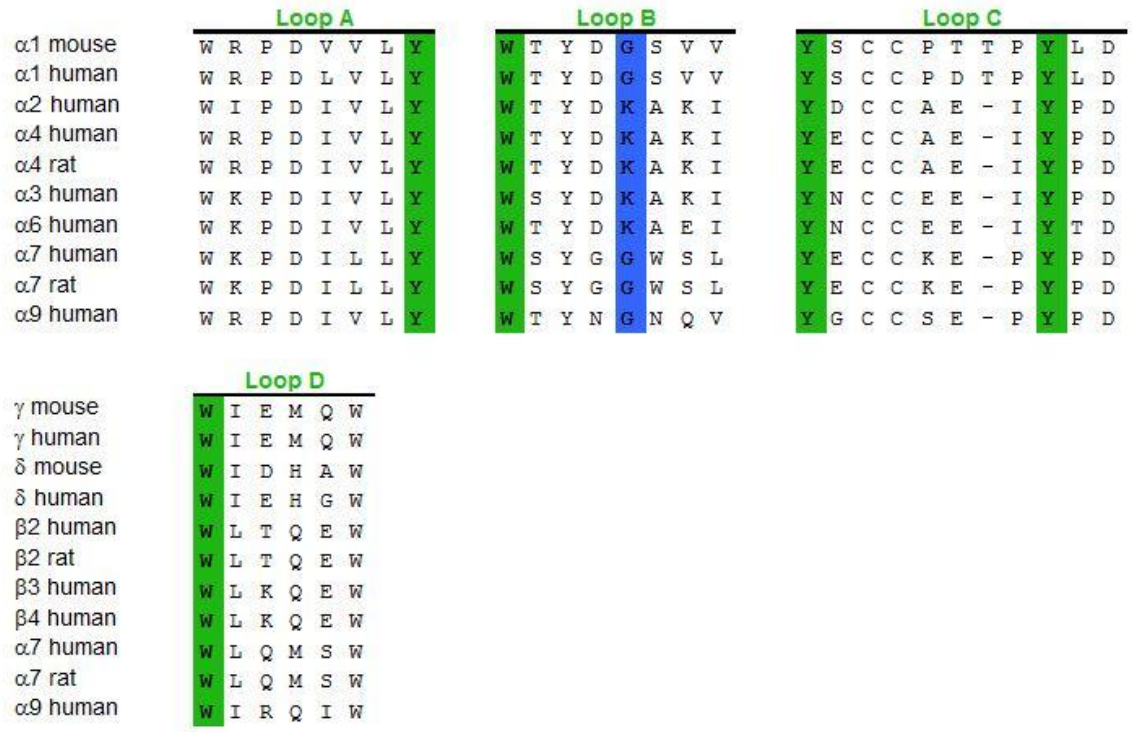

Figure 5.7. Sequence alignment for Loops A, B, C, and D in the vicinity of the aromatic binding box. The five residues of the aromatic box: TyrA, TrpB, TryC1, TyrC2, and TrpD, are highlighted in green. They are universally conserved in these subunits. G153 (α1) is the fourth residue after TrpB, highlighted in blue.

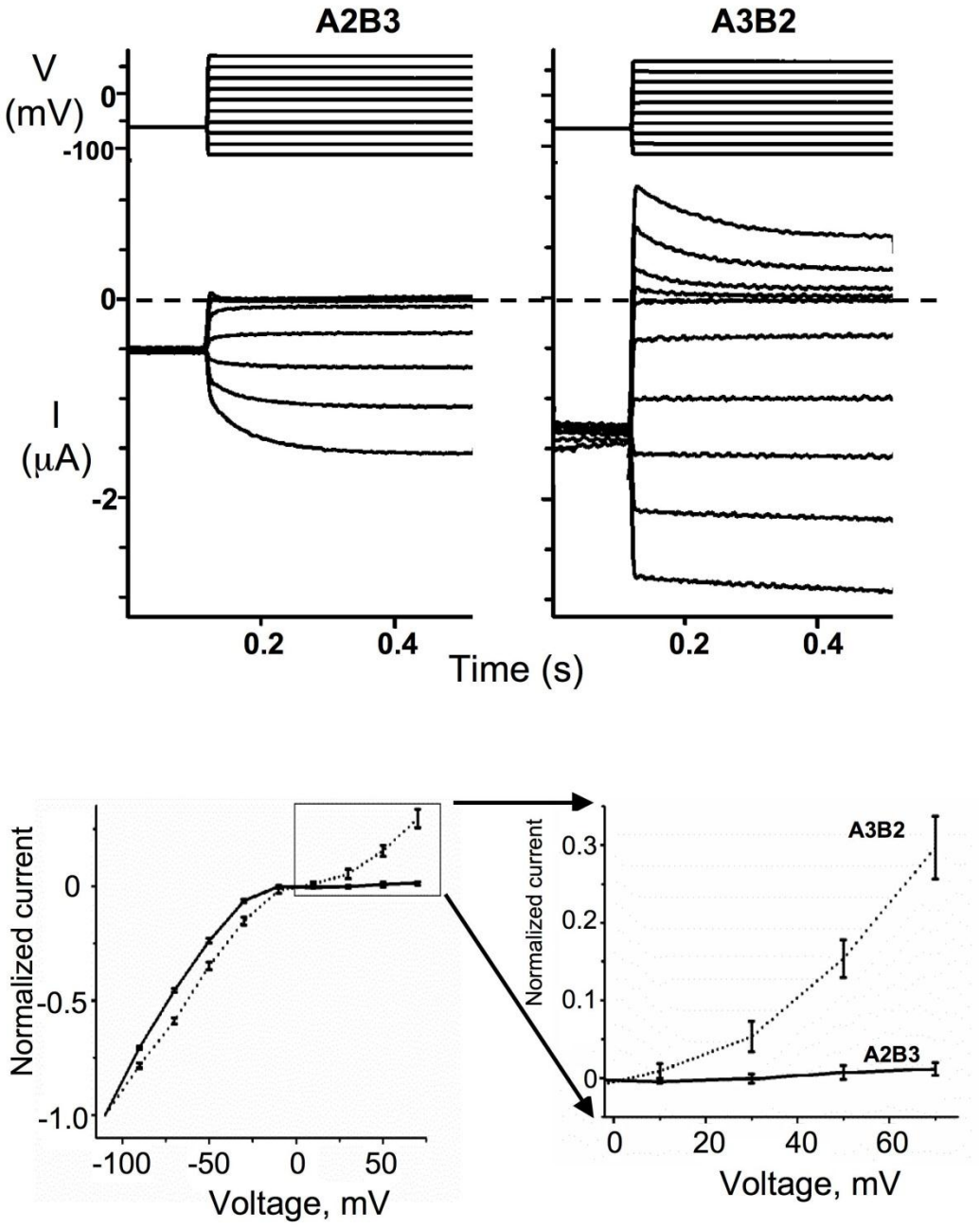

Figure 5.8. Rectification behaviors of A2B3 and A3B2 L9'A α4β2 nAChR. Upper) Representative voltage traces and current responses for voltage jump experiments. Lower) I-V curves for A2B3 (solid line) and A3B2 (dotted line). The inset shows positive voltages, where A2B3 and A3B2 exhibit markedly different behavior.

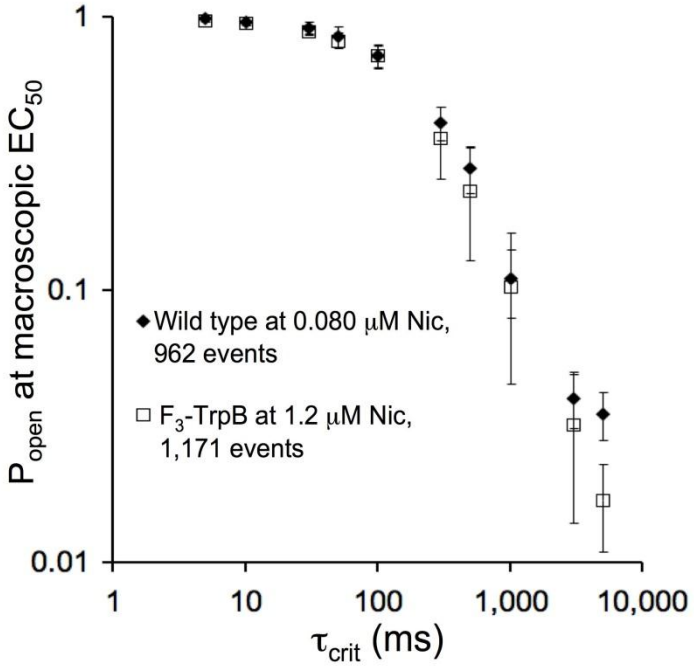

Figure 5.9. Comparison of P_{open} at macroscopic EC_{50} for wild type and F_3-TrpB $\alpha4\beta2$ (A2B3) over a range of τ_{crit} values between 5 ms and 5000 ms reveals essentially equivalent gating behaviors. Error bars are mean ± s.e.m. and are smaller than the symbol when not shown.

5.4.2 Supplementary Table

Mutation	ACh	n_H	Nicotine	n_H	Norm. I (+70mV)
			α4(L9'A)β2		
			Wild type		
A2B3	0.42 ± 0.01	1.2 ± 0.1	0.08 ± 0.01	1.2 ± 0.1	0.041 ± 0.005
A3B2	0.023 ± 0.001	1.3 ± 0.1	0.01 ± 0.001	1.7 ± 0.2	0.297 ± 0.041
			TyrA (Tyr98) A2B3		
Tyr	0.42 ± 0.03	1.2 ± 0.1	0.08 ± 0.01	1.7 ± 0.3	0.023 ± 0.009
Phe	12 ± 1	1.3 ± 0.1	0.77 ± 0.05	2.1 ± 0.3	0.064 ± 0.011
MeO-Phe	2.3 ± 0.2	1.2 ± 0.1	0.40 ± 0.02	1.7 ± 0.2	0.054 ± 0.032
F-Phe	15 ± 1	1.2 ± 0.1	0.32 ± 0.03	1.4 ± 0.2	-0.076 ± 0.046
F_2-Phe	16 ± 2	1.8 ± 0.3	0.39 ± 0.05	1.8 ± 0.4	0.028 ± 0.005
F_3-Phe	14 ± 1	1.2 ± 0.1	0.53 ± 0.04	1.4 ± 0.1	0.044 ± 0.010
Br-Phe	3.3 ± 0.2	1.2 ± 0.1	0.54 ± 0.04	1.5 ± 0.1	-0.003 ± 0.031
CN-Phe	73 ± 4	1.7 ± 0.1	8.8 ± 0.9	1.5 ± 0.2	0.075 ± 0.008
			TrpB (Trp 154) A2B3		
Trp	0.44 ± 0.03	1.3 ± 0.1	0.09 ± 0.01	1.5 ± 0.1	0.006 ± 0.014
F-Trp	1.9 ± 0.1	1.2 ± 0.1	0.26 ± 0.02	1.3 ± 0.1	-0.065 ± 0.047
F_2-Trp	2.0 ± 0.1	1.3 ± 0.1	0.32 ± 0.04	1.3 ± 0.1	0.032 ± 0.025
F_3-Trp	13 ± 1	1.3 ± 0.1	1.2 ± 0.1	1.4 ± 0.2	-0.073 ± 0.029
F_4-Trp	29 ± 2	1.1 ± 0.1	4.2 ± 0.4	1.3 ± 0.2	-0.027 ± 0.023
CN-Trp	12 ± 1	1.2 ± 0.1	0.90 ± 0.07	1.4 ± 0.1	0.009 ± 0.017
Br-Trp	1.1 ± 0.1	1.3 ± 0.1	0.20 ± 0.02	1.3 ± 0.2	0.020 ± 0.005
			TyrC1 (Tyr195) A2B3		
Tyr	0.42 ± 0.03	1.5 ± 0.1	0.07 ± 0.01	1.3 ± 0.1	0.042 ± 0.014
Phe	53 ± 4	1.3 ± 0.1	3.3 ± 0.2	1.2 ± 0.1	0.059 ± 0.014
MeO-Phe	48 ± 5	1.4 ± 0.2	2.8 ± 0.4	1.2 ± 0.2	0.064 ± 0.028
CN-Phe	210 ± 10	1.6 ± 0.1	19 ± 2	1.6 ± 0.2	0.057 ± 0.011
			TyrC2 (Tyr202) A2B3		
Tyr	0.42 ± 0.03	1.3 ± 0.1	0.09 ± 0.01	1.6 ± 0.1	0.057 ± 0.016
Phe	0.32 ± 0.02	1.4 ± 0.1	0.14 ± 0.01	1.4 ± 0.1	0.014 ± 0.010
MeO-Phe	0.33 ± 0.02	1.3 ± 0.1	0.097 ± 0.006	1.7 ± 0.2	0.034 ± 0.033
CN-Phe	0.42 ± 0.04	1.4 ± 0.2	0.11 ± 0.01	1.6 ± 0.2	0.066 ± 0.046
			Thr (B+1) (Thr 155) A2B3		
Thr	0.41 ± 0.02	1.4 ± 0.1	0.09 ± 0.01	1.6 ± 0.1	0.044 ± 0.007
Tah	0.37 ± 0.02	1.3 ± 0.1	1.71 ± 0.14	1.2 ± 0.1	0.018 ± 0.013
			Muscle-type Receptor*		
			Thr (B+1) (Thr150)		
Thr	*0.83 ± 0.04*	*1.8 ± 0.1*	*57 ± 2*	*2.1 ± 0.1*	ND
Tah	*0.25 ± 0.01*	*1.4 ± 0.1*	*92 ± 4*	*1.7 ± 0.1*	ND
			Muscle-type Receptor α1(G153K)		
Trp	0.019 ± 0.001	1.5 ± 0.1	0.59 ± 0.04	1.8 ± 0.2	ND
F-Trp	0.094 ± 0.004	1.6 ± 0.1	2.8 ± 0.1	1.3 ± 0.1	ND
F_2-Trp	0.079 ± 0.004	1.3 ± 0.1	2.3 ± 0.1	1.3 ± 0.1	ND
F_3-Trp	1.05 ± 0.03	1.3 ± 0.1	11 ± 1	1.5 ± 0.1	ND
F_4-Trp	7.5 ± 0.5	1.2 ± 0.1	32 ± 4	1.5 ± 0.2	ND
CN-Trp	2.4 ± 0.1	1.5 ± 0.1	36 ± 3	1.7 ± 0.2	ND
Br-Trp	0.047 ± 0.001	1.4 ± 0.1	4.45 ± 0.42	1.2 ± 0.1	ND

Table 5.1. Functional characterization of α4(L9'A)β2 wild type A3B2, and A2B3 TyrA, TrpB, TyrC1, TyrC2, Thr (B+1), and muscle-type receptor Thr (B+1) and α1(G153K) nAChRs. All muscle-type receptors contain a L9'S mutation in the β subunit. EC_{50} values (μM), Hill coefficients (n_H) and current size at +70 mV (normalized to current size at -110 mV). ND = not determined. *Muscle-type Thr150 and Thr150Tah values (*italicized*) were previously reported*(25)*.

5.4.3 Supplementary Discussion

5.4.3.1 Controlling the Stoichiometry of α4β2 Receptors

As in the case of previous studies[20,21], we find that the stoichiometry of α4β2 receptors can be controlled by altering the ratio of the subunits of mRNA during injection. Our criteria for defining a pure population of A2B3 α4(L9'A)β2 receptors are whole-cell dose-response curves that fit a single component and very strong inward rectification such that (I_{max} at +70 mV)/(I_{max} at -110 mV) < 0.1. An alternative analysis which can also demonstrate a mixed population of receptors is the production of intermediate EC_{50} values when fit to a single component. As shown below, by a 3:1 α4:β2 mRNA ratio, the EC_{50} value has reached the higher EC_{50} value, which is the A2B3 stoichiometry.

α4:β2 ratio	**EC_{50} (μM ACh)**
100:1	0.023 ± 0.002
10:1	0.023 ± 0.001
6:1	0.15 ± 0.02
3:1	0.44 ± 0.03
1:1	0.40 ± 0.01
1:10	0.43 ± 0.02

Injection of an mRNA ratio α4(L9'A):β2 of 10:1 or higher produces pure populations of A3B2, while a ratio of 1:3 or lower guarantees a pure population of A2B3. In the experiments described here, we injected a 1:3 ratio of mRNA.

Note that the α4(L9′A) mutation lowers EC_{50} in a multiplicative fashion, depending on how many α4 subunits are present. As such, our A3B2 receptor (with three L9′A mutations) actually has a lower EC_{50} than our A2B3 receptor

(with two L9′A mutations), even though the binding site from the A2B3 stoichiometry is clearly that of the high sensitivity receptor.

5.4.3.2 TyrA, TyrC1, and TyrC2 Display Similar Interactions in Muscle-Type and α4β2

In addition to TrpB, we have performed extensive studies of other aromatic residues in and around the aromatic box (**Table 5.1**). Briefly, when comparing α4β2 to the muscle-type receptor, very similar results are seen. TyrC1 is very sensitive to substitution, establishing a key role for this residue, likely in receptor gating. TyrA appears to be a hydrogen bond donor (large effects for Phe and MeO-Phe substitutions), and while it is generally more sensitive to perturbations in the neuronal receptor, the basic trends are the same. TyrC2 is very permissive in both the muscle-type and α4β2 receptors.

5.4.3.3 Single-Channel Recording and Analysis of Select α4β2 Receptors

Here we have used single-channel measurements to convincingly establish that the fluorination approach is changing agonist binding, not channel gating. Macroscopic data establish the large successive shift in function (EC_{50}) upon fluorination, and single-channel data establish that gating is unperturbed, since the probability that the channel is open, P_{open}, is essentially indistinguishable for wild type and F_3-TrpB at corresponding points on the dose-

response relation. At saturating agonist concentrations, $P_{open,max}$ approaches $\Theta/(\Theta+1)$ for the 4-state model given below. Our analysis starts by comparing the P_{open} values at the macroscopic EC_{50}. The P_{open} values that we report are directly related to the gating equilibrium constant, Θ, by $½ * \Theta/(\Theta+1)$.

Definition of clusters and calculation of P_{open}

Because (a) single-channel channel measurements of P_{open} are seldom reported for $\alpha4\beta2$ receptors, and (b) we find that P_{open} depends strongly on the value chosen as the critical closed duration, τ_{crit}, we report P_{open} values for the range 5 ms ≤ τ_{crit} ≤ 5000 ms using two different methods to identify τ_{crit} (below and **Figure 5.4**, above). The first is the commonly used method: the longest one or more components of the closed dwell time histogram are considered as sojourns in the desensitized state for all of the channels in the patch(*37*). The value for τ_{crit} was defined based on the closed dwell time histograms fitted with multiple components, as previously described(*38*). These components are similar for wild type and F_3-TrpB, resulting in similar τ_{crit} values: τ_{crit1} of 1470 vs 1530 ms and τ_{crit2} of 42 vs 52 ms, respectively. The similarity of the closed dwell time histograms for these receptors (and the resultant τ_{crit} values) can be taken as evidence that fluorination does not significantly impact desensitization. Moreover, whole-cell data show that the wild type and the F_3-TrpB receptors exhibit similar extent and kinetics of macroscopic desensitization (data not shown). When either of the τ_{crit} values calculated from the closed dwell time histogram is applied, P_{open}

is essentially indistinguishable for wild type and F_3-TrpB. The P_{open} values for wild type and F_3-TrpB at τ_{crit1} and τ_{crit2} are given here ± s.e.m.

Receptor	**P_{open} (τ_{crit1})**	**P_{open} (τ_{crit2})**
Wild type	0.07 ± 0.02	0.88 ± 0.06
F_3-TrpB	0.06 ± 0.03	0.82 ± 0.05

Because our recordings are at an intermediate concentration (EC_{50}), some closed dwells may reflect agonist dissociation, others may reflect channel closure followed by re-opening without agonist dissociation, while still others may reflect sojourns in desensitized states of varying duration. As a result, a definition of τ_{crit} can be distorted by the relatively low number of long non-conducting sojourns. Thus, we also compared calculated P_{open} values for a wide range of possible τ_{crit} values (3 orders of magnitude), including those calculated from the closed dwell time histogram. **Figure 5.9** shows that, regardless of how we define τ_{crit} (5 ms ≤ τ_{crit} ≤ 5000 ms), no systematic difference in P_{open} is observed between wild type and F_3-TrpB with nicotine as agonist—their gating behaviors are essentially indistinguishable. Thus, the value chosen for τ_{crit} does not affect our conclusion that the gating behavior, as measured by P_{open}, is not significantly impacted upon fluorination in the F_3-TrpB mutant.

A small shift in the channel open duration does not account for the EC_{50} shift of F_3-TrpB

Fits to open dwell time histograms reveal that the main component of the channel open duration, which accounted for > 90% of the conductance in both wild type and F_3-TrpB receptors, is shifted 2.4-fold, from 23 ms (wild type) to 9.6 ms (F_3-TrpB). Because the closed dwell time histograms, fitted with multiple components, displayed similar contributions from the major components for wild type and F_3-TrpB, interpreting the 2.4-fold shift in open duration in terms of the channel closing rate, α, would imply a modest 2.4-fold shift in Θ in the F_3-TrpB receptor. We consider these results in terms of a standard, linear 4-state model with two sequential agonist binding steps followed by a gating step:

$$A + R^c \underset{k_{-1}}{\overset{2k_1}{\rightleftharpoons}} A + AR^c \underset{2k_{-1}}{\overset{k_1}{\rightleftharpoons}} A_2R^c \underset{\alpha}{\overset{\beta}{\rightleftharpoons}} A_2R^o$$

for which,

where K_D is the equilibrium agonist dissociation constant (k_{-1}/k_1) and Θ is the gating equilibrium constant (β/α). We see that a 2.4-fold change in Θ accounts for at most a 1.5-fold shift in EC_{50}. Thus, both comparison of P_{open} as well as consideration of kinetics, to the extent possible for data at EC_{50}, indicate that the overwhelming majority of the 15-fold increase in nicotine's EC_{50} in the F_3-TrpB receptor versus wild type is caused by changes to binding rather than the subsequent conformational changes that open the channel. Taken together, macroscopic and single-channel experiments show that fluorination modulates nicotine binding in a way that is systematically correlated to the energy of a cation-π interaction.

5.5 Additional Figures: Single-Channel Nicotine Data and Dwell Time Histograms

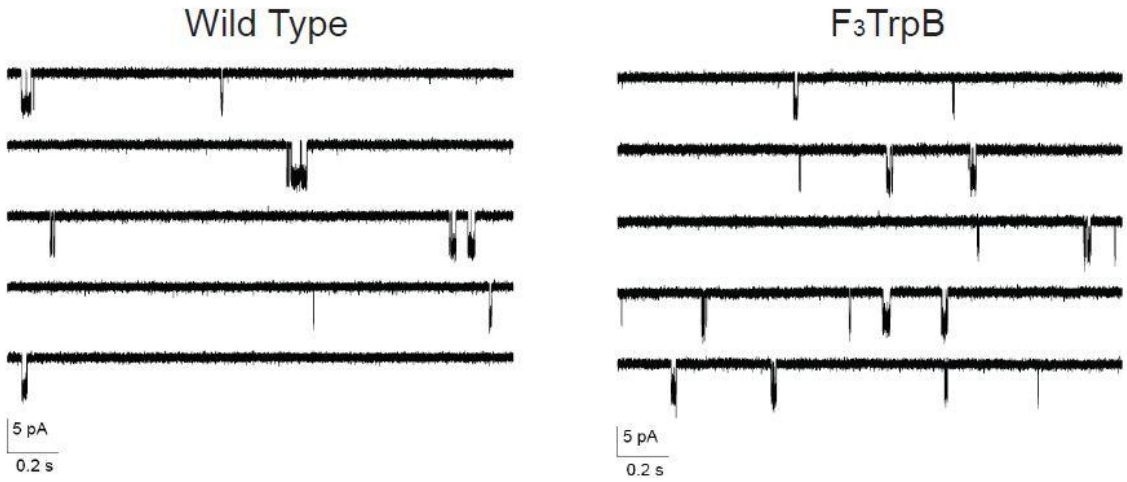

Figure 5.10. This figure shows longer traces of the single-channel data that was shown in Figure 5.6, above. As in that figure, nicotine was applied at macroscopic EC_{50} and channel openings are shown as downward deflections.

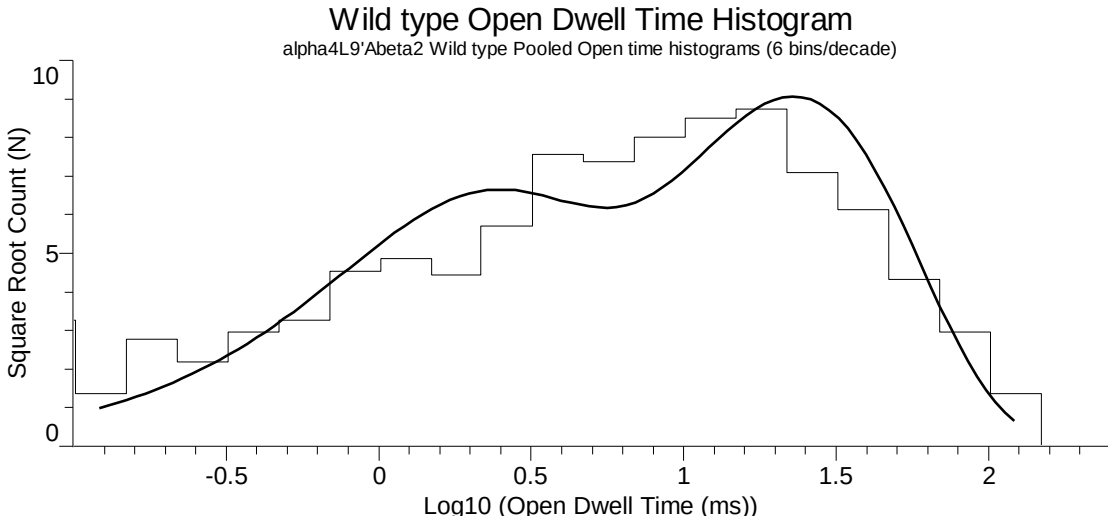

Figure 5.11. Pooled open dwell time histogram for multiple patches of single-channel events of wild type A2B3 with nicotine applied at its EC_{50}. A 2 component fit is shown as an overlaying black line. The components (% in parenthesis) are: 23 ms (66%) and 1.7 ms (34%).

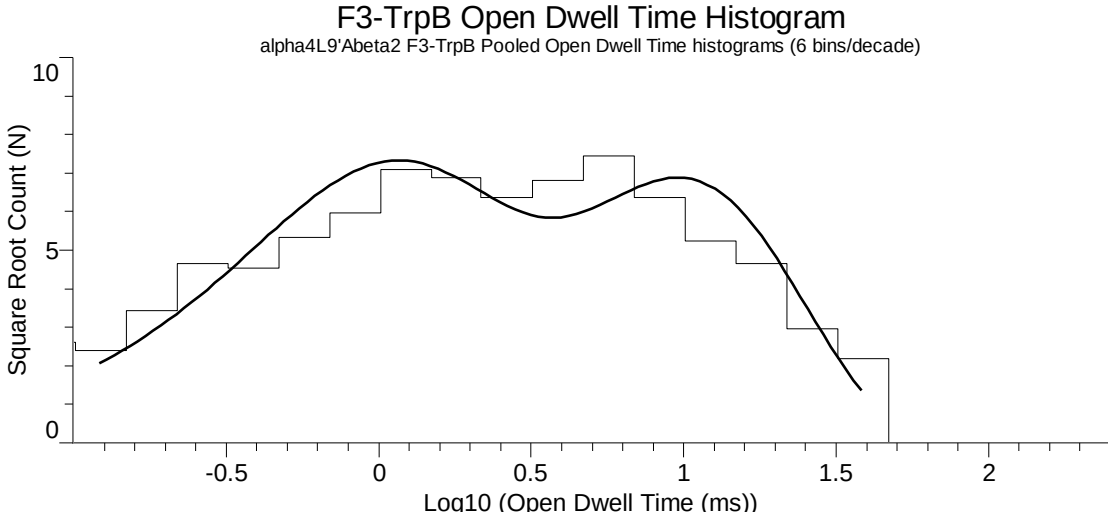

Figure 5.12. Pooled open dwell time histogram for multiple patches of single-channel events of F_3-TrpB in A2B3 with nicotine applied at its EC_{50}. A 2 component fit is shown as an overlaying black line. The components (% in parenthesis) are: 9.6 ms (55%) and 0.87 ms (45%).

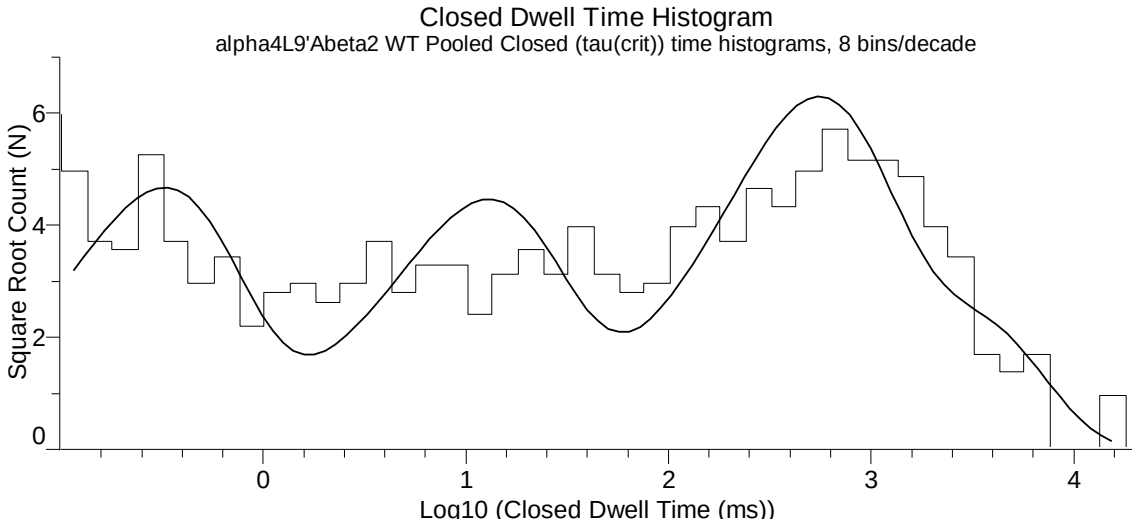

Figure 5.13. Pooled closed dwell time histogram for multiple patches of single-channel events of wild type A2B3 with nicotine applied at its EC_{50}. A 4 component fit is shown as an overlaying black line. The components (% in parenthesis) are: 2800 ms (15%), 480 ms (33%), 12 ms (25%), and 0.31 ms (27%).

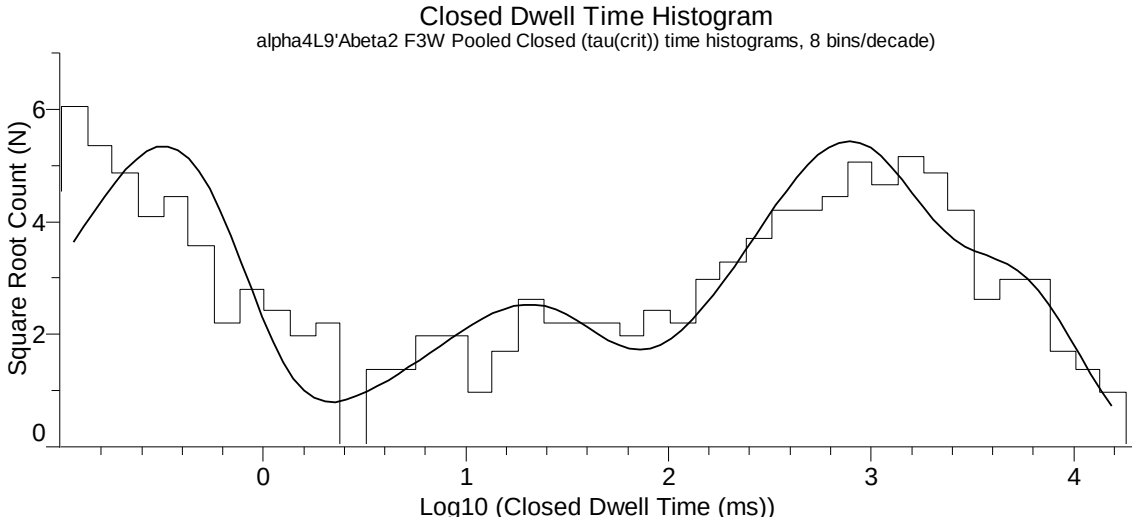

Figure 5.14. Pooled closed dwell time histogram for multiple patches of single-channel events of F_3-TrpB in A2B3 with nicotine applied at its EC_{50}. A 4 component fit is shown as an overlaying black line. The components (% in parenthesis) are: 4000 ms (22%), 610 ms (28%), 17 ms (15%), and 0.32 ms (35%).

5.6 Introduction to Varenicline Binding to Nicotinic Acetylcholine Receptors

Having shown that nicotine binds to neuronal nAChRs via a cation-π interaction to TrpB, a natural next question is how this information is relevant to the treatment of nicotine addiction. Cytisine (**Figure 5.15**) is a small molecule that has been used to help people quit smoking in Eastern Europe for several decades(*39*). Cytisine is a partial agonist of neuronal nAChRs(*40*), though it has markedly different efficacy at the A3B2 and A2B3 stoichiometries. Cytisine's structure displays some key features of the nicotinic pharmacophore(*41*), including a hydrogen bond acceptor and a positive charge. These features are also present in ACh and nicotine (**Figure 5.15**).

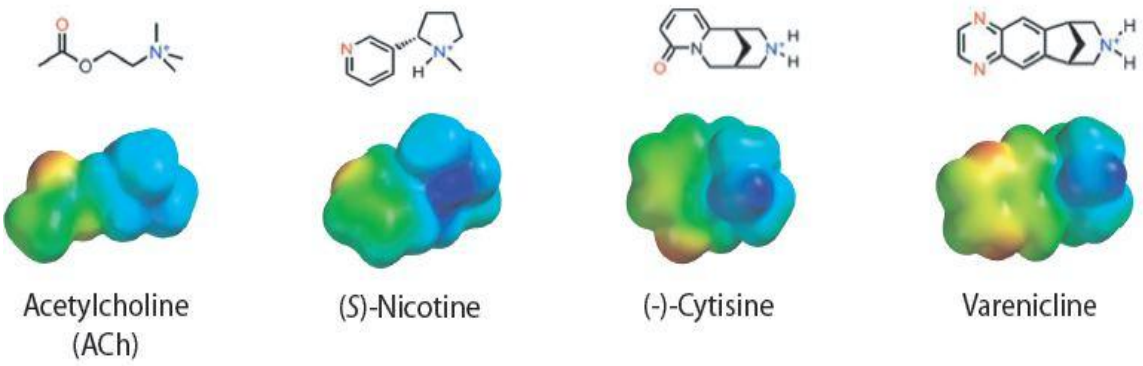

Figure 5.15. 4 agonists of the neuronal nAChRs. Upper) The molecules are drawn with hydrogen bond acceptors in red and cationic nitrogens in teal. Lower) The corresponding electrostatic potential surface for each molecule. In these plots, 'warmer colors' (red and orange) represent regions of higher electron density, as measured by interaction with a probe positive charge (sodium ion). 'Colder colors' (teal, blue) represent relatively positively charged regions.

However, at best, cytisine increases smoking cessation < twofold above placebo(*2*). One path to the design of small molecule therapeutic strategies that aid smoking cessation began with cytisine. Using cytisine as a lead compound and making direct modifications to it produced α4β2 antagonists (**Figure 5.16**). A revised strategy was to develop a partial agonist of α4β2 that also had a very high affinity for the receptor.

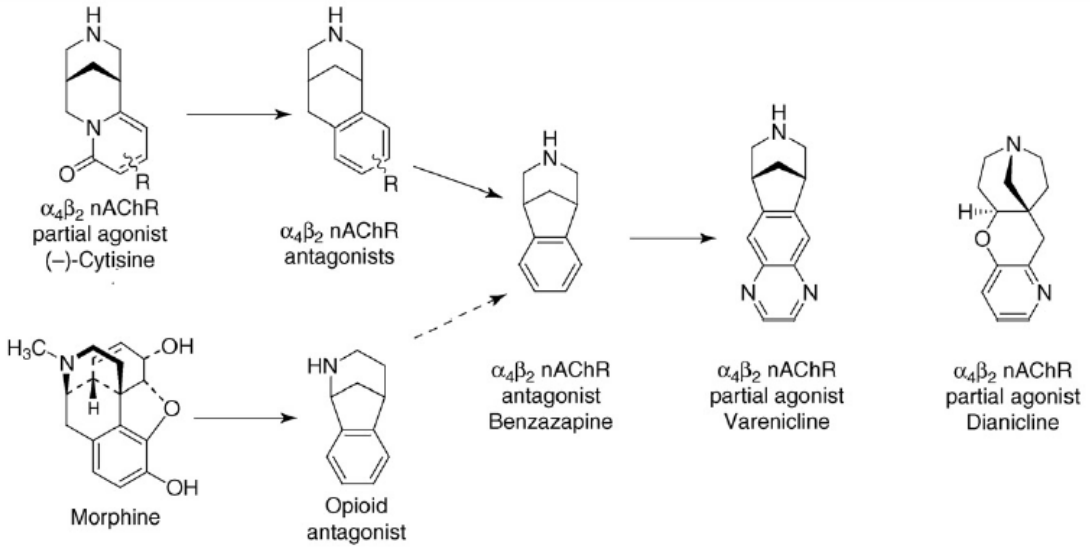

Figure 5.16. This figure shows the structures of several molecules that have played key roles in the history of strategies for smoking cessation as well as ongoing efforts to improve these strategies. Varenicline (Chantix®) is the focus of the remaining studies in this chapter. Figure is from(*2*).

In May of 2006 varenicline (Chantix®) was approved as an aid to smoking cessation treatments. It is believed that varenicline achieves its therapeutic effect by binding the α4β2 receptor, where it acts as a partial agonist (**Figure 5.17, Left**). With high binding affinity, varenicline appears to act as a competitive antagonist of nicotine when they are simultaneously present (**Figure 5.17, Right**), though the detailed mechanism of action is not known(*2*).

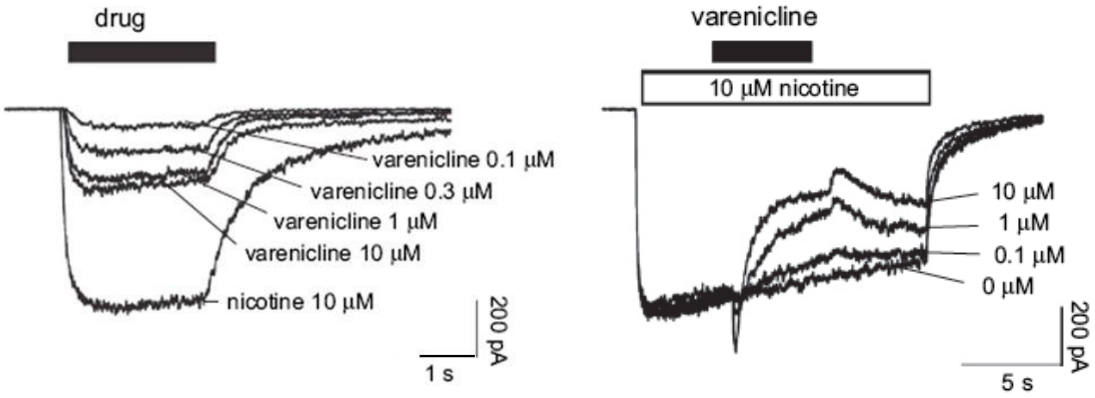

Figure 5. 17. Left) The current responses of α4β2 receptors to various doses of varenicline and a high dose of nicotine. In these experiments in HEK cells, varenicline's efficacy relative to nicotine was ~ 45%. Right) When varenicline is added to α4β2 receptors activated by nicotine, the nicotine response is decreased in a dose-dependent way. Figures are from(*42*).

Varenicline more than doubles the chance of smoking cessation, from 18% with placebo to 44%; the odds of long-term abstinence (through 1 year) are more than threefold higher than placebo with varenicline(*2*). While clearly a major benefit in fighting smoking addiction, these numbers also highlight how addictive nicotine is. Even with varenicline, most people still can't quit smoking. These numbers also indicate the need for continued improvement in smoking cessation treatments. Varenicilne was designed specifically to have high potency at α4β2, but not α3β4 human nAChRs(*2, 42*). However, it is becoming increasingly clear that other receptors also can be activated by many nAChR agonists. This can lead to unwanted side effects. Additional concerns have been raised specifically about varenicline producing adverse mental health consequences, including suicidal ideation and suicide(*43, 44*).

In order to design a drug that is more effective and has better specificity, the detailed mechanism of action must be known. We therefore sought to

determine how varenicline binds to the A2B3 and A3B2 α4β2 nAChRs. Whole-cell experiments performed by Ximena Da Silva, Nyssa Puskar, and Angela Blum indicate that varenicline binds to these neuronal receptors in a similar way as nicotine. Specifically, a systematic increase in EC_{50} was seen upon successive fluorination at TrpB. We then used single-channel recording with varenicline to determine if the gating properties of the receptor change upon fluorination of TrpB.

5.7 Results

Single-channel recording was performed in the cell-attached configuration on the wild type A2B3 and A3B2 receptors as well as A2B3 and A3B2 receptors with F_3W introduced at TrpB by nonsense suppression. In each case, data reported here are for varenicline applied at 10 times the EC_{50}.

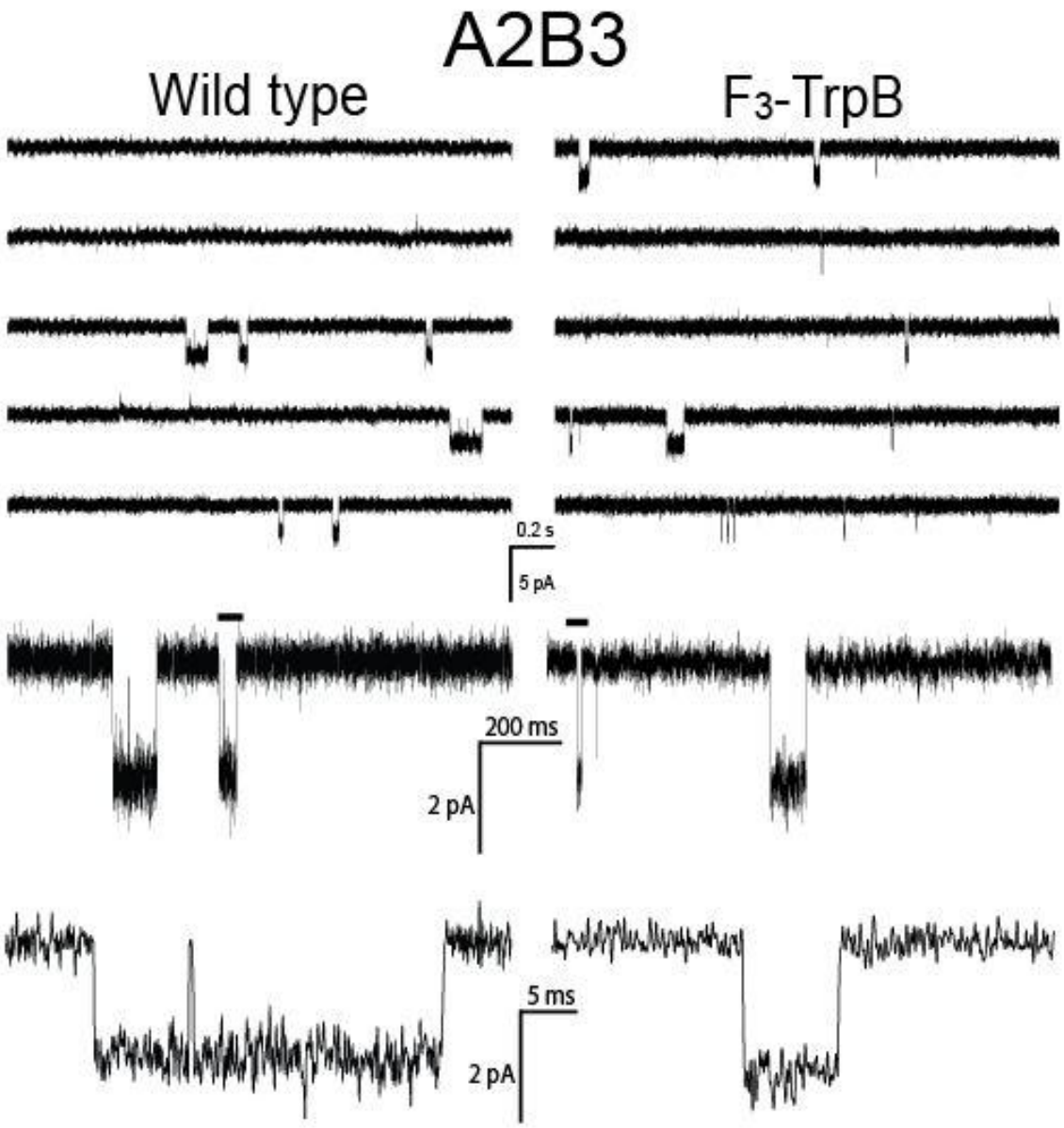

Figure 5.18. Single-channel records of wild type A2B3 (conventional expression; Left) and F_3-Trp introduced at TrpB (nonsense suppression; Right). All recordings are in the cell-attached configuration with a pipette potential of +60 mV. Data are filtered at 2 kHz for display and openings are shown as downwards deflections. Varenicline concentrations (in the pipette) are: wild type (28.5 nM) and F_3-TrpB (270 nM). The single-channel conductances were 43 pS and 42 pS, respectively. Each set of traces represents 10 seconds (upper), 1 second (middle), and 50 ms (lower). The lower traces are expansions of the regions in the middle traces designated with bar over the trace.

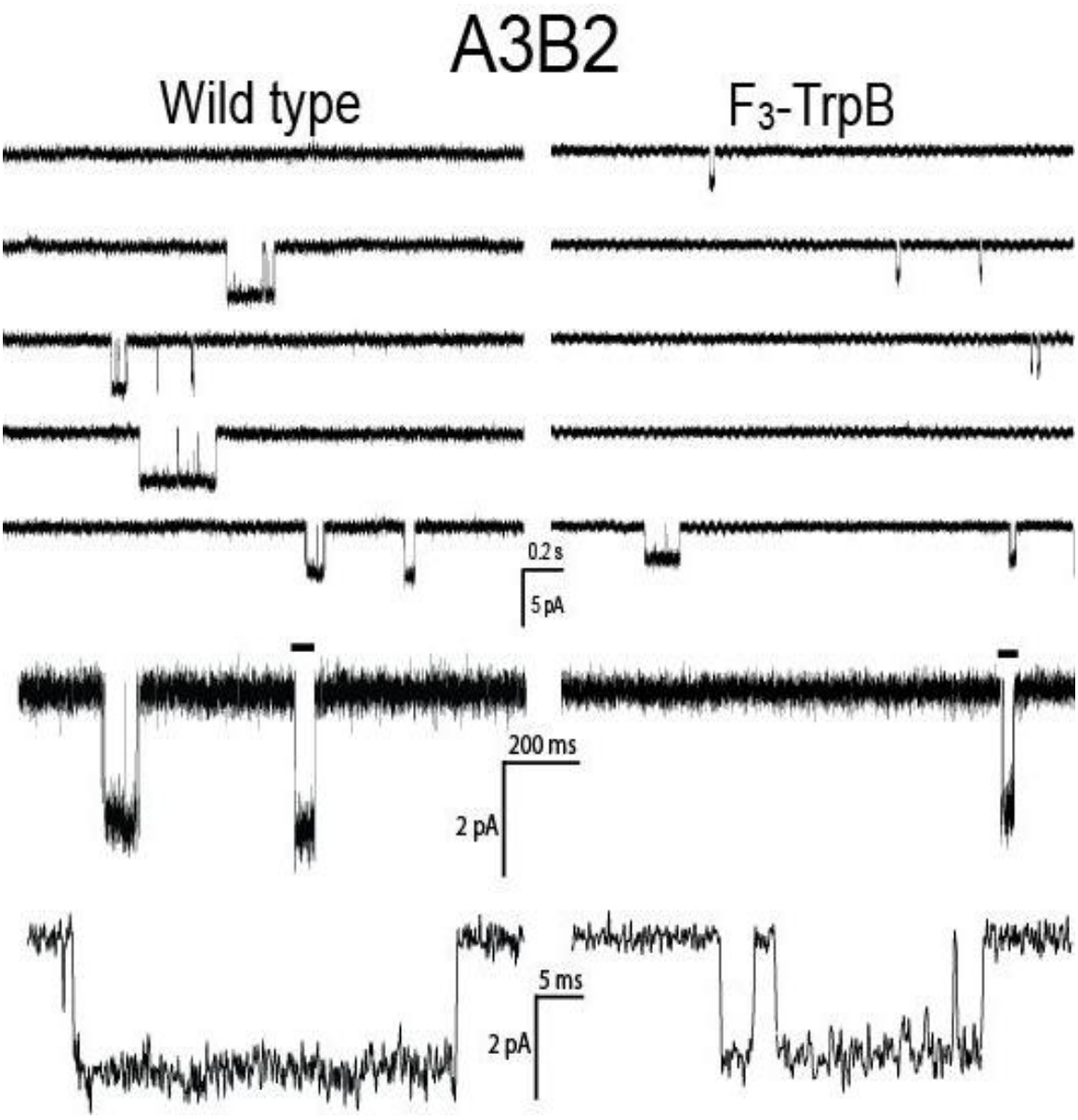

Figure 5.19. Single-channel records of wild type A3B2 (conventional expression; Left) and F_3-Trp introduced at TrpB (nonsense suppression; Right). All recordings are in the cell-attached configuration with a pipette potential of +60 mV. Data are filtered at 2 kHz for display and openings are shown as downwards deflections. Varenicline concentrations (in the pipette) are: wild type (9 nM) and F_3 F_3-TrpB (120 nM). The single-channel conductances were slightly variable: wild type A3B2 (50–55 pS), and ~ 40 pS for F_3-TrpB. Each set of traces represents 10 seconds (upper), 1 second (middle), and 50 ms (lower). The lower traces are expansions of the regions in the middle traces designated with bar over the trace.

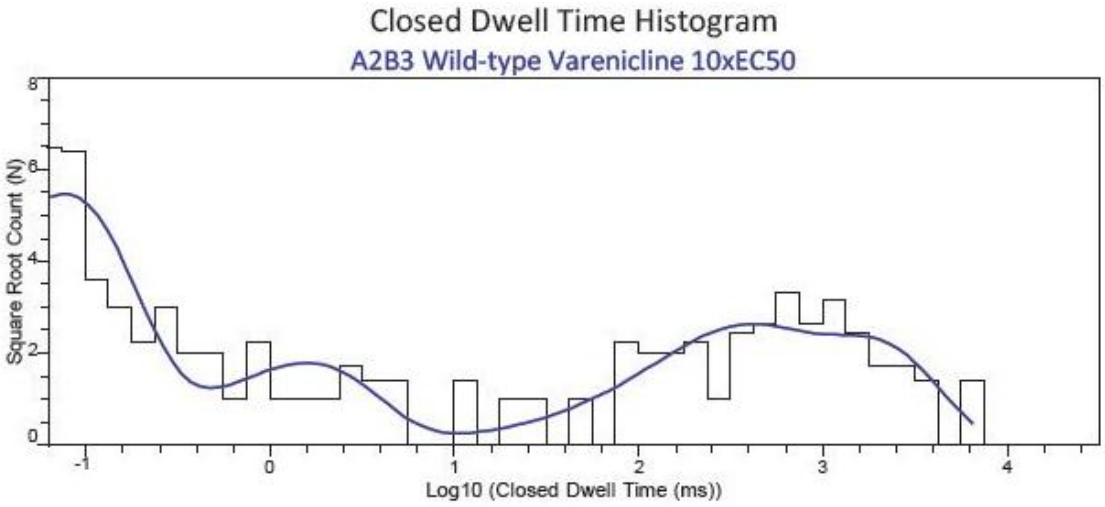
Closed Dwell Time Histogram
A2B3 Wild-type Varenicline 10xEC50
Square Root Count (N)
Log10 (Closed Dwell Time (ms))

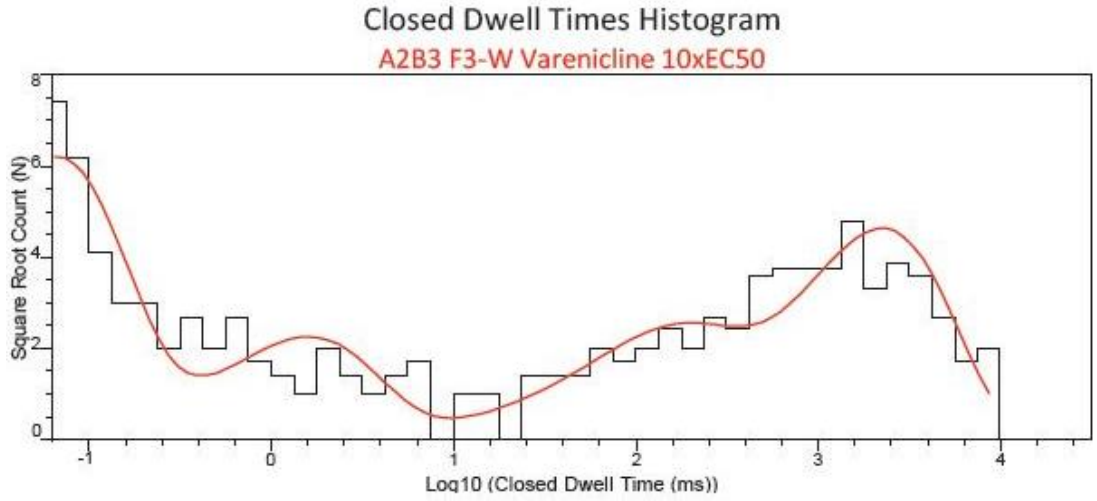
Closed Dwell Times Histogram
A2B3 F3-W Varenicline 10xEC50
Square Root Count (N)
Log10 (Closed Dwell Time (ms))

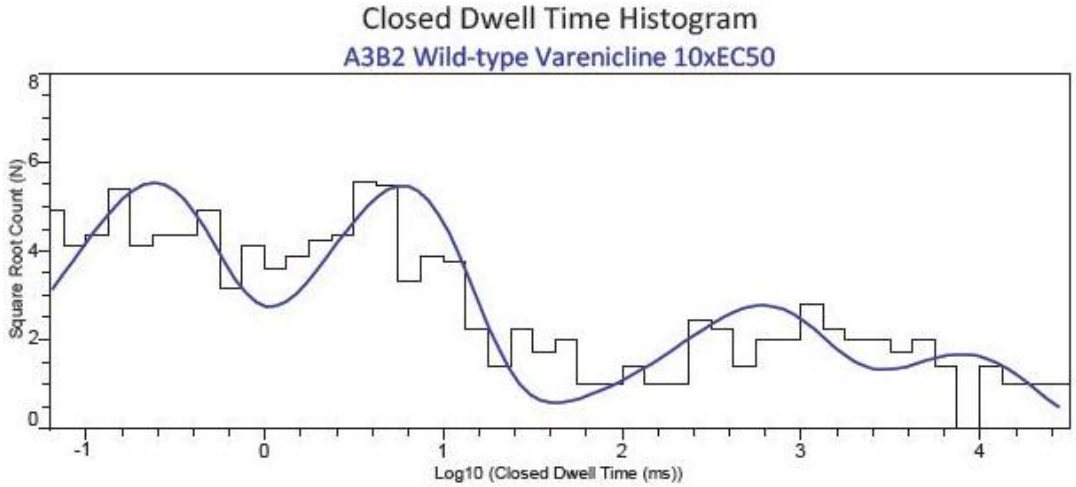
Closed Dwell Time Histogram
A3B2 Wild-type Varenicline 10xEC50
Square Root Count (N)
Log10 (Closed Dwell Time (ms))

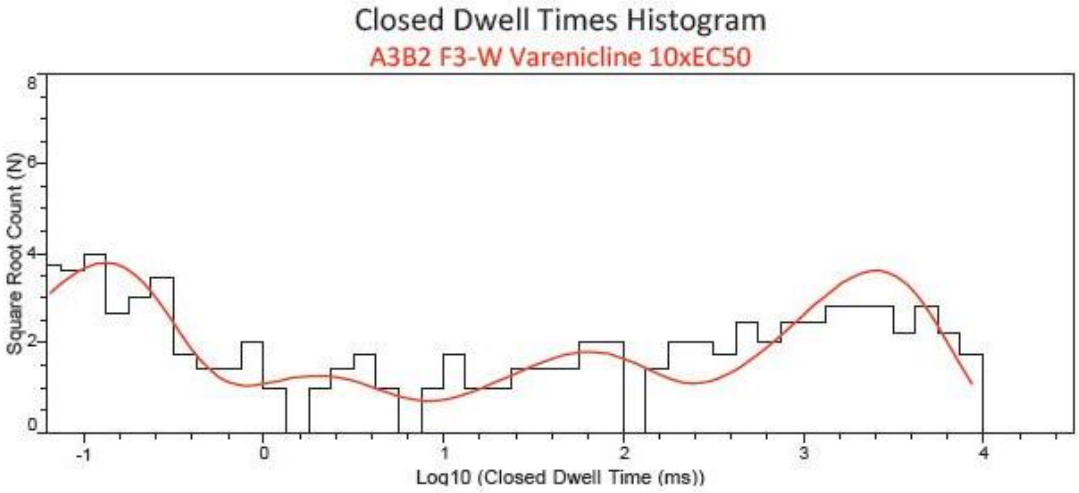

Figure 5.20. (Above and previous page) 4 closed dwell time histograms each representing data from 1 patch for each of the 4 receptors studied in these single-channel experiments. In each case, varenicline is applied at 10 times the respective macroscopic EC_{50} values at the concentrations stated above. In each case, the histogram is fitted to 4 components. These histograms were used to determine the values of τ_{crit}.

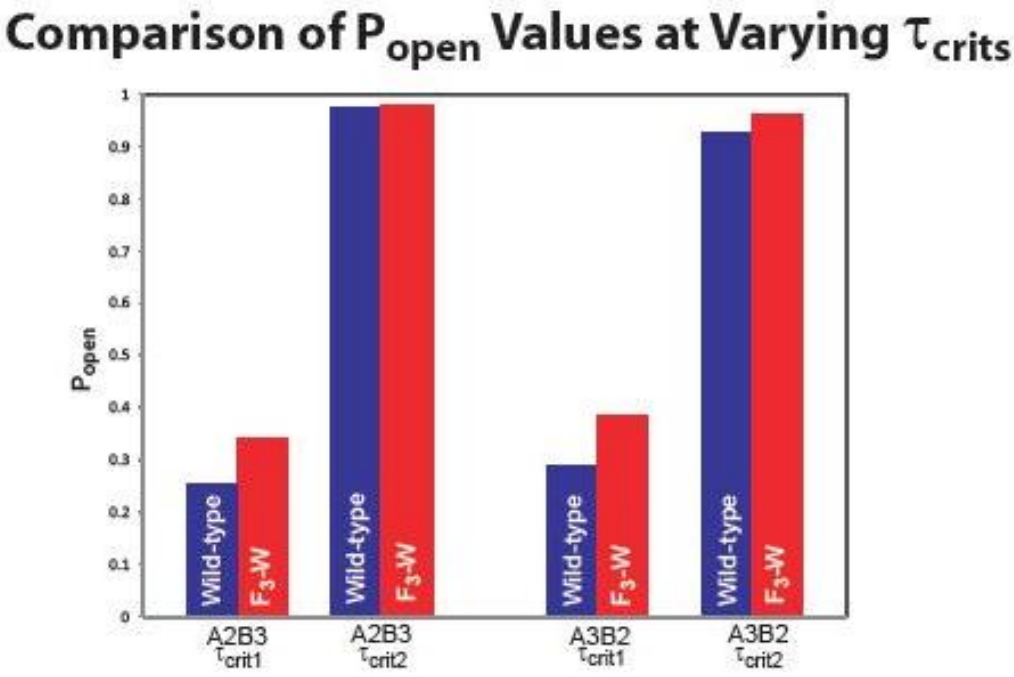

Figure 5.21. Calculated P_{open} values when 2 different values of τ_{crit} are used. Under both analyses, for both A2B3 and A3B2, the difference in P_{open} between wild type and F_3W at TrpB is minimal (see discussion).

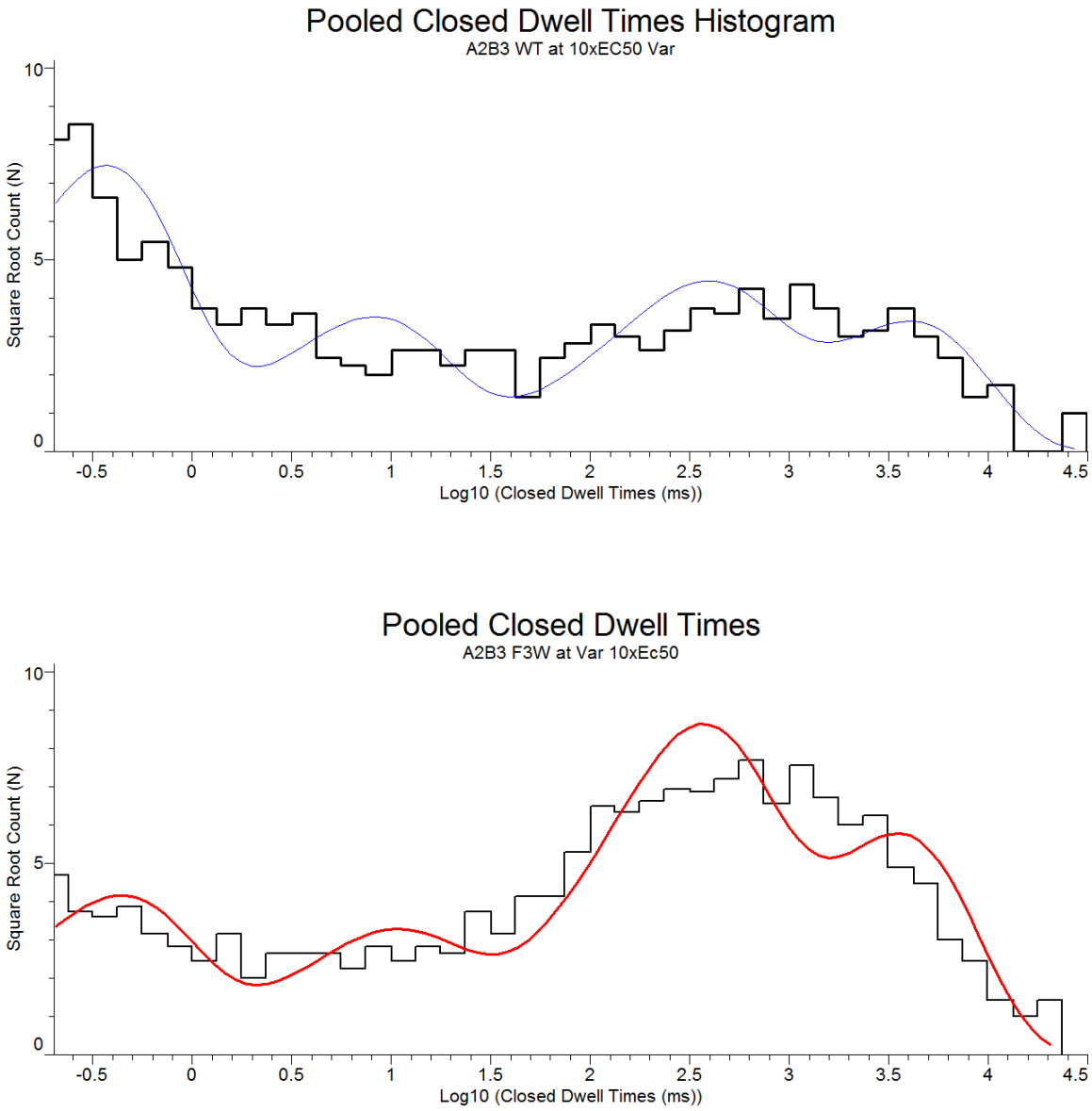

Figure 5.22. Pooled closed dwell time histograms of multiple patches, each at 10 times the respective macroscopic EC_{50} values for wild type A2B3 (28.5 nM varenicline) and A2B3 with F_3W at TrpB (270 nM varenicline). There is a greater contribution from the long dwell time components in the F_3-TrpB (lower) histogram than the wild type (upper) distribution (see discussion).

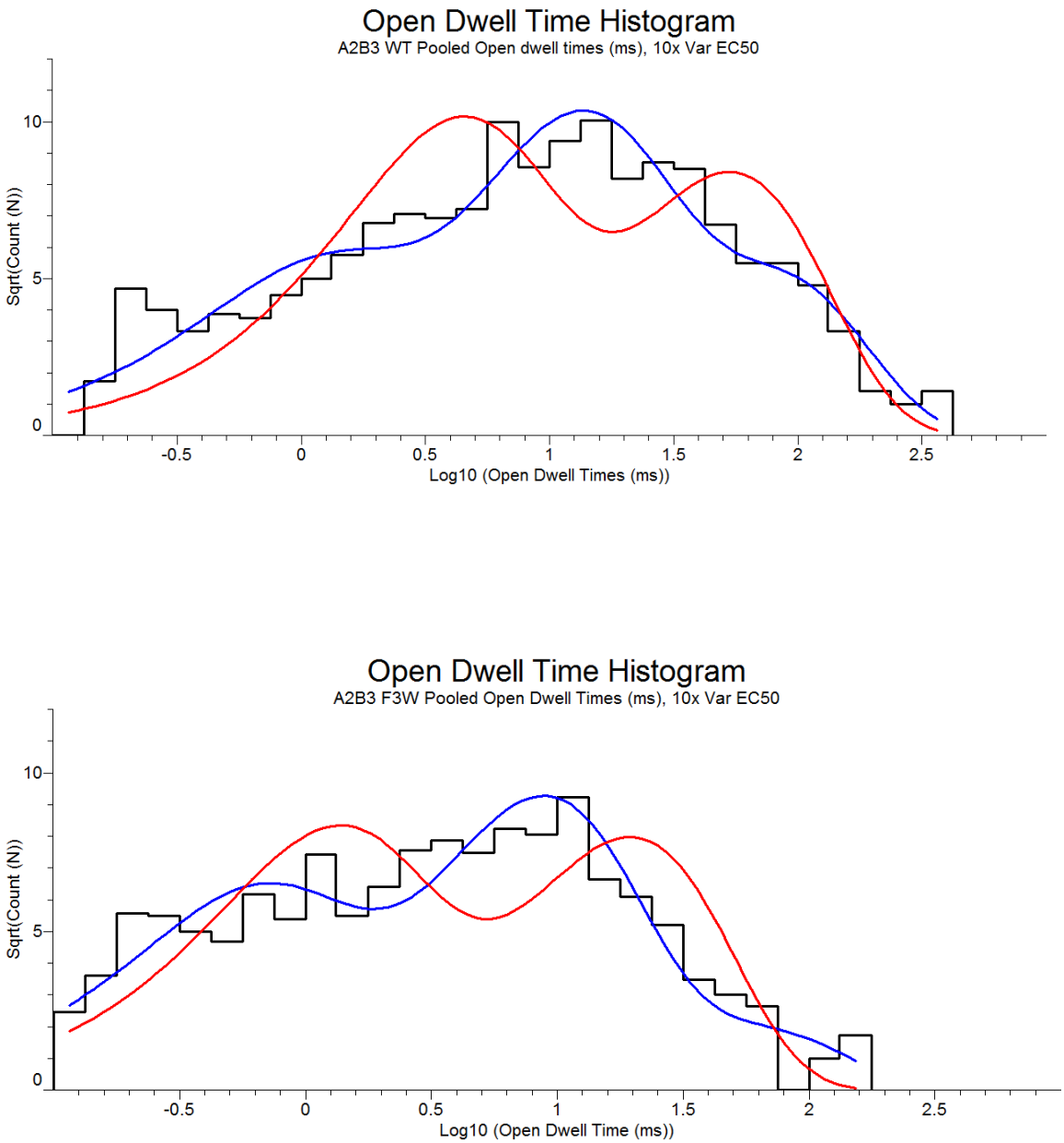

Figure 5.23. Pooled open dwell time histograms of multiple patches each at 10 times the respective macroscopic EC_{50} values for wild type A2B3 (28.5 nM varenicline) and A2B3 with F_3W at TrpB (270 nM varenicline). Overlaying the histogram are shown 2-component fits (red) and 3-component fits (blue). For the 2 component fit, the components (% in parenthesis) are (upper histogram, wild type): 53 ms (50%) and 3.8 ms (50%); (lower histogram, F_3-TrpB): 19 ms (53%) and 1.2 ms (47%). It is not clear what states the two or three open dwell times in the above histogram represent. However, openings of monoliganded receptors could account for at least one additional component (see discussion).

5.8 Discussion and Future Studies

5.8.1 P_{open} and Dwell Times

The quantitative analysis of P_{open} under different analysis scenarios shows that P_{open} is similar for wild type and F_3-TrpB A2B3 and A3B2 (**Figure 5.21**). This is true whether τcrit1 or τcrit2 are used. These different values of τcrit impact which of the long components of the closed dwell time histogram are excluded from the calculation of P_{open}. Either way, the conclusion is the same—P_{open}, which depends only on the gating equilibrium constant, Θ—is not significantly altered by incorporation of F_3W at TrpB at either stoichiometry. Specifically, as with nicotine, successive fluorination of TrpB causes a systematic decrease in varenicline's potency (increase in EC_{50}). EC_{50} depends on just two properties: binding and gating. Thus, since this single-channel data indicate that this decrease in potency is not caused by any significant change in the channel's gating properties, based on this combination of single-channel and whole-cell data, we conclude that varenicline makes a cation-π interaction to TrpB.

A more detailed analysis of the dwell time histograms is instructive. Here I will consider the A2B3 data in detail. Open dwell times give information about the channel closing rate, α. As with the nicotine A2B3 data, the open dwell time histograms and resulting fitted distributions are quite similar for the wild type and F_3W-TrpB. Specifically, consider the open dwell time distributions when fitted to two components (blue lines in **Figure 5.23**). Both components of the wild type distribution are shifted to ~ threefold longer times than in F_3-TrpB. Specifically,

the longest component shifts 2.7-fold from 53 ms in wild type to 19 ms, and the shorter component shifts 3.3-fold from 3.8 ms in wild type to 1.6 ms. Since both components contribute roughly equally (50% versus 53% and 50% versus 47%; see **Figure 5.23**), we can quantitatively relate these shifts to potency. Based on the quantitative relationship between EC_{50} and Θ given in Section 5.4.3, the decrease in open dwell time for the F_3-TrpB receptor can account for, at most, a 1.7-fold increase in EC_{50}. This is a small amount of the actual 9.5-fold EC_{50} shift (2.85 nM to 27 nM).

A similar quantitative analysis of the A2B3 closed dwell time histograms to determine kinetic parameters would require recording with varenicline across multiple concentrations. However, qualitatively and based on fairly similar τ_{crit} values, the closed dwell time histograms do not appear to indicate a significant systematic shift in the duration of any of the closed dwell time components. On the other hand, there is an increase in the relative contribution of the two longer closed components in **Figure 5.22** from wild type to F_3-TrpB. The difference in these relative contributions to the long closed components is also apparent qualitatively in some single-channel traces—the raw P_{open} values in some wild type and F_3-TrpB varenicline patches appear different. Although these impact the apparent P_{open}, these longest closed dwells (usually 1–10 seconds) almost certainly reflect a desensitized state for these recordings, since they are performed at 10 times EC_{50}. Additionally, the rate of entry into the desensitized state for F_3-TrpB may be faster than for wild type, producing briefer clusters.

These changes to desensitization should not impact EC_{50}, so they do not factor into the quantitative analysis except for the purposes of defining τ_{crit}.

5.8.2 Recording and Analysis at Low Agonist Concentrations

In general, it is important when working with potent agonists such as varenicline (and epibatidine) to take into account the experimental concentrations used. For experiments at nM or lower concentrations, the forward rate for agonist association (k_+) can impact data analysis. For example, in single-channel recording, assuming a k_+ value of 10^8 M^{-1} s^{-1}, an experiment at 100 nM will produce closed dwells of ~ 100 ms that correspond to this binding rate. For whole-cell experiments, time resolution isn't quite as high. Nevertheless, a drug application of 0.1 nM could require ~ 100 seconds to reach the maximal response based on the forward binding rate alone. It is therefore particularly important to inspect opus traces at concentrations < ~ 10 nM to ensure that they reach a stable, maximal current value during the drug application.

5.8.3 Nicotine, Varenicline, and Partial Agonism

Varenicline is a partial agonist, and the single-channel conductance does not appear significantly lower for it than for nicotine. Therefore, τ_{crit1}, which produces P_{open} values of ~ 0.2–0.4 is probably a more realistic value. In fact, these values produce agreement with other data. For example, compare P_{open} values in this range to the relative activation achieved by saturating doses of varenicline and nicotine in **Figure 5.17**(*2*).

In further single-channel work characterizing these agonists, it would be interesting to elucidate the mechanism of partial agonism for nicotine and varenicline. This could be pursued in the context of recent models of nAChR partial agonism(*45, 46*). Consistent with some of these models, I observe brief closures in α4β2 single-channel data with both nicotine and varenicline. Since these occur even at low concentrations—nM in these experiments—they are probably not due to open channel block. A more likely explanation is that they correspond to the channel re-opening and therefore reflect the channel opening rate, β. Since these are brief closures, β is large. From the closed dwell time histograms above (**Figures 5.13, 5.14,** and **5.22**) there is one component that is << 1ms.

5.8.4 Other Further Studies

I regularly observe multiple components in open dwell time histograms for nAChRs, including muscle-type and neuronal receptors. This is even true for spontaneous openings (of α1β1L9'SgγδL9'S; see Chapter 4). When agonist is present, for nAChRs with two binding sites different open dwell times could correspond to receptors that have agonist bound at just one of the binding sites. These are termed monoliganded openings. Another possibility is that the two different monoliganded openings of receptors with two nonequivalent binding sites have different durations and/or conductances. The binding sites of the muscle-type fetal nAChR ($(\alpha1)_2\beta1\gamma\delta$) do not have equivalent K_Ds(*47-49*). If monoliganded openings of different binding sites account for some of the

different components of the open dwell time histograms, I would predict that the more similar binding site affinities of the ($(\alpha1)_2\beta1\varepsilon\delta$) receptor (adult nAChR) would produce open dwell time distributions that were more similar than those of the fetal type.

For both nicotine and varenicline, the agonist potencies are markedly different between the A2B3 and A3B2 stoichiometries. Determining the cause of this difference would be of interest. These further studies would be most interesting on wild type receptors without the L9'A mutation, which significantly impacts agonist potency. However, without the L9'A mutation α4β2 receptors, especially the A2B3 stoichiometry, express at relatively low levels. The next chapter develops and implements methods for single-channel characterization of the wild type α4β2 receptor.

5.9 Materials and Methods for Varenicline Experiments

5.9.1 Whole-Cell Electrophysiological Characterizations of the Agonist-Induced Responses

Same as the description of α4L9'Aβ2 in the nicotine studies, above.

5.9.2 Unnatural Amino Acid Incorporation

Same as the description of α4L9'Aβ2 in the nicotine studies, above.

5.9.3 Single-Channel Characterization of α4β2

Recording solutions, electrodes, and experimental setup was the same as in the nicotine studies, above. Various concentrations of varenicline were used, including 10 and 100 times the macroscopic EC_{50} value. In a few experiments, lower concentrations (0.1 times EC_{50}) were used. The data that produced all dwell time histograms in the results section are for 10 times the respectively macroscopic EC_{50} values.

Because defining the closed dwell times accurately was essential for the P_{open} analysis, we sought a strategy that minimized the number of both misdetected channel openings and brief openings that did not reach full conductance. These openings must otherwise be manually rejected. Data were filtered offline (Gaussian, -3 dB, 2–5 kHz) and electrical interference at harmonics of 60 Hz or other frequencies was removed if necessary. Event transitions were detected with Clampfit 9.2 (single-channel search). Analyses were performed at various dead times, τ_d, between 40 and 200 µs. Dead times were applied either to all events or to events from the baseline only.

Open and closed dwell time histograms were generated as described previously(*36*) and fitted using the predefined log-transformed exponential probability density function in Clampfit 9.2. To delineate clusters, two critical closed durations based on the long components of the closed dwell time histograms were defined. These values (τ_{crit1} and τ_{crit2}) were determined, as described in the supplementary discussion (Section 5.4.3), above. Closed dwell times longer than the respective τ_{crit} values were excluded from further analysis.

Sojourns to a subconductance state (< 70% of the full conductance level) were treated as closed and accounted for < 10% of the total openings in all records when τ_d of 200 μs was applied from the baseline. The time-average probability that the channel is open (P_{open}) was calculated as the total open time divided by the revised total closed time. Only sections of data files that showed no simultaneous activations were analyzed. For each mutant, this was ≥ 3 patches obtained from oocytes from ≥ 2 different donor frogs.

5.10 References

1. Lester, H. A., Xiao, C., Srinivasan, R., Son, C. D., Miwa, J., Pantoja, R., Banghart, M. R., Dougherty, D. A., Goate, A. M., and Wang, J. C. (2009) Nicotine is a selective pharmacological chaperone of acetylcholine receptor number and stoichiometry. Implications for drug discovery, *Aaps J 11*, 167-177.
2. Rollema, H., Coe, J. W., Chambers, L. K., Hurst, R. S., Stahl, S. M., and Williams, K. E. (2007) Rationale, pharmacology and clinical efficacy of partial agonists of alpha4beta2 nACh receptors for smoking cessation, *Trends Pharmacol Sci 28*, 316-325.
3. Zhong, W., Gallivan, J. P., Zhang, Y., Li, L., Lester, H. A., and Dougherty, D. A. (1998) From ab initio quantum mechanics to molecular neurobiology: a cation-pi binding site in the nicotinic receptor, *Proc Natl Acad Sci U S A 95*, 12088-12093.
4. Beene, D. L., Brandt, G. S., Zhong, W., Zacharias, N. M., Lester, H. A., and Dougherty, D. A. (2002) Cation-pi interactions in ligand recognition by serotonergic (5-HT3A) and nicotinic acetylcholine receptors: the anomalous binding properties of nicotine, *Biochemistry 41*, 10262-10269.
5. Romanelli, M. N., Gratteri, P., Guandalini, L., Martini, E., Bonaccini, C., and Gualtieri, F. (2007) Central Nicotinic Receptors: Structure, Function, Ligands, and Therapeutic Potential, *ChemMedChem 2*, 746-767.
6. Corringer, P. J., Le Novere, N., and Changeux, J. P. (2000) Nicotinic receptors at the amino acid level, *Annu Rev Pharmacol Toxicol 40*, 431-458.
7. Coe, J. W., Brooks, P. R., Vetelino, M. G., Wirtz, M. C., Arnold, E. P., Huang, J. H., Sands, S. B., Davis, T. I., Lebel, L. A., Fox, C. B., Shrikhande, A., Heym, J. H., Schaeffer, E., Rollema, H., Lu, Y., Mansbach, R. S., Chambers, L. K., Rovetti, C. C., Schulz, D. W., Tingley, F. D., and O'Neill, B. T. (2005) Varenicline: An alpha 4 beta 2 nicotinic

receptor partial agonist for smoking cessation, *J. Med. Chem. 48*, 3474-3477.

8. Gotti, C., Zoli, M., and Clementi, F. (2006) Brain nicotinic acetylcholine receptors: native subtypes and their relevance, *Trends Pharm. Sci. 27*, 482-491.
9. Mansvelder, H. D., Keath, J. R., and McGehee, D. S. (2002) Synaptic Mechanisms Underlie Nicotine-Induced Excitability of Brain Reward Areas, *Neuron 33*, 905.
10. Nashmi, R., Xiao, C., Deshpande, P., McKinney, S., Grady, S. R., Whiteaker, P., Huang, Q., McClure-Begley, T., Lindstrom, J. M., Labarca, C., Collins, A. C., Marks, M. J., and Lester, H. A. (2007) Chronic nicotine cell specifically upregulates functional alpha 4* nicotinic receptors: basis for both tolerance in midbrain and enhanced long-term potentiation in perforant path, *J Neurosci 27*, 8202-8218.
11. Tapper, A. R., McKinney, S. L., Nashmi, R., Schwarz, J., Deshpande, P., Labarca, C., Whiteaker, P., Marks, M. J., Collins, A. C., and Lester, H. A. (2004) Nicotine activation of alpha4* receptors: sufficient for reward, tolerance, and sensitization, *Science. 2004 Nov 5;306(5698):1029-32.*
12. Kuryatov, A., Luo, J., Cooper, J., and Lindstrom, J. (2005) Nicotine acts as a pharmacological chaperone to up-regulate human alpha4beta2 acetylcholine receptors, *Mol. Pharm. 68*, 1839-1851.
13. Zhong, W., Gallivan, J. P., Zhang, Y., Li, L., Lester, H. A., and Dougherty, D. A. (1998) From *ab initio* Quantum Mechanics to Molecular Neurobiology: A Cation-π Binding Site in the Nicotinic Receptor, *Proc. Natl. Acad. Sci. (USA) 95*, 12088-12093.
14. Brejc, K., van Dijk, W. J., Klaassen, R. V., Schuurmans, M., van Der Oost, J., Smit, A. B., and Sixma, T. K. (2001) Crystal structure of an ACh-binding protein reveals the ligand-binding domain of nicotinic receptors, *Nature 411*, 269-276.
15. Sixma, T. K., and Smit, A. B. (2003) Acetylcholine binding protein (AChBP): a secreted glial protein that provides a high-resolution model for the extracellular domain of pentameric ligand-gated ion channels, *Annu Rev Biophys Biomol Struct 32*, 311-334.
16. Dougherty, D. A. (2008) Cys-loop Neuroreceptors: Structure to the Rescue?, *Chem. Rev. 108*, 1642-1653.
17. Beene, D. L., Brandt, G. S., Zhong, W. G., Zacharias, N. M., Lester, H. A., and Dougherty, D. A. (2002) Cation-pi interactions in ligand recognition by serotonergic (5-HT3A) and nicotinic acetylcholine receptors: The anomalous binding properties of nicotine, *Biochemistry 41*, 10262-10269.
18. Dougherty, D. A. (2008) Physical organic chemistry on the brain, *J Org Chem 73*, 3667-3673.
19. Nowak, M. W., Gallivan, J. P., Silverman, S. K., Labarca, C. G., Dougherty, D. A., and Lester, H. A. (1998) *In vivo* incorporation of unnatural amino acids into ion channels in a *Xenopus* oocyte expression system, *Methods Enzymol 293*, 504-529.

20. Fonck, C., Cohen, B. N., Nashmi, R., Whiteaker, P., Wagenaar, D. A., Rodrigues-Pinguet, N., Deshpande, P., McKinney, S., Kwoh, S., Munoz, J., Labarca, C., Collins, A. C., Marks, M. J., and Lester, H. A. (2005) Novel seizure phenotype and sleep disruptions in knock-in mice with hypersensitive alpha 4* nicotinic receptors, *J Neurosci. 2005 Dec 7;25(49):11396-411.*
21. Filatov, G. N., and White, M. M. (1995) The role of conserved leucines in the M2 domain of the acetylcholine receptor in channel gating, *Molecular pharmacology 48*, 379-384.
22. Labarca, C., Nowak, M. W., Zhang, H., Tang, L., Deshpande, P., and Lester, H. A. (1995) Channel gating governed symmetrically by conserved leucine residues in the M2 domain of nicotinic receptors, *Nature 376*, 514-516.
23. Kearney, P., Nowak, M., Zhong, W., Silverman, S., Lester, H., and Dougherty, D. (1996) Dose-response relations for unnatural amino acids at the agonist binding site of the nicotinic acetylcholine receptor: Tests with novel side chains and with several agonists, *Molecular Pharmacology 50*, 1401-1412.
24. Moroni, M., Zwart, R., Sher, E., Cassels, B. K., and Bermudez, I. (2006) alpha4beta2 nicotinic receptors with high and low acetylcholine sensitivity: pharmacology, stoichiometry, and sensitivity to long-term exposure to nicotine, *Mol Pharmacol. 2006 Aug;70(2):755-68. Epub 2006 May 23.*
25. Nelson, M. E., Kuryatov, A., Choi, C. H., Zhou, Y., and Lindstrom, J. (2003) Alternate Stoichiometries of alpha 4beta 2 Nicotinic Acetylcholine Receptors, *Mol Pharmacol 63*, 332-341.
26. Celie, P. H., van Rossum-Fikkert, S. E., van Dijk, W. J., Brejc, K., Smit, A. B., and Sixma, T. K. (2004) Nicotine and carbamylcholine binding to nicotinic acetylcholine receptors as studied in AChBP crystal structures, *Neuron 41*, 907-914.
27. Hansen, S. B., Sulzenbacher, G., Huxford, T., Marchot, P., Taylor, P., and Bourne, Y. (2005) Structures of Aplysia AChBP complexes with nicotinic agonists and antagonists reveal distinctive binding interfaces and conformations, *Embo J. 24*, 3635-3646.
28. Talley, T. T., Yalda, S., Ho, K. Y., Tor, Y., Soti, F. S., Kem, W. R., and Taylor, P. (2006) Spectroscopic analysis of benzylidene anabaseine complexes with acetylcholine binding proteins as models for ligand-nicotinic receptor interactions, *Biochemistry 45*, 8894-8902.
29. Cashin, A. L., Petersson, E. J., Lester, H. A., and Dougherty, D. A. (2005) Using physical chemistry to differentiate nicotinic from cholinergic agonists at the nicotinic acetylcholine receptor, *J. Am. Chem. Soc. 127*, 350-356.
30. Deechongkit, S., Nguyen, H., Powers, E. T., Dawson, P. E., Gruebele, M., and Kelly, J. W. (2004) Context-dependent contributions of backbone hydrogen bonding to beta-sheet folding energetics, *Nature 430*, 101-105.
31. England, P. M., Zhang, Y., Dougherty, D. A., and Lester, H. A. (1999) Backbone mutations in transmembrane domains of a ligand-gated ion channel: implications for the mechanism of gating, *Cell 96*, 89-98.

32. Koh, J. T., Cornish, V. W., and Schultz, P. G. (1997) An experimental approach to evaluating the role of backbone interactions in proteins using unnatural amino acid mutagenesis, *Biochemistry 36*, 11314-11322.
33. Grutter, T., de Carvalho, L. P., Le Novere, N., Corringer, P. J., Edelstein, S., and Changeux, J. P. (2003) An H-bond between two residues from different loops of the acetylcholine binding site contributes to the activation mechanism of nicotinic receptors, *Embo J. 22*, 1990-2003.
34. Sine, S. M., Ohno, K., Bouzat, C., Auerbach, A., Milone, M., Pruitt, J. N., and Engel, A. G. (1995) Mutation of the acetylcholine receptor alpha subunit causes a slow-channel myasthenic syndrome by enhancing agonist binding affinity, *Neuron 15*, 229-239.
35. Hamill, O. P., Marty, A., Neher, E., Sakmann, B., and Sigworth, F. J. (1981) Improved patch-clamp techniques for high-resolution current recording from cells and cell-free membrane patches, *Pflugers Arch 391*, 85-100.
36. McManus, O. B., Blatz, A. L., and Magleby, K. L. (1987) Sampling, Log Binning, Fitting, and Plotting Durations of Open-and-Shut Intervals from Single Channels and the Effects of Noise, *Pflugers Archiv-Eur. J. of Physiol. 410*, 530-553.
37. Sakmann, B., Patlak, J., and Neher, E. (1980) Single acetylcholine-activated channels show burst-kinetics in presence of desensitizing concentrations of agonist, *Nature 286*, 71-73.
38. Jackson, M. B., Wong, B. S., Morris, C. E., Lecar, H., and Christian, C. N. (1983) Successive openings of the same acetylcholine receptor channel are correlated in open time, *Biophysical journal 42*, 109-114.
39. Etter, J. F. (2006) Cytisine for smoking cessation: a literature review and a meta-analysis, *Arch Intern Med 166*, 1553-1559.
40. Papke, R. L., and Heinemann, S. F. (1994) Partial agonist properties of cytisine on neuronal nicotinic receptors containing the beta 2 subunit, *Molecular pharmacology 45*, 142-149.
41. Blum, A. P., Lester, H. A., and Dougherty, D. A. (2010) Nicotinic pharmacophore: the pyridine N of nicotine and carbonyl of acetylcholine hydrogen bond across a subunit interface to a backbone NH, *Proc Natl Acad Sci U S A 107*, 13206-13211.
42. Rollema, H., Chambers, L. K., Coe, J. W., Glowa, J., Hurst, R. S., Lebel, L. A., Lu, Y., Mansbach, R. S., Mather, R. J., Rovetti, C. C., Sands, S. B., Schaeffer, E., Schulz, D. W., Tingley, F. D., 3rd, and Williams, K. E. (2007) Pharmacological profile of the alpha4beta2 nicotinic acetylcholine receptor partial agonist varenicline, an effective smoking cessation aid, *Neuropharmacology 52*, 985-994.
43. Harrison-Woolrych, M. (2009) Varenicline and suicide. Safety data from New Zealand, *Bmj 339*, b5654.
44. Moore, T. J., and Furberg, C. D. (2009) Varenicline and suicide. Risk of psychiatric side effects with varenicline, *Bmj 339*, b4964.
45. Lape, R., Colquhoun, D., and Sivilotti, L. G. (2008) On the nature of partial agonism in the nicotinic receptor superfamily, *Nature 454*, 722-727.

46. Mukhtasimova, N., Lee, W. Y., Wang, H. L., and Sine, S. M. (2009) Detection and trapping of intermediate states priming nicotinic receptor channel opening, *Nature 459*, 451-454.
47. Dahan, D. S., Dibas, M. I., Petersson, E. J., Auyeung, V. C., Chanda, B., Bezanilla, F., Dougherty, D. A., and Lester, H. A. (2004) A fluorophore attached to nicotinic acetylcholine receptor beta M2 detects productive binding of agonist to the alpha delta site, *Proc Natl Acad Sci U S A 101*, 10195-10200.
48. Akk, G., Sine, S., and Auerbach, A. (1996) Binding sites contribute unequally to the gating of mouse nicotinic alpha D200N acetylcholine receptors, *The Journal of physiology 496 (Pt 1)*, 185-196.
49. Zhang, Y., Chen, J., and Auerbach, A. (1995) Activation of recombinant mouse acetylcholine receptors by acetylcholine, carbamylcholine and tetramethylammonium, *The Journal of physiology 486 (Pt 1)*, 189-206.

Chapter 6

Single-Channel Recording Distinguishes the High and Low Affinity Stoichiometries of the α4β2 Neuronal Nicotinic Receptor

6.1 Introduction

The $\alpha4\beta2$ nicotinic acetylcholine receptor (nAChR) is a pentameric neurotransmitter-gated ion channel that mediates fast synaptic transmission in the brain. The α4 and β2 subunits can be arranged in at least 2 different stoichiometries(*1, 2*): $(\alpha4)_2(\beta2)_3$ and $(\alpha4)_3(\beta2)_2$, abbreviated A2B3 and A3B2, respectively(*3*). Receptors containing $\alpha4$ and $\beta2$ subunits account for 90% of the high affinity nicotine binding sites in the brain(*4*). In addition to being targets for smoking cessation drugs(*5, 6*), nAChRs are therapeutic targets for pain, Alzheimer's disease, Parkinson's disease, epilepsy, autism, attention deficit–hyperactivity disorder, depression, and schizophrenia(*7, 8*).

In order to optimize therapeutic treatments of these diseases and disorders, it is essential to specifically target the appropriate receptor subtypes(*9*). We therefore sought to identify a unique phenotype that discriminates the two $\alpha4\beta2$ stoichiometries. Here we report that the $\alpha4\beta2$ A2B3 and A3B2 rectification behaviors are significantly different at the single-channel level. Based on these differences, we develop and present the first method for identifying essentially pure populations of functional A2B3 receptors.

6.2 Results

In this study we expressed rat A2B3 and A3B2 receptors in *Xenopus laevis* oocytes by biasing the ratios of injected $\alpha4$:$\beta2$ mRNA. An mRNA ratio of 1:1 produced pure A2B3 with an EC_{50} of 0.6 μM acetylcholine (ACh), while 30:1

produced essentially pure A3B2 with an EC_{50} of ~ 100 μM ACh (see discussion). These EC_{50} values are similar to previously published values(*10, 11*). α4:β2 mRNA ratios of 1:2 produced significantly smaller whole-cell currents (< 50 nA in response to 500 μM ACh at 96 h post-injection versus ~ 1 μA for 1:1), and α4:β2 ratios of 1:5 and 1:8 gave no response to 500 μM ACh after 36 h.

Our strategy for uncovering a distinct phenotype for the two α4β2 stoichiometries was inspired by recent whole-cell studies of the receptor that contained a mutation in the channel pore termed α4L9'A(*3, 12*). This mutant receptor showed a significant difference between the whole-cell rectification behaviors of the A2B3 and A3B2 stoichiometries. A2B3 was significantly more inwardly rectifying than A3B2, a difference that allowed for sufficiently pure populations to be identified using voltage jump and voltage ramp experiments. Here, we report that whole-cell data for the wild type α4β2 receptor showed similar rectification behavior for the two stoichiometries, with both displaying nearly complete inward rectification (**Figure 6.1**).

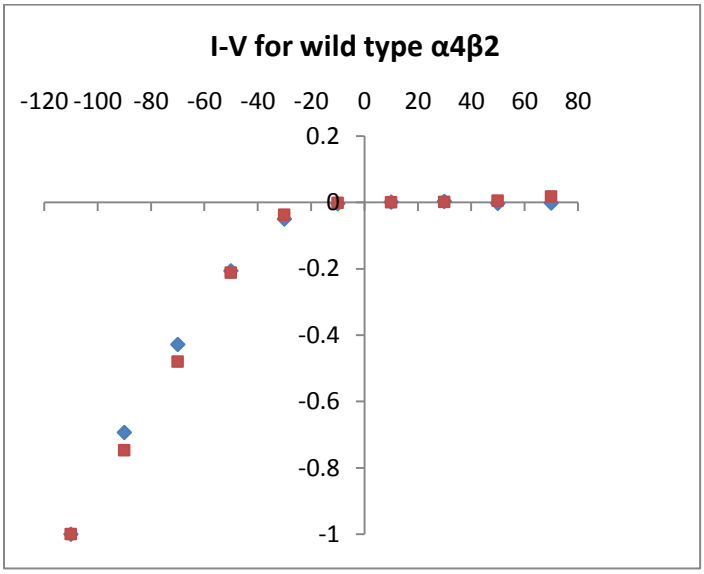

Figure 6.1. Current voltage relationship for wild type α4β2. Blue: 1 μM ACh on A2B3 (1:1). Red: 20 μM ACh on A3B2 (30:1). Both showed significant activation of inward currents at -110 mV (> 1 μA), but very little current in the outward direction at up to +70 mV. Each data point is the average of 2 oocyte's responses. Cells with lower activation (~ 300 nA) may display slightly more outward current, but these values were difficult to measure reliably.

Surprisingly, then, single-channel recording of a patch with an A2B3 channel recorded at multiple pipette potentials revealed that these channels have non-trivial outward conductances (**Figure 6.2**). The 30:1 stoichiometry displayed a qualitatively similar single-channel IV relationship. These data cannot be readily correlated to the whole-cell data of **Figure 6.1**. We therefore characterized rectification behavior, as well as NP_{open} (the probability that exactly one channel in the patch is open), single-channel conductance(s), and channel open dwell time (τ_o). Our goal was to determine if single-channel recording could be used to distinguish the high (A2B3) and low (A3B2) affinity receptors.

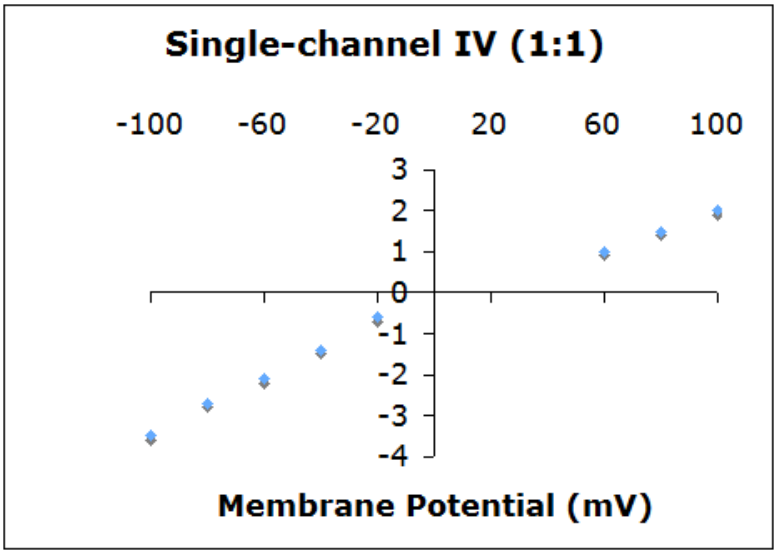

Figure 6.2. The current voltage (IV) relationship for A2B3 (1:1). The slope conductance is 26 pS over the entire voltage range. The slope conductance at negative membrane voltages is 36 pS. Current values near the reversal potential (~ 0 mV) were difficult to measure, especially in the outward direction (rare events).

Because previous experiments have been performed with nicotine(*3, 13*), preliminary studies began using 50 μM nicotine (**Figures 6.3, 6.4, and 6.5**).

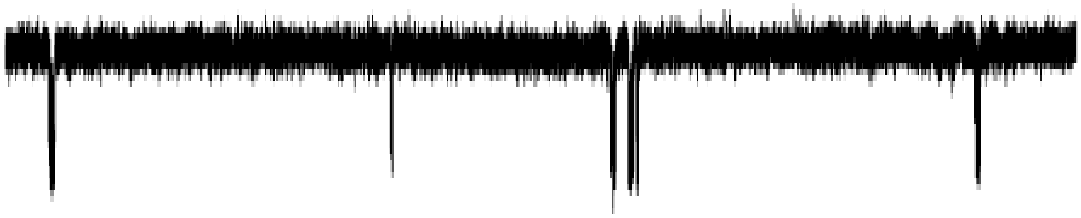

Figure 6.3. 1.0-second single-channel recording of 10:1 α4β2 channels with 50 μM nicotine (predominantly A3B2; see text for discussion). Recordings are in the cell-attached configuration with a pipette potential of +100 mV; f_c = 5 kHz. The openings were raggedy and difficult to quantitatively analyze.

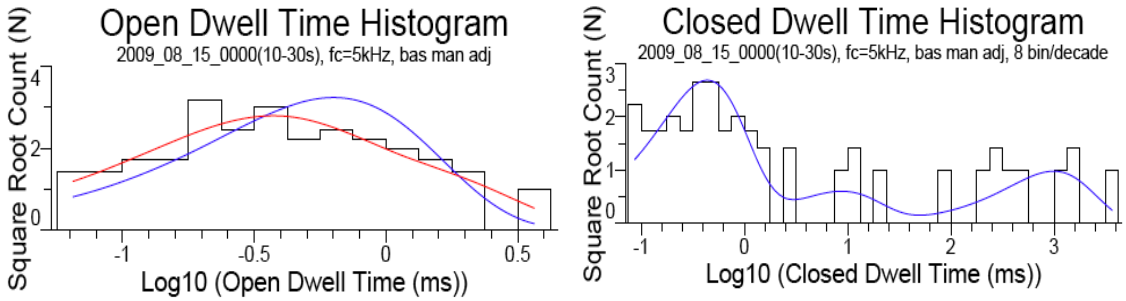

Figure 6.4. Dwell time histograms for single-channel data corresponding to the nicotine data shown in Figure 6.3, above. Left) Open dwell time histogram with the distribution fitted to one component (blue) and two components (red). Very few openings longer than 1 ms were observed. Right) Closed dwell time distribution fitted to three components (blue)

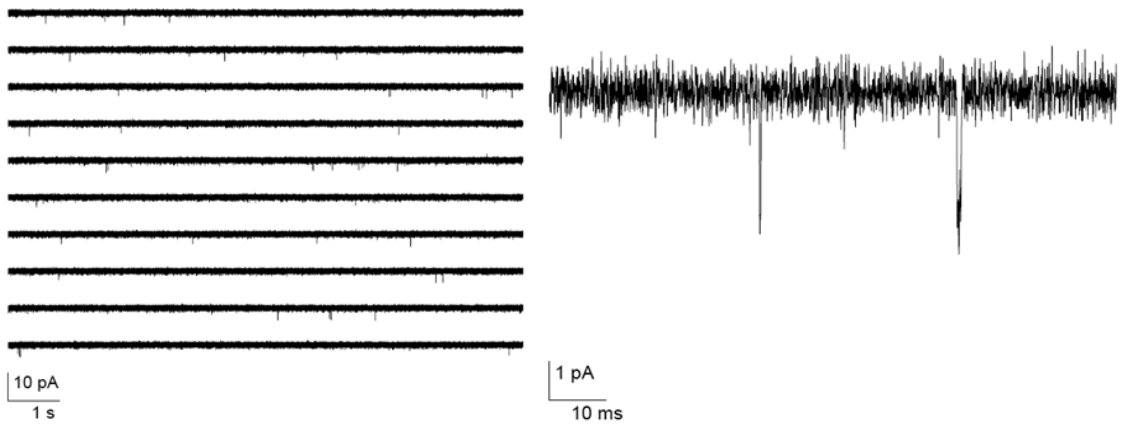

Figure 6.5. Single-channel recording of A2B3 channels with 50 μM nicotine. Recordings are in the cell-attached configuration with a pipette potential of +100 mV; f_c = 5 kHz. Left) 100 second trace. Right) 50 ms trace highlighting two channel openings. These openings were of low conductance and very brief duration, making quantitative analysis difficult.

As these nicotine single-channel events show, the openings were brief and low conductance. Based on the analysis that we proposed, the fact that nicotine's outward openings would likely be either less frequent, shorter, or both, meant that it was not a viable agonist. ACh, though, produced more events, including some outward events of measurable duration for both stoichiometries (**Figure 6.6**).

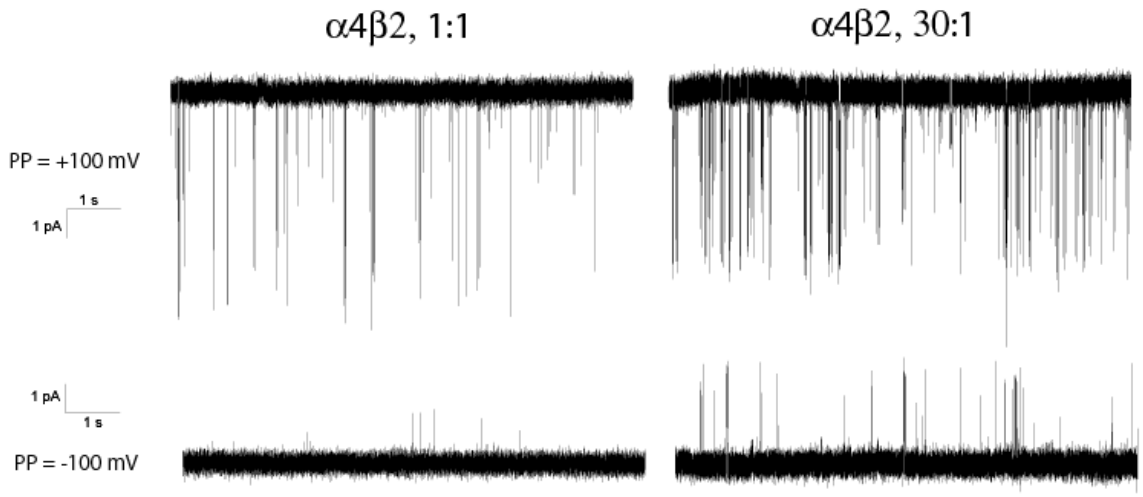

Figure 6.6. ACh-induced single-channel currents of the α4β2 receptor in the cell-attached configuration. Each respective upper trace is at a pipette potential of +100 mV (inward currents are shown as downward deflections), while the lower traces are at pipette potentials of -100 mV (outward currents are shown as upward deflections). Traces are filtered at 2 kHz for display. Left) the A2B3 stoichiometry (1:1) at 500 μM ACh. Right) A3B2 at 10 μM ACh

We find a significant difference between the single-channel rectification of the two stoichiometries. A2B3 receptors pass essentially no outward current, with NP_{open} < 0.0001 at a pipette potential (PP) of -100 mV (**Figure 6.6, Table 6.1**). We now define a pure population of A2B3 receptors as having an NP_{open} ratio (NP_{open} at +100 mV)/(NP_{open} at -100 mV) of < 0.03. On the other hand, A3B2 receptors show small but significant outward currents at negative PP and display an NP_{open} ratio of ~ 0.1 (**Figure 6.6, Table 6.1**). While the channel rectification measured by NP_{open} ratio is different for the two stoichiometries, this difference is not evident from the single-channel I-V relations (**Figure 6.2**; see Discussion).

PP (mV)	NP_{open}, 1:1	NP_{open}, 30:1
100	0.0057	0.0057
-100	0.00006	0.00059
ratio	**0.01**	**0.10**

Table 6.1. NP_{open} values for A2B3 and A3B2. These numbers are based on ~ 500 inward events and 30 outward events at each stoichiometry. Each number represents data from 1 cell-attached patch at the concentrations used in Figure 6.6.

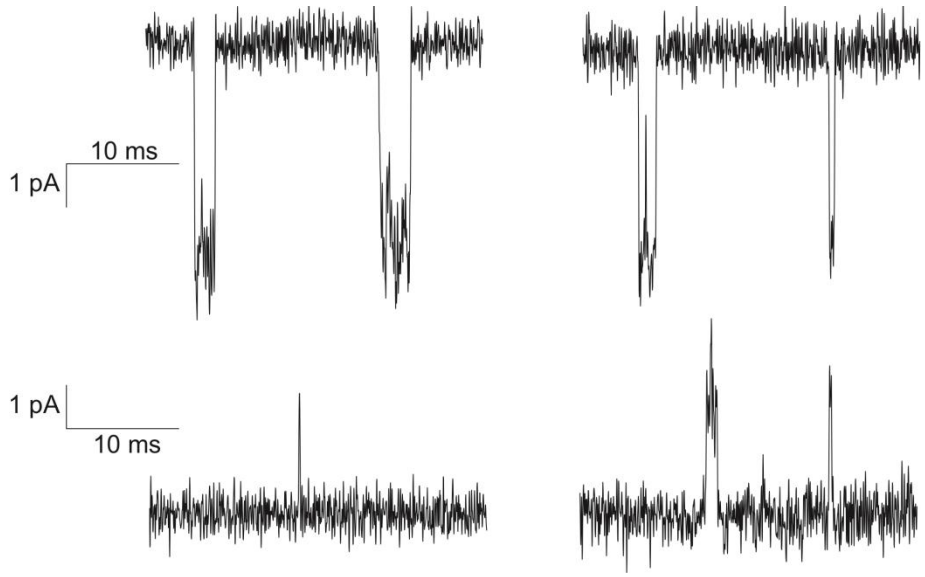

Figure 6.7. High resolution traces of the data in Figure 6.6. Here, the data are filtered at 5 kHz to allow brief events to be visualized. As in Figure 6.6, each respective upper trace is at a pipette potential of +100 mV (inward currents are shown as downward deflections), while the lower traces are at pipette potentials of -100 mV (outward currents are shown as upward deflections). Left) the A2B3 stoichiometry (1:1) at 500 μM ACh. Right) A3B2 at 10 μM ACh

As can be seen qualitatively in **Figure 6.7**, and quantitatively in **Figure 6.8**, τ_{open} contains two components at positive pipette potentials for both stoichiometries. While the longer of these two components is essentially unchanged in the two stoichiometries (2.1 ms versus 1.7 ms), the shorter duration component shifts from 0.12 ms to 0.22 ms, a 1.8-fold increase from A2B3 to A3B2. Moreover, we find that the single component that describes the open dwell time distributions of both stoichiometries at negative pipette potentials

is of similar duration to the short duration component of the inward currents and also increases from A2B3 to A3B2. In this case 2.7-fold from 0.09 ms to 0.24 ms (**Figure 6.9 and Table 6.2**).

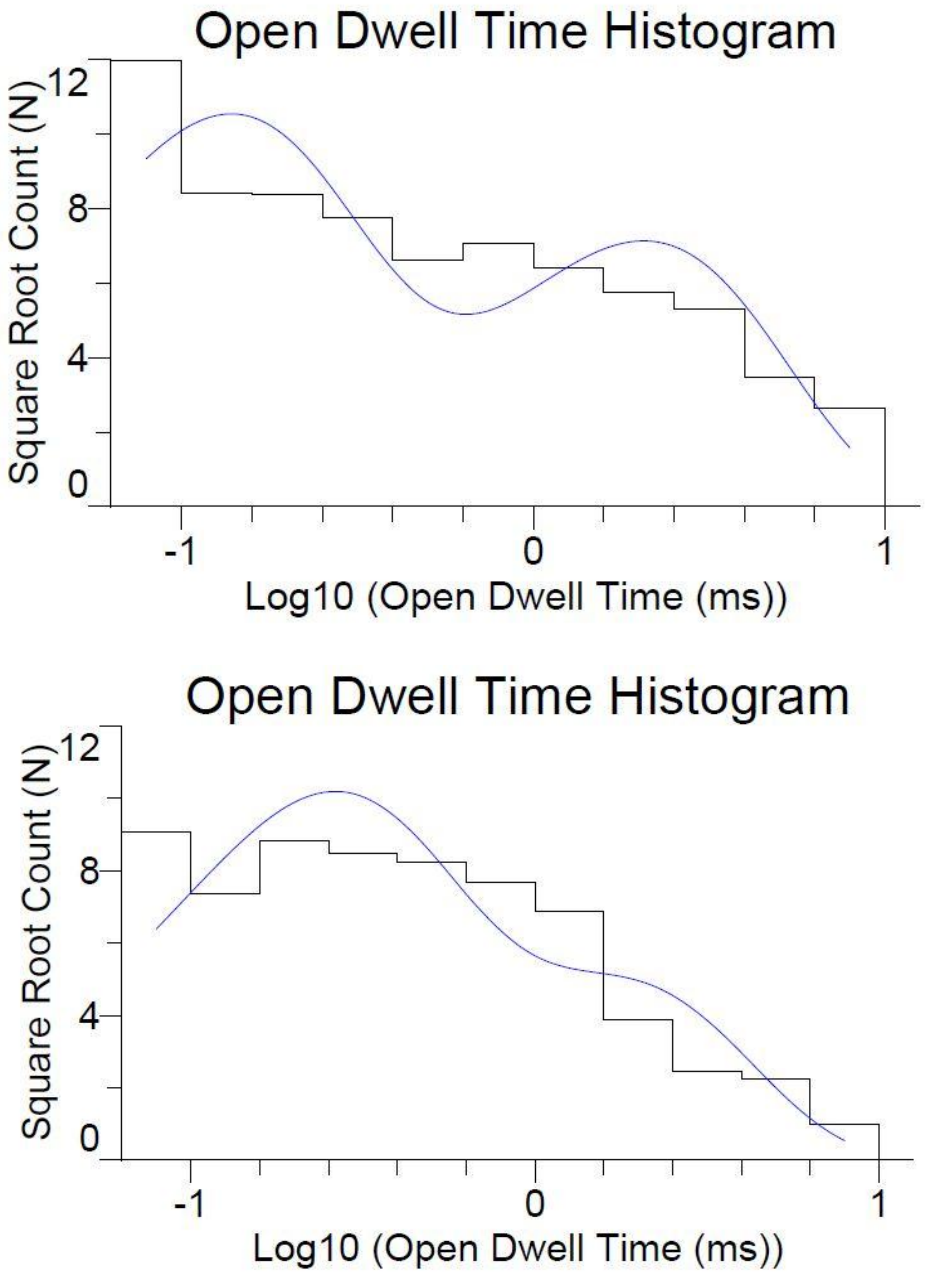

Figure 6.8. Open dwell time histograms for inward currents of α4β2 receptors. Each histogram is fitted to two components (blue). Upper) A2B3. Lower) A3B2. As is summarized in Table 6.2, the longer dwell time component is ~ 2 ms for both stoichiometries, while there is a twofold shift in the duration of the shorter component.

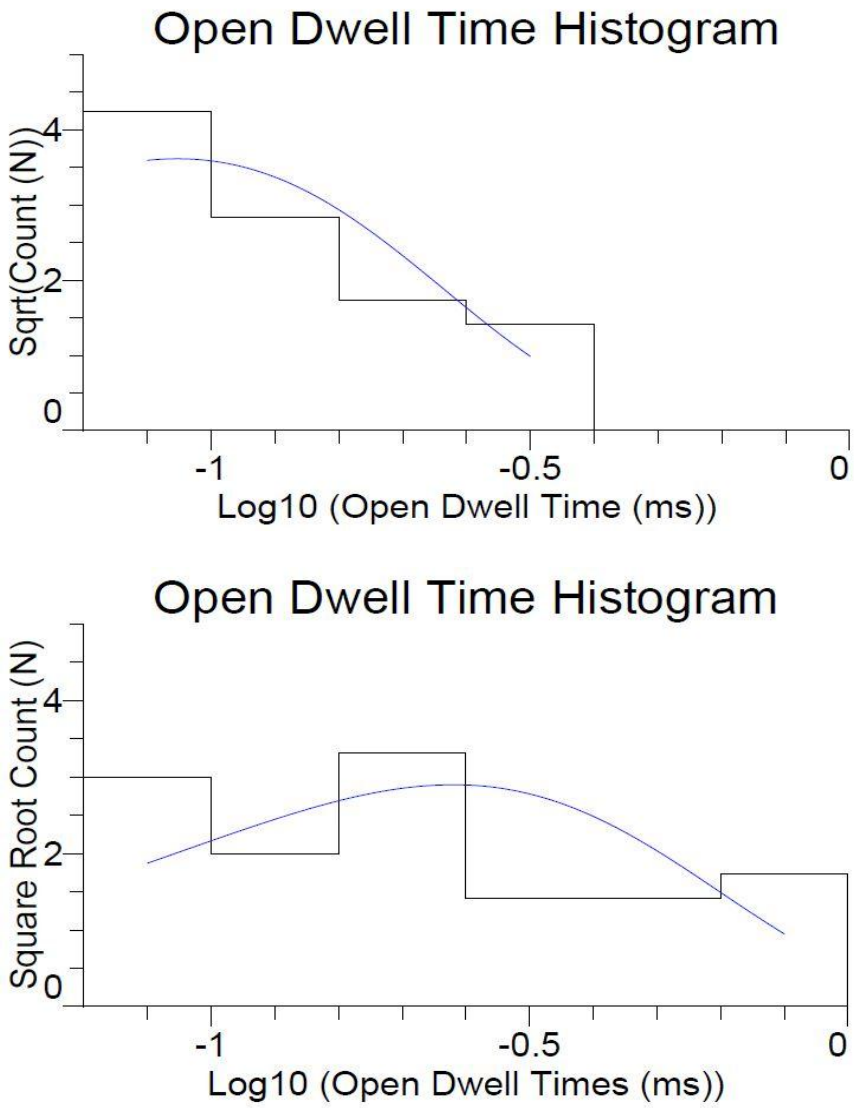

Figure 6.9. Open dwell time histograms for outward currents of α4β2 receptors. Each histogram is fitted to one component (blue). Upper) A2B3. Lower) A3B2. As is summarized in Table 6.2, the there is an approximate 2.7-fold shift in open dwell times from 0.09 ms (A2B3) to 0.24 ms (A3B2).

PP (mV)	g (pS)	# events	$\tau_{open1,}$ ms (%)	$\tau_{open2,}$ ms (%)
1:1, 100	40 +/- 8	558	0.12 (57)	2.1 (43)
1:1 , -100	19 +/- 4	30	0.09 (100)	NA
30:1, 100	48 +/- 5	486	0.22 (63)	1.7 (37)
30:1, -100	28 +/- 6	31	0.24 (100)	NA

Table 6.2. (Previous page). Single-channel conductances and τ_{open} for A2B3 and A3B2. Shown are values recorded at +100 mV and -100 mV pipette potentials. The τ_{open} values are from the fitted components of the open dwell time histograms in Figures 6.8 and 6.9.

Finally, we analyze the conductances (g) of A2B3 and A3B2 and find no significant difference in average conductance at positive pipette potentials (**Table 6.2**). A2B3 channels appear to have a lower conductance at negative pipette potentials (**Table 6.2**); however, these openings of A2B3 receptors are sufficiently rare and brief that rigorous characterization of their conductance proved difficult. In order to verify the open dwell times of outward currents for both stoichiometries, we performed a systematic analysis of τ_{open} over a range of applied dead times (τ_d). We find that over the range 0.06 ms–0.24 ms, τ_{open} decreases with increasing τ_d. For both stoichiometries, the decrease seems to level off at the lowest values of τ_d. Quantitatively, when fit with an exponential function and extrapolated to a τ_d of 0, the values of τ_{open} are very similar to the values in **Table 6.2**. For A2B3 the values are 0.08 ms (τ_d analysis) versus 0.09 ms (histogram). For A2B3 the values are 0.24 ms (τ_d analysis) versus 0.24 ms (histogram).

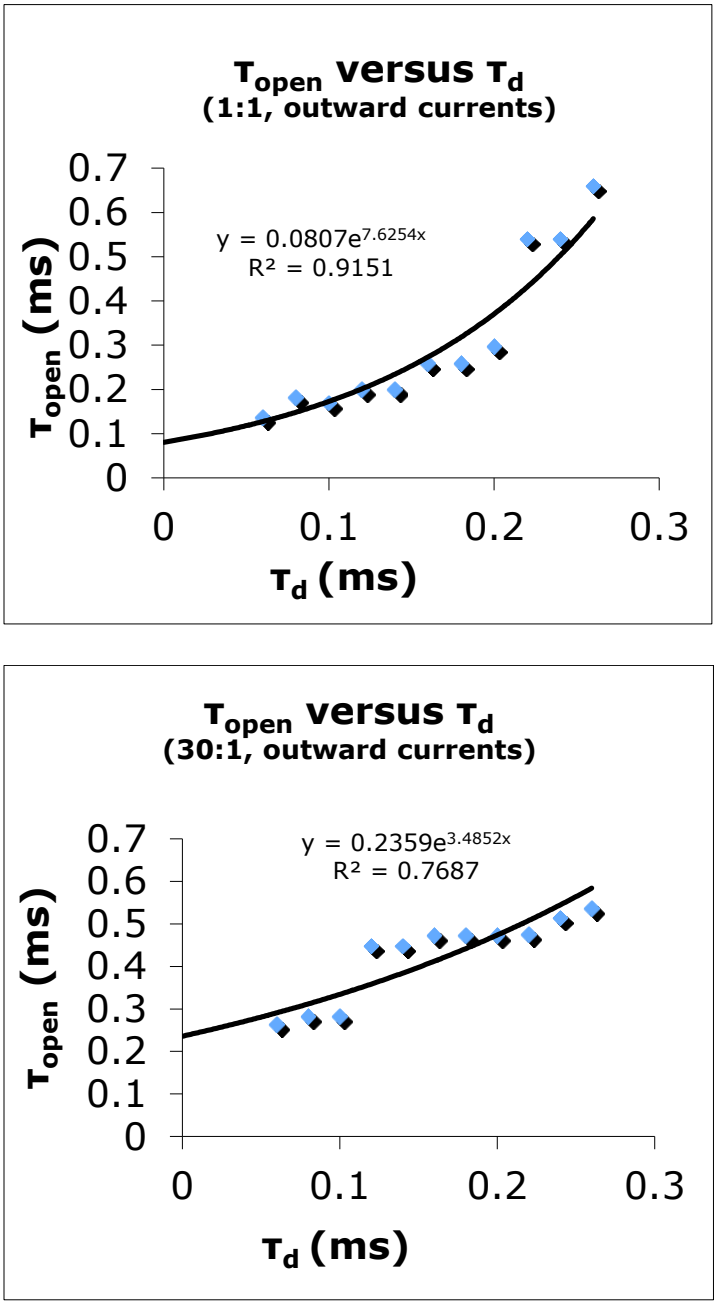

Figure 6.10. Graphs of τ_{open} versus τ_d for A2B3 (upper) and A3B2 (lower). In both cases, dead times were applied in 20 µs increments between 0.06 ms and 0.26 ms. The sampling rate was 50 kHz. Extrapolation to τ_d = 0 produces τ_{open} values of 0.08 ms and 0.24 ms for A2B3 and A3B2 receptors, respectively. These values are in strong agreement with the values in Table 6.2 and open dwell time graphs in Figure 6.9.

Our quantitative analysis of single-channel events at +100 mV and -100 mV pipette potentials is qualitatively supported by voltage ramp experiments (**Figure 6.11**).

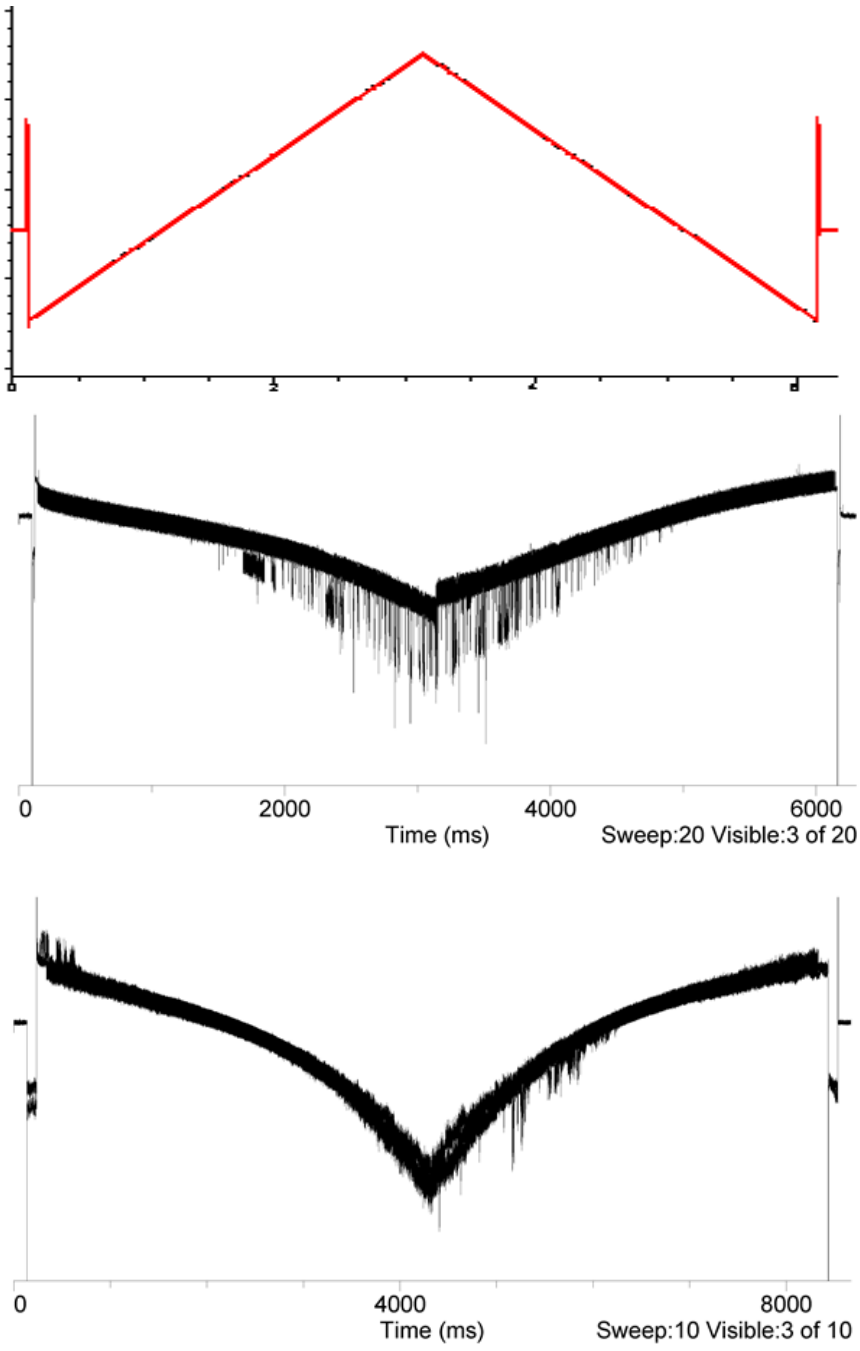

Figure 6.11. (Previous page). Voltage ramp experiments support quantitative analysis. In each case, single-channel recording was performed in the cell-attached configuration and ACh was applied at 10 μM. Pipette potentials (voltage on y-axis) Upper) The voltage ramp protocol used. The red line shows the applied pipette potential, which started at +60 mV, then was stepped to -100 mV and ramped over 3 seconds (A2B3) or 4 seconds (A3B2) to +100 mV. The pipette potential was then ramped symmetrically back to -100 mV and stepped to + 60 mV. Middle) A2B3 channels show inward current (downward deflections), but essentially no outward current (upward deflections). Lower) A3B2 channels show inward current (downward deflections), but also outward current (upward deflections).

6.3 Discussion and Future Studies

Previous studies of the α4β2 receptor have reported multiple open dwell times and conductances(*1, 10, 11, 14-17*). However, these properties have not been investigated in controlled stoichiometry. We sought to use single-channel methods to distinguish between the wild type high (A2B3) and low (A3B2) affinity α4β2 receptors. Consistent with previous reports, we find significant inward rectification of the α4β2 receptor(*11, 16, 18, 19*). We further find that both A2B3 and A3B2 exhibit this rectification at the whole-cell (**Figure 6.1**) and single-channel (**Figure 6.6**) levels.

6.3.1 Open Dwell Times

This difference in single-channel rectification is attributable to a nearly tenfold shift in the NP_{open} ratio (**Table 6.1**). This quantitative difference is supported qualitatively by **Figure 6.11**. Another characteristic difference of the two stoichiometries is their open dwell time distributions. When inward open dwell times are fitted to two components, both A2B3 and A3B2 have a short duration component that accounts for ~ 60% of openings and longer duration components that account for ~ 40% of openings (**Table 6.2**). However, the

duration of the short openings is shifted from 0.12 ms (A2B3) to 0.22 ms (A3B2). This ~ twofold difference is paralleled by an even larger, ~ threefold difference in the open duration of the outward currents of the A2B3 and A3B2 receptors: 0.09 ms to 0.24 ms. Interestingly, in the outward direction, the long openings are completely absent at both stoichiometries—there is only one component in each open dwell time histogram (**Figure 6.9**). The disappearance of this component may reflect part of the underlying mechanism of rectification of these receptors: two types of openings in the inward direction, but only one type of opening in the outward direction. Although the outward openings reported here are brief and rare, our measurement of τ_{open} is further supported by the analysis shown in **Figure 6.10**.

In experiments on the A3B2 receptor at 100–200 μM ACh (EC_{50} and above) single-channel currents displayed very raggedy openings that could not be analyzed quantitatively for conductance, NP_{open} ratio, or τ_{open}. Thus, our single-channel recordings on A3B2 are at lower ACh concentrations. On the other hand, the A2B3 showed activations that could be quantitatively analyzed over a wider concentration range. The A2B3 data in **Figure 6.7** was recorded at 500 μM ACh, well above the macroscopic EC_{50}. At this concentration, binding should be saturated and all openings should be visible. In particular, outward openings, which aren't diminished by channel block. These high concentration data on A2B3 convincingly establish the relatively stronger inward rectification versus A3B2. Our NP_{open} measurements at high ACh concentration (data not

shown) agree with recent results indicating that the low affinity A3B2 stoichiometry has a higher P_{open} than the A2B3 stoichiometry(*20*).

6.3.2 Single-Channel Conductance, NP_{open}, and Rectification

Previous studies considered the single-channel conductances of human $\alpha4\beta2$ A2B3 and A3B2 receptors and reached different conclusions concerning their relative assignment(*1, 10*). While experimental conditions differed for the two studies, it remains possible that the difficulty in assigning the A2B3 and A3B2 conductances is a result of their being multiple conductances in both populations. We find that with rat A2B3 and A3B2 receptors, the more significant difference is in single-channel rectification, with A2B3 receptors exhibiting essentially complete inward rectification.

One of the quantitative descriptions of channel behavior that we present here is NP_{open}, a parameter that combines the intrinsic probability of the channel being open (P_{open}) with the number of receptors in each patch (N). A potential complication in any experiment that compares NP_{open} values is the possibility of multiple channels in the patch. While a lower limit for N can be determined based on the maximal number of simultaneous, overlapping openings in a given record, the exact number of channels cannot be determined. This is especially true for low values of NP_{open}.

In order to make comparisons that avoid a potential impact of varying N, we compare parameters unaffected by it: the ratio of NP_{open}'s at two different voltages for the same patch, single-channel conductance, and τ_{open}. Our results

indicate that the primary mechanism by which the difference in rectification of the A2B3 and A3B2 stoichiometries is achieved is via changes in the single-channel NP_{open} ratio. This provides a clear-cut criterion for the identification of pure populations of the high affinity A2B3 receptor in single-channel experiments. The ~ twofold shift in the short duration inward openings and the ~ threefold shift in the duration of the outward openings provide a further quantitative basis for a difference between the two stoichiometries that is not impacted by N.

The previously identified mechanism for strong inward rectification of both stoichiometries of the $\alpha4\beta2$ receptor is block by intracellular polyamines, especially spermine(*16, 19*). Thus, we speculate that a specific interaction between intracellular residues of the $\beta2$ subunit is responsible for the more favorable interactions that make A2B3 more strongly inward rectifying than A3B2. Adenosine triphosphate (ATP) chelates spermine. In preliminary experiments, we've found that injection of oocytes with 50 nl of 100 mM ATP (final concentration in oocyte ~ 5 mM ATP) 1 hour prior to opus recording significantly decreased oocyte health and increased oocyte leak. This made determination of rectification difficult. In order to pursue the possibility that ATP can modulate rectification at the single-channel and whole-cell level, I recommend longer recovery times of 2–6 hours post ATP injection.

A recent study(*18*) has addressed rectification of nAChRs by expressing muscle-type nAChR in oocytes. They related the excitation-contraction coupling of motor control to inward rectification and Ca^{2+} permeability, and modulated these properties with mutations in the nAChR channel pore. The L9'A mutation

that we have used in the past to differentiate the high and low affinity α4β2 receptors in whole-cell recording is also a pore mutation of the nAChR. Many further studies of the relationship between rectification, pore mutations, and spermine would be of interest.

6.3.3 Control of α4β2 Expression Levels and Stoichiometry

The α4L9'A mutation had previously been used to increase expression levels to enable studies of the α4β2 receptor with unnatural amino acids(*3*). In an effort to increase expression and sustain pure populations of A2B3, I injected oocytes with a 1:1 mRNA ratio and incubated them post injection in 5 μM nicotine for up to a few days. Subsequent rinsing of the oocytes in incubation media for 5 hours produced a whole-cell response to nicotine that was < 50 nA, versus > 500 nA response to ACh. Consistent with previous findings about nicotine sequestration in oocytes, experiments with multiple rinses and a total of 27 hours in incubation media after nicotine exposure did not fully restore responses to nicotine or ACh(*21*). The method developed below was sufficient to control stoichiometry.

In order to get sufficient expression of the wild type α4β2 receptor (**Figure 6.12**), I used post-injection incubation times of up to several days (see Materials and Methods).

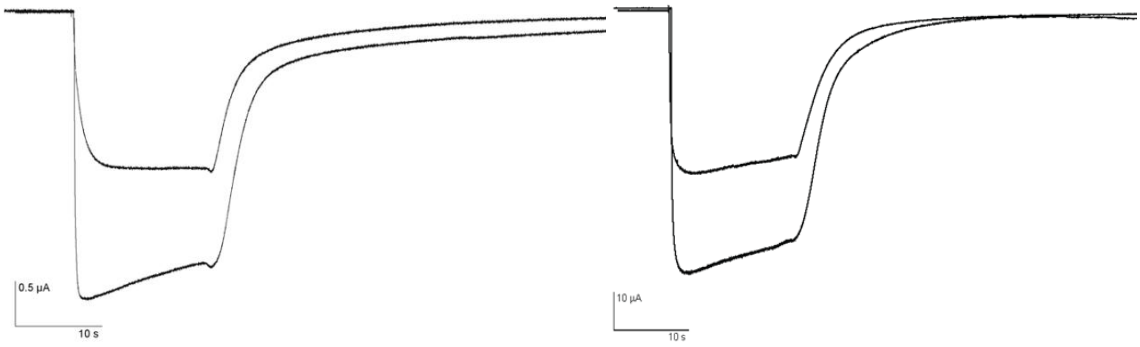

Figure 6.12. Whole-cell voltage-clamp recordings performed on the OpusXpress 6000A. Left: A2B3 at 1 and 100 µM ACh. Right A3B2 at 100 and 1000 µM ACh. As the scale bars indicate, the expression of A3B2 is significantly higher than A2B3.

Even after 204 hours α4β2 receptors expressed at a 1:1 ratio produced a pure population of the high affinity, A2B3 with EC_{50} of ~ 0.6 µM ACh (**Figure 6.13**). Once incubated for several days, expression levels were high enough (2–5 µA) that single-channel experiments could be performed with a reasonable chance of getting patches with channel activity. I did not find a significant difference in expression between cells injected with 3 µg or 30 µg total mRNA.

For expression of A3B2 receptors, fairly high expression was seen (2.5–50 µA) after 96 hours (**Figure 6.14**). Over the course of the long incubations that facilitated recording of A2B3, injection of a 30:1 mRNA ratio resulted in some contamination of a high affinity component. The EC_{50} of this component was consistent with it arising from A2B3 receptors. This slow increase in percent A2B3 may be due to an insufficient amount of α4 mRNA being present in the oocyte after several days. Nevertheless, taken together, these long incubations of α4β2 receptors indicate that at least some of the wild type neuronal receptors can be expressed in oocytes for several days without changes to pharmacology.

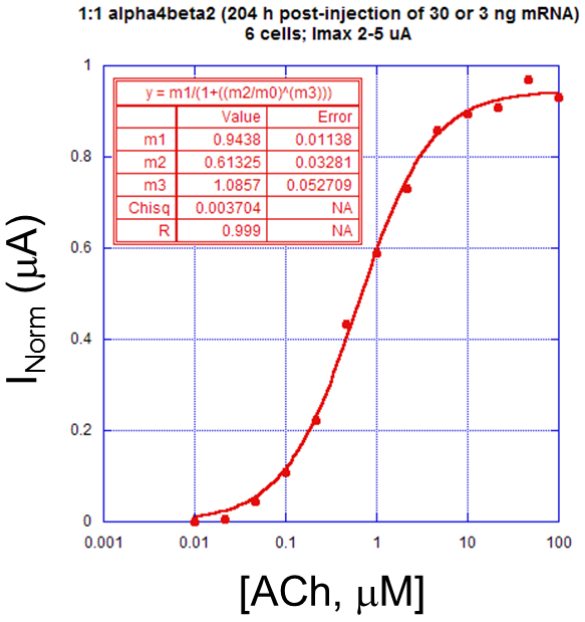

Figure 6.13. ACh dose-response curves for whole-cell experiments with oocytes injected with a 1:1 ratio of α4:β2 mRNA. These produce a pure population of the high affinity (A2B3) receptor, even after a long incubation (204 hours, in this case). m2 is the EC_{50} and m3 is the Hill coefficient.

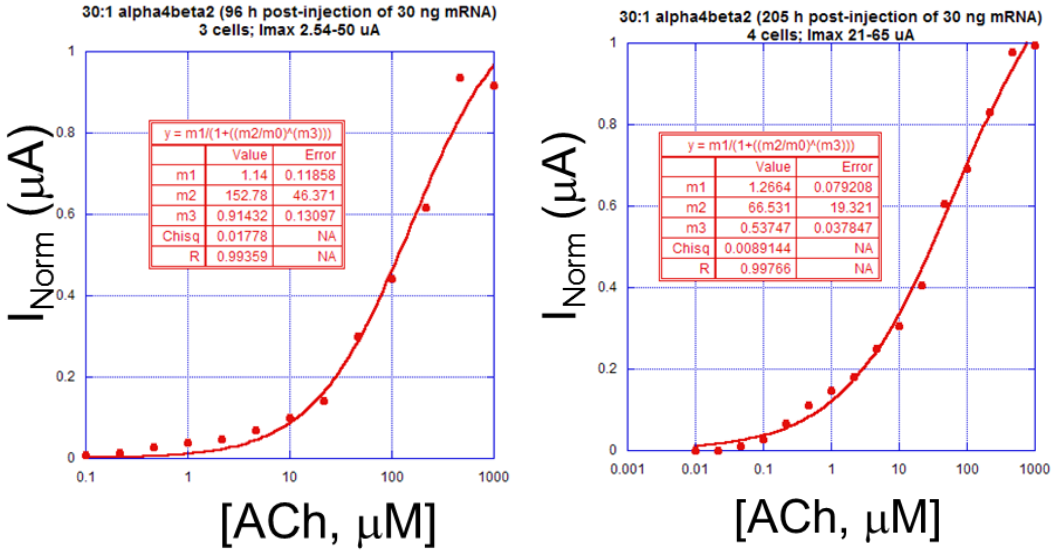

Figure 6.14. ACh dose-response curves for whole-cell experiments with oocytes injected with a 30:1 ratio of α4:β2 mRNA. Left) After 96 hours of incubation, the A3B2 population is > 90% pure. Right) After 205 hours of incubation, 10–20% of a second, higher affinity component is evident. This additional component reduced the EC_{50} (m2) and Hill coefficient (m3) relative to the 96 hour incubation. Note that, at an equivalent incubation time (204 hours), the α4β2 population of oocytes injected with a 1:1 ratio appears to be pure A2B3 (previous figure).

A question arises for single-channel experiments performed with nicotine in the pipette: could the nicotine from the pipette leak into the bath and impact recordings and stoichiometry(*21, 22*)? The following calculation suggests that this should not present a major issue in our experimental setup. The calculated volume of the solution in the pipettes that I use for cell-attached single-channel recording is: ~ 20 mm * 0.4 mm^2 * π = ~ 10 μL. A direct measurement of the volume of a few filled pipettes gave a range of 5–7 µl. The resultant calculation of the concentration of nicotine in the recording chamber is based on a chamber volume of 200–300 µl, which is the solution level during recording (see chapter 2). The volume of solution that leaks out of the pipette is not macroscopically significant, even over a long recording (1 hour). Assuming that 5% of a 10 µl solution of 50 µM nicotine leaks during a recording, the eventual concentration of nicotine in the recording chamber would be 0.13 µM. This is a fairly low concentration. As long as adequate rinses are done between each recording, concentrations of nicotine in the µM concentration range in the pipette (nM in the bath solution) are unlikely to impact recordings and stoichiometry over the course of the average lifetime of an oocyte for single-channel recording (a few hours).

6.4 Materials and Methods

6.4.1 Receptor Expression

Neuronal rat nicotinic acetylcholine receptor (nAChR) $\alpha 4$ and $\beta 2$ subunits were expressed in pAMV vectors. Not1 linearized circular bacterial plasmid

DNAs were used as templates for *in vitro* transcription using T7 mMessage mMachine enzyme kits (Ambion) to make mRNA. mRNA concentrations were determined using a NanoDrop-1000 spectrophotometer (Thermo Scientific, Inc., Wilmington, DE).

Injection ratios of the $\alpha 4$ and $\beta 2$ mRNA ranged from 30:1 to 1:8 by mass at a total concentration of 0.06–0.6 μg/μl. Stage V-VI *Xenopus laevis* oocytes (Nasco, Fort Atkinson, WI) were injected with 50 nl of the mRNA mixture (3–30 ng). To overcome low expression, oocytes were incubated for 2 to 9 days post-injection, especially for studies of the A2B3 receptor. Oocytes were incubated in media containing 2% equine serum at 17±2˚C.

6.4.2 Whole-Cell Recording

The OpusXpress 6000A (Axon Instruments, Union City, CA) was used in the two-electrode voltage clamp mode for whole-cell dose-response measurements. Oocytes were superfused with Ca^{2+}-free ND96 (contents, in mM: 96 NaCl, 2 KCl, 1 $MgCl_2$, 5 HEPES) at flow rates of 4 ml min^{-1} during 15 s drug application and 3 ml min^{-1} during 115 s wash periods. Dose-response data were obtained for ≥ 5 oocytes at ≥ 12 ACh concentrations each and fitted to the Hill equation to determine EC_{50} values. Before single-channel recording, expression levels were verified with 500 μM ACh, typically ~ 1 μA for 1:1 and ~ 10 μA for 30:1.

Whole-cell voltage jumps were performed in the absence of ACh and at 1 μM ACh (1:1) and 20 μM ACh (30:1). As previously described, membrane

potentials were held at -60 mV, then stepped to 10 test potentials at 20 mV increments between +70 mV and -110 mV for 400 ms at each potential(*3*). Voltage was held at -60 mV for 600 ms between each episode. To isolate the ACh-induced currents, currents from the control traces ([ACh] = 0) were subtracted from the steady-state amplitudes of the ACh-induced currents of the test pulses. Normalized I-V curves were generated by normalizing all current amplitudes to responses at -110 mV.

6.4.3 Single-Channel Recording

Single-channel recording was performed in the cell-attached configuration on devitellinized oocytes at 20 ± 3°C with an applied pipette potential of +100 mV, as described previously(*23, 24*). Pipettes fabricated from thick-walled (I.D. = 0.80 mm, O.D. = 1.60 mm) KG-33 glass (Garner Glass Company, Claremont, CA) and coated with Sylgard (World Precision Instruments, Sarasota, FL) typically had resistances of 8–20 MΩ. The bath solution contained, in mM, 120 KCl, 5 HEPES, 1 $MgCl_2$, 2 $CaCl_2$, pH = 7.4, so that the transmembrane potential of the patch was ~ -100 mV and the reversal potential for agonist-induced currents of devittelinized oocytes was ~ 0 mV. The pipette solution contained, in mM, 100 KCl, 10 HEPES, 1 $MgCl_2$, 10 K_2EGTA, pH = 7.4, and was supplemented with the indicated concentrations of ACh from a 1.00 M stock solution.

Data were collected using a GeneClamp 500B amplifier (Axon Instruments, Union City, CA) with a CV-5 GU headstage at full bandwidth (4-pole

Bessel, -3 dB, 50 kHz). The signal was then low-pass filtered (8-pole Bessel, -3 dB, 20 kHz) and sampled with a Digidata 1320A and Clampex 9.2 (Axon Instruments, Union City, CA) at 50 kHz. The voltage ramp protocol was described in **Figure 6.11**. Data were filtered offline (Gaussian, -3 dB, 5 kHz) and electrical interference at harmonics of 60 Hz was removed, if necessary. After manual baseline adjustment, event transitions were detected with Clampfit 9.2 (single-channel search). A dead time, τ_d, of 60 μs was applied to all events, except for the τ_d analysis, when values between 60 μs and 240 μs were applied. The time-average probability that exactly one channel in the patch is open (NP_{open}) was calculated as the total open time divided by the total closed time. Open dwell time histograms were generated from the Clampfit results files and fitted using Clampfit's predefined log-transformed exponential probability density function(*25*). The number of components used in the fit was determined by using compare models with a confidence level of 0.95.

6.5 References

1. Nelson, M. E., Kuryatov, A., Choi, C. H., Zhou, Y., and Lindstrom, J. (2003) Alternate stoichiometries of alpha4beta2 nicotinic acetylcholine receptors, *Molecular pharmacology 63*, 332-341.
2. Moroni, M., Zwart, R., Sher, E., Cassels, B. K., and Bermudez, I. (2006) alpha4beta2 nicotinic receptors with high and low acetylcholine sensitivity: pharmacology, stoichiometry, and sensitivity to long-term exposure to nicotine, *Mol Pharmacol 70*, 755-768.
3. Xiu, X., Puskar, N. L., Shanata, J. A., Lester, H. A., and Dougherty, D. A. (2009) Nicotine binding to brain receptors requires a strong cation-pi interaction, *Nature 458*, 534-537.
4. Jensen, A. A., Frolund, B., Liljefors, T., and Krogsgaard-Larsen, P. (2005) Neuronal nicotinic acetylcholine receptors: structural revelations, target identifications, and therapeutic inspirations, *J Med Chem 48*, 4705-4745.

5. Mansvelder, H. D., and McGehee, D. S. (2002) Cellular and synaptic mechanisms of nicotine addiction, *J Neurobiol 53*, 606-617.
6. Mansvelder, H. D., Keath, J. R., and McGehee, D. S. (2002) Synaptic mechanisms underlie nicotine-induced excitability of brain reward areas, *Neuron 33*, 905-919.
7. Romanelli, M. N., Gratteri, P., Guandalini, L., Martini, E., Bonaccini, C., and Gualtieri, F. (2007) Central nicotinic receptors: structure, function, ligands, and therapeutic potential, *ChemMedChem 2*, 746-767.
8. Laviolette, S. R., and van der Kooy, D. (2004) The neurobiology of nicotine addiction: bridging the gap from molecules to behaviour, *Nat Rev Neurosci 5*, 55-65.
9. Hogg, R. C., and Bertrand, D. (2007) Partial agonists as therapeutic agents at neuronal nicotinic acetylcholine receptors, *Biochem Pharmacol 73*, 459-468.
10. Buisson, B., and Bertrand, D. (2001) Chronic exposure to nicotine upregulates the human $\alpha4\beta2$ nicotinic acetylcholine receptor function, *J Neurosci 21*, 1819-1829.
11. Buisson, B., Gopalakrishnan, M., Arneric, S. P., Sullivan, J. P., and Bertrand, D. (1996) Human $\alpha4\beta2$ neuronal nicotinic acetylcholine receptor in HEK 293 cells: A patch-clamp study, *J Neurosci 16*, 7880-7891.
12. Fonck, C., Cohen, B. N., Nashmi, R., Whiteaker, P., Wagenaar, D., Rodrigues-Pinguet, N., Deshpande, P., Kwoh, S., Munoz, J., Labarca, C., Collins, A., Marks, M., and Lester, H. (2005) Novel seizure phenotype and sleep disruptions in knock-in mice with hypersensitive $\alpha4$ nicotinic receptors, *J Neurosci 25*, 11396-113411.
13. Rollema, H., Coe, J. W., Chambers, L. K., Hurst, R. S., Stahl, S. M., and Williams, K. E. (2007) Rationale, pharmacology and clinical efficacy of partial agonists of alpha4beta2 nACh receptors for smoking cessation, *Trends in pharmacological sciences 28*, 316-325.
14. Rodrigues-Pinguet, N. O., Pinguet, T. J., Figl, A., Lester, H. A., and Cohen, B. N. (2005) Mutations linked to autosomal dominant nocturnal frontal lobe epilepsy affect allosteric Ca^{2+} activation of the $\alpha4\beta2$ nicotinic acetylcholine receptor, *Mol Pharmacol 68*, 487-501.
15. Papke, R. L., Boulter, J., Patrick, J., and Heinemann, S. (1989) Single-channel currents of rat neuronal nicotinic acetylcholine receptors expressed in *Xenopus* oocytes, *Neuron 3*, 589-596.
16. Haghighi, A. P., and Cooper, E. (1998) Neuronal nicotinic acetylcholine receptors are blocked by intracellular spermine in a voltage-dependent manner, *J Neurosci 18*, 4050-4062.
17. Akk, G., and Auerbach, A. (1999) Activation of muscle nicotinic acetylcholine receptor channels by nicotinic and muscarinic agonists, *British journal of pharmacology 128*, 1467-1476.
18. Nishino, A., Baba, S. A., and Okamura, Y. (2011) A mechanism for graded motor control encoded in the channel properties of the muscle ACh receptor, *Proc Natl Acad Sci U S A 108*, 2599-2604.

19. Haghighi, A. P., and Cooper, E. (2000) A molecular link between inward rectification and calcium permeability of neuronal nicotinic acetylcholine alpha3beta4 and alpha4beta2 receptors, *J Neurosci 20*, 529-541.
20. Li, P., and Steinbach, J. H. (2010) The neuronal nicotinic alpha 4 beta 2 receptor has a high maximal probability of being open, *British journal of pharmacology 160*, 1906-1915.
21. Jia, L., Flotildes, K., Li, M., and Cohen, B. N. (2003) Nicotine trapping causes the persistent desensitization of $\alpha 4\beta 2$ nicotinic receptors expressed in oocytes, *J Neurochem 84*, 753-766.
22. Srinivasan, R., Pantoja, R., Moss, F. J., Mackey, E. D., Son, C. D., Miwa, J., and Lester, H. A. (2011) Nicotine up-regulates alpha4beta2 nicotinic receptors and ER exit sites via stoichiometry-dependent chaperoning, *The Journal of general physiology 137*, 59-79.
23. Sakmann, B., Patlak, J., and Neher, E. (1980) Single acetylcholine-activated channels show burst-kinetics in presence of desensitizing concentrations of agonist, *Nature 286*, 71-73.
24. Hamill, O. P., Marty, A., Neher, E., Sakmann, B., and Sigworth, F. J. (1981) Improved patch-clamp techniques for high-resolution current recording from cells and cell-free membrane patches, *Pflugers Arch 391*, 85-100.
25. McManus, O. B., Blatz, A. L., and Magleby, K. L. (1987) Sampling, log binning, fitting, and plotting durations of open and shut intervals from single channels and the effects of noise, *Pflugers Arch 410*, 530-553.

Appendix A

Derivation of an Equation for EC_{50}

Although an expression (**Equation A.1**) for EC_{50} of a receptor in terms of the binding equilibrium constant (K_D) and the gating equilibrium constant (Θ) has been given(*1*), we were unable to find a published derivation of this equation. This appendix provides a derivation of **Equation A.1**.

$$EC_{50} = K_D * \frac{1+\sqrt{2+Q}}{Q+1} \qquad \textbf{Equation A.1}$$

This specific equation is based on the following, **4-state model** for activation of an allosteric receptor (R) that requires the separate, sequential binding of two molecules of agonist, A, before the inactive, closed receptor (R^c) becomes the active receptor (R^o).

$$2A + R^c \underset{k_{-1}}{\overset{2k_1}{\rightleftharpoons}} A + AR^c \underset{2k_{-1}}{\overset{k_1}{\rightleftharpoons}} A_2R^c \underset{\alpha}{\overset{\beta}{\rightleftharpoons}} A_2R^o \qquad \textbf{Model A.1}$$

where,

$$K_D = \frac{k_{-1}}{k_1} \text{ and, } Q = \frac{b}{a}$$

Through other modeling studies (personal communications from Kristin Gleitsman and Shawna Frazier) we know that similar models have a relationship between EC_{50}, K_D, and Θ that is at least qualitatively similar to that given in

Equation A.1. Additionally, plots with unequal binding affinities (different K_Ds for the first and second binding steps) produce similar relationships.

We begin by writing the expression for the proportion of activated receptors—the open receptors divided by the total number of receptors:

$$\frac{[A_2R^o]}{[R^c]+[AR^c]+[A_2R^c]+[A_2R^o]}$$ **Expression A.1**

We know that, at EC_{50}, half of all receptors that can be activated are activated. Therefore, at EC_{50}, the probability that the channel is open, P_{open}, reaches half of its maximal value. Thus, since:

$P_{open,\max} = \frac{Q}{Q+1}$, we can write

$P_{open,EC50} = \frac{Q}{2(Q+1)}$.

This expression for $P_{open,EC50}$ represents the scenario that occurs when the applied drug concentration, [A], is the EC_{50} (**Concept A.1**)

The next step is to transform **Expression A.1** to be in terms of K_D and Θ, as in **Equation A.1**. We start by writing the expressions for these values—the equilibrium dissociation constant (K_D) and equilibrium gating constant (Θ)—based on the definition of equilibrium constants. In this case, because there are two receptor binding sites, we effectively write an expression for a value that is twice the first equilibrium constant and half the second equilibrium constant.

From the first binding equilibrium:

$$K_D = \frac{2[R^c][A]^2}{[AR^c][A]}.$$

alternatively, $[R^c] = \frac{K_D[AR^c]}{2[A]}$ **Equation A.2**

From the second binding equilibrium:

$$K_D = \frac{[A][AR^c]}{2[A_2R^c]}$$

alternatively, $[A_2R^c] = \frac{[A][AR^c]}{2K_D}$. **Equation A.3**

And finally from the gating equilibrium:

$$\Theta = \frac{[A_2R^o]}{[A_2R^c]}$$

alternatively, $[A_2R^o] = \Theta[A_2R^c]$. **Equation A.4**

To eliminate all of the terms, I chose to write the numerator of **Expression A.1**, as well as each of the 4 terms of the denominator, solely in terms of [A], [AR^C] (which will drop out of the equation entirely), K_D, and Θ. **Equations A.2** and **A.3** meet this criterion, but **Equation A.4** doesn't; substituting **Equation A.3** into **A.4**, gives:

$$[A_2R^o] = \frac{\Theta[A][AR^c]}{2K_D}.$$ **Equation A.5**

Substitution of **Equations A.2, A.3,** and **A.5** into **Expression A.1** yields the following expression:

$$\frac{\frac{\Theta[A][AR^c]}{2K_D}}{\frac{K_D[AR^c]}{2[A]}+[AR^c]+\frac{[A][AR^c]}{2K_D}+\frac{\Theta[A][AR^c]}{2K_D}} \quad .$$

Simplifying gives,

$$\frac{\frac{\Theta[A]}{K_D}}{\frac{K_D}{[A]}+2+\frac{[A]}{K_D}+\frac{\Theta[A]}{K_D}} \quad .$$

The expression for the proportion of activated receptors is now in the terms of the desired parameters. So now we invoke **Concept A.1** and rearrange for EC_{50}. Before doing that, we may find it convenient to take the inverse, yielding **Expression A.2**:

$$\frac{\frac{K_D}{[A]}+2+\frac{[A]}{K_D}+\frac{\Theta[A]}{K_D}}{\frac{\Theta[A]}{K_D}} \quad . \qquad \textbf{Expression A.2}$$

Since we took an inverse, when we apply **concept 1**, we'll use the inverse:

$$\left(\frac{\Theta}{2(\Theta+1)}\right)^{-1}=\frac{2(\Theta+1)}{\Theta} \quad . \qquad \textbf{Equation A.6}$$

Moving K_D in the denominator of the denominator of **Expression A.2** to the numerator and distribution gives:

$$\frac{\frac{K_D{}^2}{[A]} + 2K_D + [A] + \mathrm{Q}[A]}{\mathrm{Q}[A]} \quad .$$

Which produces the following expression for the inverse of the proportion of activated receptors:

$$\frac{K_D{}^2}{\mathrm{Q}[A]^2} + \frac{2K_D}{\mathrm{Q}[A]} + \frac{1}{\mathrm{Q}} + 1 \quad .$$

Next we invoke the inverse of **Concept A.1** (by applying the result of **Equation A.6**). At [A] = EC_{50}, we have:

$$\frac{K_D{}^2}{\mathrm{Q}EC_{50}{}^2} + \frac{2K_D}{\mathrm{Q}EC_{50}} + \frac{1}{\mathrm{Q}} + 1 = \frac{2(\mathrm{Q}+1)}{\mathrm{Q}} \quad .$$

Rearranging gives:

$$\frac{K_D{}^2}{\mathrm{Q}EC_{50}{}^2} + \frac{2K_D}{\mathrm{Q}EC_{50}} = \frac{\mathrm{Q}+1}{\mathrm{Q}} \quad .$$

Which simplifies to:

$$\frac{K_D{}^2}{EC_{50}{}^2} + \frac{2K_D}{EC_{50}} = \mathrm{Q}+1 \quad .$$

Now let's add 1 to both sides and factor:

$$\frac{K_D{}^2}{EC_{50}{}^2} + \frac{2K_D}{EC_{50}} + 1 = Q + 2 \quad .$$

which can also be written as:

$$\left(\frac{K_D}{EC_{50}} + 1\right)^2 = Q + 2 \quad .$$

Finally, we can rearrange for EC_{50} in terms of K_D and Θ:

$$EC_{50} = \frac{K_D}{\sqrt{Q+2} - 1} \quad . \qquad \textbf{Equation A.7}$$

Rationalize the denominator to yield:

$$EC_{50} = \frac{K_D}{\sqrt{Q+2} - 1} x \frac{\sqrt{Q+2} + 1}{\sqrt{Q+2} + 1} = K_D \frac{\sqrt{Q+2} + 1}{Q + 2 - 1} \quad .$$

Rearranging and simplifying yields **Equation A.1**:

$$EC_{50} = K_D * \frac{1 + \sqrt{Q+2}}{Q+1} \quad . \qquad \textbf{Equation A.1}$$

I prefer leaving this expression in the form of **Equation A.7**, which is simpler and clearly shows the relationship between the three parameters, especially since Θ only occurs once in it. **Equation A.7** readily captures the following important qualitative characteristics of the relationship between EC_{50}, K_D, and Θ:

(1) As the strength of the binding interaction increases—K_D decreases—the receptor can be activated with less drug, so EC_{50} goes down. EC_{50} and K_D are directly proportional.

(2) As the channel becomes easier to gate—Θ increases—the receptor can be activated with less drug, so EC_{50} goes down. EC_{50} and K_D are inversely proportional.

(3) Since the exponent on K_D is 1, while the exponent on Θ is ½, changes to binding will have a more significant impact on EC_{50} than changes in gating.

(4) At small values of Θ (< 2) the relationship between EC_{50} and Θ will have an asymptote because the "+ 2" component of the sqrt(Θ + 2) in the denominator will dominate the expression. This is a crucial feature that leads to **Figure 3.2** and the behavior that facilitates ELFCAR (**see Chapter 3**).

Reference

1. Kalbaugh, T. L., VanDongen, H. M., and VanDongen, A. M. (2004) Ligand-binding residues integrate affinity and efficacy in the NMDA receptor, *Mol Pharmacol 66*, 209-219.

Appendix B

Single-Channel Data Analysis:

Theory and Practice

B.1 Theoretical Considerations in Single-Channel Recording

The aim of a single-channel recording experiment may be to determine an average open time (τ_{open}) and/or closed time (τ_{closed}), the probability that a channel is open (P_{open}), or to determine a set of several rate constants. Such rate constants can provide a detailed description of the transition probabilities between several kinetically distinct states. The nAChRs often have two main conductance levels termed *classes*. In this case the classes are conducting and non-conducting. Single-channel recording provides a *direct observation* of the agonist-induced interconversion between the conducting and non-conducting classes. However, in each class, there may be any number of *states*. States are thermodynamically and/or conformationally distinct physical manifestations of the channel which are *not directly observable* by measurement of current. Considering a 3-state kinetic model with one bound, closed state, **Figure B.1** characterizes the relationship between states and classes. The time spent continuously in a given class is known as a dwell (or sojourn), thus green lines represent closed dwells and red lines represent open dwells. In this case there are two closed states that have the same observable property (0 conductance) but are physically different (one has ligand bound (blue) the other is unbound

(yellow)). This type of process is known as an aggregated Markov process and the following discussion will outline the process for determining transition rates (kinetics) between states of aggregated Markov processes.

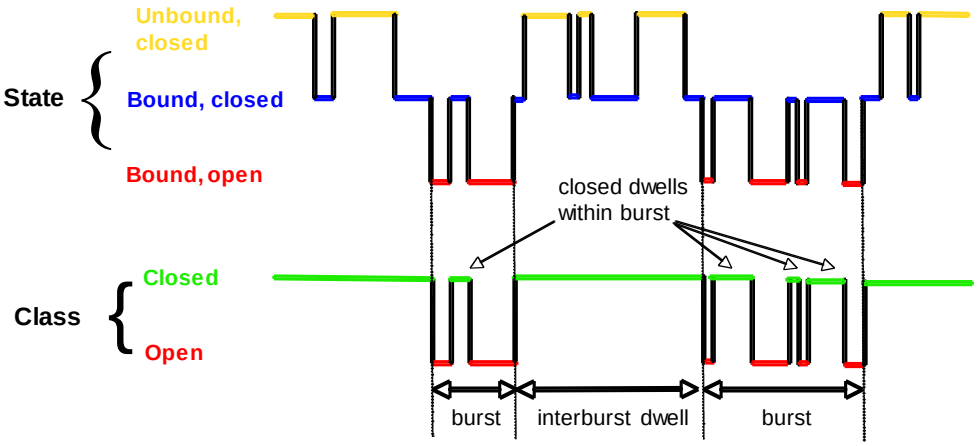

Figure B.1. Activity of a single ion channel. The observable class is open (red) or closed (green). The time spent in the open dwells is τ_{open}, while time spent in closed dwells is τ_{closed}. Single-channel recording can also be used to determine the transitions of a channel between various kinetic states (see text).

B.1.1 Homogeneous and Aggregated Markov Processes

In order to generate a set of rate constants, a model that relates the various states, which are hypothesized to be kinetically distinct, is proposed. In addition to bound versus unbound states, common examples of physically distinct states of the nAChR that are thought to correspond to kinetically distinct states include desensitized states, as well as open states in which only 0 or 1 of the 2 binding sites are occupied. These types of open states are termed unliganded and monoliganded, respectively. Desensitized states are ligand bound states that are non-conducting and don't arise from a gating transition(*1*).

The transitions of LGICs between open and closed in the presence of agonist are stochastic. Thus, the class that a channel is in at any given time is

independent of all classes that the channel was in previously. Moreover, the class of the channel after a time interval, Δt, depends *only* on the present class. For most single-channel data, the transition probabilities do not vary over time—they are stationary, homogeneous Markov processes. Thus, the interconversion of states of the receptor is characterized by being memoryless (Markov processes) and time independent (homogenous). If a record contains only one open channel at a time and much of the record is open, then the assumption of stationarity can be tested by comparing rate estimates from early bursts to rate estimates separately generated for later bursts. In single-channel experiments performed at high agonist concentrations (>> EC_{50}), the nAChR will usually be predominantly in the desensitized state. Typically, these states manifest as long non-conducting (closed) dwells and should be removed for P_{open} analysis and should be incorporated as additional non-conducting states in kinetic analysis.

B.1.2 Event Detection (Idealization)

In order to determine τ_{open}, τ_{closed}, and P_{open}, and perform detailed kinetic analysis, single-channel data must first be converted to a form that can be readily analyzed. In the case of detailed kinetic analysis, a variety of statistical calculations (particularly matrix algebra and log likelihood (LL) determination) are required. Since the gating of nAChRs, once agonist is bound, is proposed to take place nearly instantaneously(*2, 3*), the first step is to convert the data to a series of binary events—either open or closed. Once a section of data has been baseline corrected and cleaned-up as described below, the final step is to

translate it into a set of binary dwell times (assuming that no subconductances(*4*) are observed). This process, known as event detection (or idealization), prepares data for determination of dwell time and/or modeling by assigning each data point to one of the classes. Each such section of data analyzed may represent one or more bursts, or clusters at higher agonist concentrations.

One method for event detection involves assigning each data point to a class simply based on which class' current amplitude that data point's current value is closest to. This half-amplitude threshold detection method can be applied rapidly, particularly to filtered data (**Figure B.2**). Note that a high level of filtering will cause loss of information of brief events. The other event detection method that is used is segmental k-means (SKM) (**Figure B.2**). SKM is a statistical method, which uses a user-defined model to determine the most likely sequence of *states* present in the data. In each iteration of SKM, the model parameters are re-estimated and the most likely sequence of *states* re-determined. This process is iterated until the likelihood is maximized.

Once data are in the idealized form, we can ascertain information beyond measures of the single-channel current amplitude(s) of events in a patch. With hundreds or thousands (and sometimes tens-of-thousands) of events, detailed kinetic information about the states of the ion channel and interconversion between them can be obtained. We now have idealized single-channel data from which we can plot a histogram of either the time that the channel spends open or closed. Section B.3 of this appendix details how to produce these histograms in Clampfit 9.2.

Half-Amplitude Idealization (f_c = 20 kHz)

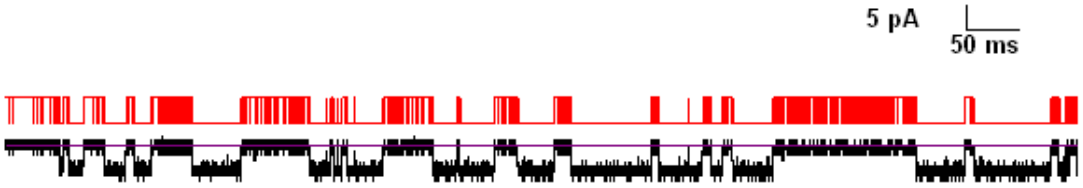

Half-Amplitude Idealization (f_c = 10 kHz)

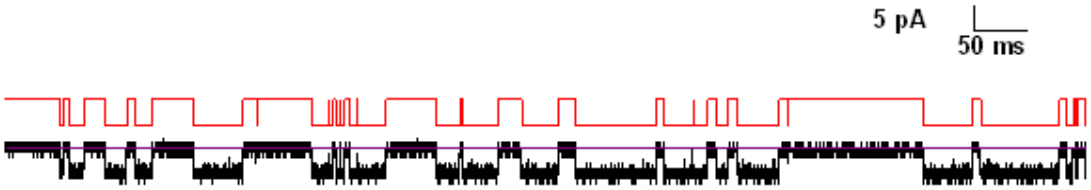

SKM Idealization (f_c = 20 kHz)

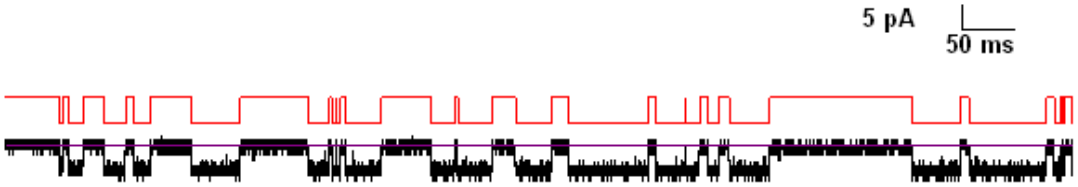

Figure B.2. Comparison of data and the event detected form of data (red lines). The 3 traces are each of the same 1.00 s section of data. Inward currents are displayed as downward deflections (cell-attached patch with 2 mM choline on $\alpha1_{W\alpha49F1\text{-}W}\beta1L9'S\gamma\delta L9'S$). These figures illustrate the relationship between idealized results and the data from which they are generated. In each case, the baseline was defined as the purple line. Upper) half-amplitude idealization of data that has been filtered at a cut-off frequency, f_c, of 20 kHz. Middle) half-amplitude idealization of data with f_c = 10 kHz. Lower) SKM idealization of data with f_c = 20 kHz. For half-amplitude idealization, the appropriate level of filtering is particularly important as can be seen from the *many* misestimations, mainly of brief openings from a closed state, at f_c = 20 kHz.

B.1.3 Probability Distribution Functions and Transition Rate Matrices

If detailed kinetic models for an ion channel are desired, the next step is to determine the components of the Q matrix(*5*), whose entries are the transition rates between different kinetic states. We start by fitting the dwell time histograms with probability density functions (pdfs), whose lifetimes in a given class equal a multiexponential with a number of components equal to the number of (unobservable) states in that class. The pdf for channel open (or closed) lifetime is an exponential distribution, and the mean of any pdf is given by:

$$\int_{-\infty}^{\infty} t f(t) dt.$$

This mean is the inverse of the sum of all transition rates leading out of the class, and can therefore be used to find the lifetime of the channel for any given state. Consequently, we can learn about the kinetics of a state provided that a probability density is present in the corresponding dwell time histogram. Thus, if there are multiple states in a class, the pdf for that class is a mixture of exponential densities for which:

$$f(t) = a_1\lambda_1 e^{-\lambda 1 t} + a_2\lambda_2 e^{-\lambda 2 t} + \ldots + a_n\lambda_n e^{-\lambda n t}.$$

and the probability of a *given* dwell time (t) in class a is given by:

$$f_a(t) = \pi_a e^{Q_{aa}t} \sum_{b \neq a} (Q_{ab}\mathbf{1})$$

Here, π_a is a row vector representing the equilibrium probabilities for the process to enter the states, and **1** denotes a column vector of ones of appropriate length. The joint probability distribution of the dwell time *series* a_1, a_2, …, a_L is often simplified as:

$$f(t,a) = \pi_{a_1} G_{a_1 a_2}(t_1) G_{a_2 a_3}(t_2) \dots G_{a_L a_{L+1}}(t_L)\mathbf{1}$$

where,

$$G_{a_1 a_2}(t_1) = e^{Q_{11}t} e^{Q_{11}t} Q_{12}.$$

Thus, for the case of X(t), a stationary Markov process in continuous time, the (finite) number of states, designated 1, 2, …, N, and the interstate transitions are given by the Q matrix, whose off-diagonal elements (q_{ij}) are the transition rates between states i and j. In more familiar terms:

$$q_{ij} = \lim_{t \to 0} \left[\frac{Prob(state\ j\ at\ time\ t+\Delta t | state\ i\ at\ time\ t)}{\Delta t} \right].$$

Considering, then, a 3-state model in which there is one conducting state (open, R^O) and two nonconducting states (desensitized, R^D) and (closed, R^C), we have:

$$R^C \underset{\alpha}{\overset{\beta'}{\rightleftharpoons}} R^O \underset{k_{-D}}{\overset{k_{+D}}{\rightleftharpoons}} R^D \quad . \qquad \textbf{(Model B.1)}$$

For **Model B.1**, the corresponding transition rate matrix is:

$$\begin{bmatrix} -k_{+D} - \alpha & k_{+D} & \alpha \\ k_{-D} & -k_{-D} & 0 \\ \beta' & 0 & -\beta' \end{bmatrix} .$$

Here β' is the apparent channel opening rate and α is the channel closing rate. The rate at which the channel enters R^D is k_{+D}, while k_{-D} is the rate that the channel re-enters the open state from R^D. In each case, the rates are related to dwell time histograms. For example, consider a channel that can be in only one of two states: R^C or R^O. In this case, every time the channel opens, it leaves the closed, non-conducting state. This represents the length of a dwell in the closed dwell time histogram. Thus, the channel opening rate, β, for this channel is the inverse of the average closed dwell times. The channel closing rate, α, for this

channel is the inverse of the average open dwell times. In **Model B.1**, β' is used to represent the fact that this rate may be concentration dependent. If that is the case, then it is the higher concentration values, where β' has an asymptote when plotted versus concentration, that represent the actual channel opening rate, β.

For more complex models with more states, the precise correlation between closed and open dwells and rate constants often becomes more complicated. For example, the transition rate matrix for a 5-state model (**Model B.2**) can be written. **Model B.2** allows openings from the monoliganded or doubly liganded closed states. Note that there are still only 2 classes: conducting and non-conducting.

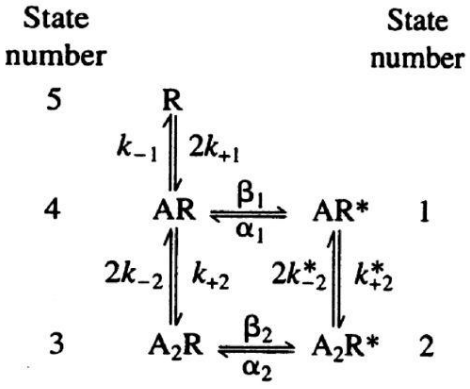

(Model B.2)

In this model, the opening rate constants are represented by subscripts indicating the number of ligands, for example, β_1 is the monliganded channel opening rate. The resultant Q matrix is:

$$\mathbf{Q} = \begin{array}{c} \\ 1 \\ 2 \\ 3 \\ 4 \\ 5 \end{array} \begin{array}{c} \begin{array}{ccccc} 1 & 2 & 3 & 4 & 5 \end{array} \\ \begin{bmatrix} -(\alpha_1 + k^*_{+2}x_A) & k^*_{+2}x_A & 0 & \alpha_1 & 0 \\ 2k^*_{-2} & -(\alpha_2 + 2k^*_{-2}) & \alpha_2 & 0 & 0 \\ 0 & \beta_2 & -(\beta_2 + 2k_{-2}) & 2k_{-2} & 0 \\ \beta_1 & 0 & k_{+2}x_A & -(\beta_1 + k_{+2}x_A + k_{-1}) & k_{-1} \\ 0 & 0 & 0 & 2k_{+1}x_A & -2k_{+1}x_A \end{bmatrix} \end{array}.$$

In order to determine what each transition probability (rate) is, we employ maximum likelihood estimation. In this technique, the goal is to determine the most likely value for the unknown parameter(s), Θ, given the observation of the data, x. The likelihood function is:

$$L(\Theta) = f(x_1, x_2, \ldots x_n|\Theta).$$

Most frequently, the logarithm is taken, and so the log-likelihood (LL) is the relevant function. In order to determine the values of the transition rates (unknown parameters) that best fit the observed data, the partial derivative of the LL is computed with respect to each parameter of interest. Thus, having characterized the likelihood surface, a search of that surface for the global maximum in all parameters is undertaken, giving the maximum likelihood estimation (MLE).

This procedure can be thought of as the inverse procedure of linear regression. Instead of using the data to generate a model, we are setting the model and determining the extent to which the data support that model—the LL. For the exact same set of data, the LLs for different models can be compared—higher LLs indicate a higher chance of generating the data actually found in the experiment from the postulated model. Of course, arbitrarily adding states to the

model will increase the global maximum on the likelihood surface, since the number of free parameters has been increased. Thus, if the number of states in a class cannot be determined with some confidence from that class' dwell time histogram, LLs are compared as states are added, until a plateau in LL is found (for example, see **Table 4.1**)(*6, 7*). For large data sets (> ~ 10,000 events, and LL/event ~ 5 or more), a criterion of ΔLL > 10 is often imposed.

B.1.4 Faster is Better—An Analytical Derivative of the Likelihood Function

In a key finding, Qin *et al.(7)* derived an analytical derivative of the likelihood function, thereby greatly decreasing the computational time necessary to maximize the likelihood function. This reduced computational time was also valuable since it facilitates increased comparison of the LL of various models, as well as increased fine tuning of dead time (τ_d). Moreover, their technique allows for rate constant constraints to be used, and for global fitting across multiple sets of experimental conditions (concentration, voltage, temperature, etc.)(*8, 9*).

B.1.5 Likelihood Surfaces

The more well-defined the likelihood surface and clearer the global maxima, the more likely the calculation will converge to the correct value. We will now consider several factors that affect the quality of likelihood surfaces. Each derives from experimental parameters, and so can be controlled by appropriate forethought in experimental planning.

Figure B.3 shows two dimensions (of several) for 3 likelihood surfaces(*7*). These represent variations in the ratio of the rate constant to the sampling rate at which the data were collected. Higher sampling rates (f_s), which correspond to lower $k\Delta t$, give a better-defined likelihood surface, which increases chances of a successful convergence and generally reduces computational time.

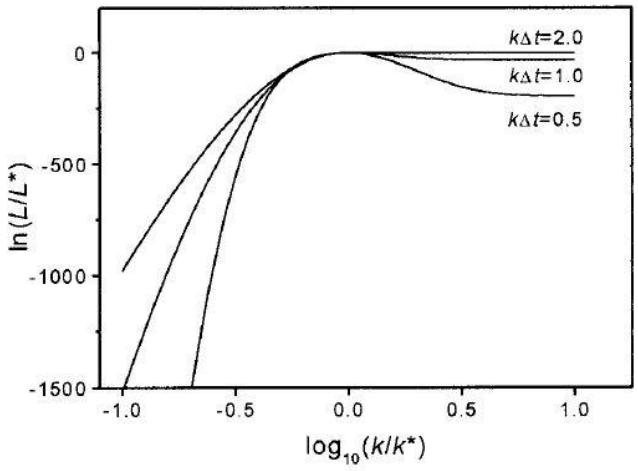

Figure B.3. The impact of sampling rate on the likelihood surface. Higher sampling rate (lower $k\Delta t$) sharpens the likelihood surface significantly over this fourfold range.

Figures B.4A and **B** demonstrate the impact of significant amounts of noise (standard deviations, σ, of 0.5, 1, and 2 times the current measured)(*7*). Not surprisingly, the likelihood surface for σ = 2 times the channel current (i.e., the signal-to-noise ratio (SNR) = 0.5) is almost entirely flat—this calculation would not converge since the noise is *larger* than the signal.

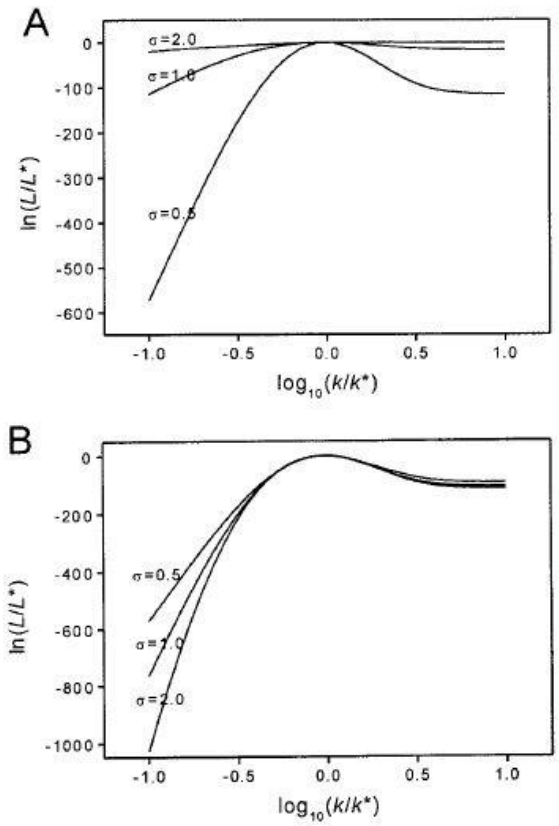

Figure B.4. Impact of signal-to-noise ratio (SNR) on the likelihood surface. Note that at these levels of SNR, if fast rate constants are being considered (> 1000 s^{-1}), then the data must be analyzed directly, without filtering. In the rig used for collection of most data for this thesis, typical RMS noise was 0.3–0.5 pA. Since most signals were 2–6 pA, this gave SNR of ~5–10 and thereby allowed for significantly faster rates to be considered, even with filtering. Interestingly, it was determined that the likelihood surface at the maximum can be made equivalent by collection of extra data. In this case, 60 times as much data is required for σ = 2.0 versus σ = 0.5(*7*).

It is also worth noting that, while adding more parameters increases the global maximum, it also flattens the maximum of the likelihood surface; thus if there are more parameters than actual states, the model will often not converge. This optimization method (with analytical derivative calculation of the likelihood slopes and missed event correction) was then incorporated into kinetic modeling software (along with standard MLE and SKM event detection) called QuB(*7, 10-*

12). Our methods for application of this software are similar to those published, and are outlined in the *Preparing for Data Analysis* section below.

B.2 Experimental Considerations in Single-Channel Recording

B.2.1 Signal Conditioning

In its most basic form, single-channel data recording just involves measurements of current over time. In order to obtain the best possible temporal resolution, a high sampling rate (f_S)—the number of data points taken per second (Hz)—is desirable. Specifically, according to the Shannon-Nyquist sampling theorem, the signal must be sampled at at least twice the rate of the fastest component of interest in the signal, otherwise distortion may occur (**Figure B.5**).

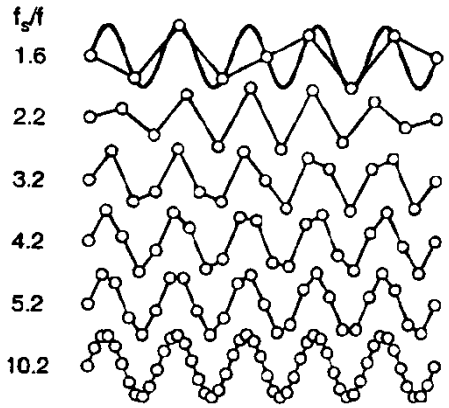

Figure B.5. Sampling rates slower than 2 times the fastest component do not accurately represent the signal. Usually > 2.5x the fastest rate is a safe cut off. More data (higher f_s) can be collected if the quantity is reasonable given available disk storage. This figure is from Chapter 3, Figure 2 of(*13*).

In the particular case of wild type muscle nAChR, the fastest rate constant (channel opening) is near the detection limit, so often it is desirable to use as high of a sampling rate as possible. Taking data at a high rate (i.e., > ~ 50,000

samples per second), though, results in significant noise. Even if the seal resistance is high, noise arising in the patch (shot noise, dielectric noise), the electrode (RC-noise, dielectric noise of electrode glass, flicker noise), and the pipette holder (dielectric noise, flicker noise) impact the baseline recording and greatly reduce the SNR. In order to eliminate these components, while preserving the integrity of the original signal, the data is low-pass filtered—the amplitude of signals with frequencies above a set cut-off frequency (f_c) are attenuated (**Figure B.6**).

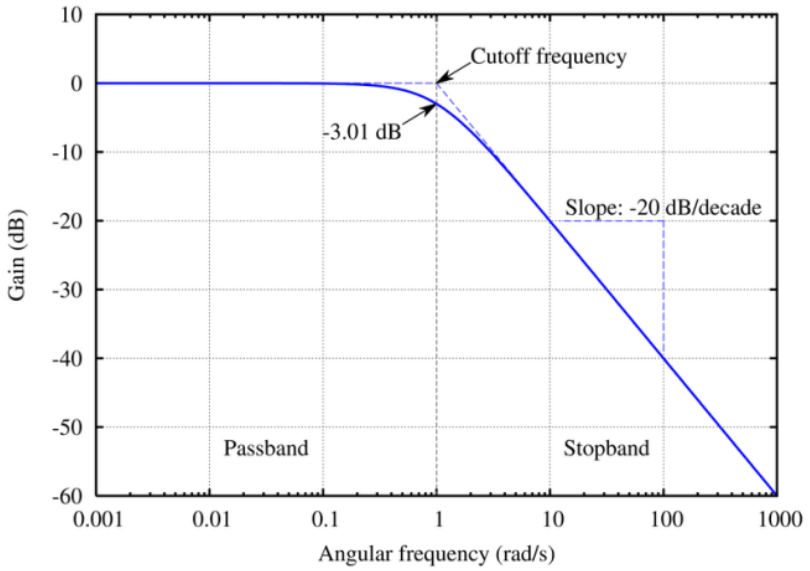

Figure B.6. The attenuation of a filtered signal is proportional to its frequency. This figure is from *The Axon Guide, 2nd Edition*.

Thus, low-pass filtering is the process by which the amplitude of events of duration less than $1/(f_c)$ are reduced proportional to the extent to which the event has duration shorter than f_c. High frequency events (e.g., fast, brief events) are eliminated while low frequency events are passed essentially unchanged (**Figure B.7**). This task of filtering can be accomplished electronically (through the use of

networks of capacitors and resistors) or by a mathematical algorithm that accomplishes an analogous transformation. The *important* consequence is that increasing filtering of the signal increases the SNR, but does so at the expense of losing information about fast events (**Figure B.7**).

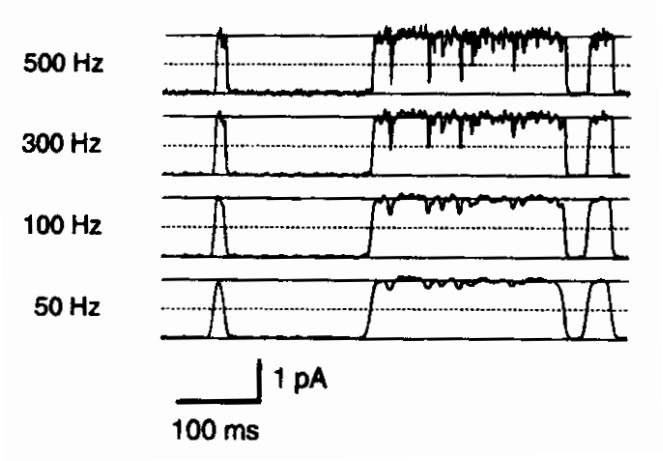

Figure B.7. An illustration of the impact of filtering. The same signal is filtered at 4 different cut-off frequencies (fc): 500 Hz, 300 Hz, 100 Hz, and 50 Hz. In this case, the open channel is displayed as an upward deflection and the dotted lines in each of the four traces represent the half-amplitude cut off. The long opening doesn't appear to have any brief closings when filtered at 50 Hz, yet it has several when only filtered at 500 Hz. The data will yield different dwell times and different rate constants depending on how it is filtered. This figure is from Chapter 3, Figure 5 of *(13)*.

Another consideration is the type of filter used. For single-channel analysis of the nAChR, in which moderate-to-high time resolution (> 1000 Hz) is desired, consensus has developed around using Bessel filters. Bessel filters, unlike Butterworth and Tschebycheff filters, introduce far less ringing (< 1% overshoot of initial signal amplitude; **Figure B.8**). For an 8-pole Bessel filter, the filter rise time (t_r), which is the time that it takes for the filter to go from 10% to 90% of the response, is given by:

$$t_r = \frac{0.3321}{f_c} \quad .$$

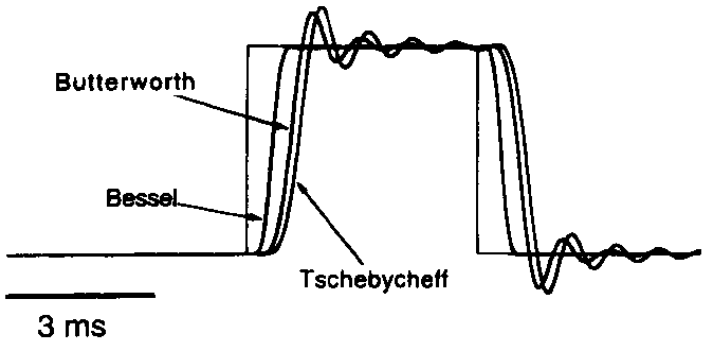

Figure B.8. Comparison of Bessel, Butterworth, and Tschebycheff filters. Only the Bessel filter does not introduce significant overshoot. This figure is from Chapter 3, Figure 3 of *(13)*.

This gives a measure of the time resolution of events that can be achieved when using a given level of low-pass filtering, because the amplitude of events shorter than t_r will be significantly diminished. For example, at f_c = 5,000 Hz, t_r = 0.3321/(5,000 s^{-1}) = 66.5 µs. Thus, events shorter than 66.5 µs will experience a significant reduction of amplitude when low-pass filtered with f_c = 5,000 Hz, and therefore be distorted or less likely to be detected during data analysis.

The second limitation on resolution is imposed by noise, which may reach the detection threshold (in the case of half-amplitude) or simply be miscategorized as being an event (in the case of SKM idealization). It has been found that the three most significant factors that enable attainment of very low noise, stable recordings (provided that the patch clamp amplifier noise has been minimized) are: the ratio of outer to inner diameter (OD:ID) of electrode glass, very small electrode pore diameter, and minimization of the depth of immersion of electrode in the bath(*14*). We consistently use thick walled glass in order to have a fairly large OD:ID. Moreover, the last of these (depth of electrode in

recording bath) can be controlled, since positioning of the electrode is done under a dissecting microscope. Unfortunately, the size of the electrode pore cannot be made too small as this will make the probability of finding one or more channels in a patch too low.

One of the most frequently observed types of noise is 60 Hz noise, which can arise from a number of everyday electrical components, including lights. In order to eliminate this noise, data may be notch filtered or have electrical interference removed subsequent to acquisition. Alternatively, a device is used that monitors the noise at this frequency and generates an equal but opposite signal, which is subsequently added to the original signal resulting in destructive interference of the noise. This device is called a HumBug (see Chapter 2), and it works fairly well, but can introduce noise of its own.

B.2.2 Preparing for Data Analysis of Single-Channel Records—Baseline Correction and Data Clean-Up

The data produced from a single-channel recording may be of several types. I'll highlight three types. (1) Often a record, even with a gigaseal, will show no channel activity. (2) In other cases, current variations may be seen that are not of the correct conductance or which exhibit dependence on some other property (such as mechanosensitive channels or voltage-gated channels) (**Figure B.9**). In any region of data for which such channel activity is present, the data are usually discarded—frequently this involves discarding the whole record. (3) On the other hand, for the nAChR, if clear current transitions are visible

(binary, assuming that there are only 2 classes), then these current variations can be correlated to channel events—actual openings and closings (**Figure B.10**).

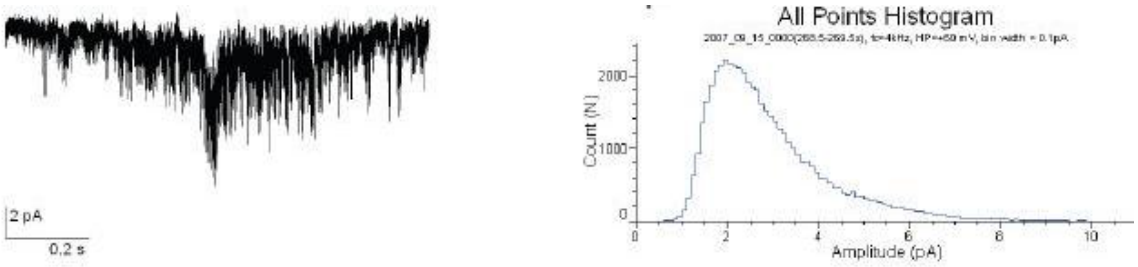

Figure B.9. Left) 1.00 seconds of messy data. There are no clear conductance levels, rather the current fluctuations likely correspond to an endogenous channel (mechanosensitive or voltage-gated) or low seal resistance. Right) The corresponding all points histogram for the data at left. There are clearly *not* two classes.

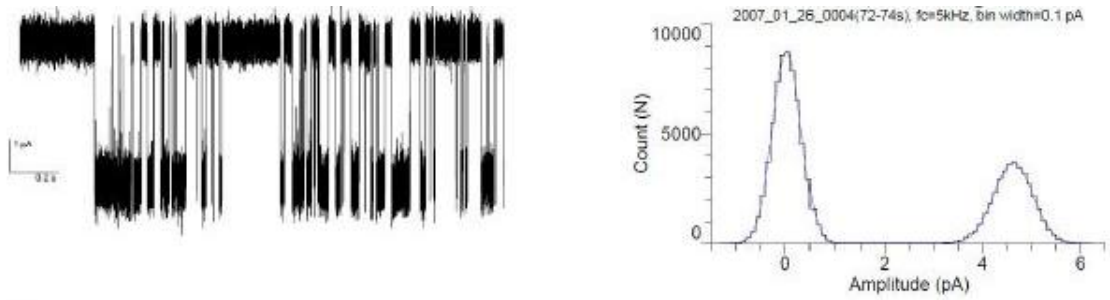

Figure B.10. Left) single-channel data for a cell-attached configuration of an nAChR ($(\alpha1_{W149F1W})_2\beta1L9'S\gamma\delta L9'S$) with 2.0 mM Ch in the pipette. Openings are shown as downward deflections and qualitatively exhibit two different levels (classes). Right: a ll points histogram corresponding to the 2 seconds of data shown at left. There are clearly two distinct components in the histogram—0 pA for the closed state and ~4.6 pA for the open state. Since this recording was at a pipette potential of +70 mV, the single-channel conductance is ~ 66 pS.

The first step in preparing a single-channel recording for data analysis is to correct for any gross irregularities in the record. These may result from sudden changes in the seal resistance, or gradual deterioration of the seal, which can cause a sloping baseline. A sloping baseline may be corrected by manual

re-estimation (by eye). If a record has been chosen that exhibits any background channels (mechanosensitive, voltage-gated, etc.), then those regions must be completely excluded. Lastly, channel events that are decidedly abnormal—i.e. events that do not reach full amplitude or that do not reach full amplitude within ~ 100 μs—are excluded.

In the data clean-up procedure (**Figure B.11**)(*15*), the goal is to ensure that each current fluctuation that deviates from baseline actually corresponds to current flowing through the ion channel(s) of interest in the patch. Although **Figure B.11** clearly shows that type (a) events are qualitatively different than the main channel events in this record, a more quantitative approach may be in order. In this case, data clean-up may amount to going through some sections of the data point-by-point in order to make quantitative determinations about event amplitude and duration before a decision about inclusion is made. We take the additional precaution, where possible, of analyzing the excluded data, especially of type (a), in order to ensure that the current deflections are below the time resolution of the experiment, do not reach full amplitude, or are a different type of current peak. Often, we include type (a) data in the final analysis, where they produce an additional component of the open dwell time histogram. Type (b) events: the case that a channel of significantly different amplitude (single-channel conductance) is seen, it is removed. Type (c) events: these types of current readings may also occur when a channel is near or under the electrode rim. For a variety of reasons—mechanical instability, physical disruption by particles in the bath media, disruption of membrane integrity, etc., the seal resistance may

be quickly altered. The case of cleanup for events of type (a) can be more difficult, as these events sometimes reach half-amplitude or more. These types of events have been attributed to ‘kinetic heterogeneity’ of the receptor(*15*).

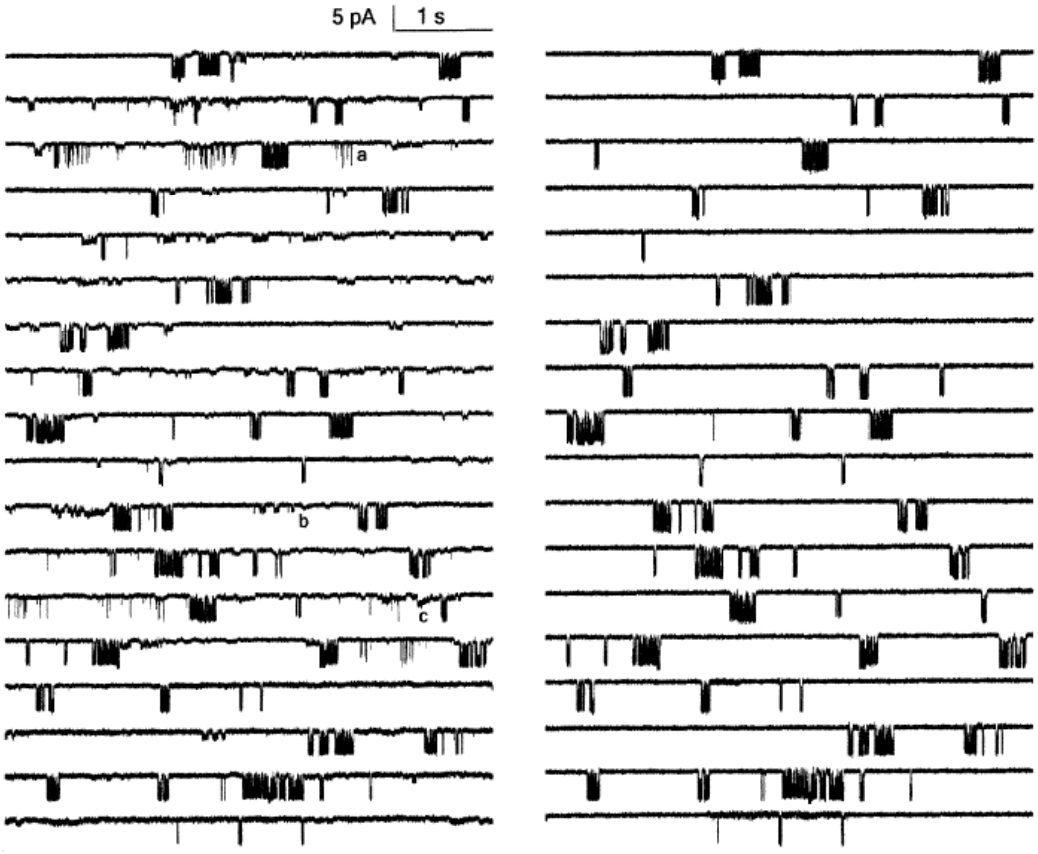

Figure B.11. Single-channel data clean-up procedure. Channel openings are shown as downward deflections. Left) The original data that was collected. Right) Final cleaned-up data that is actually analyzed; see text for description. Figure and description are from(*15*), with differences in procedure noted in text.

Once the data have been cleaned up as described, a histogram of all of the data points (current values—all points histogram, as in **Figure B.10**) can tell us about the number of channels in the patch (at least a lower estimate, as some channels may be desensitized). This histogram can also give an estimate of the percentage of time that the channels are open, and the percentage of time that

multiple channels are open at overlapping times. Additionally, if only one channel is active, the current amplitude can be calculated as the difference between peak of the open distribution and the peak of the closed (or baseline) condition. Even a short recording may give unambiguous data. Note that oftentimes the open state exhibits more current noise than the closed state. An example of this is the larger width of the component at 4.6 pA in the all points histogram in **Figure B.10,** Right than the width of the closed component at 0 pA. For ion channels in general, this is at least partially due to so-called 'transport' or 'shot' noise, which arises from the statistical nature of ions being translocated over a potential barrier. In the case of the nAChR in particular, a larger variation in amplitude of the open state is sometimes attributed to thermal fluctuations of channel structure, which cause concomitant fluctuations in channel conductance (termed 'channel breathing')(*16*). At high concentrations, it may be caused by agonist associating with the channel pore, which is termed 'open channel block'.

B.3 A Brief Guide to Single-Channel Data Analysis in Clampfit 9.2

The procedures for pre-processing data in Clampfit 9.2 (version 9.2.0.11), performing a single-channel search (event detection), and producing and fitting all points, open, and closed dwell time histograms are briefly outlined here. For applications and examples, see the relevant analyses in each chapter. For more detailed examples of data analysis, see my lab notes (Word files with associated Excel summary files (P_{open} and τ_{crit}, and physical data sheets).

1. Open the file to be analyzed (as an '**Analysis**' window in Clampfit): '**File/Open Data…**'.
    a. If needed, select sections with channel activity (clusters and/or bursts depending on the analysis) and save as a new file ('**File/Save As…**'). When saving a new file, be sure to specify under '**Current Options**' the data range to be used. The parameters can be changed by clicking the '**Options**' button. It is usually easiest to select '**Duration of window**' and set the window to the desired data before saving the data segment. I also check '**Start first data point at time 0**' and note the actual time range in the file name.
    b. If selection of a data subset is performed at this stage, this process is merely '**by eye**' selection and could alter resultant calculated values of desensitization (clusters) and agonist binding (bursts). However, most of the following analysis is intended for data which is ~ 500–10,000 events (i.e., ~ 100 ms to 100 s of nAChR activity), so some sectioning of data is often recommended. I don't recommend trying to work with data sets of > 10,000 events in Clampfit 9.2, which may crash or freeze during event detection.
2. Pre-process the data.
    a. Filter the data with '**Analyze/Filter...**'.
        i. The level of filtering will depend on the initial bandwidth in which the data were recorded and the anticipated fastest

rate constants of interest, as well as the seal resistance/RMS noise of the particular section of data to be analyzed. Generally:

ii. Select '**Lowpass**' at the top of the box.

iii. In the lowpass section, under '**Type**', select **Gaussian filter**.

iv. Set the '**-3 dB cutoff (Hz)**'. For first filtering of data, usually use between 2,000 and 10,000 Hz.

v. At the bottom of the box, under '**Trace Selection**', select the '**Region to filter**'. Almost always, this is the '**Full trace**'.

vi. Click OK. The filtering may take a while; for large (> ~ 10 MB) files and for files of up to several minutes of data (with a sampling frequency, $f_{s,}$ of 50 kHz), filtering may take a few minutes.

vii. '**File/Save As…**' a new file. (Since filtering *can't be undone* in Clampfit).

b. '**Analyze/Adjust/Baseline…**'.

i. This process is only needed if there is significant variation or slope in the baseline (non-conducting class). Baseline adjustment is especially important if there are sudden shifts in the baseline, which can make subsequent analysis difficult.

ii. For baseline drift in a file, use '**Subtract slope of**:' and specify region. This is very rare in single-channel recording, but the same correction can be applied for whole-cell data.

iii. For sudden baseline shifts, use the '**Adjust manually'** option.

1. Left-click on the line to create new (yellow) square handles and position them with the left mouse button (right-click to delete). The pink line in-between the yellow squares specifies where the new baseline will be.

NOTE that steps a and b can be done in either order. If extreme low-pass filtering is being used, it might be best to set the baseline first (but not if it is too difficult to determine the baseline from the original signal). Also, for early analysis and/or analysis that may be performed at multiple different levels of low-pass filtering, I recommend adjusting the baseline first. Similarly, this may be preferable for analysis that will be performed at multiple different dead times (τ_d).

3. Determining current levels and single-channel conductance.

a. Create all points amplitude histogram:

i. Choose '**Analyze/Histogram…**'.

ii. Under **Distribution**, select '**Conventional**'.

iii. Under Bins, enter the desired width. For conventional histograms, the unit is pA. Usually 0.1 or 0.2 pA is a good

bin width, but considering using larger values for smaller data sets (< ~ 100,000 data points).

iv. In the **Data** box, select the desired '**Region to process**:' (usually **Full trace**) and in the **Data Range** box, check **Full**.

v. Select **OK** and the histogram will appear in a new 'Graph' window. For large data sets (> 50,000,000 data points), this could take a minute or two.

vi. If there is only ever one channel open, and the baseline is good, then this resulting 'all points histogram' should have two clearly defined components, one corresponding to closed, the other to the open channel current.

vii. Fit the all points histogram using: '**Analyze/Fit…**'. I usually fit with the **Predefined Function: 'Gaussian'** and set the '**Number of terms(n)**' to 2. In the **Data/Options** tab, make sure that '**Compare Models**' is not checked. In the '**Seed Values**' tab, check the values to see if they make sense based on the histogram and your guess about the open channel current from the data. If not, change them.

viii. If P_{open}/NP_{open} is << 0.05, then it can be difficult to get Clampfit to fit the smaller area component. If you're having lots of trouble fitting this histogram even after altering some of the '**Seed Values**', consider fixing some of these values. If that doesn't work, consider just zooming in on the y axis

and determining the peak of the component by eye. This will produce a reliable estimate if there are lots of data points (e.g., for a long record with low NP_{open}).

NOTE: Clampfit fits what it can 'see' on the screen.

b. Determine the conductance (technically chord conductance, g).

i. Take the fitted (or by eye) open channel current value and apply Ohm's law (V = I*R) to calculate the single-channel conductance. For example, if the observed open channel current is 4.1 pA and the applied pipette potential was 60 mV, then the patch potential was ~ 60 mV (see Chapter 2 for supporting data). In this case, the single-channel conductance is:

$$g = R^{-1} = \frac{I}{V} = \frac{4.1\ pA}{0.060\ V} = 68\ pS.$$

1. If there are multiple conductances/subconductances, their values can be calculated in the above way as well, as long as they are present in the all points histogram. If not, then use the open dwell time current values for these below to calculate the corresponding subconductance values.

c. Format the title and axes as desired in the '**Graph Window Properties**' box, by double-clicking on the graph. This applies for all histograms, including the open and closed dwell time histograms, below.

i. In the '**General**' tab, set the graph name.

ii. For direct comparisons of a series of mutants or agonists, it is desirable to use the same axes/scales. This applies to the open and closed dwell time histograms, below, too. These can be set in the '**X Axis**' and '**Y Axis**' tabs.

iii. In the '**Plots**' tab, increase the line thickness of the plots and fitted data to 3 or 4.

iv. In the '**Color/Fonts**' tab, use large fonts (> 18 point for axes/labels, > 26 point for title) if exporting for display in PowerPoint so that they can be read.

*Note that the following section on event detection can often require multiple iterations at different parameters, such as levels of filtering of the original data file (varying f_c), the level set for the open current, varying dead time (changing the '**ignore short level changes**' duration), etc. These iterations should be performed for a single file for each mutant/agonist/concentration to be analyzed until satisfactory results are obtained, then applied to other files at the same conditions. The results will be satisfactory and worth pursuing once they are stable to small variations in analysis parameters, produce a number of events that is statistically meaningful and not too large for efficient analysis, and generally allow for efficient use of the time of the person doing the analysis. Putting in extra time at this stage can save a lot of time in analysis in later steps.*

It is worth considering comparing a given event detection of a file to event detection (both half-amplitude and SKM) performed in QuB from time to time. Both the level of misdetections and resulting fitted open and closed dwell time histograms should be compared. In some cases, I found that analysis to be faster in QuB. The downsides are that in QuB it is not as easy to have direct control of the data, such as for pooled histograms, user determination of τ_{crit}, and presentation of data. In general it is more automated. I won't provide a complete guide on analysis in QuB here, but sections B.1 and B.2 of this appendix (above) contain significant information on the theory behind the analysis used, including in QuB. Section B.2.2 contains a description of preparing data for analysis in QuB. In Chapter 4 I show some results of applied analysis using QuB. Other analyses can be found in my lab notes. They are often titled 'Word Reports' from QuB. More information (and free download of all software) are available at: http://www.qub.buffalo.edu/wiki/index.php/Main_Page. A detailed description of the features and use is available in the online QuB manual at: http://www.qub.buffalo.edu/wiki/index.php/Outline. There is a printed copy of an old version of the QuB manual in lab.

4. Use half-amplitude criterion for event detection.
    a. '**Event Detection/Single-channel Search…**'.
    b. Set the values. In '**Levels**', level 0 (pA) should be the baseline value. For good or adjusted baselines, this should be close to 0.0 pA. One additional level (level 1) is automatically added. Set this value to the open channel current. Ideally these values come from

the all points histogram produced above in step 3. The green line on the y-axis will adjust accordingly when these values are adjusted. If an all points histogram has not been produced, zoom into a few open dwells and physically place the green line in the middle of the noise for the closed and open states. For analysis of multiple conductances, click '**Make**' to add additional levels and set their current values as above.

c. Decide if you want to have a dynamic analysis.
    i. Check '**Update levels automatically**' if the baseline is not stable. If the open current is stable, select '**Update baseline, keep deltas**', otherwise, select '**Update all levels independently**' if the open current and baseline vary over time.
    ii. Note that if there is a variation in the open channel current or duration, it probably indicates either kinetic heterogeneity of the receptors or some other change. This must be considered separately later as part of the analysis by viewing the stationarity of both the open/closed dwell times and the open/closed dwell currents. However, an automatic, dynamic analysis can provide a useful tool for a first rapid analysis of a file, especially when combined with the '**Accept Entire Category**' feature (see below).
d. Set the dead time (τ_d). All events shorter than τ_d are ignored.

i. Initial τ_d selection will depend on a number of factors, including level of filtering (see above).

ii. In Clampfit, dead time is set in the '**Ignore short level changes**' box. You can set a duration and decide to apply this dead time to all levels, or some subset. Typically starting parameters are τ_d = 100 µs; with a range of 40 µs–300 µs being common.

e. Set the '**Search Region**'. This is usually the '**Full trace**', especially for sectioned data.

f. Start the single-channel search by clicking '**OK**'. The event viewer is displayed automatically, along with the first event.

g. You can now manually accept (**a**), reject (**r**), suppressed (**s**), or accept and tag (**t**) each event. Keyboard shortcuts are in parenthesis. If you change your mind on a given event, its selection can be undone (**u**). If a specific criterion for accepting events, such as 80% of the conductance, is being applied, this can be done by accepting the event and using the event monitor ('**Event Detection/Event Monitor…**') to compare each event's duration and amplitude with the average of all previously accepted events for the file.

h. For a rapid, first pass analysis, you can use: '**Event Detection/Accept Entire Category**'. Do this for each level. Once selected for the final level, Clampfit will automatically detect and

accept events based on the values set in the initial single-channel search. A quick comparison of the number and types of mis-estimations can be a good gauge of what parameters in the single-channel search should be changed and in what direction.

i. Once the search is completed, all of the corresponding data will be in the Results sheet. I recommend going to: '**Event Detection/Event Statistics…**' and copying the data corresponding to each level to the clipboard, then pasting in lab notes. This gives a quick overview of the number of events detected and their average amplitude and dwell time.

j. The data at this stage will have blue lines (for closed dwells) and red lines (for open dwells). I often print a copy of these data ('**File/Print…**'), then quit the event detection and print a copy of the pure data to pdfs. In each case, the exact parameters of what is printed are controlled under '**File/Page Setup…**'. Under '**Printed Windows**', the '**Number per page**' is the number of lines of data. I usually do 4–10 per page. The '**Width**' is the number of data points. The '**X units**' unit is ms. Under items to print, I uncheck everything except '**Scale bars**'.

5. Plot logarithmic histograms of open and closed dwell times

   a. Go to the **Results** window. It is a good idea to save a copy of this now with a new file name.

b. Click on the '**Dwell Time**' column and go to '**Analyze/Extract Data Subset…**'. Usually I want open and closed dwells separately with no other specifications. To do this, click: '**Condition 1**' and under the '**Column**' drop down menu, select '**C: Level**', then under Inclusive range, select '**From 1 To 1**' for open dwells. On the right, select a Destination sheet and click '**Apply**'. Then, do the same for closed dwells by selecting '**From 0 To 0**' and selecting a separate destination sheet.

c. To produce the histogram, go to '**Analyze/Histogram…**'.

d. Under Distribution, select '**Logarithmic**'.

e. Under **Bins**, enter the desired width. For dwell time histograms, the unit is bins/decade. Usually 6–8 is a good bin width, but consider using larger values for larger data sets (several thousand events).

f. In the **Data** box, select the desired '**Row Range**' (usually **Full Column**) and in the **Data Range** box, check **Full**.

g. Select **OK** and the histogram will appear in a new '**Graph**' window.

6. Format and fit the dwell time histograms. The process is the same for open and closed dwell time histograms.

   a. Format the histogram by taking the square root of the y axis and rescaling.

b. Scale the x-axis to contain all of the dwell times that you wish to include in your fit. Generally don't include dwell times below your dead time.

c. Set to '**Analyze/Fit…**'. I usually fit the dwell time histograms with the Predefined Function: '**Exponential, log probability**'. Set the number of components (parameters) under '**Number of terms (n)**'. If you don't know how many components there are, then you can go to the '**Data/Options**' tab and select '**Compare Models**', then set the '**Confidence Level**' (usually 0.95).

d. Now click '**OK**' and a line will be fit to the histogram.

e. As with the all points histogram, parameters in the '**Data/Options**' tab and '**Seed Values**' tab can be altered to optimize the fit. I recommend that after each fit performed, you go to '**Analyze/Fitting Results…**' and copy the results to the clipboard and paste into lab notes.

*Many other types of analyses are possible in Clampfit; see the **Help** menu for further guidance. Another useful resource is the Axon CNS Guide: mdc.custhelp.com/euf/assets/images/Axon_Guide.pdf.*

B.4 References

1. Auerbach, A., and Akk, G. (1998) Desensitization of mouse nicotinic acetylcholine receptor channels. A two-gate mechanism, *The Journal of general physiology 112*, 181-197.
2. Maconochie, D. J., Fletcher, G. H., and Steinbach, J. H. (1995) The conductance of the muscle nicotinic receptor channel changes rapidly upon gating, *Biophysical journal 68*, 483-490.
3. Zhang, Y., Chen, J., and Auerbach, A. (1995) Activation of recombinant mouse acetylcholine receptors by acetylcholine, carbamylcholine and tetramethylammonium, *The Journal of physiology 486 (Pt 1)*, 189-206.
4. Hamill, O. P., and Sakmann, B. (1981) Multiple conductance states of single acetylcholine receptor channels in embryonic muscle cells, *Nature 294*, 462-464.
5. Colquhoun, D., and Hawkes, A. G. (1982) On the stochastic properties of bursts of single ion channel openings and of clusters of bursts, *Philosophical transactions of the Royal Society of London 300*, 1-59.
6. Qin, F., Auerbach, A., and Sachs, F. (2000) Hidden Markov modeling for single channel kinetics with filtering and correlated noise, *Biophysical journal 79*, 1928-1944.
7. Qin, F., Auerbach, A., and Sachs, F. (2000) A direct optimization approach to hidden Markov modeling for single channel kinetics, *Biophysical journal 79*, 1915-1927.
8. Gupta, S., and Auerbach, A. (2011) Mapping heat exchange in an allosteric protein, *Biophysical journal 100*, 904-911.
9. Gupta, S., and Auerbach, A. (2011) Temperature dependence of acetylcholine receptor channels activated by different agonists, *Biophysical journal 100*, 895-903.
10. Qin, F., Auerbach, A., and Sachs, F. (1996) Estimating single-channel kinetic parameters from idealized patch-clamp data containing missed events, *Biophys J 70*, 264-280.
11. Qin, F., Auerbach, A., and Sachs, F. (1997) Maximum likelihood estimation of aggregated Markov processes, *Proceedings 264*, 375-383.
12. Qin, F. (2004) Restoration of single-channel currents using the segmental k-means method based on hidden Markov modeling, *Biophys J 86*, 1488-1501.
13. Sakmann, B., and Neher, E. (1995) *Single-channel recording*, 2nd ed., Plenum Press, New York.
14. Benndorf, K. (1995) Low-Noise Recording, In Single-Channel Recording, pp 129-145, Plenum Press, New York.
15. Elenes, S., and Auerbach, A. (2002) Desensitization of diliganded mouse muscle nicotinic acetylcholine receptor channels, *The Journal of physiology 541*, 367-383.
16. Läuger, P. (1995) Conformational Transitions of Ionic Channels, In Single-Channel Recording, pp 651-662, Plenum Press, New York.

Appendix C

Other Possible Names for ELFCAR

CRARDMCA
Coupling of Residues in an Allosteric Receptor Determined by Mutant Cycle Analysis

CRAPMCA
Coupling of Residues in an Allosteric Protein Determined by Mutant Cycle Analysis

CONARAR
Coupling Of Non-Adjacent Residues in Allosteric Receptors

FCARDMCA
Functional Coupling in Allosteric Receptors Determined by Mutant Cycle Analysis

SIDRFC
Screen for the Identification of Distant Residues that are Functionally Coupled

SLIAR
Screen for the identification of Long-range Interactions in Allosteric Receptors

SLIMCA
Screen for Long-range Interactions by Mutant Cycle Analysis

SLIMCAAR
Screen for Long-range Interactions by Mutant Cycle Analysis in an Allosteric Receptor

SDCDRAR
Screen for Determination of Coupling of Distant Residues in an Allosteric Receptor by Mutant Cycle Analysis

LIARMCA
Long-range Interactions in an Allosteric Receptor determined by Mutant Cycle Analysis

LARDMCA
Long-range interactions in an Allosteric Receptor Determined by Mutant Cycle Analysis

LARDRMS
Long-range interactions in an Allosteric Receptor Determined by Reporter Mutation Screen

Miscellaneous targeted choices:
DRACULA
Distant Residues of Allosteric receptors CoUpling identified by mutant cycLe Analysis

SICNARALR
Screen for the Identification of Coupled, Non-Adjacent Residues of an ALosteric Receptor

CALTECHNAR
mutant Cycle Analysis of Long-range Transmission of Events of a CHemical Nature in Allosteric Receptors

SOCAL
Screen Of Coupled residues in an ALosteric receptor

DRCARFARM
Determination of Remote Coupling of residues in an Allosteric Receptor FAcilitated by Reporter Mutation

The following are a bit longer and less elegant:
RMIFLCAR
Reporter Mutation for the Identification of Functional Long-range Coupling in an Allosteric Receptor

RMSFCNARAR
Reporter Mutations as a Screen for Functionally Coupled, Non-Adjacent Residues in Allosteric Receptors

MCASLCAR
Mutant Cycle Analysis Screen for determination of Long-range Coupling in an Allosteric Receptor

MCASCDRAR
Mutant Cycle Analysis Screen for the determination of Coupling of Distant Residues in an Allosteric Receptor

MCADCRAR
Mutant Cycle Analysis for the determination of Coupling of Residues in an Allosteric Receptor

MCATILFCAR
Mutant Cycle Analyis for The Identification of Long-rage Functional Coupling in an Allosteric Receptor.

MCALCAR
Mutant Cycle Analysis of Long-range Coupling in an Allosteric Receptor

MCARLIRAR
Mutant Cycle Analysis Reveals Long-range Interactions of Residues in an Allosteric Receptor

MCAIDCR
Mutant Cycle Analysis for the Identification of Distant Coupled Residues